University of Bath

PHD

The influence of thermal corrosion upon the mechanical properties of nuclear graphites.

Pickup, I. M.

Award date:
1984

Awarding institution:
University of Bath

Link to publication

Alternative formats
If you require this document in an alternative format, please contact:
openaccess@bath.ac.uk

Copyright of this thesis rests with the author. Access is subject to the above licence, if given. If no licence is specified above, original content in this thesis is licensed under the terms of the Creative Commons Attribution-NonCommercial 4.0 International (CC BY-NC-ND 4.0) Licence (https://creativecommons.org/licenses/by-nc-nd/4.0/). Any third-party copyright material present remains the property of its respective owner(s) and is licensed under its existing terms.

Take down policy
If you consider content within Bath's Research Portal to be in breach of UK law, please contact: openaccess@bath.ac.uk with the details. Your claim will be investigated and, where appropriate, the item will be removed from public view as soon as possible.

Download date: 05. May. 2023

THE INFLUENCE OF THERMAL CORROSION UPON THE MECHANICAL PROPERTIES OF NUCLEAR GRAPHITES.

Submitted by I.M. PICKUP

for the degree of PhD

of the University of Bath

1984

Copyright

Attention is drawn to the fact that copyright of this Thesis rests with its author. This copy of the Thesis has been supplied on condition that anyone who consults it is understood to recognise that its copyright rests with its author and no quotation from the Thesis and no information derived from it may be published without the prior written consent of the author.

This Thesis may be made available for consultation within the University Library and may be photocopied or lent to other libraries for the purposes of consultation.

Signed. ..... Ian M. Pickup.

ProQuest Number: U345907

All rights reserved

INFORMATION TO ALL USERS
The quality of this reproduction is dependent upon the quality of the copy submitted.

In the unlikely event that the author did not send a complete manuscript
and there are missing pages, these will be noted. Also, if material had to be removed,
a note will indicate the deletion.

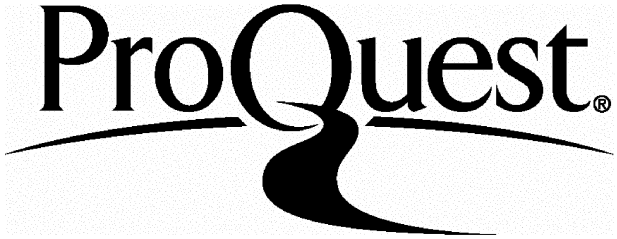

ProQuest U345907

Published by ProQuest LLC(2015). Copyright of the Dissertation is held by the Author.

All rights reserved.
This work is protected against unauthorized copying under Title 17, United States Code.
Microform Edition © ProQuest LLC.

ProQuest LLC
789 East Eisenhower Parkway
P.O. Box 1346
Ann Arbor, MI 48106-1346

UNIVERSITY OF BATH
LIBRARY
22 AUG 1984
PHD
25

X604210404 R

ABSTRACT

Two nuclear grade graphites, IM1-24 and PGA-AGL, have been thermally oxidised in an atmosphere of 5% CO/CO_2 at 900°C. Under these conditions the oxidation rate is controlled by the rate of chemical reaction. This produces an even weight loss principally from the internal surfaces. The effect of oxidation upon four mechanical properties has been studied; these are bend strength, σ_b, critical stress intensity factor, K_c, the elastic modulus, E and effective surface energy, γ. It was found that these properties were reduced by 50% as a result of approximately 7% weight loss.

Thermal oxidation is highly selective, attacking prismatic edges rather than basal planes. This results in the preferential development of filamentary shaped pores in domain structure in the binder phase of the graphites. It has been shown that the development of these high aspect ratio pores is extremely detrimental to the elastic modulus and effective surface energy (more detrimental than if there had been equal development of all classes of pore). The reduction in E and γ account for the observed reduction in K_c. The critical defect size was found to be larger than any individual microstructural feature and thus required sub-critical development of the flaw. Upon oxidation the critical defect size did not significantly alter, nor did the observed fracture mechanism. The strength reduced as a consequence of reduced tolerance to flaws as K_c reduced with oxidation. An analytical fracture model was used to relate the oxidation induced changes in microstructure with mechanical property changes.

Stress induced acoustic emission was monitored during flexural strength testing to aid evaluation of sub-critical failure events. It was found that acoustic emission, in terms of onset stress, total counts to failure and amplitude distribution, was characteristic of the graphite microstructure, more specifically the fine scale optical texture. The onset stress is believed to be representative of the cleavage strength of contiguous areas in the grains of the graphites which have common basal plane orientation. These areas are believed to dominate sub-critical flaw development.

CONTENTS

CHAPTER 1

INTRODUCTION

Graphite has been used for almost 40 years in nuclear reactors as a moderator and reflector material, because of its strength and high temperature stability, as well as its favourable nuclear properties. In gas-cooled reactors, graphite may be subjected to a combination of : (i) nuclear radiation; (ii) medium-to-high temperature (150-800^{o}C); (iii) a mildly corrosive atmosphere from the coolant. In magnox reactors, in which carbon dioxide is the primary, heat-exchanging medium, coolant attack of the moderator is insignificant because of the low temperature (150-400^{o}C). However, in Advanced Gas-Cooled Reactors (300-650^{o})carbon dioxide within the pores of the graphite is subjected to radiolysis, creating active species, capable of gasifying the surrounding moderator. Thermal corrosion of graphite with carbon dioxide is only significant at the highest temperature in the gas circuit of Advanced Gas Cooled reactors.

The strength and modulus of graphite is reduced severely by corrosion, whether due to radiolytic or thermal oxidation. For a given weight loss, radiolytic corrosion is generally less detrimental to mechanical properties than thermal corrosion. However, because of its importance in the nuclear industry, the effects of radiolytic corrosion on the mechanical properties of nuclear graphite have received more attention than the effects of thermal oxidation. Whilst thermal corrosion will not be a significant factor in controlling the reactor life, a greater understanding of its

effects upon the fracture properties of nuclear graphites will compliment studies of the effects of radiolytic oxidation and provide a more complete appreciation of the effects of corrosion in general. Much early work in this area consisted of surveys of the effects of progressive oxidation upon strength and modulus of graphite, often in order to obtain design parameters for nuclear reactor engineers. In recent years there has been much interest in applying the concepts of fracture mechanics to ceramic materials, including graphite.The resulting improvements in our understanding of fracture in graphites, warrant new studies of the effect of corrosion on the strength of graphite.

This thesis describes an investigation of the effects of thermal oxidation upon the strength of nuclear graphite and attempts to identify critical factors in the microstructure controlling the strength and fracture processes. In addition to providing information which is relevant to the performance of nuclear graphites, such a study will also provide an interesting model system for investigating the effects that systematic variation in porosity have upon fracture of electrode graphites and other porous ceramics. In many early studies the effect of oxidation up to about 50% weight loss was studied. The strength of graphite may be halved by as little as 10% weight loss due to thermal oxidation and therefore, in this study, oxidation was limited to the first few percent weight loss in order that the critical initial stage in the deterioration of the graphite may be studied in detail.

Structural and mechanical properties of the graphites were evaluated before and after oxidation with carbon dioxide. Structural evaluation includes measurements of density, porosity, grain size and grain orientation. Two graphites of distinctly different microstructures have been chosen for detailed study. Mechanical properties which are measured include dynamic elastic modulus, flexural strength, stress intensity factor and specific surface energy. Acoustic emission during mechanical testing is also monitored to aid evaluation of sub-critical failure events. Micromechanisms of failure are identified and variations in microstructure due to oxidation are examined using Polarised light microscopy and Image Analysis. The change in microstructure and properties are related using an analytical model for fracture of graphites.

This thesis is structured as follows. Chapter 2 reviews the general field of graphite structure and fracture behaviour including the effects of oxidation. Chapter 3 details the experimental techniques used in this work and also includes illustrative data from unoxidised material. Chapter 4 presents the experimental results from microstructural examination and mechanical testing and Chapter 5 discusses the significance of these results in detail. Chapter 6 lists the most significant conclusions and suggests areas in which this work could be extended.

CHAPTER 2

REVIEW OF THE STRUCTURE AND STRENGTH OF GRAPHITE

This study is concerned with relationships between strength and structure of graphite, with particular reference to the effects of oxidation. Accordingly, this review contains two main elements. The first part of the review considers the structure of both single crystal and polycrystalline graphite; the second part deals with processes which lead to fracture of graphite, including deformation mechanisms and micromechanisms of failure. The use of fracture mechanics in the study of failure of graphite is also discussed, as is the use of statistical approaches to failure. Previous work on the effects of oxidation is also reviewed.

2.1 THE STRUCTURE OF GRAPHITE

2.1.1 The Graphite Single Crystal

The atomic structure of graphite was shown by x-ray studies, (Bernal, 1924) to consist of layer planes of carbon atoms arranged in parallel layers of regular hexagons in an ABAB... stacking sequence, thus resulting in a hexagonal unit cell (Fig.2.1). The bonds within the basal plane are covalent, whereas the interplanar bonding is by relatively weak Van der Waals forces, which have approximately 1/100 the strength of the C-C bond (1). Because of the weak interplanar bonding, displacement parallel to the planar directions is easy and stacking faults occur. Consequently,

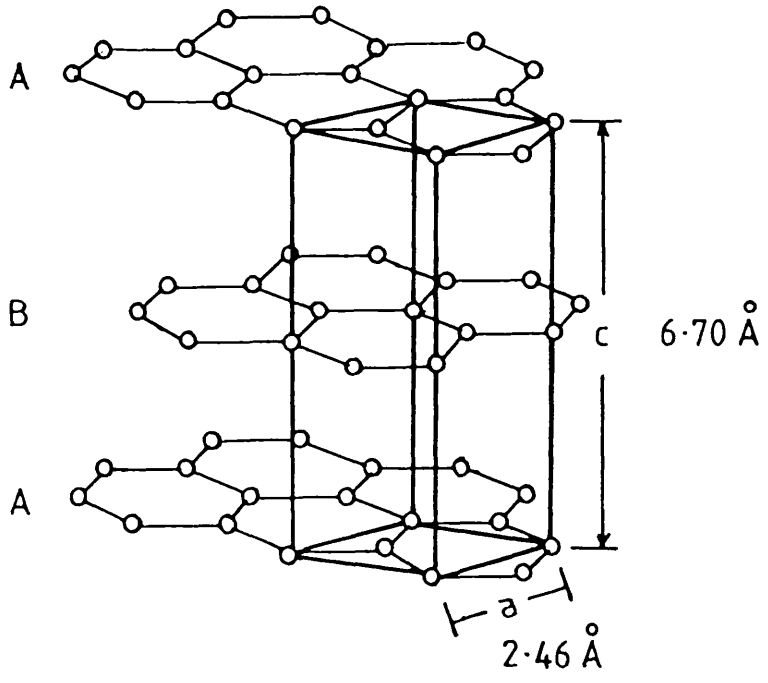

Fig. 2.1 The graphite unit lattice.

graphites may contain 10-30% of a less stable, rhombohedral form in which the stacking sequence of the layer planes is ABCABC.... The proportion of rhombohedral may be increased by mechanical treatment, e.g. grinding, or reduced by heat treatment at temperatures above 1700 K, when it is converted back to the hexagonal form, however this conversion may not be complete until 3000 K(2).

The large differences in types and strengths of bonds within the planar arrays compared to those in the interplanar direction are reflected in the anisotropy of the graphite crystal with respect to properties such as strength, elastic modulus, conductivity and expansion.

2.1.2 Manufacturing Polycrystalline Graphites

Most artificial graphites are made from a petroleum coke filler and a coal-tar pitch binder. These are sized, mixed and formed according to some proprietary technique, to optimise the performance of the graphite according to its requirements. The processing steps used in manufacture are summarised in Fig.2.2. Nuclear graphites are produced by modifications of conventional manufacturing methods, for example, by selection of high purity raw materials to ensure a low neutron absorption cross-section. This may be further reduced by treatment of the graphite with chlorine or fluorine to convert metal carbide impurities to volatile halides.

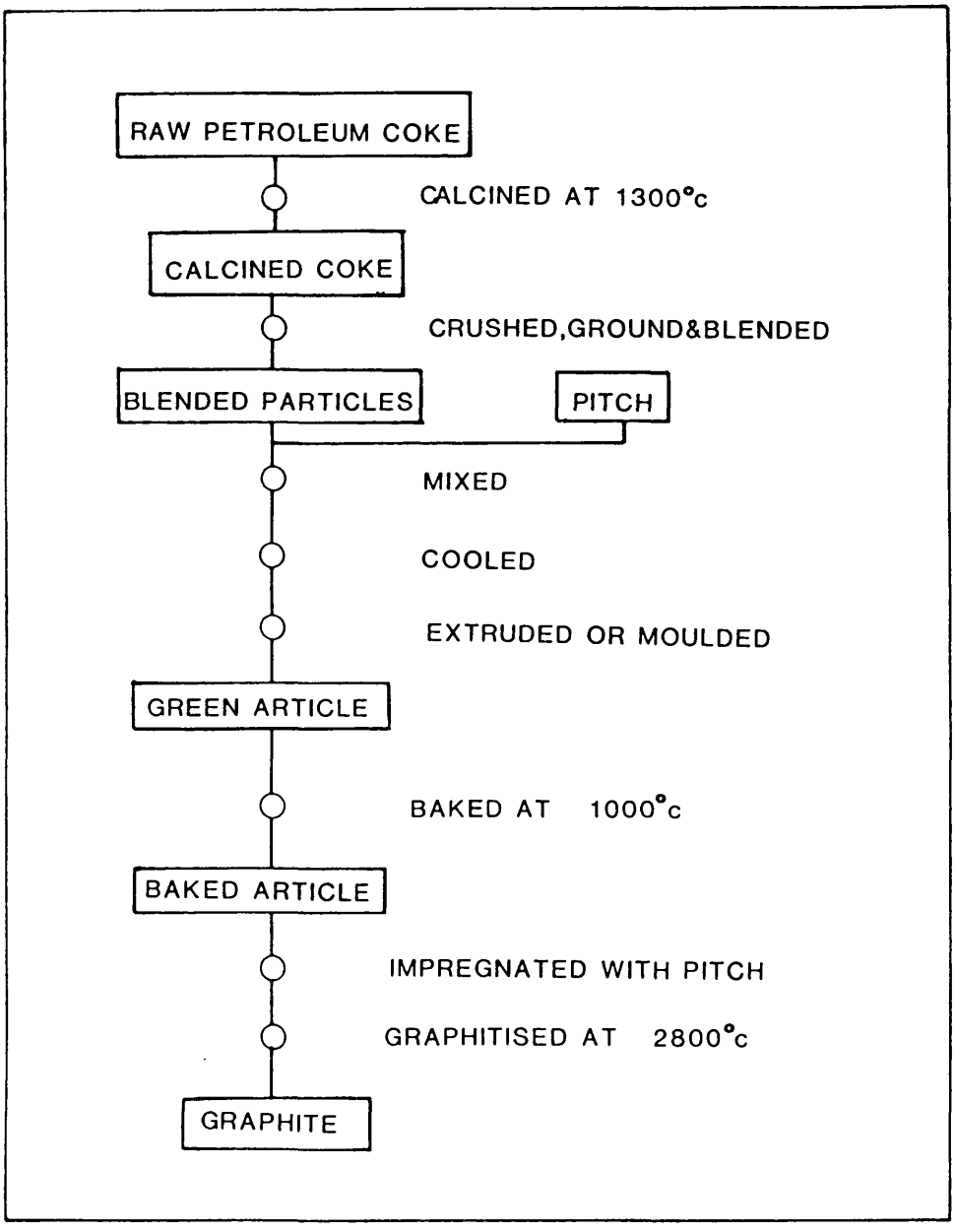

Fig. 2.2 Materials and processes used in graphite manufacture.

Petroleum pitch coke is favoured as a filler material because it is easily obtainable, easily graphitised and has low electrical resistivity. Coal-tar is the usual binder as it is: a low cost, widely available material; it softens at a low temperature (350 K) and is plastic over a large temperature range; also it has a very high carbon content, approximately 93% (3), which will minimise gas evolution porosity. Ragan (4) has recently reviewed the technology of graphite manufacture and discusses the use of other binder materials, e.g. furfuryl alcohol and polyfurfuryl alcohol.

By careful selection of the starting materials and control over the pitch to coke transition, the resultant properties of the finished artefact can be affected dramatically. Marsh (5) describes how the selection of the correct type of coke, parent material determines the subsequent optical texture, i.e. basal plane development and orientation of the coke filler grains. During pitch to coke transformation at temperatures circa 670-720 K an optically active phase appears in the liquid pitch. Increasing carbonisation temperature promotes molecular weight increase of this newly formed optically anisotropic phase. At a critical concentration these molecules interact to develop perpendicularly to their planar directions. These "liquid crystals" have been called mesophase (intermediate phase) (6,7). The mesophase is subjected to thermal convection currents and bubble percolation from the evolution of volatile materials. Depending upon its viscosity and various other chemical and physical parameters

(8), the mesophase will have a characteristic shape, which may vary from small spheroids to a large needle like structure. As an example of this structural variation with pitch type, Gilsonite pitch will produce small anisotropic units of mesophase, which on contact only adhere and retain a separate identity, thus forming a mozaic structure which is still identifiable in the graphite stage. However, Ashland A200 petroleum pitch grows larger units of mesophase which on contact coalesce, with total loss of original identity, giving rise to large optically anisotropic domains, hundreds of micrometres in size.

It is for the reasons discussed above that coke filler grains used in graphite manufacture may have vastly different properties ranging from highly anisotropic needle cokes to the more isometric Gilsocarbon filler grains. Not only may there be anisotropy within the filler grain, but the method of manufacture will greatly affect the bulk properties of any artifact. For example, the extrusion process will tend to align filler grains in a parallel direction to the extrusion axis. The extent to which this happens will be dependent upon the grain shape. Moulding tends to produce more isotropic bulk properties.

The industrial producers of graphite have many options to control the properties of their product. As an example of the extremes, a highly anisotropic material may result from extruding needle-like filler grains which have strong basal plane orientation parallel to their long axis.

Alternatively an isotropic material may be produced by moulding isometric filler grains that have a sub-structure of thousands of crystallites with random orientation.

After moulding or extrusion the green article is baked at temperatures circa 1000-1300 K. The baking operation is a critical stage in the production of graphite and is performed with great care, using heating rates in the order of 2-10 K per hour. It has two main functions:- (i) to convert the thermoplastic pitch to solid coke; (ii) to reduce the volatile content; weight losses of up to 30-40% may occur (4). The green article is virtually impermeable and the development of venting porosity has to be gradual to avoid cracking and gross porosity formation.

For high performance graphites, e.g. nuclear grades, the baked artifact is further impregnated before graphitisation, usually with low melting point petroleum or coal-tar pitch. The final stage in production is graphitisation. This involves, electrically heating the impregnated article to a temperature of approximately 3000K, usually in an Achesan furnace. The graphitisation process develops a more ordered crystallographic structure from the graphitisable carbon. It does not affect either the crystal orientation or size, as these are inherent in the coke structure prior to graphitisation.

Chard et al (9) reviewed processing techniques and they described some of the modern processes in graphite

manufacture, e.g., hot-isostatic-pressing and binderless graphites which produce high density materials.

2.1.3 Graphite Microstructure

In this section, features of the microstructure of graphite that are commonly observed and referred to in the literature will be reviewed.

Techniques for preparation and examination of graphite using optical and electron optical methods have been covered extensively by other authors (5,8,10). One of the most useful instruments for examining graphite is the reflecting polarized light microscope which has the facility of inserting a sensitive tint plate (5 and section 3.5.1). Without the sensitive tint plate anisotropic regions of the graphite structure, i.e., areas of strong basal plane orientation will exhibit extinction contours when rotated between crossed polars. With the sensitive tint plate these areas will appear coloured, according to their orientation with respect to the polarizer and the analyser. Isotropic areas will remain dark (without sensitive tint) or purple (with sensitive tint). Using the above technique it is possible to categorise the microstructure of graphite by examination of the nature of optical texture. Crystallites may be described as the unit of the structure in which atoms are arranged in a periodic array and should not be confused with the grain/grist size. A single grain is an agglomeration of hundreds or thousands of crystallites. A

graphitic region which is made up of crystallites of common orientation is referred to as having optical texture due to its optically isochromatic appearance using sensitive tint. White (11) used the term mozaic to describe features, built up of isochromatic areas of 0.1 to 5μm. Areas of greater size, i.e., 5μm upward are known as 'domains'. These domains often deviate from planarity due to shearing forces from bubble percolation, acting upon the plastic mesophase to cause a 'flow-type' anisotropy. Areas of extreme distortion due to bending, folding or twisting the mesophase are known as disclinations. (11).

Another important feature of graphite microstructure, apart from the binder and grains, is the porosity. Nuclear grade graphites have typical densities of about 1.6 to 1.9 g/cm^3, compared to the theoretical single crystal density of 2.26 g/cm^3. The difference is attributed to the porosity which is present in a spectrum of pore sizes which are categorised as follows; macro-, meso- and micro-pores of diameter, above 50nm, 50nm - 2nm and less than 2nm respectively (12). The origins of porosity at various stages of graphite production were reviewed by Evans (8) and are summarized below.

During the pitch to mesophase transition, mesophase which is in a late stage of development may encapsulate a gas bubble, preventing it reaching the surface thus producing a pore. Pores formed in this way are generally greater than 5μm. Similar factors that affect the size

of the optical texture, affect the porosity size, e.g., pyrolysis chemistry and viscosity of the pitch. The pitch/mesophase transition for the binder occurs in the presence of grist particles and consequently their shape and orientation will also influence the shape of the pores in the binding graphite which may be distinctly different to those in the grist particle.

The solid carbon to graphite transition involves non-uniform shrinkage due to the structural anisotropy of polycrystalline graphite. Stresses caused by this phenomenon are relieved by the formation of shrinkage voids, (pores). These voids may be nucleated at temperatures as low as 800K and develop in width and length as the temperature increases up to 3000K. The shrinkage porosity runs parallel to basal planes (13) and may follow the optical texture around its bends and twists giving the void an acicular appearance. Disclinations are also common nucleation sites for shrinkage porosity.

Porosity may be open or closed. Open porosity is an interconnected network, accessible to penetrating gases and liquids, whereas closed porosity is isolated, although a small number of closed pores may become open at elevated temperature, e.g. up to 1300K.

2.2 MECHANICAL ASPECTS OF GRAPHITE TECHNOLOGY

2.2.1 Lattice Defects and Deformation Mechanisms

Graphitic structures are never perfect and contain both line and point defects. Both basal and non-basal dislocations have been observed (14). Dislocation lines which are in the basal plane, move easily even at low temperatures because they do not involve breaking co-valent bonds. For similar reasons twins and stacking faults may also be created and displaced with relative ease thus allowing the uniform bending of graphite crystals (15); an example of this is the twisted scroll of graphite sheets that constitute a graphite whisker. Kelly (16) describes in detail, common dislocations in the graphite system and their reactions as well as the formation and associated energies of point defects.

The stress-strain relationship of a polycrystalline graphite is characterized by non-linearity. A hysteresis effect on unload-reload curves with permanent set at zero load was first reported by Arragon and Berthier (16). This permanent strain may be removed by annealing. A decreasing elastic modulus with increasing stress was also observed by Jenkins (15). He described this behaviour using a rheological model in which an increasing proportion of the elements deform plastically against the restraining effect of an elastic matrix, i.e., the response to stress will be governed by the presence of a continuous carbon network.

The strain pattern follows interlamellar weaknesses, e.g. dislocations and vacancies. The presence of a continuous elastic network means that all strains at low temperatures are wholly elastic, although hysteresis will occur due to internal friction. Jenkins also developed an analysis based on a dislocation model of the spread in plastic yield from the tips of pre-existing microcracks, the matrix remaining elastic. The effect of pores upon mechanical properties will be covered in greater detail in section 2.2.3.

Souele and Nezbeda (17) demonstrated the importance of basal plane dislocation systems in their single crystal studies. The stress-strain behaviour showed marked basal plane slip, activated at a low critical resolved shear stress (0.03 MNm^{-2}). They examined the effect of pinning dislocations by boron doping, which had the effect of greatly increasing shear modulus. Hall (18), showed that the decrease in Youngs modulus caused by compressive prestressing could be recovered by annealing. After large prestressing, i.e. 75% of failure stress Youngs modulus could only be partly recovered by thermal annealing. He concluded that at low prestress levels the fall in modulus was due entirely to an increase in dislocation density but microcracking contributed at higher levels.

2.2.2 Micromechanisms of Failure in Graphite

In the previous section the ease with which dislocations can be created and displaced has been

mentioned, yet the observed fracture behaviour in graphite is essentially brittle. This suggests that strain due to slip is restricted. Groves and Kelly (19) point out that graphite deforms readily by slip due to only two dislocation systems and therefore does not meet the Von Mises criterion of five independent slip systems for homogeneous deformation to occur. This results in strain accommodation difficulties at grain boundaries in polycrystalline graphites. Some grain deformation may be unopposed by restraints, e.g. if it occurs into an adjacent pore, but the majority is restricted, resulting in dislocation pile-ups and a corresponding increase in stress concentration. If this concentration is not relieved by either a new slip system operating or diffusion processes allowing dislocations to become free, then stress is relieved by fracture. The amount of deformation before microcracking occurs is controlled by the density and grain boundary, area to volume ratio. Once microcracks have been nucleated they may grow under the influence of the applied stress and interlink to form critically sized flaws which will propagate catastrophically when the elastic strain energy release rate is greater than the new effective surface energy created, according to a Griffith type crack mechanism (20). Fracture mechanics will be examined in greater detail in section 2.2.4. Effective surface energies of polycrystalline graphites are several orders of magnitude greater than that of the single crystal (21), e.g. $100Jm^{-2}$ compared to $0.1Jm^{-2}$; this is attributed to multiple crack formation and non basal plane fracture.

A valuable insight into the micromechanisms of failure may be gained by sequential microscopical examination during mechanical testing. Such a technique was employed by Jenkins (22), who bonded graphite to brass strip and observed the sequence of events in the plane of maximum stress, subjected to increasing strain. The material was a large grained, needle-coke graphite and fracture was observed to proceed preferentially along striations within the highly oriented structure of the grist particles but also travelled between pores. Secondary isolated cracks formed ahead of the major crack front. He concluded that fracture occurred mainly by interlamellar separation within the grist particles but was inhibited by less well orientated binder material, making propagation more difficult than crack initiation. Slagle (23) used similar techniques on a Texas coke graphite S.G.B.F. to examine fracture initiation in both tensile and compressive stress gradients. Initiation was observed at pores and followed interlayer paths. This subcritical cracking was observed in the tensile region at about 0.5 σ_f, where σ_f is the stress at which complete failure occurs. He also noted a crack density increase as cracks arrested at pores and new ones formed. On complete failure, some of the secondary cracks closed up. This was assumed to be the result of internal stress relief. Knibbs (24) studied three, microstructurally different graphites, ranging from coarse grained Morgans EY9 to a fine grained POCO AXF. He concluded that in the coarse and medium grained materials, the major weaknesses were

associated with grain cleavage and the particle/binder interface. Regions of greater pore density tended to be initiation sites for secondary cracking. He attributed anisotropy in strength to variations in degree of crack path tortuosity, as cracks deviated around non-favourably orientated filler particles. Meyer and Buch (25) in their S.E.M. studies on crack initiation and propagation in a variety of graphites, were also in agreement with other workers on the role of larger, highly orientated filler particles. They measured the angle of deviation of the crack path from the tensile plane and found localised deviation may be as much as 50^{o}, yet deviation averaged over the length of the total crack path varies by only ± 5 degrees.

Meyer et al (26) subjected a number of different graphites to tensile tests whilst observing them in a scanning electron microscope. They defined several distinct microstructural features which influence crack propagation, as follows:-
(A) grain orientation; since grain cleavage is associated with graphitic planes in the grain, its orientation relative to an applied stress will govern the cleavage process; (B) grain boundaries; these are not well defined but regions between adjacent grains have an inherent weakness and grain boundary failure can occur; (C) pore structure; fine distributions of small pores are the predominant feature in controlling crack propagation in fine-grained graphites. This porosity is often interconnected thus providing an easy

crack path; (D) grain agglomeration; this is most relevant to fracture where the grain size is very small, normally less than 10μm. The effect is mostly indirect, i.e. the pore structure tends to outline the agglomeration in a fine distribution, thus causing a weakness. However, there may be a more direct effect, for example, the agglomeration can act as an individual grain which might fracture and therefore aid crack growth.

2.2.3 The Effect of Porosity upon Mechanical Properties

Many empirical relationships have been proposed relating a mechanical property, usually strength or modulus, to porosity; much of this work has been on ceramics as well as graphites. Various workers, Knudsen (27) Duckworth (28) and Barrachin (29) suggested that modulus and strength reduced exponentially with porosity e.g.

$$X = X_o \, e^{-bP} \qquad (2.1)$$

Where X is the value of the parameter considered, for a material with a fractional porosity P. X_o is the parameter value of zero porosity material and b is a constant. It is obvious that as the porosity level increases there will be less material to support the load and hence a reduction in apparent strength. However the nature of the pores will determine the severity of the property reduction and therefore the value of the constant, b, is related to the geometry and mixture of pore types

(30). There is an associated stress intensification with a discontinuity in a stressed body, e.g. a pore. The degree of intensification is dependent upon the shape of discontinuity; for example a spherical pore within a stressed body may locally intensify the stress to a level twice that of the nominal stress, whereas a cylindrical pore may increase the local stress threefold (31). Rossi (32) suggested that the constant b in equation 2.1 may be representative of the stress intensification of the pores. Data on glass (33), with well formed spherical bubbles, yielded a value of approximately 2.1 for b which is equivalent to the stress intensification for spherical voids.

Empirical relationships have been developed to account for other microstructural features as well as pore volume fraction. Knibbs (24) using modulus of rupture data from twelve graphites with grain sizes, d, ranging from 15 to 1000μm, derived the following relationship.

$$\sigma_f = A\, d^x\, e^{-bP} \qquad (2.2)$$

where σ_f is the rupture strength and A, x and b are constants with values of 1200, -0.47 and 6.8 respectively. From fracture mechanics

$$\sigma_o \propto a^{-0.5} \qquad (2.3)$$

where σ_o is the strength of the material and a is

the flaw size. From equations 2.1 and 2.3 the following relationship may be derived

$$\sigma = A\, c^{-0.5}\, e^{-bP} \qquad (2.4)$$

This is similar to equation 2.2 which Knibbs derived and since the value of x was so close to that of -0.5 it was proposed that the grain size, d, may be related to the critical flaw size, c.

Stacey (31) who was working on coke whose critical flaw was thought to be equivalent to the largest porosity, developed an empirical relationship between failure strength and the mean maximum and minimum dimensions of that critical flaw

$$\sigma = 450\, (F_{max})^{-0.5} \exp(-2(F_{max}/F_{min})^{0.5}P) \qquad (2.5)$$

where F_{max} and F_{min} are the maximum and minimum dimensions of the specific pore type. The correlation with the data was good and at zero porosity levels gave a finite strength prediction of similar form to equation 2.4.

Pampuch and Konsztowicz (35) repeatedly impregnated a fine grained graphite and regraphitised it; initially the smaller spherical porosity was preferentially closed, then at a later stage the larger disc shaped porosity was filled. The strength-porosity relationship slope varied according to the volume reduction of a particular type of pore. They

concluded that this was due to the variation in stress concentration between different shapes of porosity.

Barrachin et al (29) proposed an expression which could quantify the relative effects of macroporosity, P', and microporosity, p, (e.g. that produced by anisotropic thermal contraction), upon the modulus, E, of typically extruded stock, as follows

$$E = E_o \frac{(1 - aP')\ (1-qp)}{1-MqP} \qquad (2.6)$$

where $P' = P - p$ and a, M and q are constants. From 2.6 and an appreciation of the rate of microfissure closure with temperature, dp/dT, they were able to explain how the apparent modulus of graphite aggregates varies with temperature. The Young's modulus of polycrystalline graphite may increase by as much as 50% when heated to 2000^{o}C even though the elastic moduli of single crystals may decrease by 40% over the same temperature range. The reason for this is that as temperature increases thermal expansion closes the microfissures and therefore reduces the pore volume available for adjacent material to bend and buckle into, thus reducing the possible strain accommodation and resulting in increased modulus.

From the relative variations in single and polycrystalline moduli, Jenkins (15) concludes that microfissures contribute to half the elastic compliance at room temperature. Even if the porosity is filled with material whose modulus is considerably less than that of

graphite, the effect of closing these voids may increase the modulus by a factor of two. (15).

Summarizing this section, pores have three main effects upon the mechanical properties of solids:- (i) they reduce the volume available to distribute loads, effectively increasing stress; (ii) locally, they intensify stresses; the degree of intensification being dependent upon their geometry;(iii) pores increase the volume available for accommodation of grain deformation.

2.2.4 Fracture Mechanics and Statistics of Fracture

The details of fracture mechanics have been reviewed thoroughly elsewhere (36). In this section only the basic principles will be discussed so as to provide sufficient background to the subject to enable the application of fracture mechanics to graphite to be discussed.

In the twenties, Griffith (20) explained the discrepancies between theoretical and observed fracture strength by the presence of microcracks and derived the following relationship

$$\sigma_f^2 = \frac{2\gamma_S E}{\pi a} \qquad (2.7)$$

where γ_s is the surface energy; a is the flaw size

(see Fig.2.4). This expression is applicable to plane stress, (σ = 0 in the thickness direction), but is modified for plane strain, (zero strain in the thickness direction) by dividing the modulus by ($1-\nu^2$). In practice ν is small for most graphites (≈0.2) and therefore the term ($1-\nu^2$) is small and often ignored.

Orowan (37) and Irwin (38) modified Griffith's relationship to take into account plastic flow which virtually all materials exhibit, (particularly around crack tips even before brittle failure) as follows

$$\sigma_f = \left(\frac{E^* G_{IC}}{\pi a}\right)^{0.5} \qquad (2.8)$$

Where $E^* = E/(1-\nu^2)$ and G_{IC} is the critical, potential energy release rate for opening mode displacement (Fig.2.3), i.e. the rate of elastic strain energy release due to crack extension. Rearranging equation 2.8

$$G_{IC} = \pi a \, \sigma^2 / E^* \qquad (2.9)$$

The effective surface energy, γ, = -du/da where u is the elastic strain energy and is related to the fracture toughness parameter, G, by

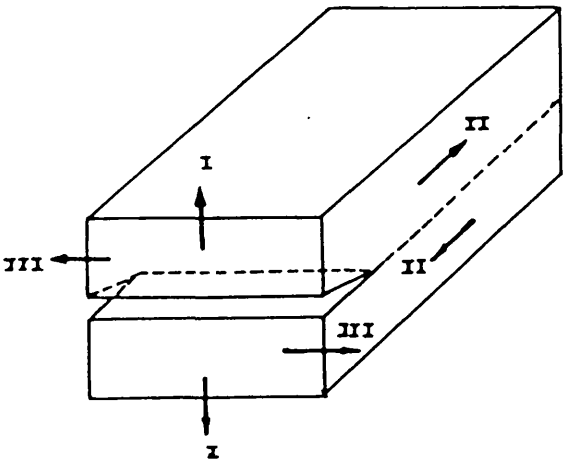

Fig. 2.3 The three modes of stress application to a crack:- I, opening displacement; II, plane shear; III, anti-plane shear.

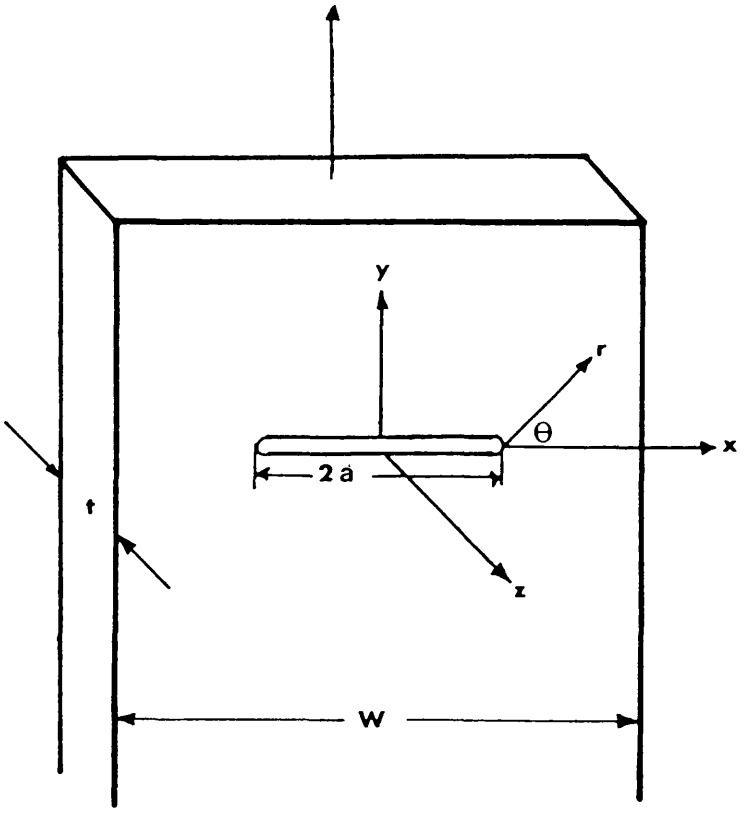

Fig. 2.4 The coordinates used to describe stresses around a crack tip.

$$G = 2\gamma \qquad (2.10)$$

If the plastic zone around the crack is small relative to the specimen size and plane strain conditions exist, then the fracture toughness parameter, G_{IC}, is a material property. Fracture may also be defined by critical values of stress. The stress distribution around a crack tip has been calculated by Westergaard (39) in terms of the coordinates in figure 2.4

$$\sigma_x = \sigma\left[\frac{a}{2r}\right]^{0.5} \left[\cos\frac{\theta}{2} \quad (1 - \sin\frac{\theta}{2}\sin\frac{3\theta}{2})\right]$$

$$\sigma_y = \sigma\left[\frac{a}{2r}\right]^{0.5} \left[\cos - (1 + \sin\frac{\theta}{2} \quad \sin\frac{3\theta}{2})\right] \qquad (2.11)$$

$$\tau_{xy} = \sigma\left[\frac{a}{2r}\right]^{0.5} \left[\sin\frac{\theta}{2}\cos\frac{\theta}{2} \quad \cos\frac{3\theta}{2}\right]$$

These equations are valid for a > r > notch root radius. Directly ahead of the crack ($\theta = 0$) and,

$$\sigma_x = \sigma(a/2r)^{0.5} \text{ and } \tau_{xy} = 0 \qquad (2.12)$$

Irwin noted that local stresses near a crack depend upon the product of the nominal applied stress and the square

root of the half-flaw size. From this relationship he defined the stress intensity factor, K.

$$K = f(a/w)\sigma\sqrt{\pi a} \qquad (2.13)$$

where $f(^a/w)$ is a parameter that depends upon the specimen and crack geometry. As with G, when plane strain conditions apply and the specimen is in opening mode displacement, I, the intensity factor is denoted K_{IC} and is a material property. The fracture toughness parameters K and G are simply related by combining equations 2.9 and 2.13 to give

$$K_c^2 = EG \quad \text{plane stress} \qquad (2.14)$$

$$K_c^2 = EG/(1-\nu^2) \quad \text{plane strain} \qquad (2.15)$$

When determining the effective surface energy Davidge and Tappin (40) distinguished between the value of γ at the initiation of fracture, denoted γ_i and γ_f the work of fracture, averaged over the whole fracture process. γ_i is the value used in the Griffith equation and was determined using either an analytical method or compliance technique. For the Pile Grade A graphite they were working with, they showed that γ_i did not vary systematically with varying notch depths, whereas γ_f decreased with increasing notch depth. In all cases γ_f was greater than γ_i,

γ_i having values around 50 Jm^{-2}, whereas γ_f 100 - 200 JM^{-2}, (according to notch depth). Their conclusion was that, propagation was more difficult than initiation due to the tortuous crack path.

The ideal application for fracture mechanics is that it may be used as a failure criterion for graphites, hence if K or G is known and also the defect size, then in theory the failure stress can be determined irrespective of specimen geometry or type of loading. Unfortunately this is not always so. Darby (41) working on a graphite with a K_{IC} value of 1.3 $MNm^{-3/2}$ and using this material constant in conjunction with strength data from various test geometries calculated effective flaw sizes for each geometry. He found that a geometry which created a higher stress gradient produced lower effective flaw sizes. As an example of this, beams of various sizes, yet similar notch to width ratios were broken. The larger beams and hence smaller stress gradient, yielded effective flaw sizes comparable to the largest microstructural flaws. However the smallest beams with stress gradients twenty times the large beams, produced effective flaw sizes ten times smaller. He concluded that there is no constant inherent flaw size which can be employed with a constant critical stress intensity factor. However for a constant K_{IC} the effective inherent flaw size may be related to the inverse of the maximum stress gradient.

Brocklehurst (21) describes an alternative method

for determining the inherent flaw size to relating experimental K_{IC} and σ_f. The technique related the number of specimens which failed at the notch tip, to the size of the notch. At large notch depth 100% failed at the tip. On reduction of the notch size there was a critical size which less than 100% failed there, and the percentage decreased with decrease in notch dimension, thus suggesting that inherent flaws become dominant. The inherent effective flaw size, determined this way was comparable to the flaw size calculated using,

$$a' = \frac{1}{\pi}\left(\frac{K_{Ic}}{\sigma_f}\right)^2 \qquad (2.16)$$

when the σ_f used was the tensile strength. If however bend strength was used the calculated flaw size was smaller, due to the stress gradient effect. Yahr and Valachovic (42) working on ATJ and AXM (POCO) graphite, used their experimentally determined K_c values in combination with strength measurements from unnotched beams and calculated the effective inherent flaw size. They concluded that these values correspond with the size of the largest natural inhomogeneities determined by microscopical examination. Yahr et al (43) used these data to predict failure of diametral disc specimens and demonstrated a good agreement for the isotropic AXM, but a less precise one for the more anisotropic ATJ. This indicates that it is possible to use fracture toughness as a failure criterion under certain favourable conditions.

Brocklehurst (21) reports an investigation into the effect of specimen geometry on the stress intensity value of a fine grained version of IM1.24 graphite. Both bend and tension specimens were used and he summarizes the results as follows. With edge-notched beam specimens of depth 6.4 mm and width 19 mm, 3-point bend tests gave K_c values of 1.4 - 1.5 $MNm^{-3/2}$, with no significant difference in values when slot width was varied from 0.13 to 0.25: and slot depth was varied from (a/w) = 0.1 to 0.5, or the span varied from 76 - 300 mm. The compact tension specimens gave K_c values that were in good agreement with 3-point bend, i.e. 1.3 $MNm^{-3/2}$. However circumferentially slotted round bar gave considerably lower K_c values of about 0.8 $MNm^{-3/2}$.

Fracture mechanics was originally derived assuming materials were linearly elastic. Modifications have been made to allow for an amount of plasticity, but these will only apply if the volume of material subject to plasticity is small compared to the total specimen volume. Therefore there is a need to consider specimen size. Buresch (44) investigated the effect of microstructure and geometry of specimen and notch radius on K_{IC}. He postulated that there was a "process zone" at the crack tip of the notch. The process zone is the region in which there is extensive microcracking and the size of which is governed by microstructural parameters, especially specific surface energy. He compares this zone in brittle materials to the

plastic zone in more ductile materials and points out that materials such as graphite, with a relatively low effective surface energy, may have a large process zone, especially if they have a large notch root radius. In such a case the measurements may be sensitive to specimen size. Techniques have been described by Sato (45) and Szendi-Horvath (46) for determining fracture toughness using small diametral compression specimens in which there are combined tensile and compressive stresses as well as stress gradients. Results from both tests were comparable with those from more conventional small specimens, e.g. compact tension and double torsion. Both the diametral compression techniques have been examined in this work and a comparison of results with those from single-edge notch bending specimens for IM1-24 is presented in section 3.4.3.

There is another important effect of specimen size, apart from the interaction of the process zone and specimen size. A stressed volume of material has a distribution of flaws within it. Failure will occur when the stress intensity at any one flaw reaches a critical value, i.e. the weakest-link hypothesis. For any given stress state the probability of attaining a critically sized flaw increases with increasing stressed volume. This may explain to some extent the difference between bend strength and tensile strength which is observed for specimens that have the same volume. The bend specimen due to the stress gradient has a smaller stressed volume and therefore a lower probability of containing a critically sized flaw, hence a higher

probability of survival for any given applied stress. It should also be noted that failure in material subject to a stress gradient may not initiate at the point of maximum stress, i.e. failure will be dependent upon a combination of stress distribution and flaw distribution. The statistical approach to brittle fracture that is most often used is the Weibull distribution (47). The probability of failure $P_{(f)}$ at applied stress, σ, is given by

$$P(f) = 1 - \exp\left[-V\left(\frac{\sigma - \sigma_u}{\sigma_o}\right)^m\right] \qquad (2.17)$$

where V is specimen volume, σ_u is the stress below which failure probability is zero; in practice this is difficult to define and so σ_u is usually taken to be zero; σ_o is a normalising parameter and is taken to be the stress at which $P(f) = 0.63$, and m is the Weibull modulus which is supposed to be characteristic of the material, (high values of m indicate a greater uniformity in crack distribution). The value of m is determined empirically using best fit methods. Having determined m in theory it is possible to predict the dependence of strength on sample size and type of test. For example, for identical $P_{(f)}$ in bending and tension the ratio of bend to uniaxial tension strength can be calculated from

$$\frac{\sigma_B}{\sigma_T} = \left[(2m + 2)\frac{V_T}{V_B}\right]^{1/m} \qquad (2.18)$$

where σ_T and σ_B are mean tensile and bend strengths and V_T and V_B are the volumes of tension and bend test specimens respectively. Experimental work on nuclear graphite (28,49) has found that the Weibull approach overestimates the effect of volume. Marshall and Priddle's (49) results from experimentally and theoretically calculating the variation in ratio of σ_T/σ_B due to a one hundredfold increase in the volume of the tensions specimens are given below.

Table 2.1

COMPARISON OF WEIBULL AND FRACTURE MECHANICS STRENGTH PREDICTIONS FOR DIFFERENT SPECIMEN VOLUMES

(Figures refer to σ_T/σ_B)

Volume of Specimen	Weibull Prediction	Fracture Mechanics Prediction	Experimental
$V_T=V_B$	0.72-0.82	0.70-0.80	0.70-0.75
$V_T=20-40V_B$	1	0.80	0.70
$V_T=100V_B$	1.05-1.2	0.85	0.70

(After Marshall and Priddle (49))

They concluded that a fracture mechanics approach was superior to the Weibull analysis in predicting strength provided the effective flaw size can be accurately

determined.

Buch (52) used a fracture mechanics approach similar to that of reference (49) to predict the σ_T/σ_B ratio but instead of selecting one value of effective flaw size he used a distribution function and a probability model for attaining a critically sized flaw. Mason (50) found that for small bend specimens strength increased with increasing volume eventually passing through a maximum. He concluded that for small specimens, the average grain might constitute a significant proportion of the specimen and therefore almost any grain failure would be critical. In such a case the weak link theory would be invalid. Brocklehurst (21) also noted similar effects with tensile and bend tests on IM1-24 graphite speicmens of small volume. His work showed that the effect of grain size was more significant in tensile tests than in bend tests. Experimentally determined σ_B/σ_T showed that the ratio does not have a unique value, but varies from about 2 at low speicmen volumes to 1.3 at higher volumes (Fig.2.5). The latter value approaches the theoretical ratio of 1.25 predicted by the Weibull analysis for modulus $m = 16$, which was calculated from experimental data. Ho (51) modified the analysis by including the effect of grain size and allowing for the non-linearity which graphite exhibits. He claimed ± 6% accuracy in the prediction of volume dependence and the effect of stress distribution.

It is apparent that the Weibull approach can be used to

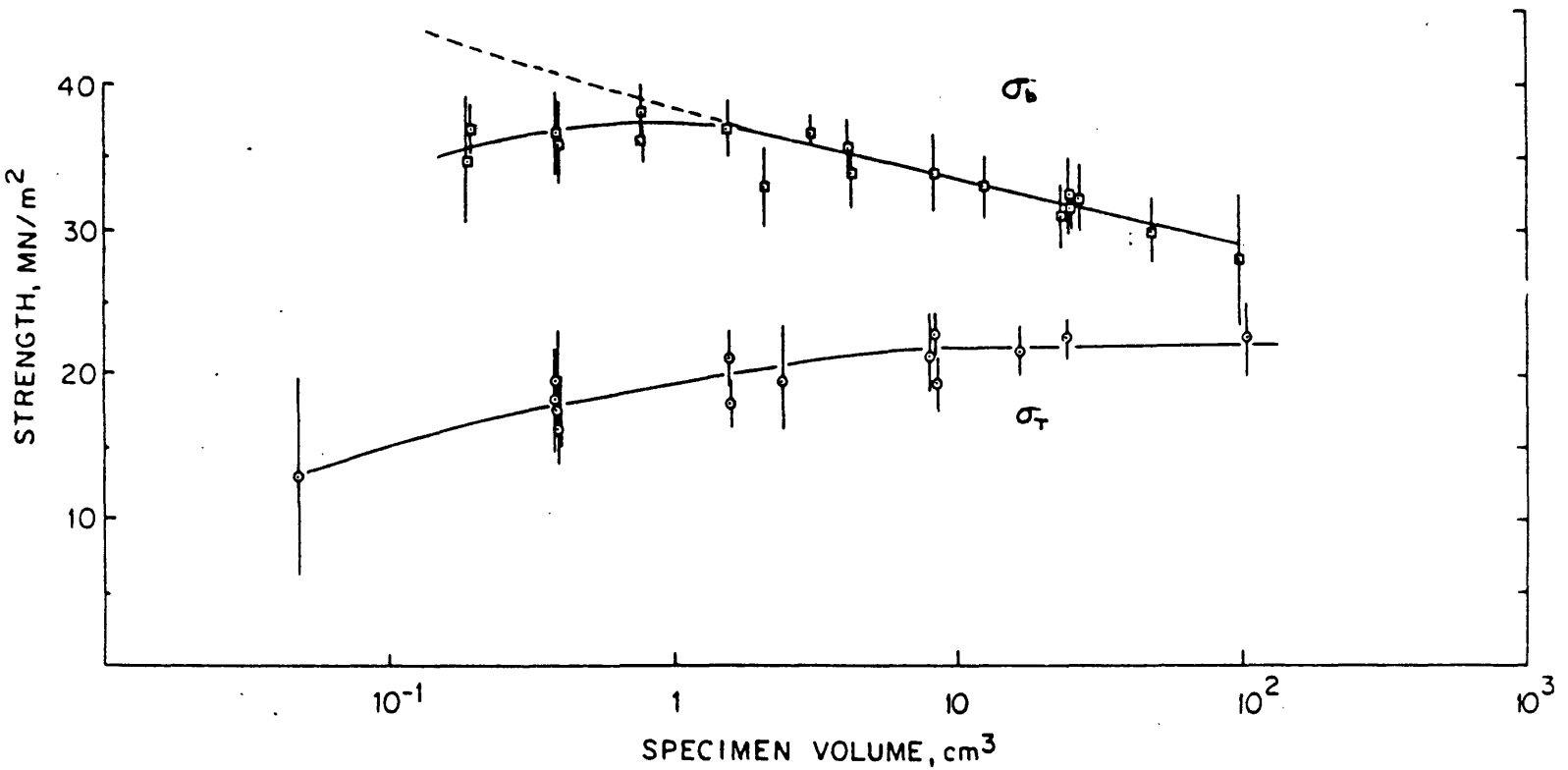

Fig. 2.5 The effect of specimen volume upon bend strength, σ_b, and tensile strength, σ_T, of IM1-24 (from ref. 21)

give a reasonable description of the statistical nature of fracture, but it does have limitations. Based upon the studies of the micromechanics of failure of Meyer et al (26), Buch (53) developed an analytical modelling technique for predicting the failure stresses of different aerospace graphites from microstructural and geometrical parameters which include grain size and specimen volume as well as fracture toughness data, the probability of formation of a macrocrack by a coincidence alignment of pores and microcracks was calculated. The probability of a critically size microcrack can be determined for any applied stress. This model is potentially superior to empirical analyses of failure probability because it proposes a fracture mechanism. The use of this model in the present work is described in detail in section 5. Rose et al (54) have developed the Buch model to allow for stress gradients. They were able to predict the dependence of three and four point bend strength on loading span.

2.2.5 Acoustic Emission Studies of Materials under Stress

Elastic stress waves result from micro mechanical events, such as slip, shear or cleavage. These waves may be monitored by placing transducers on stressed bodies. Acoustic emission (AE) has been monitored in this study and details of the equipment are given in section 3.4.1. The frequency range of the acoustic signals which can be used in practice extends from about 100 kHz to 200 MHz. For frequencies above this range attentuation of the signal becomes a

problem, below 100kHz external noise is frequently found. A great deal of care has to be taken when analysing acoustic emissions as stress waves will interact and be attenuated and therefore by the time they are monitored they have been severely modified.

Graphite emits sound well before the eventual fracture stress, at onset stresses (55,56), ranging from one percent of the failure load to immediately prior to fracture. The fraction of the load that onset occurs and the total amount of emission has been related to the grain size; coarser grains produce more noise and at earlier fractions of failure stress (55,56) than fine grained graphites.

If loading is interupted and the load removed and then reloaded, AE is not observed until the load approaches the previous maximum (57). This is known as the Kaiser effect.

According to Kraus and Semmler (56) the total amount of AE is unaffected by strain rate when the crosshead displacement in a bending test is varied from 0.05 mm/min to 1 mm/min. However, Dagleish et al (58) working on single-edge notch bending (SENB), found that as the crosshead displacement reduced from 1 mm min^{-1} to 0.01mm min^{-1} the load time relationship became non-linear at 0.1mm min^{-1} and from that rate and lesser cross- head speeds the total AE increased. They used AE monitoring to compare the amount of sub-critical micro-mechanical events for three geometries of fracture toughness specimen; double torsion (DT), double cantilever beam (DCB) and SENB. They

concluded that the amount of subcritical microcracking varied as follows, DCB > DT > SENB >, and therefore on the basis of LEFM, they considered SENB the most suitable as it was the least 'plastic', provided a/w was small and a suitable crosshead speed was used.

AE monitoring can be a useful tool for comparative examination of sub-critical events, provided the method of testing and specimen geometry remain constant.

2.2.6. The Effect of Oxidation upon the Mechanical Properties of Graphites

The oxidation of nuclear graphite may be broadly classified into two groups: (i) radiolytic oxidation, in which the oxidising gas within the graphite pores is subjected to radiolysis, resulting in the formation of active species capable of gasifying the surrounding material. (ii) thermal oxidation, where oxidation is due to a combination of temperature and an oxidising gas, for example carbon dioxide or air. For either mechanism it has been found (59, 60, 61, 62, 63) that both strength and elastic modulus decrease in a similar fashion with increasing weight loss (Fig.2.6).

From figure 2.6 it can be seen that for a given weight loss there is a greater reduction in strength or modulus for thermal oxidation than for radiolytic oxidation. Brocklehurst et al (62) observed the relative changes in

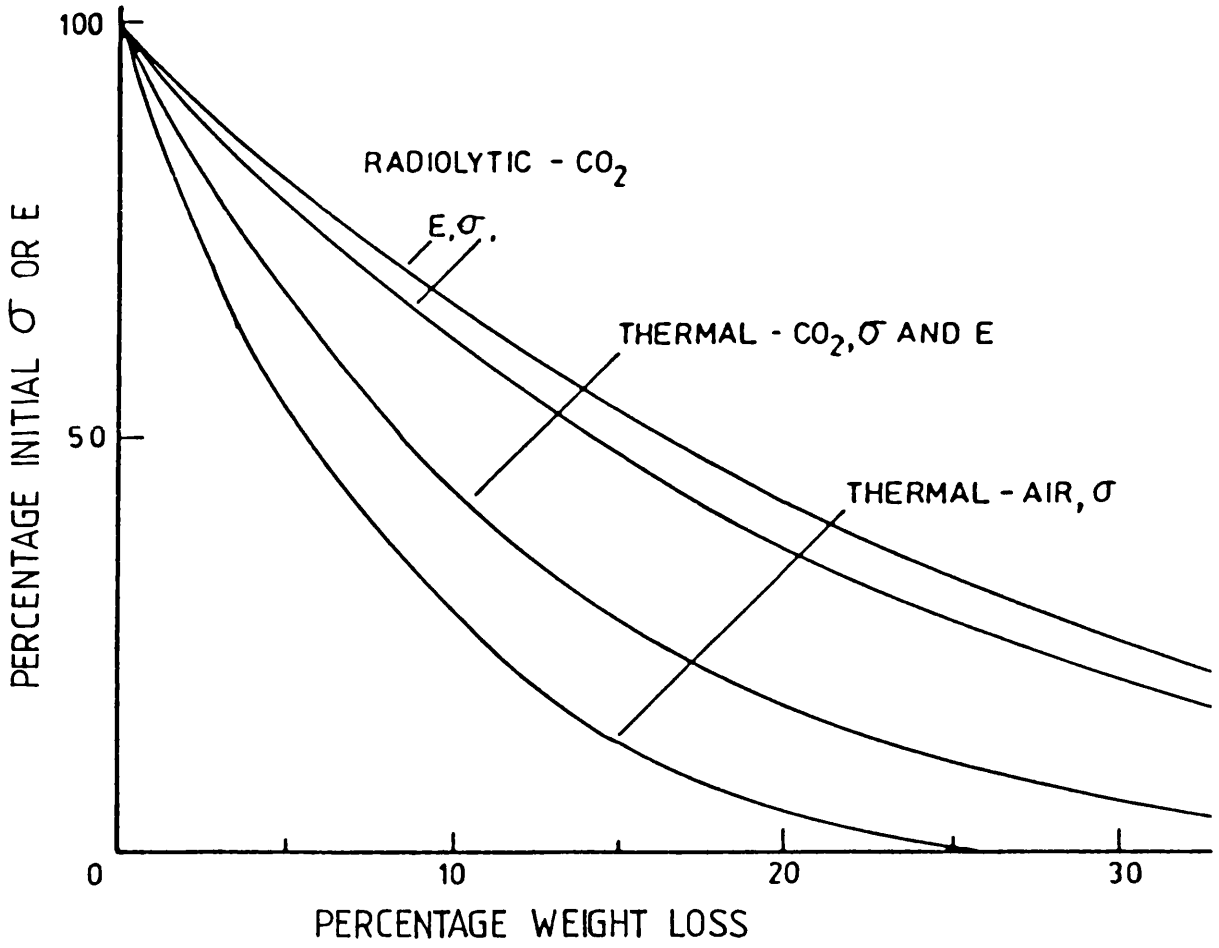

Fig. 2.6 The relationship between strength loss and weight loss for radiolytic oxidation and thermal oxidation in CO_2 and air. (from ref.21)

strength and modulus were the same for different types of graphite and were independent of the mode of testing. They mention that attempts to describe the modulus change due to oxidation, using existing models (1977), for porous bodies show that the modulus falls more rapidly than can be accounted for by an increase in the size of isolated voids. This implies that a substantial amount of the voidage is continuous throughout the matrix. The relative changes in properties may also be affected by the homogeneity of weight loss, Wood et al (64) report that mechanical properties are reduced significantly for small amounts of internal oxidation, however if weight loss is principally confined to the surface, then the mechanical properties are virtually unaffected. Homogeneity of weight loss is discussed more fully in section 4.1.

Much of the previous work on the effects of oxidation has been conducted over large weight loss ranges and most authors have reported obvious changes in the fracture mechanisms. Board and Squires (60) working on coarse grained PGA graphite noted that in unoxidised specimens and specimens oxidised to less than 5% weight loss, the principal characteristic of the fracture appearance was basal plane separation of the grains. However, oxidation preferentially attacked the binder and as a consequence fracture of higher weight loss specimens was due entirely to interbinder failure. Rounthwaite et al (61) who were also oxidising a similar graphite in CO_2 corroborated these findings. Knibbs and Morris (63) working on PGA graphite,

but oxidising in air attributed strength losses to attack of the grain-binder interface.

Thrower and Bognet (65) examined the variation in compressive strength to failure of two different graphites, Stackpole 2020 and Great Lakes H440 grades. They found that variation in oxidation rates in air over a temperature range of 500-800^{o} did not significantly alter the strength dependence of oxidation, but Board and Squires (60) found that as the oxidation rate in CO_2 increased there was a more severe strength loss for a specific weight loss.

CHAPTER 3

EXPERIMENTAL DETAILS

The programme of work required characterisation of the graphite before and after thermal oxidation. The characterisation can be sub-divided into (i) structural evaluation of the graphites, which includes density, porosity, grain size and grist particle anisotropy, and (ii) mechanical properties, which include flexural strength, dynamic modulus, critical stress intensity factor, specific surface energy and individual grain cleavage strength. In addition to the description of the various experimental techniques, illustrative data of unoxidised material are presented.

3.1 MATERIALS SELECTION

The majority of the work of this study has been on two types of nuclear graphite:- Pile grade A and IM1-24

(i) Pile Grade A referred to as PGA-AGL, has been used extensively in British reactors for many years, principally as a moderator. It is a relatively large-grained, extruded, needle-coke, graphite with a coal tar pitch binder. The extrusion process makes the material anisotropic with respect to its mechanical properties as quantified in following sections of this chapter. The microstructure (Fig.3.1a), also indicates the preferential orientation of filler grains and the maximum dimension of the pores, which

tend to lie parallel to the extrusion direction. Specimens were cut from the parent block in three orthogonal directions, Fig.3.2. To reduce the number of specimens that required oxidising and testing, the vertical orientation, i.e. specimens whose major axis lay parallel to the extrusion axis, were selected for detailed examination. Data for the other two directions are quoted where available.

(ii) IM1-24 is a more recently developed graphite than PGA AGL and is stronger and more isotropic. It is manufactured from approximately spherical, gilsocarbon filler grains, (Gilsocarbon is formed by heat-treatment of gilsonites, a naturally occurring asphaltite), which are moulded with a coal-tar pitch binder.

IM1-24 provides a good contrast to PGA-AGL, so that changes upon oxidation may be examined for graphites of distinctly different microstructural texture and mechanical strength. This microstructural difference may be seen by a comparison of Fig.3.1a and c.

A limited amount of data were collected from a third material of intermediate texture and strength, SM2-24. SM2-24 is a semi-isotropic moulded graphite with block shaped grains which are of an intermediate size to those of PGA-AGL and IM1-24. The microstructure is shown in Fig.3.1b.

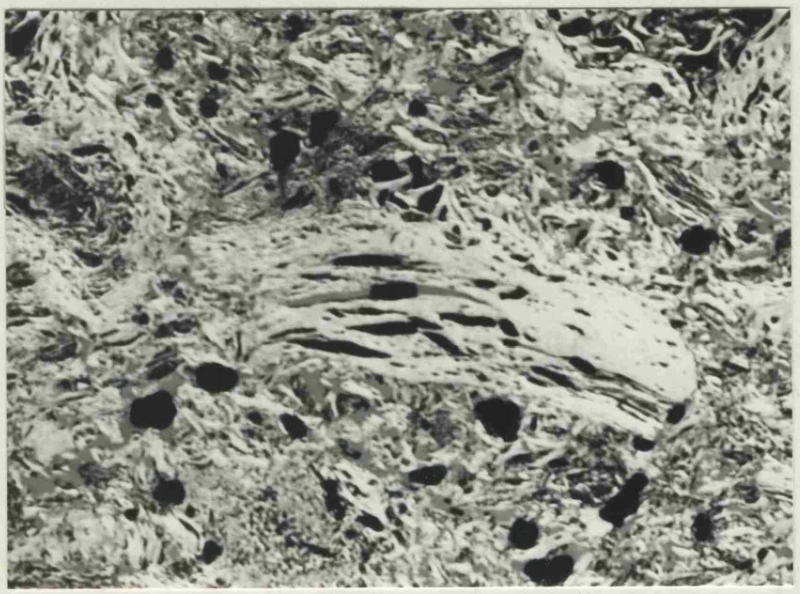

A

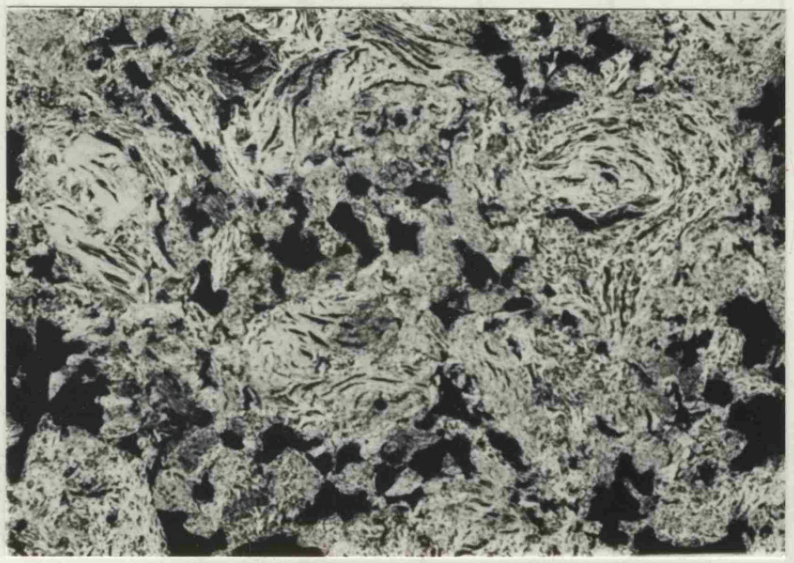

B

C

500 µm

Fig. 3.1 Low power micrographs of the general microstructure of PGA-AGL (A), SM2-24 (B) and IM1-24(C).

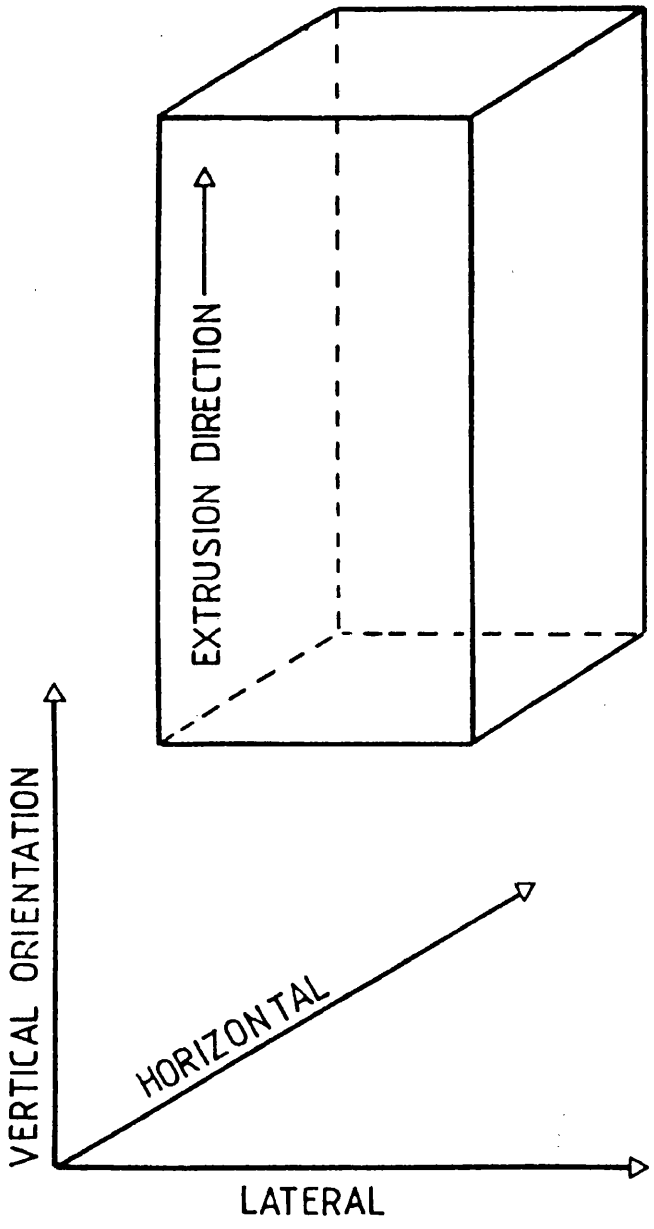

Fig. 3.2 The notation for specimen orientation of PGA-AGL graphite.

3.2 THE OXIDATION CONDITIONS

The oxidation conditions were selected to attain a maximum degree of homogeneity of weight loss throughout the specimen volume within a reasonable period of time. This was achieved by oxidising in the chemical control, temperature regime which was determined using a criterion developed by Stephen (68) which will be discussed in section 4.1.

Oxidation was caried out in a sealed-tube, three-zone, furnace. Each zone was potentiostatically controlled allowing an even temperature over a 300 mm hot-zone. The graphite specimens were loaded into the furnace in such a way as to allow good gas circulation and similar batch sizes were used for each oxidation cycle. The loads were slowly heated over a period of 12 h to the oxidation temperature of 900^{o}C in an atmosphere of nitrogen which had been dried by passage over molecular sieve 5A and silica gel. The gas circulation system is represented in Fig.3.3. When the temperature had stabilised, the dried oxidising gas was fed into the sealed tube at approximately atmospheric pressure and a flow rate of 10 ml/min or 100 ml/min according to the gas system used.

One of two oxidising gas systems was used:-

(i) Premixed and analysed bottles of 95 ± 0.4% carbon

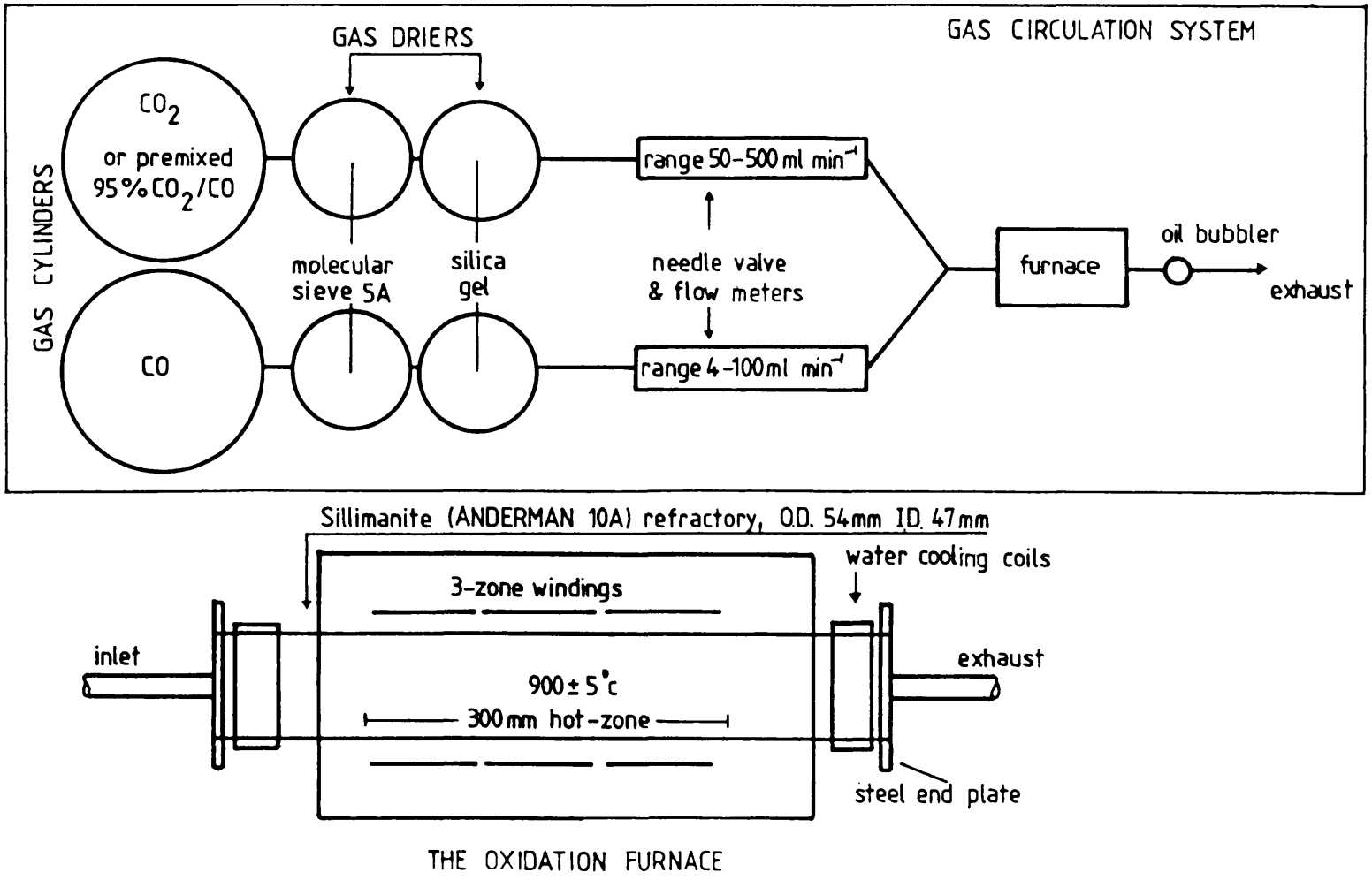

Fig. 3.3 Schematic diagram of the gas circulation system and the oxidation furnace.

dioxide, balance carbon monoxide, supplied by Air Products Limited. Due to the gas being mixed, it was necessary to use low pressure cylinders (approximately 300 psi) so that the gas released remained at constant composition as the pressure reduced. Cylinders operating at a flow rate of 10 ml/mm can be used for a maximum of 150 h; (ii) carbon dioxide and carbon monoxide were mixed *in situ* and in the same ratio as the previous systems but a higher flow rate of 100 ml/min was used to allow sufficiently accurate monitoring of the carbon monoxide. This system proved to be more economical than the premixed gas.

3.3 CHARACTERISATION OF THE GRAPHITES

To enable the effects of oxidation upon the properties of the graphite to be analysed, it is important to study variations in the individual parameters that combine to determine the strength of the graphites. The following is an account of the techniques used.

3.3.1 Grain Size

Grain size was measured using a Zeiss optical microscope at a magnification of approximately 80x. To aid definition of individual grains, i.e. to distinguish them from the binder material, the polished specimens were examined using cross-polarised light and a sensitive tint plate. This technique will be discussed in more detail in section 3.5. Sections were taken at random from the

isotropic IM1-24, but for the anisotropic PGA, sections were taken parallel to the extrusion axis. The maximum and minimum dimensions were noted for each of the 100 grains measured. The apparent grain size distribution is shown in Fig.3.4 for both graphites. It is called the apparent grain size distribution because the plane of the section will cut through some of the grains non-equatorially in the case of the spherical grains of IM1-24, thus apparently reducing the grain diameter. Similarly PGA grains may appear larger if sectioned diagonally, or small if other sections which are not parallel to grain are taken.

From figure 3.4 it can be seen that not only does PGA-AGL have a much larger grain size than IM1-24, but the range of the size distribution is also greater. Another major difference between the two materials is the grain shape. In figure 3.5 the grain shape factor (minimum dimension/maximum dimension), has been plotted against cumulative fraction of grains measured. A low grain shape factor indicates elongated grains, whereas a factor approaching 1 signifies a spherical or cubic grain shape. Figure 3.5 shows that whilst a large proportion of IM1-24 grains are not spherical, i.e. shape factor < 1, most grains are approximately spherical, whilst PGA-AGL grains tend to be elongated.

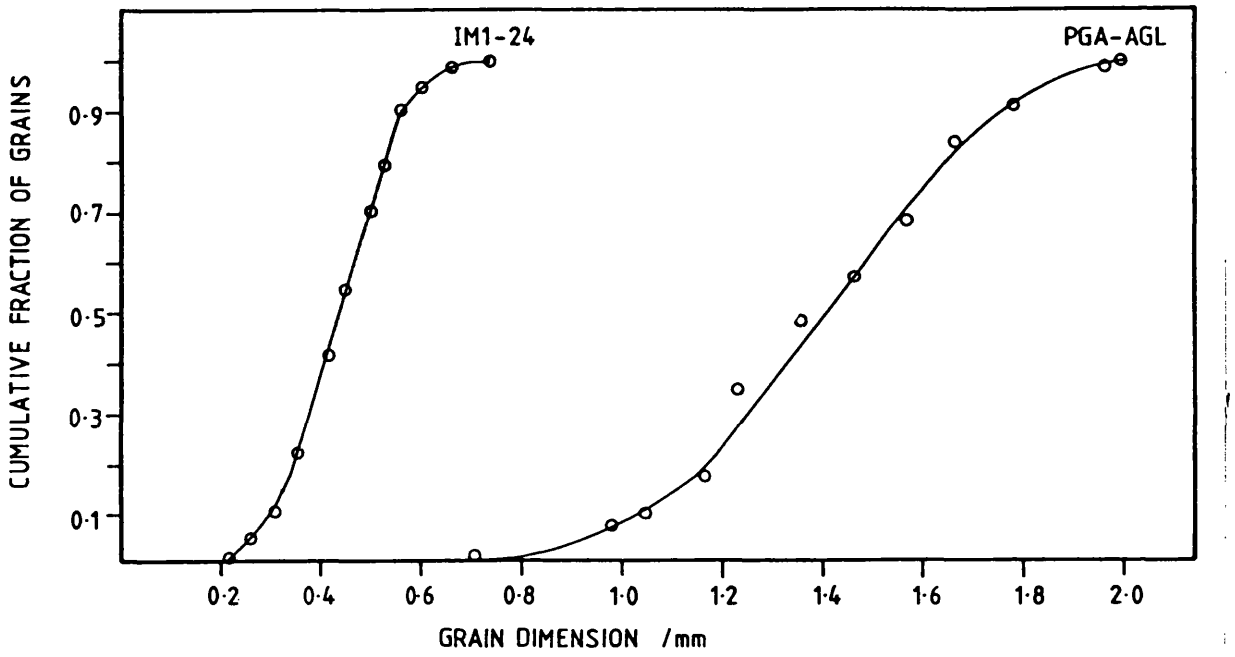

Fig. 3.4 Grain size distribution for IM1-24 and PGA-AGL.

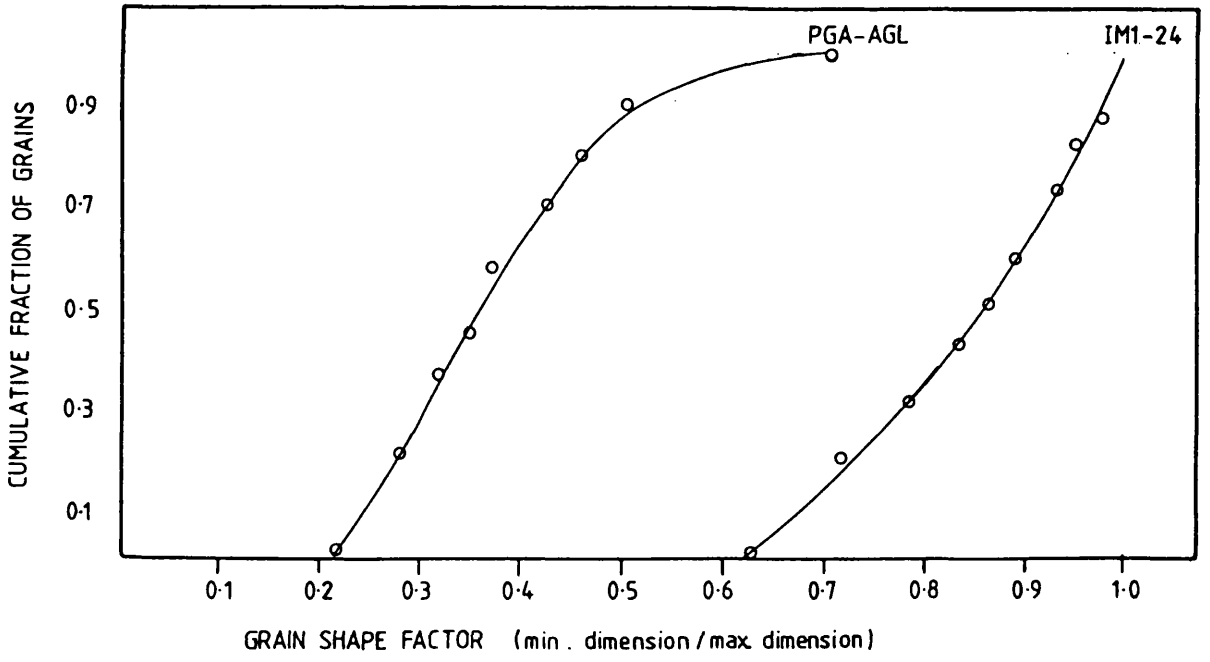

Fig. 3.5 Grain shape factor for IM1-24 and PGA-AGL.

3.3.2. Density and Porosity

The apparent density (ρ_{APP}) calculated from the mass and external dimensions was determined using cyclindrical specimens, 60 mm long x 15 diameter, that had been dried in an oven at ~ 100°C and allowed to cool either in a dessicator, in the case of unoxidised specimens, or in the oxidising furnace in a dry nitrogen atmosphere. Apparent densities for both IM1-24 and PGA are presented in table 3.1. The difference in apparent density, which is in the range 1.70-1.85 g cm^{-3} for most nuclear graphites and the single crystal density of graphite, (P_o) which is approximately 2.26 g cm^{-3} may be principally attributed to the porosity. This porosity may be either interconnected open pores or isolated closed pores. The fractional total porosity P may be calculated from

$$P = 1 - \frac{\rho_{APP}}{\rho_o} \qquad (3.1)$$

Three methods were considered for determining the open porosity:-

(i) A water displacement technique according to the German specification DIN 51056 (73), in which boiling water permeates the open pores and the open pore volume is calculated from the weight increase. This method has the disadvantage of indicating total open pore volume only, there is no information on pore size distribution.

TABLE 3.1 PORE VOLUME PERCENTAGE DETERMINED USING PYKNOMETRY

MATERIAL	PORE VOLUME PERCENT		
	TOTAL	OPEN	CLOSED*
IM1-24	18.57±0.77	8.81±1.04	9.77±1.80
PGA-AGL	23.4 ±1.1	18.25±1.24	5.18±1.49

* Closed pore volume percent is calculated by substracting the pyknometrically determined open porosity from the total fractional porosity, calculated using equation 3.1.

Results for unoxidised graphites, using this technique are presented in table 3.1.

(ii) Mercury porosimetry, where mercury is impregnated into the graphite under pressure. The applied pressure is a function of the pore orifice size and the volume of mercury for each pressure increment is noted, thus relating a pore volume fraction to a specific pore size. The pore orifice is assumed to be characteristic of the pore size. Whilst this technique would give a pore size distribution, it cannot yield any data on pore shape and was therefore rejected in favour of the following method.

(iii) Automatic image analysis involves direct observation of pores using a microscope and automatic data accumulation and analysis of pore dimensions using a computer. Thus pore morphology and pore size distributions may be determined. The technique is discussed more fully in section 3.5.

3.3.3. Grist Particle Anisotropy

It was necessary to quantify the degree of grist particle anisotropy in PGA AGL to determine an input parameter to the analytical fracture model which will be discussed in section 5.1. Measurements of the anisotropy of grist particle orientation with respect to the extrusion direction were made by the method of Bacon (71). A slice of

PGA about 2 mm thick, was cut parallel to the extrusion direction, polished and cleaned in an ultra-sonic bath and mounted perpendicular to the incident nickel filtered, CuKα radiation, Fig.3.6. Transmission x-ray photographs were taken using ten exposures of one minute duration, moving the specimen between each exposure, yet maintaining the angular relationship between the extrusion direction, x-ray beam and the film.

The resultant photograph recorded a halo whose radius subtends an angle of 26^{o}. This halo corresponds to the reflection from 0002 planes. The density of the halo varied systematically around its circumference, the most dense regions at the top and bottom, due to the greater number of layer planes which are parallel to the extrusion axis. Reflection to the sides is due to planes inclinded at $90^{o} - \theta$, where the Bragg angle $\theta = 13^{o}$for 0002 planes. A microdensitometer was used to track radially across the halo at various angles and record the integrated intensity. From this a relationship between intensity, (i.e. density of 0002 normals) and the angle with respect to the extrusion axis can be derived, Fig.3.7. The relationship between intensity and Φ is reasonably represented by the function $I(\Phi) = \sin^{3.5} \Phi$, Fig.3.7. The Bacon anisotropy factor may be calculated (71) using the following expression

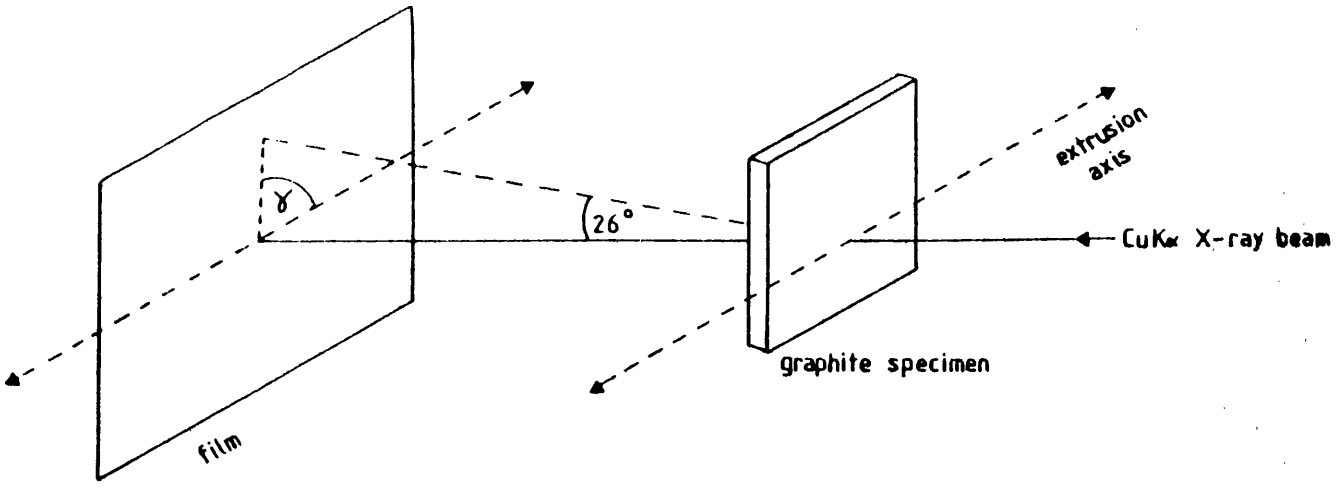

Fig. 3.6 Schematic representation of the Experimental arrangement for grain anisotropy determination.

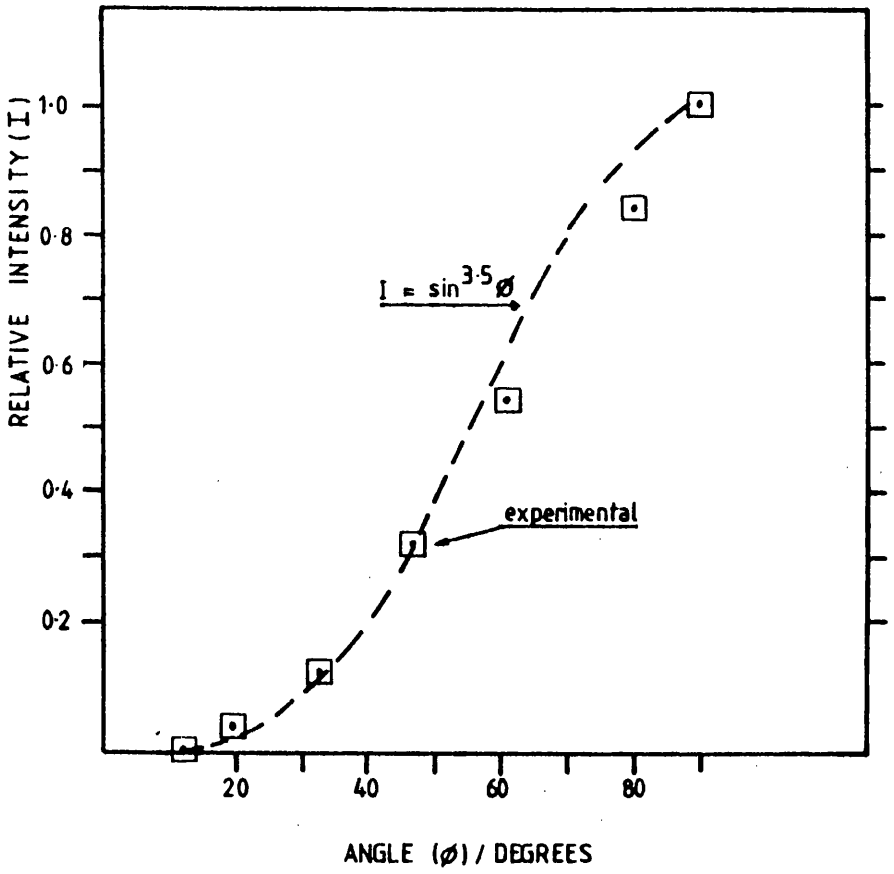

Fig. 3.7 Variation of the relative intensity of diffraction from basal planes with the angle between plane normals and the extrusion axis.

$$\text{ANISOTROPY FACTOR} = 0.5 \frac{\int_{o}^{\pi/2} I(\phi)\sin^{3} d\phi}{\int_{o}^{\pi/2} I(\phi)\ \sin\ d\theta}$$

Using $I(\Phi) = \sin^{3.5} \Phi$ an anisotropy factor of 2.75 for PGA-AGL is produced. This may be compared with values from other materials quoted by Bacon in reference 71; extremely anisotropic, pressed, Madagascar flake has an anisotropy value of 7, whilst almost isotropic coke and pitch have a value of 1.

3.4 MECHANICAL TESTING

3.4.1. Flexural Strength and Acoustic Emission Monitoring

(a) Flexural strength

Flexural strengths were determined using a screw driven Instron 1195 machine at a crosshead speed of 0.5 mm min^{-1}, fig.3.8. The flexural specimens (60 mm in length and 15 mm diameter) were loaded in a three-point bend rig which had 4 mm radius rollers set at a span length of 50 mm. The surface of the cylinders were in the as-machined condition and there was no further surface preparation after oxidation. Load and crosshead displacement were monitored, Fig.3.9 and the maximum tensile stress at failure, σ_f, was calculated using

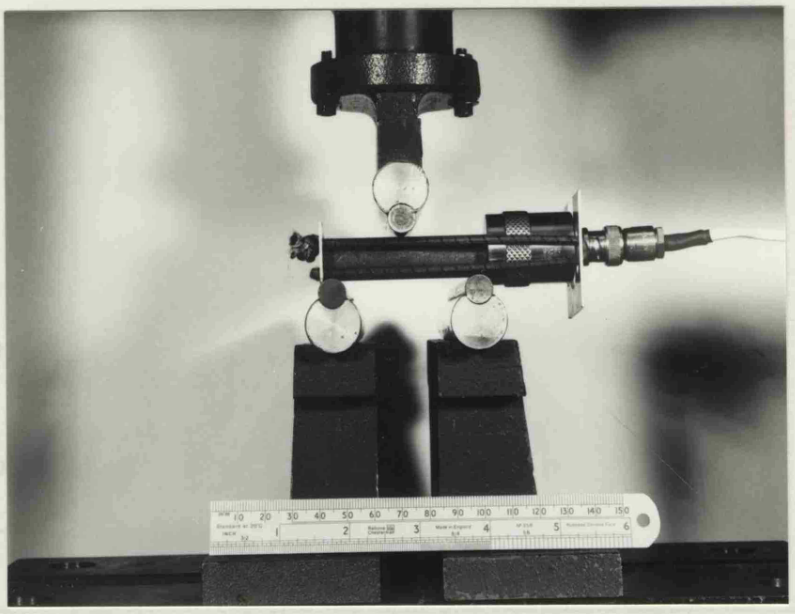

Fig. 3.8 The bend specimen in the 3-point bending rig with the AE transducer attached.

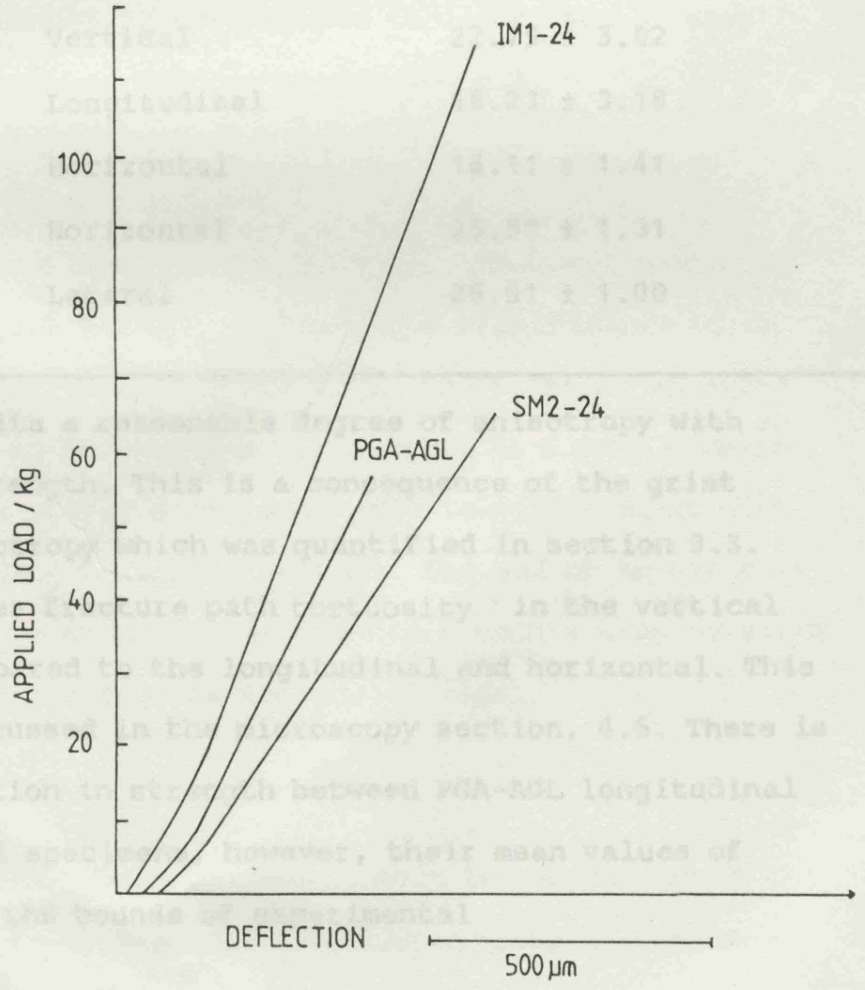

Fig. 3.9 Examples of load displacement curves from three point bending; from unoxidised graphite.

$$\sigma_f = \frac{8PL}{\pi d^3} \qquad (3.2)$$

where P is the maximum force (N), L is the loading span (m) and d is the specimen diameter, m. Mean unoxidised values of σ_f and a single, standard deviation are presented below

TABLE 3.2 FLEXURAL STRENGTH OF UNOXIDISED IM1-24, PGA-AGL AND SM2-24.

Materials		Flexural Strength/MNm^{-2}
IM1-24		43.56 ± 2.79
PGA-AGL	Vertical	22.79 ± 3.02
	Longitudinal	18.23 ± 3.18
	Horizontal	16.11 ± 1.41
SM2-24	Horizontal	25.99 ± 1.31
	Lateral	26.51 ± 1.00

PGA-AGL exhibits a reasonable degree of anisotropy with respect to strength. This is a consequence of the grist particle anisotropy which was quantified in section 3.3. which increases fracture path tortuosity in the vertical specimens compared to the longitudinal and horizontal. This effect is discussed in the microscopy section, 4.6. There is a small variation in strength between PGA-AGL longitudinal and horizontal specimens, however, their mean values of σ_f are within the bounds of experimental

uncertainty. SM2-24, although described as semi-isotropic appears to be isotropic as far as strength is concerned.

(b) Acoustic emission

To aid investigation of sub-scritical events, acoustic emission (AE) was monitored during flexural strength testing. The apparatus used was a proprietary amplitude distribution analyser made by Acoustic Emission Technology Corporation, model AETC 203. (fig.3.10). The instrument was capable of:- (i) detecting emissions in the range 0.1 MHz to 2 MHz; (ii) sorting them into 50 amplitude channels over a range of 60 db. Channel 1 holds signals with a gain of 80 db with respect to 1 μV at the piezoelectric transducer; channel 50 corresponds to 140 db on the same scale. The instrument had two main functions: -

(i) The first function was to count the total number of events during the mechanical test. The significance of an event may be realised from fig.3.11; the start of an event is considered to be when the first pulse in a wave package resulting from energy dissipation due to micro-mechanical events, exceeds a threshold voltage. The end of an event is considered to be when a predetermined time has elapsed since the last pulse crossed the threshold value.

(ii) The second function was to sort the amplitude of the maximum pulse from each event into an appropriate channel

A

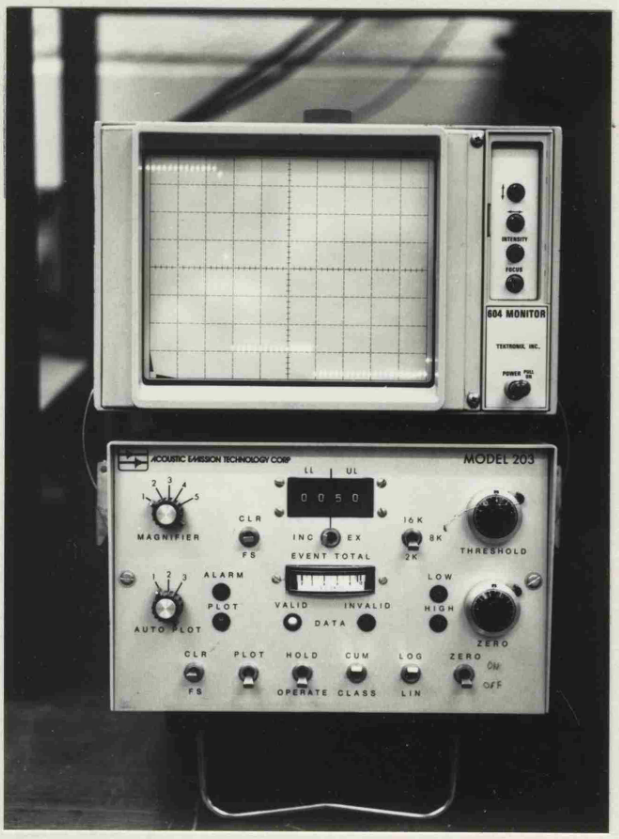

B

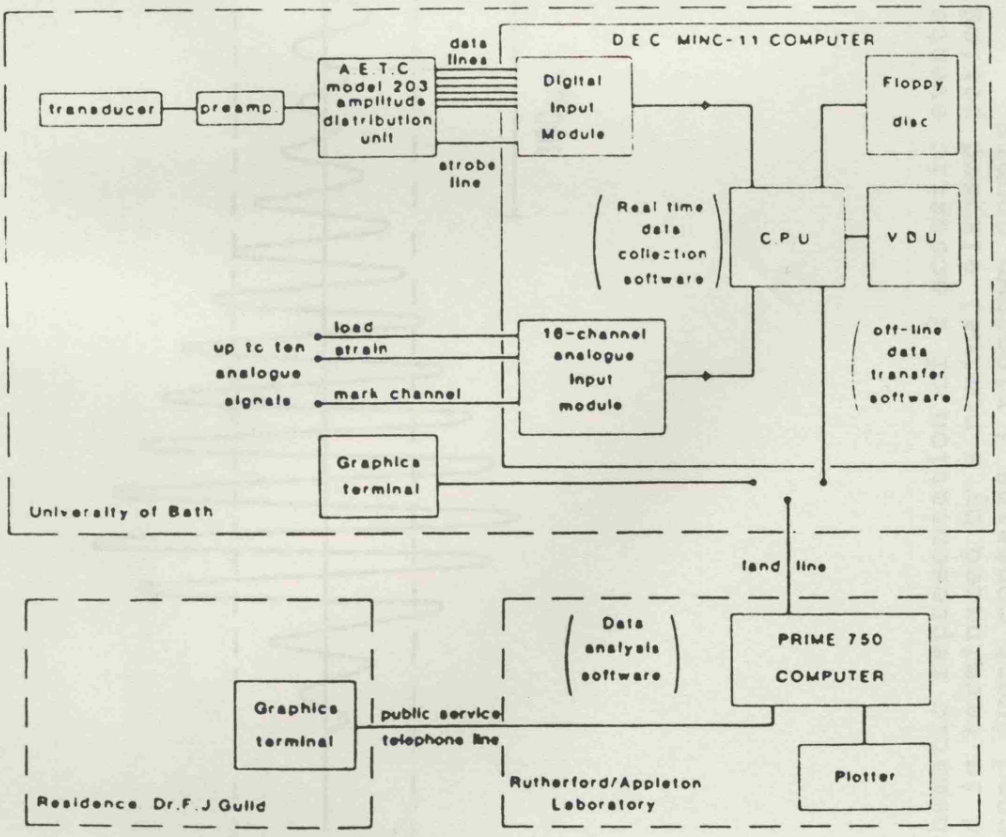

Fig.3.10 (A) The AETC 203 amplitude distribution unit
(B) Schematic representation of the AE monitoring system (from ref.76)

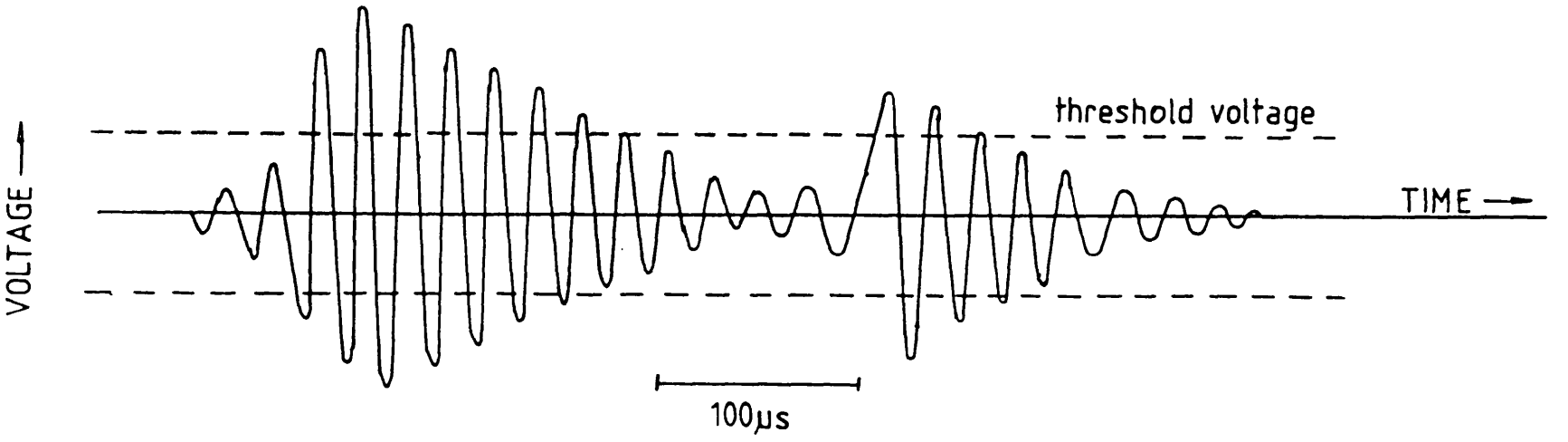

Fig. 3.11 Schematic representation of 2 acoustic events. The first event contains 8 ringdown counts and is terminated by a nominal elapsed period of sub-threshold voltage, e.g. 100μs. The second event contains 3 ringdown counts.

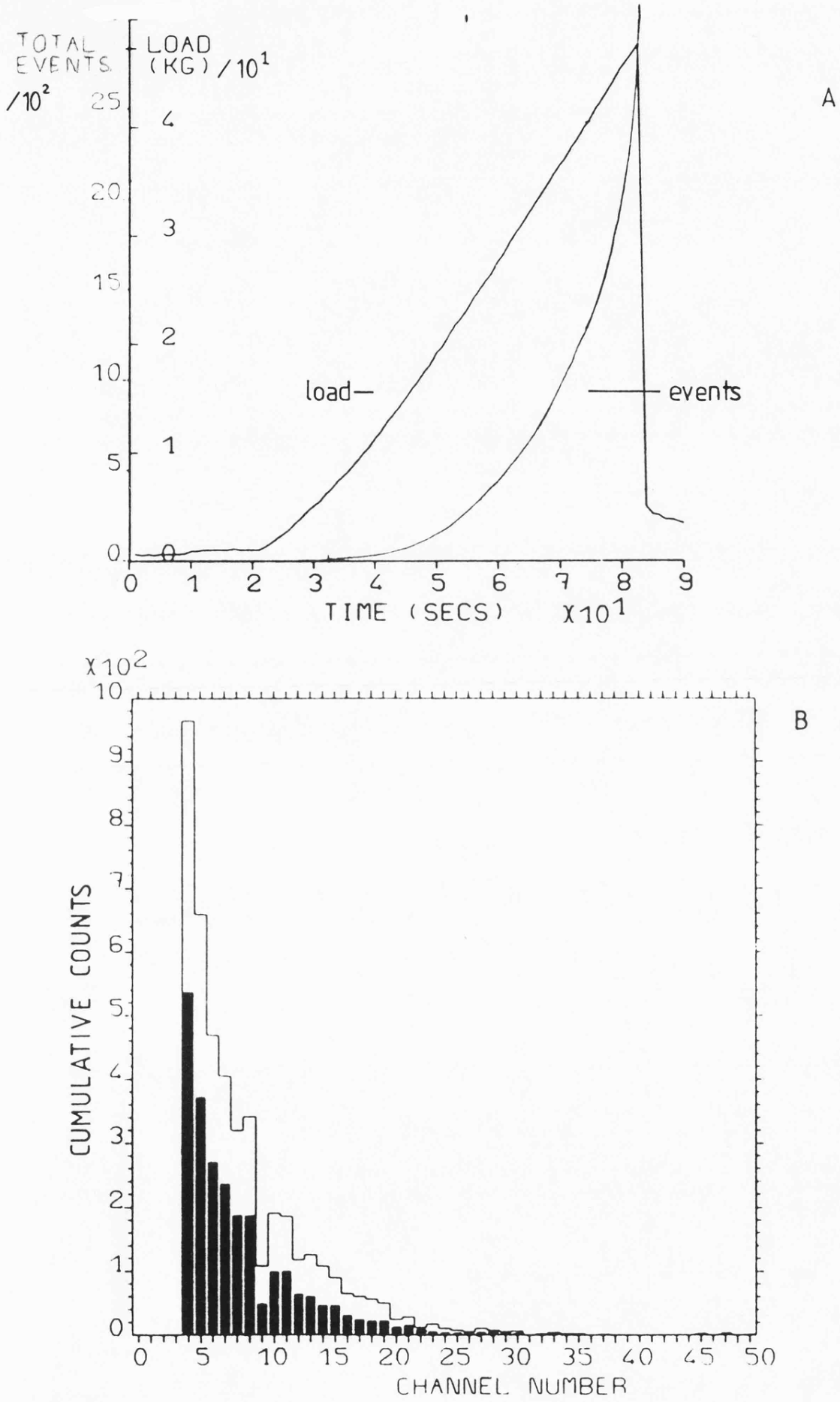

Fig.3.12 Examples of processed AE data of PGA-AGL from the Rutherford Laboratory.(see Fig.3.10) (A) Total number of counts and load versus time. (B) Amplitude distribution at fracture and 1kg prior to fracture (black).

and count the number of events in each amplitude channel. In early work data were taken from the AETC 203 instrument as: (a) continuous, cumulative total number of events against time or load and (b) as the amplitude distribution display; these were photographed from an oscilloscope at intervals during loading and at fracture. In the later stages of the work computerised accumulation and processing of acoustic emission data became available (76). Figure 3.12 a and b shows an example of the curve of total cumulative events versus load and the amplitude distributions immediately before fracture, for PGA-AGL. Occasionally during AE monitoring, events registered before any load was applied to the specimen; this was due to external noise. It was found that this noise was airborne and not due to mains interference. One source of noise was from the line printers in the testing room. However, even if these were switched off other external sources operated. To avoid monitoring these, a wire cage was erected around the specimen and transducer and this was earthed to the preamplifier. Before each test was undertaken a period of AE silence, i.e. less than 1 or 2 counts per minute was required before proceeding. On days when external noise was greater than this, testing was postponed.

3.4.2 Dynamic Elastic Modulus

The ideal requirement for modulus determination is a reproducible test which may be achieved, non-destructively on the same specimen before and after oxidation. A sonic

resonance method was employed, according to the procedure described in ANSI/ASTM C747-74 (77). This requires the measurement of the fundamental resonant frequency of a slender rod of circular cross section. The specimen used is shown in Fig. 3.13. It was supported on two P.T.F.E. pivot points at a distance of 0.224 x length, from the ends of the rod, i.e. the nodal points for fundamental frequency. One end of the specimen was vibrated using a driver unit which was connected to a variable oscillator, enabling the frequency to be controlled. A pickup was placed on the other end of the specimen. Both driver and pickup were stereo record cartridges modified to vibrate in a vertical mode. They were mounted on a counter-balanced pivot arm, which allowed both pickup and driver resting weight to be adjusted (Fig.3.14). The driver and pickup were monitored on an oscilloscope, Fig.3.15. Starting the driver at low frequencies, ≈ 100 H_z, and increasing the frequency gradually, the pickup trace was examined for signs of excitation. Below fundamental frequencies the specimen damped the driven oscillations. However, as the fundamental frequency was approached, the pickup amplitude increased to a maximum and then reduced on further increase of frequency. To test that the frequency of oscillation was fundamental and not a higher order harmonic, the pickup trace was reset to maximum amplitude and the frequency noted. The pickup cartridge was then moved towards the centre of the rod. If the amplitude was a minimum over the nodal points and a maximum at the ends and the centre of the bar, then the specimen was vibrating at fundamental frequency. The

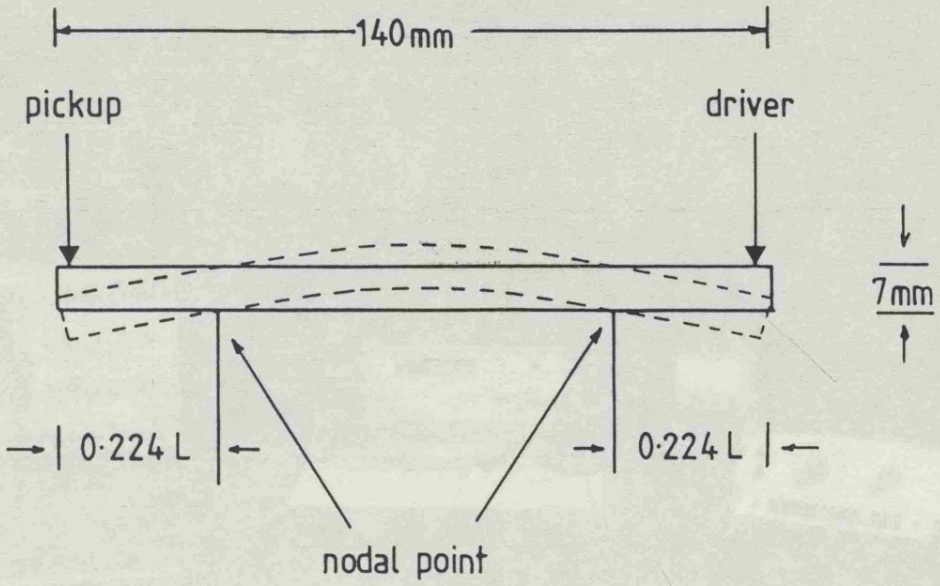

Fig. 3.13 The dynamic Modulus specimen showing the form of deflection at the fundamental resonant frequency.

Fig. 3.14 The pickup and driver units for elastic modulus determination in position on a specimen which is supported on its nodal points.

A

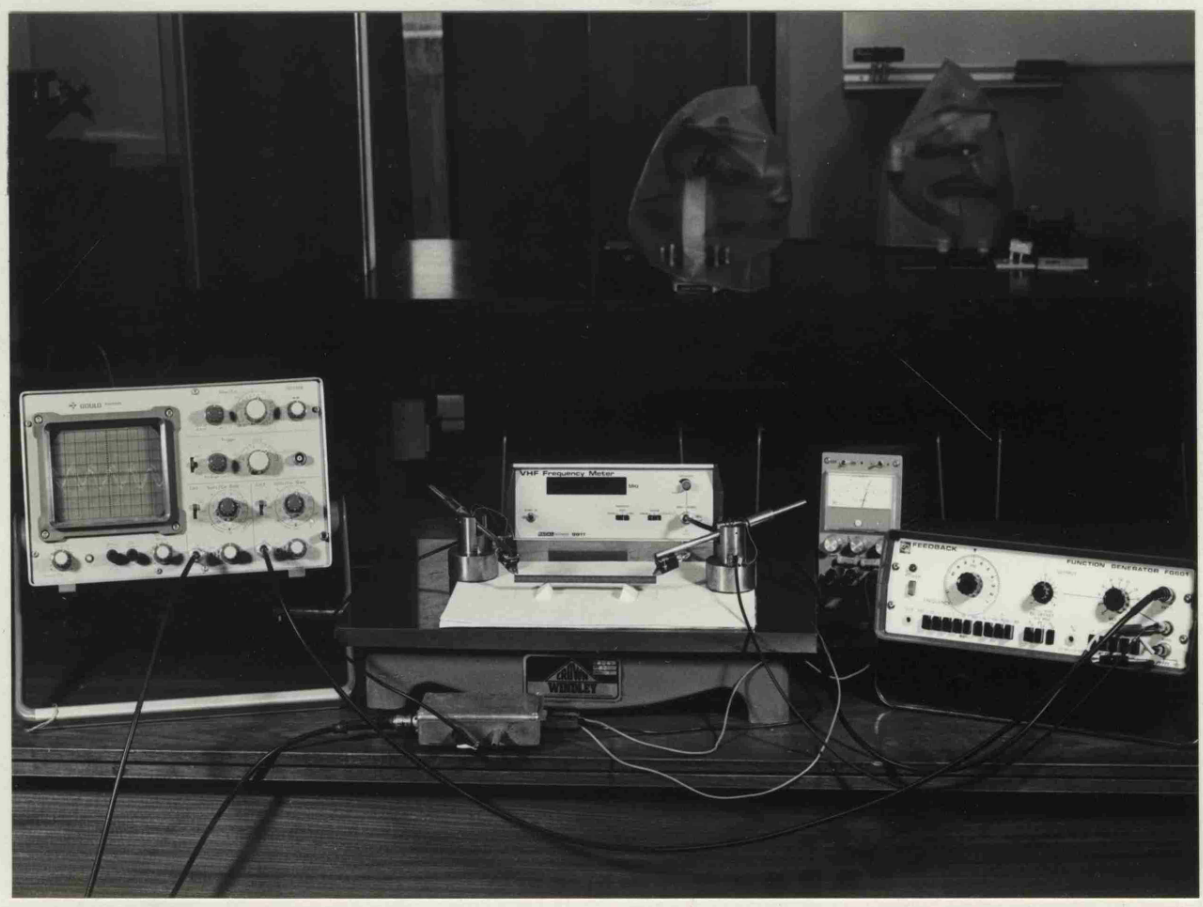

B

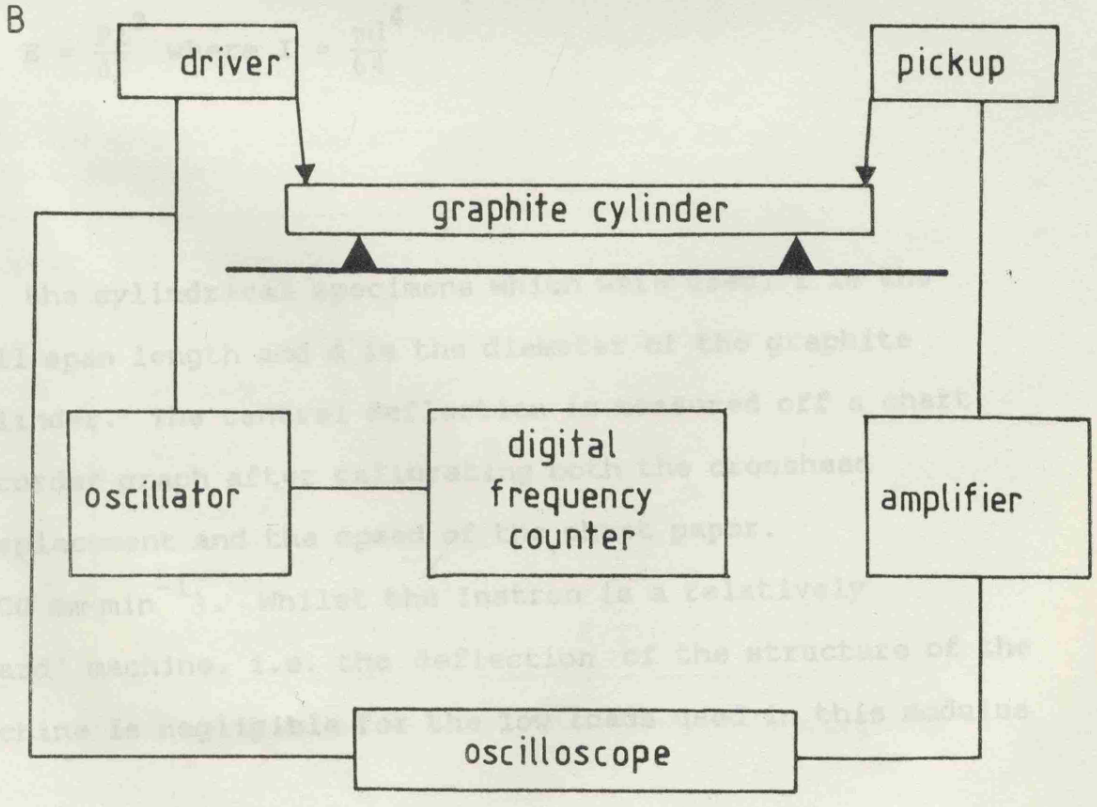

Fig. 3.15 The experimental arrangement for the determination of elastic Modulus (A); the schematic arrangement is shown in B.

elastic modulus, E, is related to the fundamental frequency, f, by,

$$E = A_c M f^2 / d \qquad (3.3)$$

where M is mass (kg), d is the diameter of rod (m), A_c is a constant which is related to geometry and ratio. Values of A_c are tabulated in reference 77. Table 3.3 gives dynamic modulus values for the unoxidised material. The dynamic modulus has been compared with the static modulus. (Table 3.3). The static modulus was determined using a three point bending rig on an Instron 1122; a cross head displacement rate of 0.5 mm min^{-1} was used. The relationship between load, central deflection and modulus is given by

$$E = \frac{P\ell^3}{\delta I} \quad \text{where } I = \frac{\pi d^4}{64}$$

For the cylindrical specimens which were used, ℓ is the full span length and d is the diameter of the graphite cylinder. The central deflection is measured off a chart recorder graph after calibrating both the crosshead displacement and the speed of the chart paper. (100 mm min^{-1}). Whilst the Instron is a relatively 'hard' machine, i.e. the deflection of the structure of the machine is negligible for the low loads used in this modulus

determination, (less than 30 Kg) there is a finite deflection within the load cell. The load cell used was an Instron 2511-312, 500 Kg, tension/compression type. To calibrate the 'softness' of the load cell, a massive piece of steel was placed in the three point bend rig and was loaded at a cross head speed of 0.5 mm min^{-1}. This was done for full scale load (f.s.d.) values of 20 Kg and 50 Kg. Apparent central deflection values of 0.05 mm and 0.1 mm were found at 20 Kg and 50 Kg respectively. The deflection rates of, 0.0025 mm Kg^{-1} (20 Kg fsd) and 0.002 mm Kg^{-1} (50 Kg fsd) were attributed to deflection of the load cell. Values of the actual central deflection are found by subtracting the load cell deflection for the appropriate load from the deflection determined from the chart recorder. This procedure is also followed when determining deflection for effective surface energy measurements (section 3.4.4).

TABLE 3.3
DYNAMIC AND STATIC MODULUS FOR UNOXIDISED IM1-24, PGA-AGL AND SM2-24.

MATERIAL	ORIENTATION	DYNAMIC GNm^{-2}	STATIC GNm^{-2}
IM1-24	Isotropic	12.4±0.7	14.4±0.9
PGA-AGL	Vertical	12.1±1.0	13.9±1.5
	Horizontal and Lateral	6.3±0.5	7.3±0.7
SM2-24	Isotropic	8.4±0.4	8.4±0.5

For all types of graphite the static modulus is slightly

larger than the dynamic modulus. However when the experimental uncertainty is taken into consideration there is an overlap of values. Both static and dynamic methods show the strong effect of grist particle anisotropy in PGA-AGL upon modulus.

3.4.3 Stress Intensity Factor (K_c)

Due to limitations of space in the oxidising furnace and the availability of material, the requirements of the stress intensity factor specimens were that they should be compact, easily machined and give reproducible results. Three specimens geometries were considered:-

(1) Centrally, through slotted discs (Fig.3.16a), which were loaded in diametral compression using the method described by Sato et al (45). The slot was machined using a jig to locate the specimen so that the 12 mm diameter, 0.1 mm thick blade cut centrally and reproducibly. The edge of the slot was finished using a razor blade. The compressive force was exerted using flat platens, and a crosshead displacement rate of 0.5 mm min^{-1}. The stress intensity factor is related to the maximum compressive load at failure by the relationship:-

$$K_c = N_{1H} \frac{P}{Rt} \sqrt{(\frac{a}{\pi})} \qquad (3.4)$$

Where N_{1H} is a dimensionless stres intensity factor corrected for Hertzian contact loading, P is the compressive load (N), R, t, and a are geometrical dimensions shown in figure 3.16a.

(ii) Diametrally grooved discs, compressively loaded along an axis parallel to the groove. Figure 3.16b, according to the method of Szendi-Horvath (46). Flats were machined as indicated in the diagram to increase the contact angle, 2α, thereby reducing the bearing pressure. Initially specimens were tested without the flats, but they often failed due to excessive bearing pressure crushing the graphite on the circumference. A contact angle, $2\alpha = 70°$ was chosen to minimise bearing pressure and to maximise the ratio of tensile stress at right angles to the groove/compressive stress parallel to the groove. The groove was machined using a saw blade, 0.1 mm thick. No further edge preparation was given. Using this geometry the stress intensity factor is related to maximum compressive load :

$$K_c = 1.246(\sin 2\alpha - \alpha)\ P\ a^{0.5}/ST \qquad (3.5)$$

Where T is the thickness (m), S is the projected contact length (m).

(iii) Edge notched beams 50 mm in length and 10 mm x 10 mm square cross section were loaded in three point bending

(Fig.3.16c), using a span to thickness ratio, S/w, of 4 and a crack length to thickness ratio, a/w, ranging from 0.35 to 0.6. A central displacement rate of 0.5 mm min^{-1} was used and K_c is given by

$$K_c = \frac{A_o+A_1(a/w)+A_2(a/w)^2+A_3(a/w)^3+A_4(a/w)^4}{(B\ w^2/6M\ a^{0.5})} \quad (3.6)$$

Where M is the applied bending moment (Nm), B is the specimen breadth and the coefficients have the following values; A_o = + 1.93, A_1 = - 3.07, A_2 = + 14.53, A_3 = - 25.11, A_4 = + 25.80.

K_c results for unoxidised IM1-24 are presented in table 3.4

TABLE 3.4 A COMPARISON OF STRESS INTENSITY VALUES ($MNm^{-3/2}$) DETERMINED FROM DIFFERENT TEST GEOMETRIES FOR IM1-24.

Single Edged	Grooved Disc Diametral Compression	Through Slotted Diametral Compress
1.34 ± 0.05	1.33 ± 0.09	1.15 ± 0.09

From table 3.4, it can be seen that the edge notched bend and the grooved disc specimens gave values which were comparable, but the through slotted discs gave stress intensity values which were 14% lower. Possible reasons for

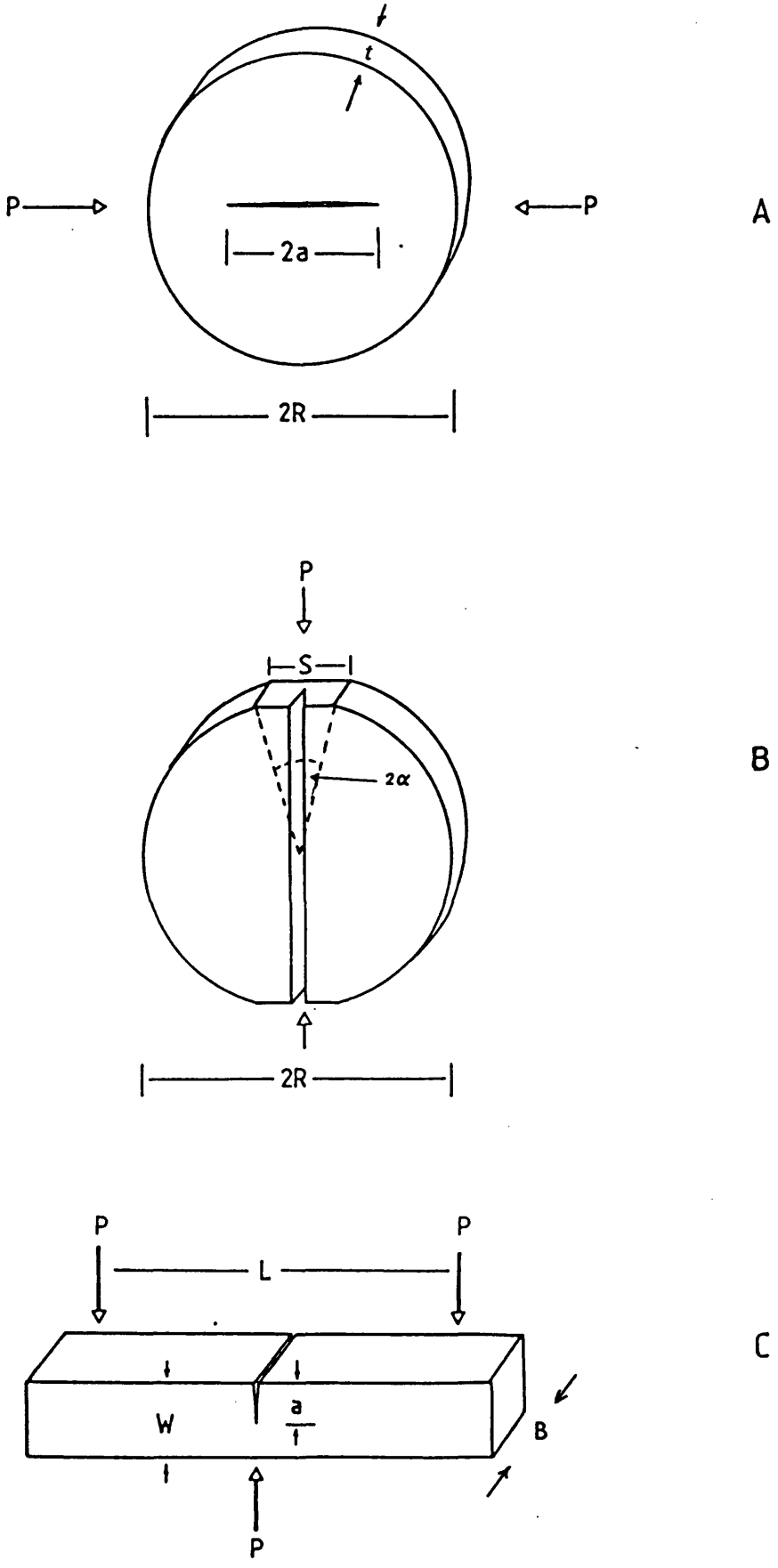

Fig. 3.16 Stress intensity factor specimens: A, through slotted disc (ref.45); B, grooved disc (ref.46); C, single edge notched beam.

this may be, insufficient specimen size, and therefore encountering the problems discussed in section 2.2.4 or, in machining and finishing the slot, adjacent grains were damaged, effectively increasing the slot length and consequently producing a low K_c value. In view of this problem and the practical inconveniences of obtaining cylinders from which discs are cut, edge notched 3-point bend specimens were selected for evaluating stress intensity factor. Also Dalgeish et al (58) suggest that this geometry is favourable as it minimises sub-critical microcracking at least compared with D.C.B. and D.T. (section 2.2.5). It is also a reasonably common geometry and this allows comparison to be made with other workers results, e.g. Brocklehurst (21) found unoxidised IM1-24 had K_c values from SENB specimens ranging from 1.3 - 1.5 $MNm^{-3/2}$, cf. 1.34 $MNm^{-3/2}$ in this work.

3.4.4 Specific Surface Energy

Specific surface energy was determined using a compliance technique similar to that used by Davidge and Tappin (40). The specimens used are illustrated in fig.3.16c. These were tested in 3-point bending, on a rig with a span length of 40 mm, using a central deflection rate of 0.5 mm min^{-1}. A family of load deflection curves were produced, Fig.3.17, by varying the a/w ratio. It can be seen from figure 3.17, which are data from unoxidised PGA-AGL, that complete separation of the specimen into two parts does not occur at maximum load. The load gradualy reduces. This

is due to the tortuous crack path absorbing all the stored elastic energy and therefore requiring externally supplied energy to propagate. Since the value of γ that is required in this investigation is the surface energy at initiation and not the energy averaged over the whole fracture process, δ_f is taken to be the deflection at maximum load. From Fig.3.17 it can be seen that the stiffness, k, (where $k = P/\delta$) reduces as the notch length/width ratio, a/w, increases. From a family of load deflection curves the relationship between stiffness and crack area, A, may be determined graphically, Fig.3.18. Crack area, $A = 2ba$, where b and a are dimensions defined in Fig.3.16 c. The elastic strain energy, u, at the instant of fracture is equal to the area under the load deflection curve, i.e.

$$u = P_f \delta_f/2 \text{ or } k \delta_f^2/2$$

Specific surface energy, γ, is equal to elastic energy release rate, i.e. the rate of energy reduction with increasing crack area, $\left(\frac{\partial U}{\partial A}\right)_\delta$

$$\text{Therefore } \gamma = - \left(\frac{\partial U}{\partial k}\right)_\delta \left(\frac{\partial k}{\partial A}\right)$$

$$\text{and} \qquad \frac{\partial U}{\partial k} = \delta_f^2/2$$

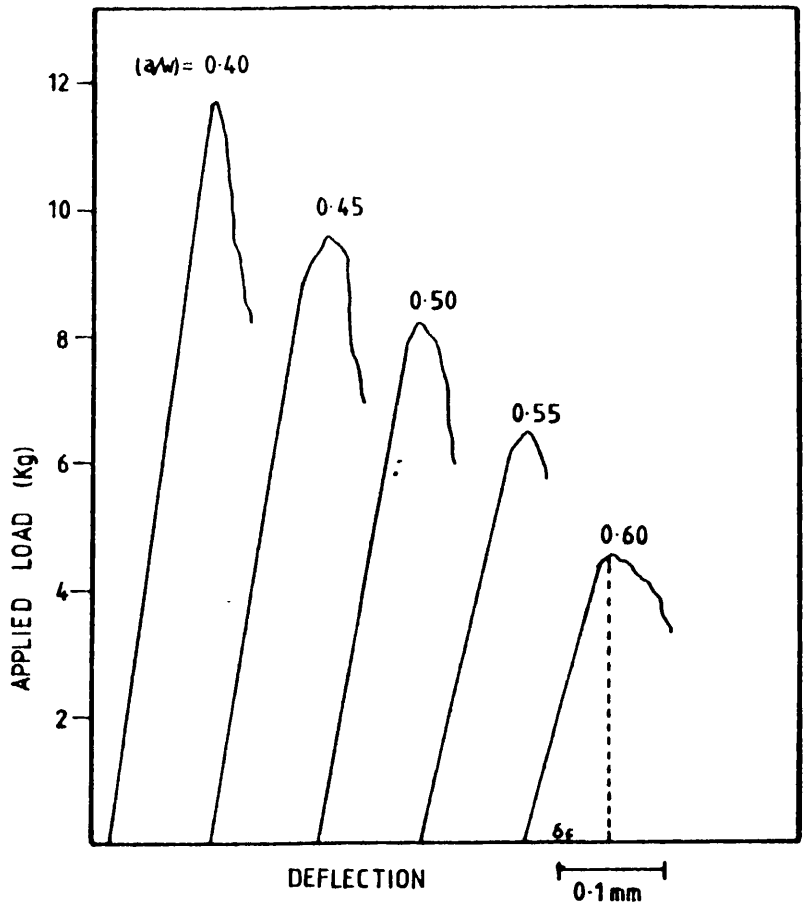

Fig. 3.17 Load/deflection curves for a range of notch lengths in SENB. specimens of unoxidised PGA-AGL.

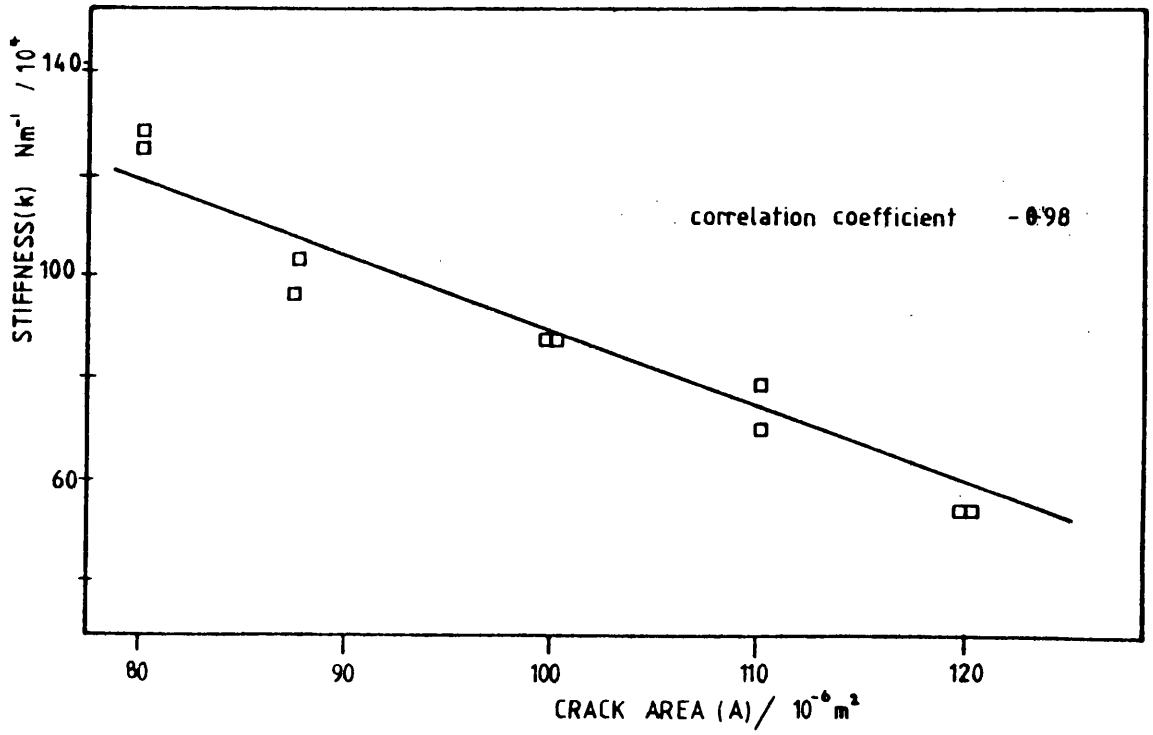

Fig. 3.18 The stiffness versus crack area relationship for unoxidised PGA-AGL.

TABLE 3.5 DATA FOR CALCULATING γ FOR UNOXIDISED PGA-AGL AND IM1-24

	$a/_w$	P_{max} /kg	k /10^4Nm^{-1}	δ_f /10^{-4}m	A /10^{-6}m^2	$\frac{\partial k}{\partial A}$ /10^9Nm^{-3}	γ /Jm^{-2}
PGA-AGL	0.40	11.7	120.8	0.95	80	-15.48	67.68
	0.40	12.3	120.7	1.00	80	"	77.40
	0.45	9.6	104.6	0.90	90	"	62.69
	0.45	8.4	96.9	0.85	90	"	55.92
	0.50	8.2	89.3	0.90	100	"	62.69
	0.50	8.2	89.3	0.90	100	"	62.69
	0.55	7.0	80.7	0.85	110	"	55.92
	0.55	6.6	71.9	0.90	110	"	62.69
IM1-24	0.40	18.0	196.2	1.00	80	-18.57	92.85
	0.40	17.2	140.6	1.20	80	"	133.7
	0.45	15.3	136.4	1.10	90	-18.04	109.1
	0.45	14.8	145.2	1.00	90	"	90.2
	0.50	13.3	124.3	1.05	100	"	99.4
	0.50	11.8	115.8	1.00	100	"	90.2
	0.55	11.0	107.9	1.00	110	"	90.2
	0.55	11.2	109.9	1.00	110	"	90.2

and therefore $\gamma = \delta_f^2 \ (\partial k/\partial A)/2$ (3.7)

γ is determined by substituting δ_f from the load deflection graph and the appropriate value of $(\partial k/\partial A)$ into equation 3.7. Data from unoxidised PGA-AGL and IM1-24 are presented in Table 3.5.

To determine γ for oxidised specimens it was necessary to oxidise a number of specimens to approximately the same weight loss value to enable k versus A relationship to be determined for that oxidation group. It is impossible to oxidise a group of specimens to exactly the same weight loss value and therefore each group had a range of weight loss values with a standard deviation of approximately 0.15% weight loss.

3.5.1 Microscopy

Specimens for micro-examination were sectioned, coarse ground on 200 grade wet and dry paper and then impregnated with a low visocisty resin, "TARB Embedding Resin". This is a four part resin mixture which can give variable hardness values according to the proportion of the constituents. A fluorescent die powder (Fluorescent Brilliant Yellow R, supplied by L.B. Holliday, Huddersfield), was added to the resin, approximately 2 ml die powder to 50 ml of resin mixture. This was to give contrast enhancement between the matrix and pores, (see section 3.5.3.). The impregnation of the open pores was done

in a vacuum chamber. Intermittently, air was allowed into the chamber to force the resin into the pores. After impregnation, the resin was cured by heating at 60°C for 24 hours. Specimens were then ground using wet and dry paper up to 600 grade, then polished using medium alumina powder. To aid definition of filler grains and indicate basal plane orientation, a sensitive tint plate (i.e. a full wave quartz plate), was used in conjunction with cross polarised light. Areas with strong basal plane orientation, e.g. filler grains that are composed of many hundreds of aligned crystallites with a similar basal plane orientation, are optically active and are coloured according to their angular relationship to the optical system. The aligned regions change from red through purple to blue when rotated through 90°, whereas non-active areas, e.g. the resin, remain purple throughout the rotation. Fig.3.19 shows a filler grain in PGA-AGL which has strong basal plane orientation, exhibiting this colour-orientation effect as it is rotated through 90°.

3.5.2. Fractography

Fracture surfaces were examined using both optical and scanning electron microscopy (SEM). The optical microscope used, was an Olympus binocular type, capable of magnification up to 20x. The SEM was a JEOL JSM 35C and was most useful in the magnification range 30 to 300 x. No special preparation was required for either examination. Fracture paths were examined by mating the two surfaces together and setting them in resin. Sections were cut

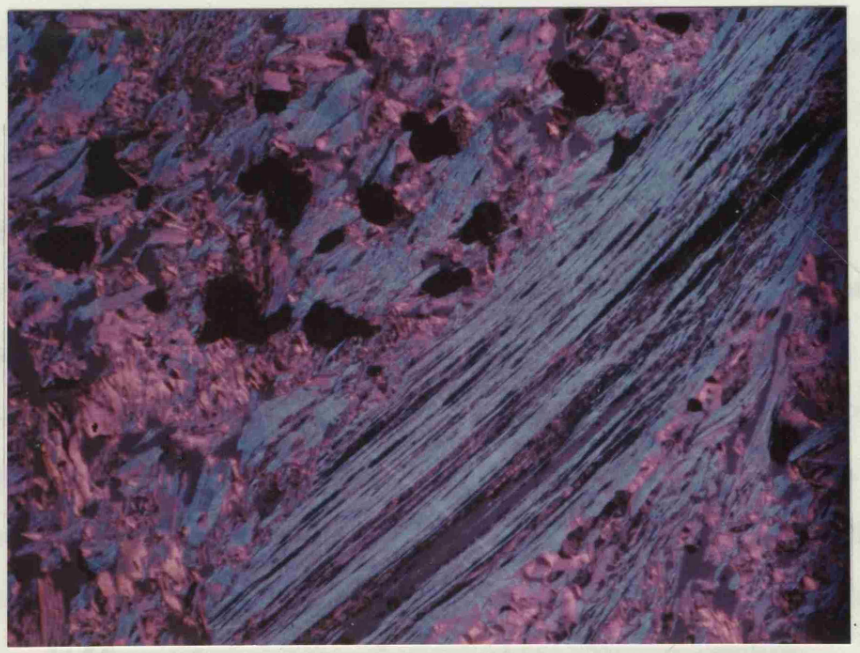

A

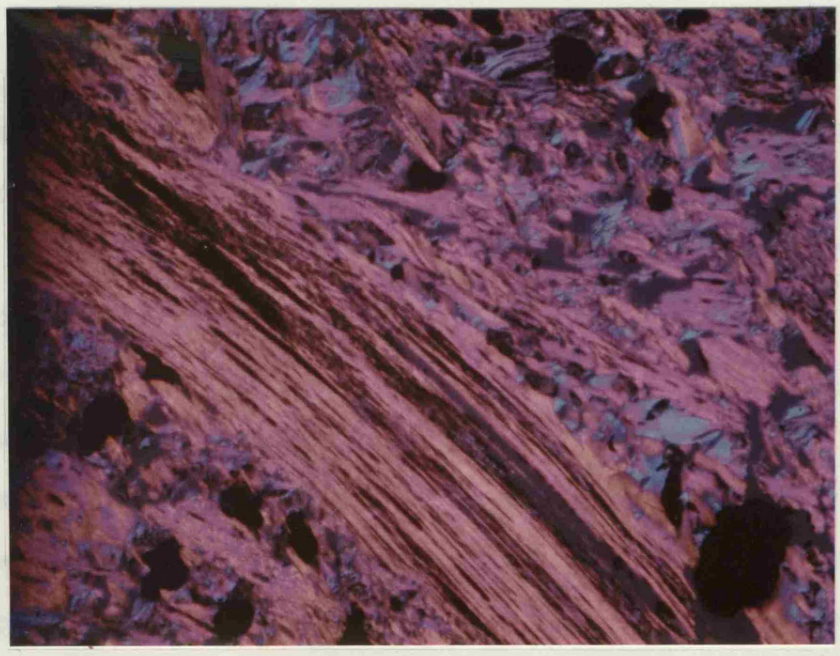

B

Fig.3.19. The colour orientation effect of prismatic edges in grains of PGA-AGL graphite, using polarised light and sensitive tint. Micrograph B is the same field as A rotated through 90°.

perpendicular to the fracture surface and then polished and examined using the microexamination techniques described in section 3.5.1.

3.5.3. Image Analysis of Pore Structure

To illustrate the effect of thermal oxidation upon the 2-dimensional pore microstructure automatic image analysis, (IA), was used. This technique utilizes a computer to analyse digitised images from a televison screen, which are transmitted from a camera mounted on a microscope. The images are of different phases within the microstructure which have different levels of contrast. The computer digitises the image within a square frame into 262000 picture element points (pixels), and can discriminate and measure a feature according to the number and distribution of pixels of a given grey level range.

In graphite, as in many other materials, there are a range of microstructural features which generate an image in which there is an overlap of grey levels. It is therefore important to have the greatest contrast possible between the feature to be measured and background features. In this work the microstructural feature to be analysed was the open porosity and this had to be differentiated from closed porosity and graphite. Using a normal reflected light microscope, graphite is quite reflective and therefore poses no real problems as far as contrast between itself and pores is concerned, (except when measuring very fine pores

~ 1 μm). However, the distinction between open and closed porosity is impossible without some form of differential contrast enhancement. When this present work started, there were several enhancement techniques being investigated at Berkeley Nuclear Laboratories, where this IA work was undertaken. The techniques included (i) bismuth or gold impregnation both of which were cumbersome and expensive, and (ii) the in situ polymerisation of a low viscosity monomer mixed with a fluorescent dye. It was found that a superior technique was to mix a fluorescent dye with a low viscosity resin commonly used in biological sciences and impregnate the graphite under vacuum (see section 3.5·1). Upon examination using an ultra-violet light microscope, the graphite absorbs the UV and therefore remains dark, the closed porosity also remains dark, but the resin in the open porosity fluoresces producing a very bright image. In this way excellent contrast is obtained between the open porosity and the other microstructural features. It is impossible to categorically state that there is total impregnation of open porosity using this technique. However, it is quite clear that the finest microstructural features which are known to be open porosity and which approach the limit of resolution of the microscope are always filled with resin. There are however occasional air bubbles in the larger of the open pores. During IA, fields with air bubbles were not measured.

The IA system used in this investigation was a Joyce-Loebl 'Magiscan' coupled with a Leitz microscope with

both visible and UV light sources. Objective lenses of x6 and x63 with water immersion were used. The computer programme to analyse the data was the 'Simple Picture Evaluation Language' (SPEL) supplied by Joyce-Loebl.

Phase identification using SPEL was a two-pass method. the first pass of the field uses a global grey level to produce an approximate representation of the structure. Grey level thresholding is the simplest form of structural analysis. A binary image is created with the feature having pixels within a specific density band assigned to the ONE state and all remaining pixels assigned to the ZERO state. During the second pass, the edge detector modifies the representation wherever the grey level changes sharply, e.g. at the edges of features. For each edge point the computer examines a 5 x 5 pixel region of nearest neighbour points and adjusts the local threshold to the half-way point between two phases. The representation of the image can be fine-tuned to fit exactly the optical image by adjusting the global grey threshold level,

CHAPTER 4

EXPERIMENTAL RESULTS

4.1 The Oxidation Programme

The rate of gasification of graphite may be controlled by one or more of three regimes: zone 1 (Chemical control), in which the rate of gasification is governed by the chemical reaction rate at the internal surface of the graphite within the pores; zone 2 (In-pore diffusion control), where transport of reactant molecules from the external surface to reaction sites within the pores and transport of products to the exterior control the rate; zone 3 (Gaseous diffusion control), in which bulk gas diffusion of reactant molecules to the external surface controls the rate.

To achieve homogeneous oxidation of a graphite it is necessary to carry out the gasification reaction at low temperatures, where zone 1 is the rate-controlling regime. At higher temperatures, a transition from zone 1 to zone 2 occurs, resulting in the development of a density gradient in the graphite (78). Zone 3 rate control is found at higher temperatures. To obtain fast reaction rates whilst maintaining chemical control, some criterion for determining

the boundary conditions for zone 1 must be used. Stephen (68) has developed such a criterion, using a dimensionless modulus, ϕ, first suggested by Thiele (79). The modulus is derived by solution of differential equations for simultaneous diffusion and reaction. It contains the chemical reactivity, the rate of diffusion within the solid and a characteristic sample dimension.

$$\phi = \frac{a^2 R}{D C_i V} \qquad (4.1)$$

Where a = characteristic specimen dimension (cm), R = rate of observed carbon monoxide formation (mol sec^{-1}), C_i = concentration of carbon dioxide (mol cm^{-3}), V = volume of specimen (cm^3) and D = effective diffusivity (cm^2 sec^{-1}). D is a function of pressure temperature and porosity, i.e.

$$D \propto \lambda \, (P^o/P)(T/T^o)^{1.7}$$

where T^o and P^o are standard temperature and pressure P and T are working pressure and temperature. λ is a factor related to porosity. Using figure 4.1, the effectiveness factor, η, was determined from the Thiele modulus. The effectiveness factor is defined as,

$$\eta = \frac{\text{Observed Rate of Reaction}}{\text{Rate of Reaction in the Absence of Diffusion Processes}}$$

TABLE 4.1 OXIDATION DATA FOR THE CALCULATION OF THE THIELE MODULUS, ϕ, AND EFFECTIVENESS FACTOR, η.

MATERIAL	SPECIMEN TYPE *	VOLUME /cm³	MEAN DENSITY/ (g/cm3)	RATE OF Wt.LOSS /(10^{-7} g/s)	CO FORMATION RATE /(10^{-7}mol/s)	CONC. CO_2 /(10^{-6} mol/cm³)	D /(10^{-2} cm²/s)	ϕ /10^{-4}	η
IM1-24									
	σ	10.6	1,85	6.74	1.12	9.86	0.83	181	0.9
	E	5.4	1.86	1.94	0.32	"	"	113	0.9
	K_{Ic}/γ	5.0	1.81	1.71	0.28	"	"	108	0.9
PGA-AGL									
	σ	10.6	1.74	4.28	0.71	9.86	1.67	57.2	1.0
	E	5.4	1.73	3.69	0.62	"	"	21.5	1.0
	K_{Ic}/γ	5.0	1.72	3.13	0.52	"	"	9.8	1.0

* SEE SECTION 3 FOR DETAILS OF SPECIMEN GEOMETRY

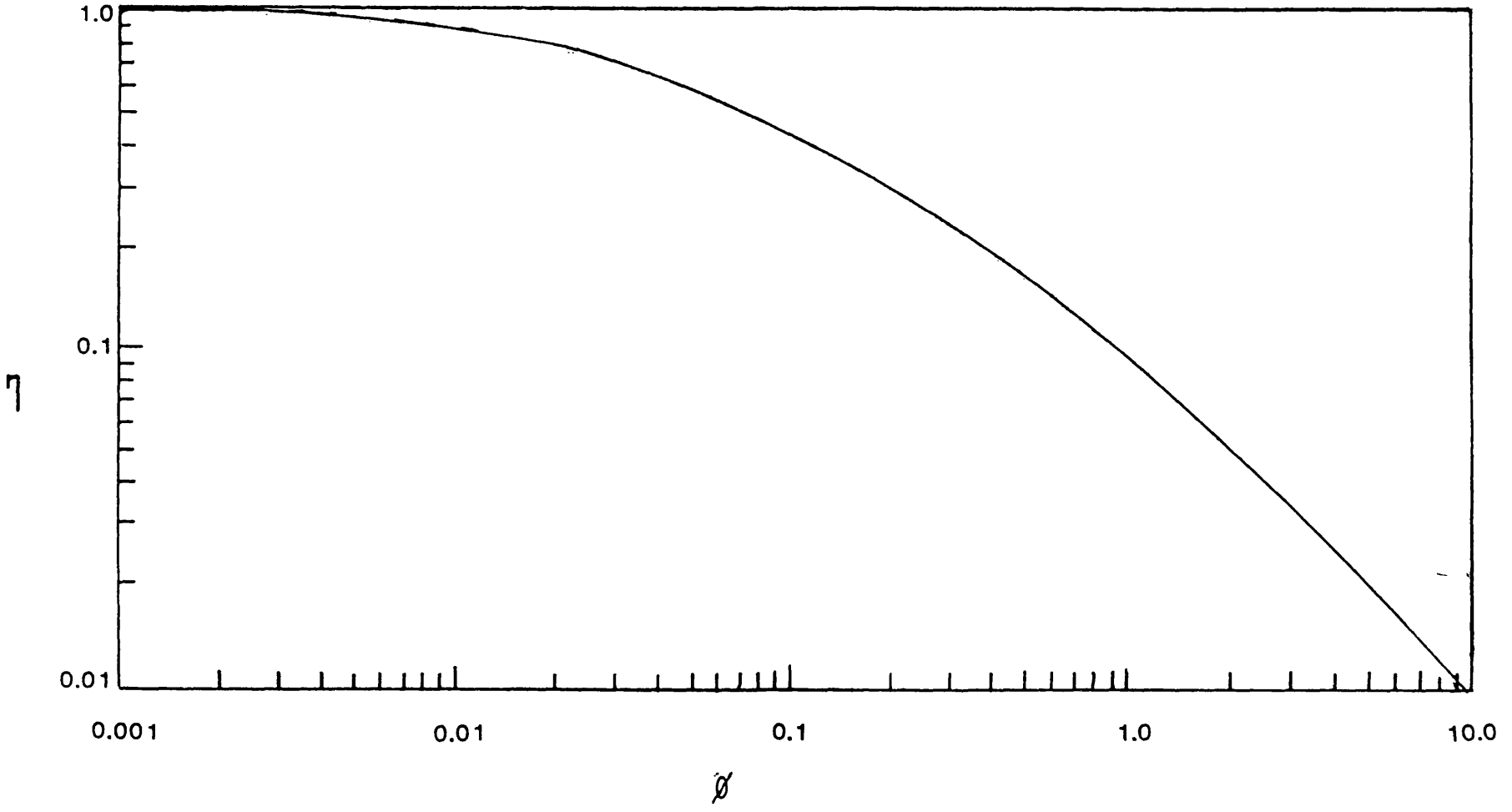

Fig. 4.1 Effectiveness factor, η, as a function of Thiele modulus, ø, (from ref. 68)

A generally accepted, but arbitrary criterion for departure from zone 1 is η=0.95. The data required to calculate Φ and the values of η obtained from Fig. 4.1 for the two graphites types of different specimen geometries are in Table 4.1.

Values of η for PGA-AGL are close to unity indicating that reaction is well within the chemical control regime. For IM1-24 the values of η are greater than 0.95 for the smallest specimens indicating chemical control, but for the larger specimens there is a contribution to the rate from diffusion of gases. The value of Φ increases with increasing specimen volume for both graphite types. From Fig.4.1. an increasing value of Φ denotes an increasing contribution to the rate from in- pore diffusion. For a given specimen geometry the value of Φ is greater for IM1-24 (I), than PGA-AGL (P). From equation 4.1, for graphites of the same specimen geometry, oxidised under the same conditions $\Phi_I/\Phi_P = R_I D_P / R_P D_I$. Thus differences in Φ reflect differences in intrinsic reactivity and diffusivity of the two graphites.

Wood *et al* (64) assessed uniformity of oxidation within the samples in two ways. Firstly, relative weight change, $\Delta W\%$ was compared with relative change in apparent density. For total internal oxidation,

$\Delta\omega\% = \Delta\rho\%$. If there is some loss of surface material, then $\Delta\rho\% < \Delta\omega\%$, and in the limiting case where weight loss is accounted for entirely by external burn off, $\Delta\rho\% = 0$. Their second method was to determine the fraction of the total burn-off that occurred within the specimen interior by calculating fractional external burn-off, Fe

$$Fe = (V_o - V)\rho_o/(M_o - M) \qquad (4.2)$$

V_o is volume as-received, V is volume after oxidation, M_o is mass as-received, M is mass after oxidation, and ρ_o is the as-received density. Wood *et al* oxidised four different types of graphite in air at a temperature of 500°C. They found that at circa 5% burn-off, weight loss was principally confined to the surface with high values of $Fe \simeq 0.9$ and $\Delta\rho/\Delta\omega\% \simeq 0.08$. At circa 20% burn-off, Fe decreased to 0.5 and $\Delta\rho\%/\Delta\omega\%$ increased to 0.63. For the graphites oxidised in this investigation no volume reductions were found. The surface machining marks were visible on specimens after more than 5% weight loss. Since there is no apparent reduction in volume, $V_o - V = 0$ and from equation 4.2, Fe = 0, also $\Delta\omega\% = \Delta\rho\%$. It would appear therefore that all the burn-off occurs internally, consistent with the kinetic analysis presented above. It is possible that there is a density profile within the specimen. However, microscopical examination and image

analysis have not revealed any variation with respect to depth from the surface.

4.2 THE EFFECT OF OXIDATION UPON MECHANICAL PROPERTIES

4.2.1 Bend Strength

Bend strength data have been reported for unoxidised material in section 3.4.1. The variation of σ_b with weight loss has been determined for both IM1-24 and PGA-AGL. Since apparent density and hence total fractional porosity, P, vary with weight loss, the variation of σ_b has been plotted as a function of P as well as weight loss. It was found that the reduction in strength was adequately described by either a linear or an exponential function of the form proposed by Knudsen *et al*(27), section 2.2.3, i.e.

$$X = X_o e^{-bP} \qquad (2.1)$$

Regression analyses of the data and correlation coefficients have been determined for the linear and exponential functions. The similarity of fit to the two functions is due to the narrow range of weight loss, i.e. 5%. However correlation coefficients are slightly higher for the exponential form. This function produces the exponential factor, b, which is supposedly indicative of the pore shape.

The best fit of the exponential curve to the experimental data is shown in figures 4.2 to 4.5. The exponential factors, correlation coefficients and property values at zero weight loss or zero porosity are tabulated for all mechanical properties examined in this investigation in table 4.2. The variations of σ_b with pore volume fraction, for IM1-24 and PGA-AGL have exponential factors, b = 12.95 and 11.67, respectively. These values are considerably greater than those reported by Rossi (32) (section 2.2.3) where a value of b of approximately 2 was found due to stress intensification of spherical pores in glass. This implies the pores responsible for the reduction in strength of graphite are sharper than the spherical pores in glass and therefore intensify the stress to a greater extent.

The variation of σ_b with weight loss for the two graphites may be compared by normalisation, using σ_b/σ_o, where σ_o is the value of σ_b for the unoxidised graphite; values of σ_b/σ_o are plotted in figure 4.18. There are two notable features of the plot. Firstly, there is a large reduction in strength, circa 50% as a result of a relatively small percentage weight loss, 7%; this is comparable to the reduction reported by Board and Squires (60). Secondly, the rate of reduction of normalised strength σ_b/σ_o is almost identical for both graphites, even though they have a distinctly different micro-structure. The strength reductions are discussed in detail in section 5.

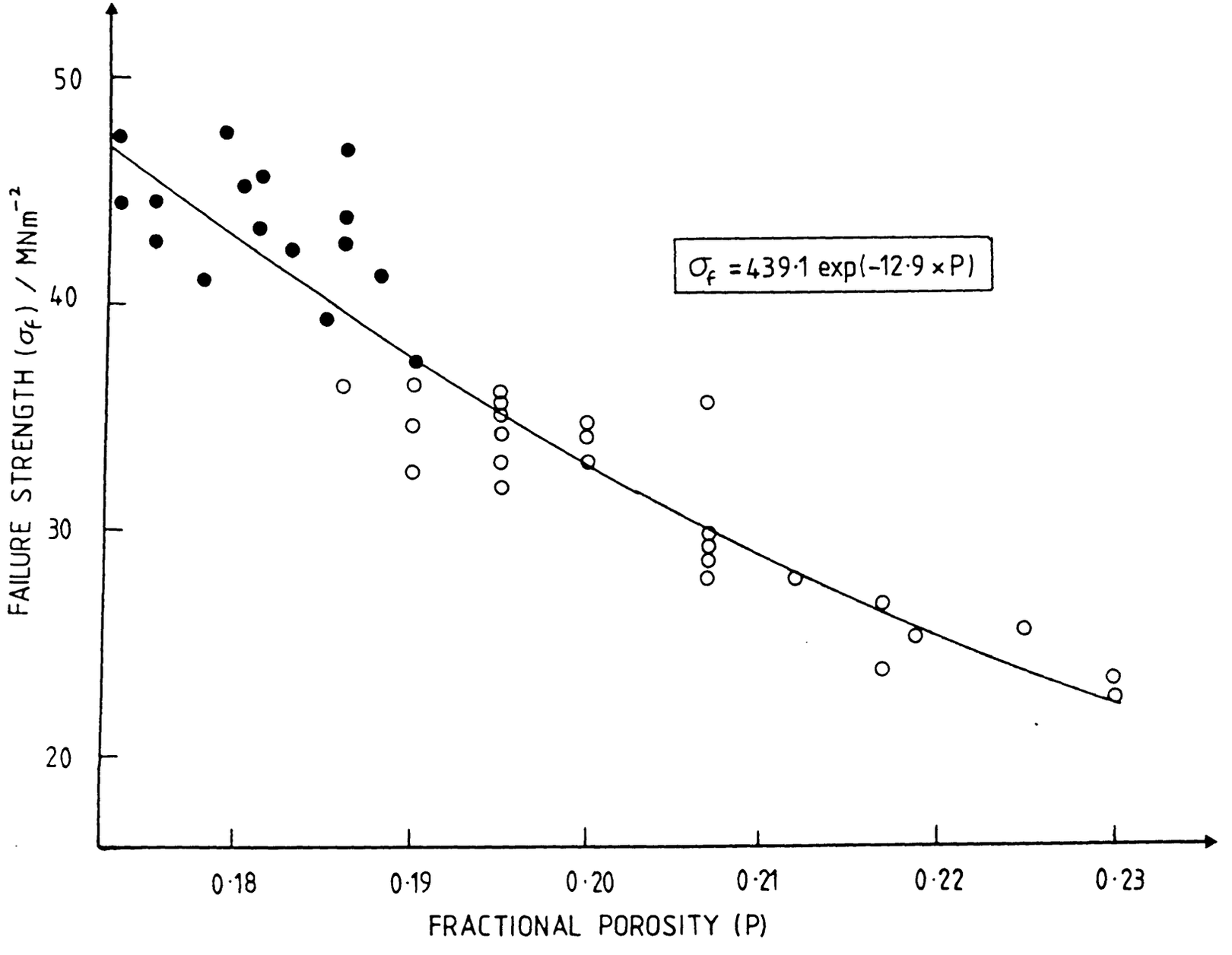

Fig.4.2 Bend strength (σ_f) of IM1-24 as a function of pore fraction (P). Closed points, unoxidised graphite; open points, oxidised graphite. The equation for the curve is shown in the inset.

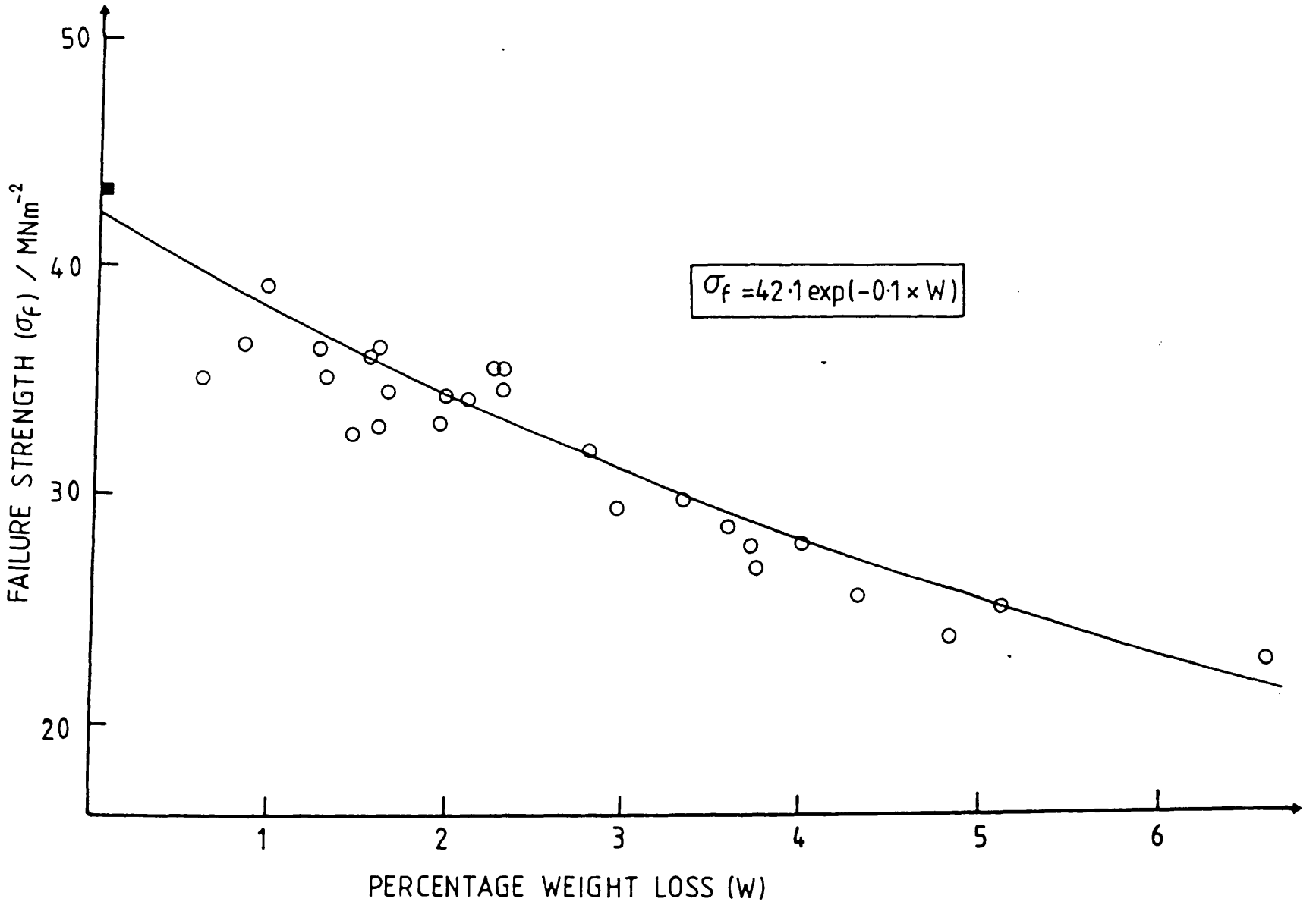

Fig.4.3 Bend strength (σ_f) of IM1-24 as a function of weight loss (w). The mean unoxidised value is represented by a closed point. The equation for the curve is shown in the inset.

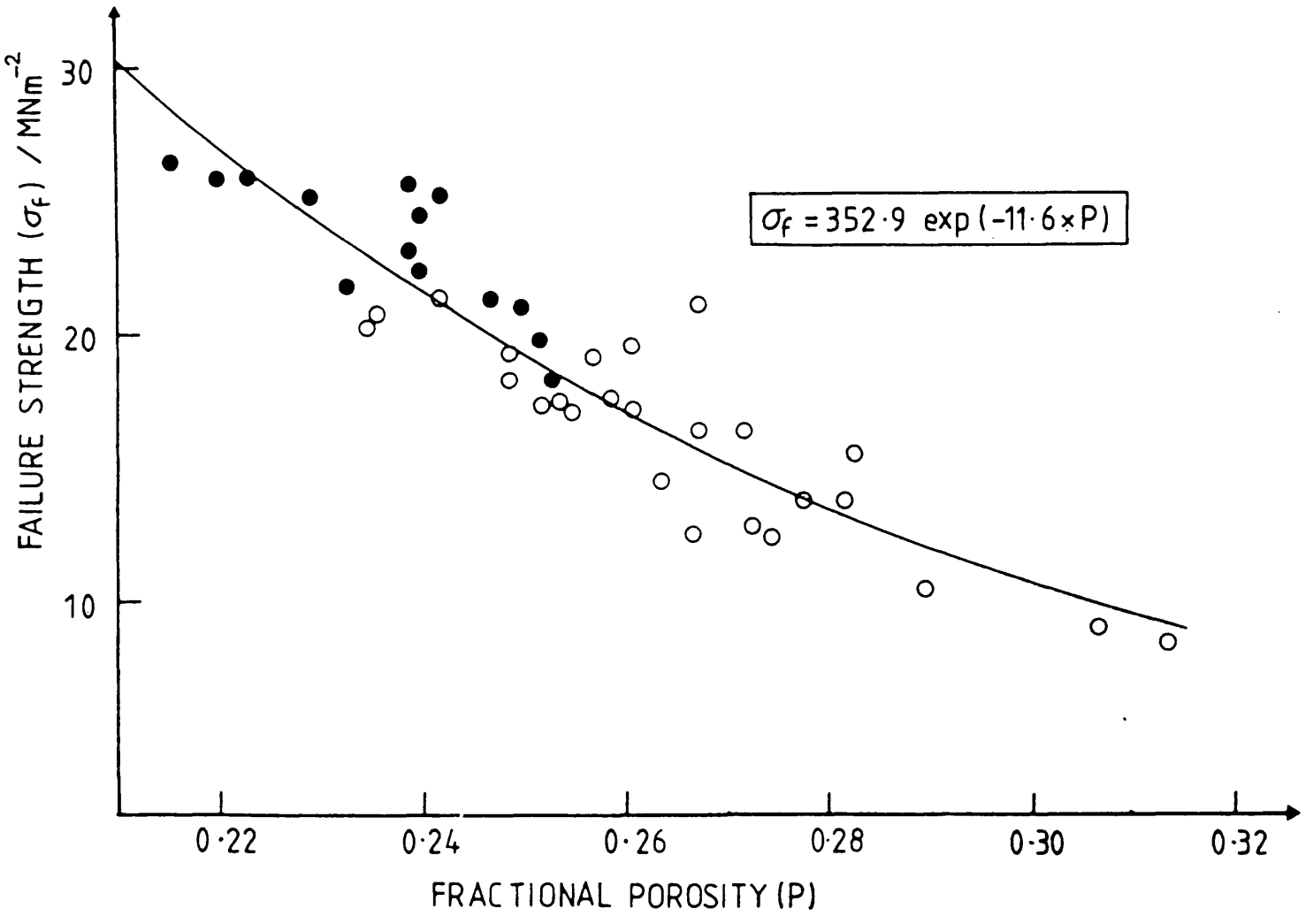

Fig.4.4 Bend strength (σ_f) of PGA-AGL as a function of pore volume fraction (P). Closed points, unoxidised graphite; open points, oxidised graphite. The equation for the curve is shown in the inset.

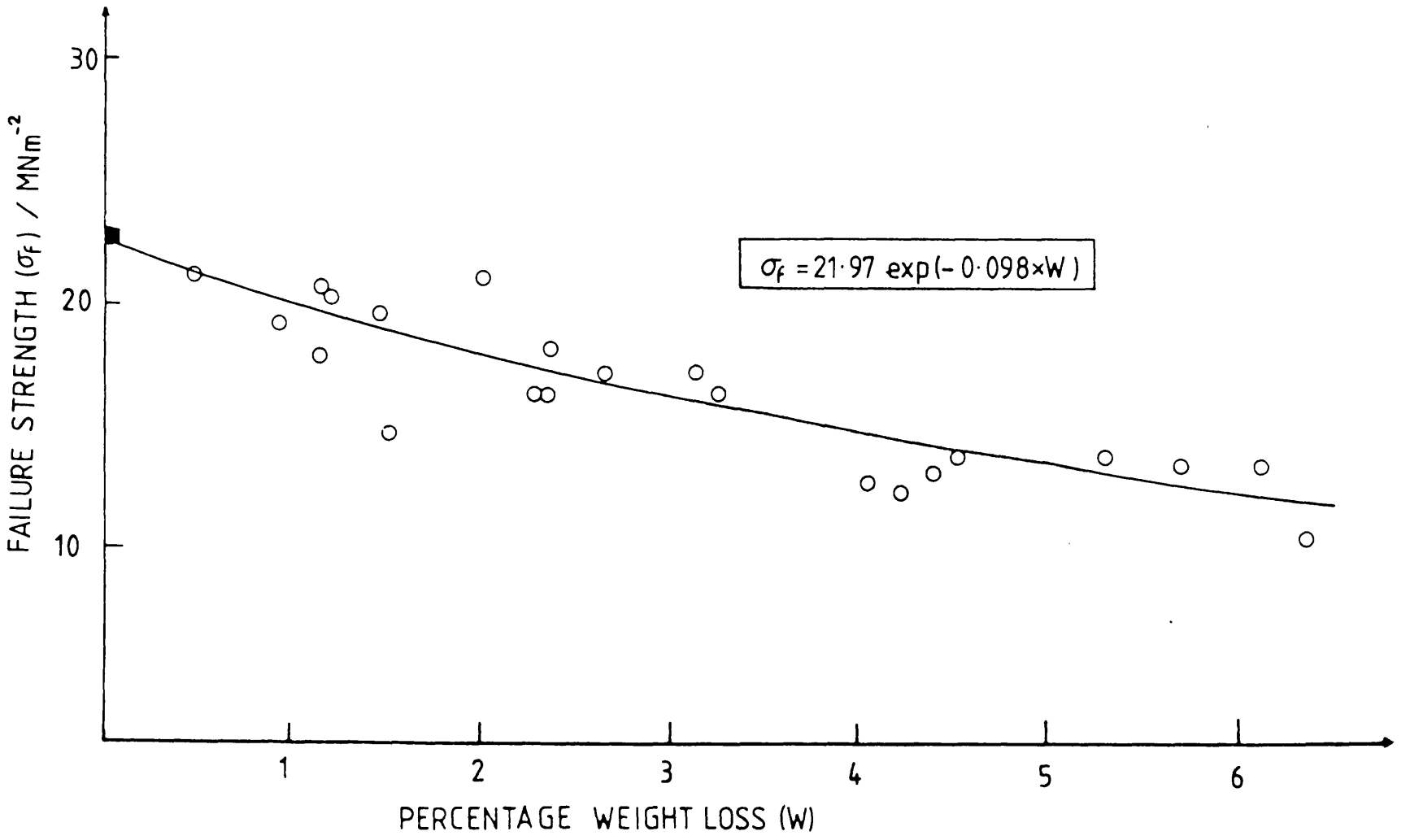

Fig.4.5 Bend strength (σ_f) of PGA-AGL as a function of weight loss (w). The mean unoxidised value is represented by a closed point. The equation for the curve is shown in the inset.

4.2.2 Dynamic Elastic Modulus

A similar approach to the presentation of strength results has been employed for the elastic modulus results. The modulus reduction as a function of weight loss and total fractional porosity for both IM1-24 and PGA-AGL are presented in Figs. 4.6-4.9. There is equally good correlation for an exponential reduction of modulus with both P and W. Correlation coefficients and functions from the exponential best fit line are given in table 4.2. From modulus variation with total fraction porosity, the exponential factor, b, for IM1-24 (b = 7.02) and PGA-AGL (b = 7.4) are similar. The b values are lower than those for strength reductions, where b ≈ 12. They are also slightly lower than the values reported by Wood *et al* for several fine grained polycrystalline graphites, which ranged from b = 9 - 17. There are large reductions in the normalised modulus E/E_o in the early stages of oxidation for the two graphites, Fig.4.18. As a result of 7% weight loss there is a reduction is modulus of 44% and 38% for IM1-24 and PGA-AGL respectively. The rate of reduction of normalised modulus is more severe for IM1-24.

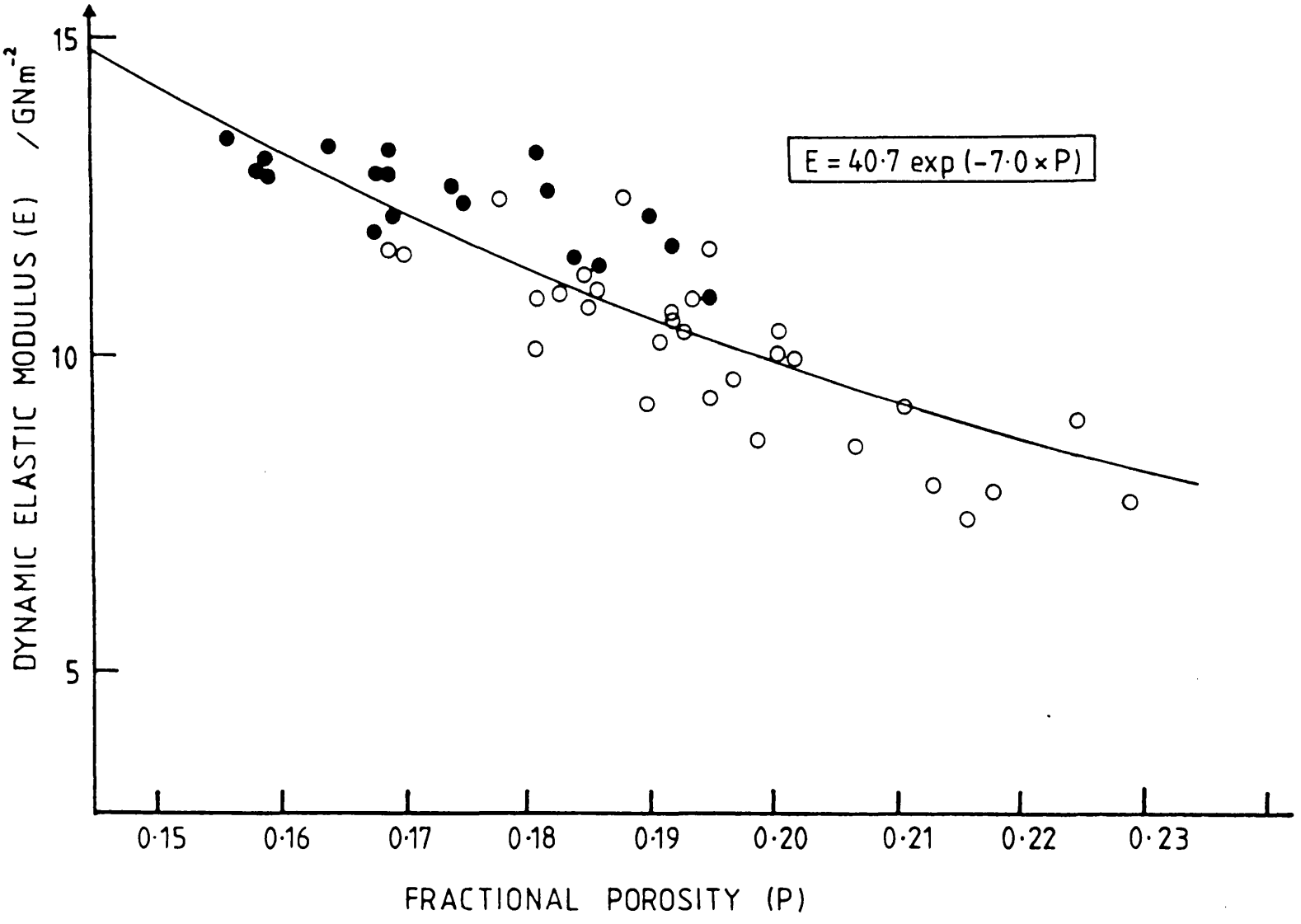

Fig.4.6 Elastic modulus (E) of IM1-24 as a function of pore volume fraction (P). Closed points, unoxidised graphite; open points, oxidised graphite. The equation for the curve is shown in the inset.

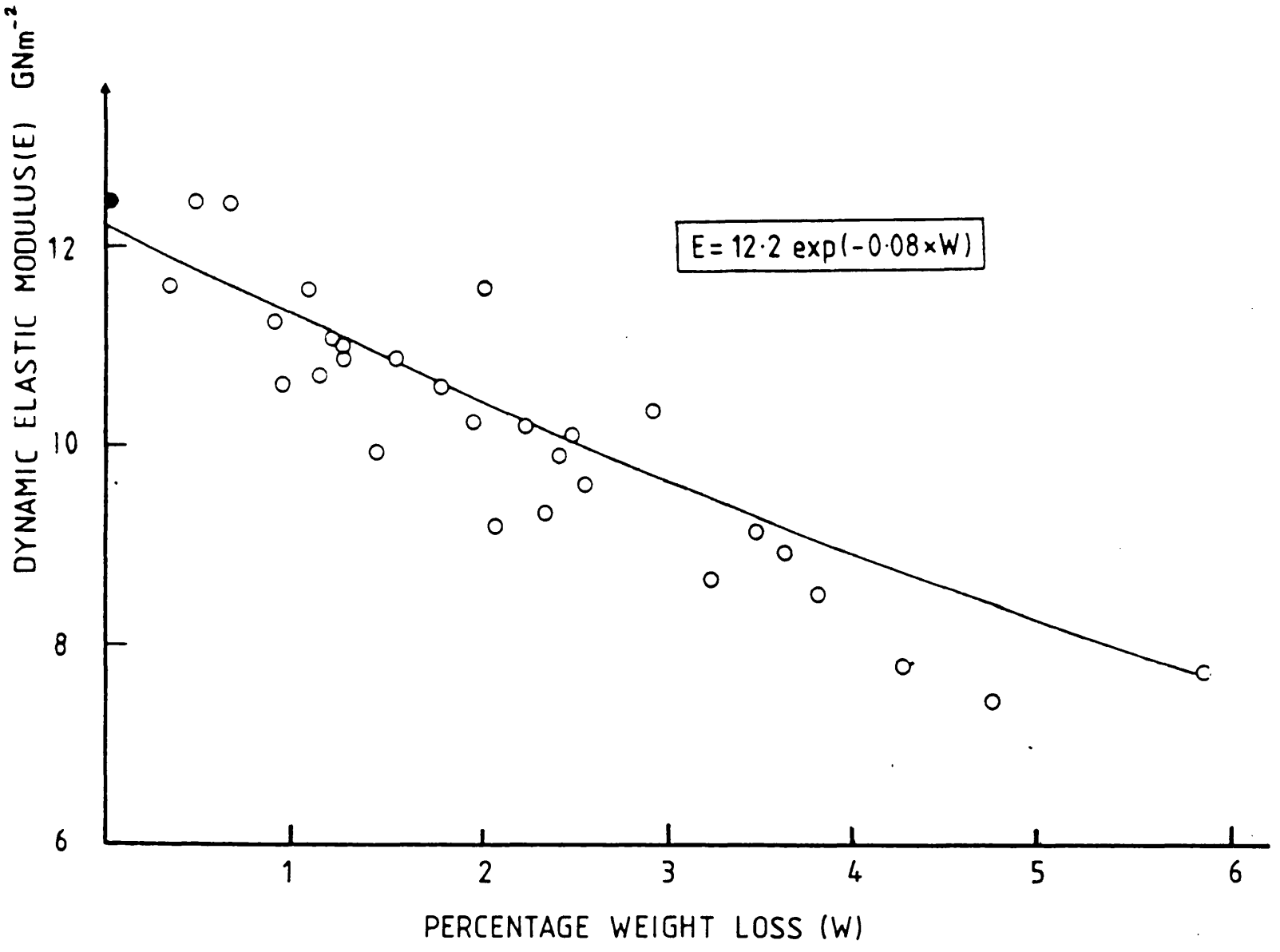

Fig.4.7 Elastic modulus (E) of IM1-24 as a function of weight loss (w). The mean unoxidised value is represented by a closed point. The equation for the curve is shown in the inset.

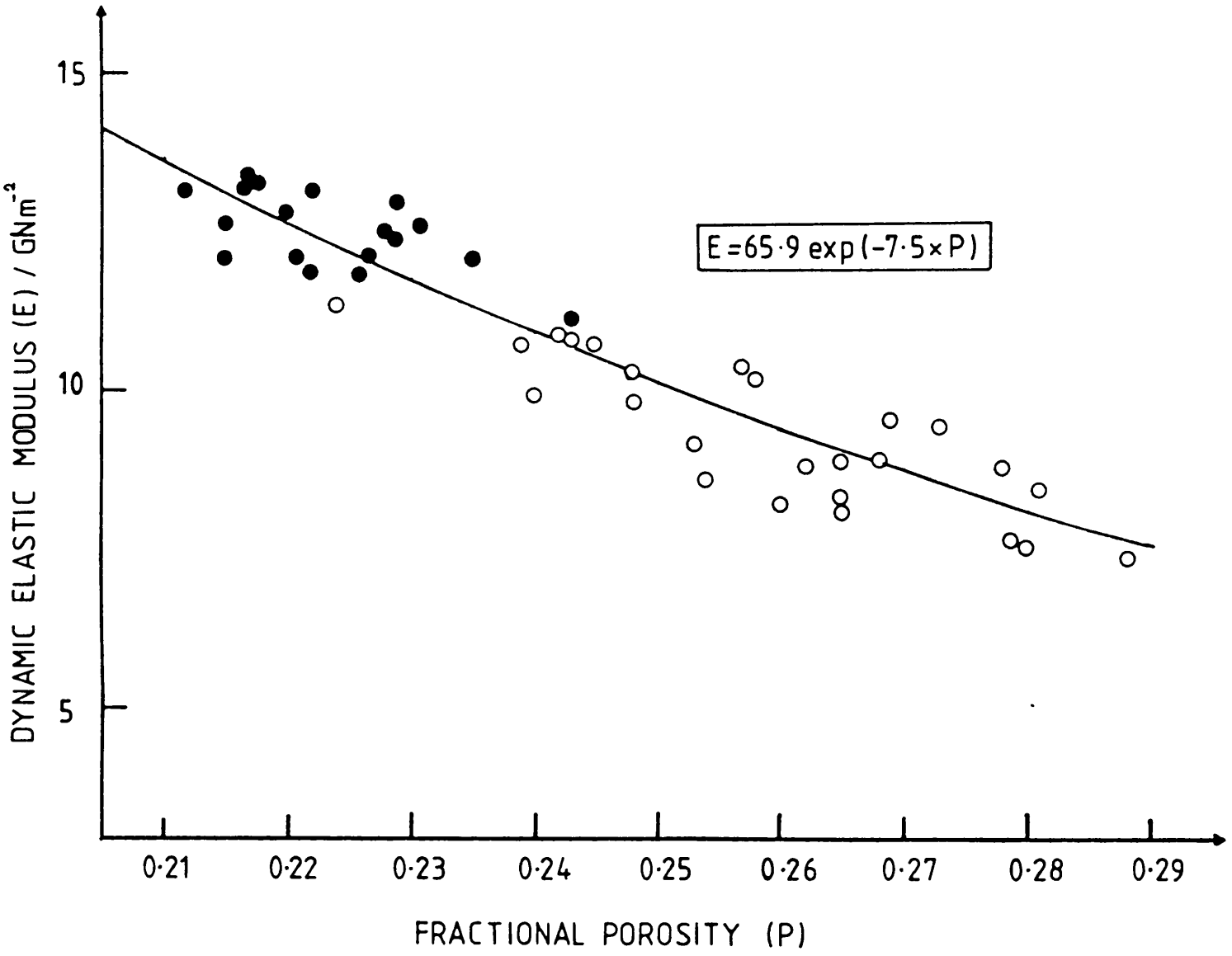

Fig.4.8 Elastic Modulus (E) of PGA-AGL as a function of pore volume fraction (P). Closed points,unoxidised graphite; open points, oxidised graphite. The equation for the curve is shown in the inset.

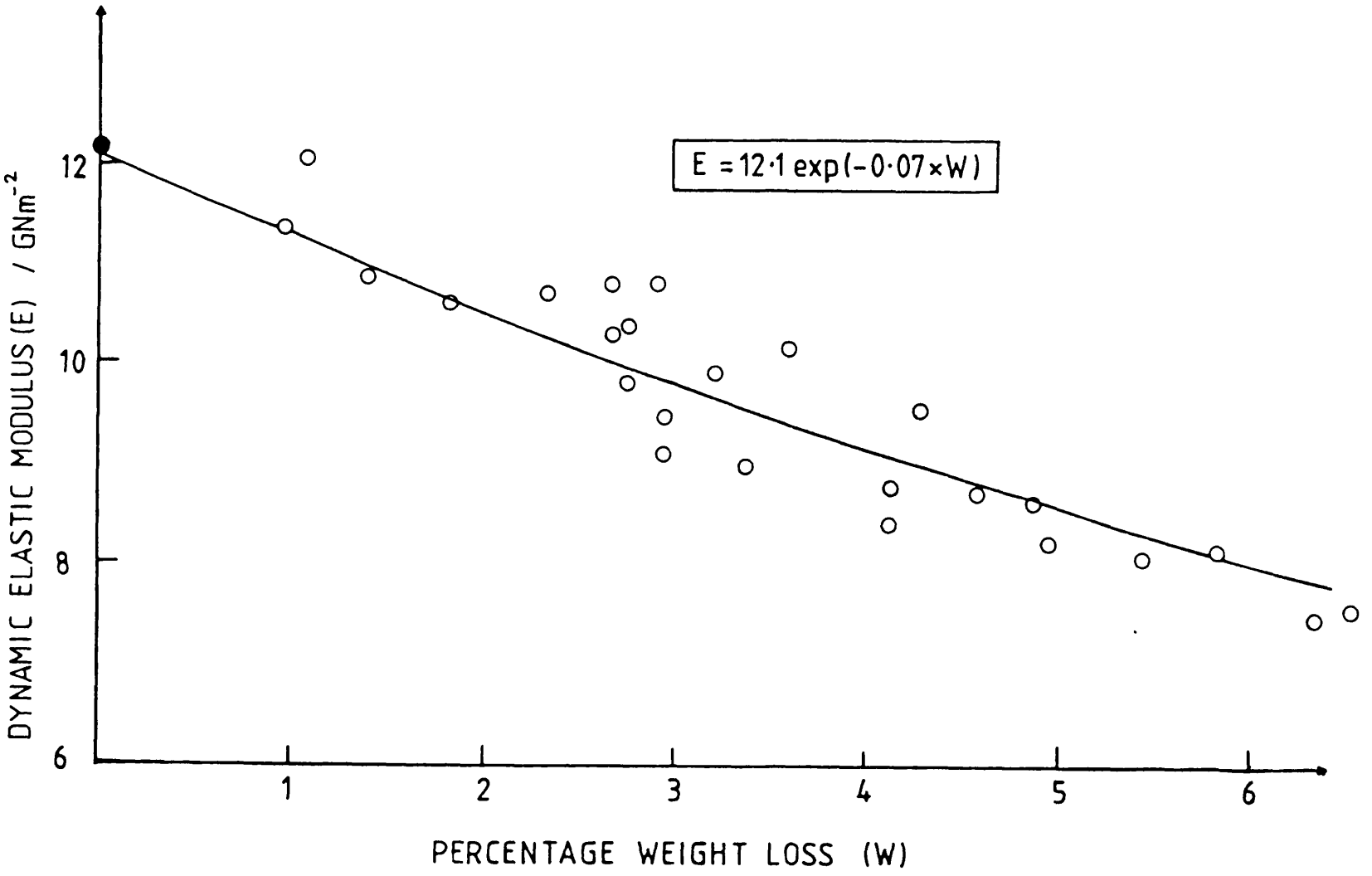

Fig.4.9 Elastic modulus (E) of PGA-AGL as a function of weight loss (w). The mean unoxidised value is represented by a closed point. The equation for the curve is shown in the inset.

4.2.3 Stress Intensity Factor

K_c reduces strongly with weight loss and hence increase in total fractional porosity. The reduction as a function of P and W are presented in Fig. 4.10-4.13 for IM1-24 and PGA-AGL, and the correlation coefficients and details of the best fit functions are given in table 4.2. Single edge notched bend specimens were used to determine K_c (section 3.4.3). The specimens had a/w values ranging from 0.35 to 0.60. It can be seen from Figs.4.10-4.13 that there is no apparent effect of the $^a/w$ ratio upon K_c variation with either P or W. The reduction in the normalised stress intensity factor, K_c/K_{co}, is almost identical for both graphites (Fig.4.18). It also indicates the extent of reduction in K_c with weight loss for the two graphites. For a 7% weight loss there is a K_c reduction of 46 and 48% for IM1-24 and PGA-AGL respectively.

4.2.4 Effective Surface Energy

To determine the effective surface energy using the compliance technique described in section 3.4.4, it was necessary to produce stiffness (k) versus crack surface area (A), curves for several weight loss groups. The value of dk/dA from each group was used to calculate γ for each specimen in that group. It is virtually impossible to produce identical weight loss values for a number of

specimens. There is an inevitable range of weight losses within each group. This can be seen in Figs.4.15 and 4.17, where effective surface energy has been plotted as a function of weight loss for IM1-24, and PGA. γ has also been plotted as a function of volume fraction for both graphites in Figs.4.14 and 4.16. The reduction of σ_b, E and K_c with oxidation produced high correlation coefficients, $|r| > 0.9$ for the exponential equation. However, reduction of γ with oxidation correlates less well, with coefficients ranging from 0.63 to 0.75. Regression analysis on the data show that there is a better fit to a linear equation relating γ with weight loss or porosity, i.e. $\gamma = \gamma_o b^*(P \text{ or } W)$. Details of the functions for the best fit curves and correlation coefficients are given in table 4.2. As with Kc, there is no apparent variation in γ with a/w ratio, this can be seen in Figs.4.14 - 4.17. The variation of the normalised surface energy γ/γ_o as a function of weight loss, Fig.4.18, for the two graphites shows that there is a greater reduction in γ/γ_o for IM1-24. For a 7% weight loss there is a reduction in γ of 51% and 42% for IM1-24 and PGA respectively.

The effect of thermal oxidation upon mechanical properties will be discussed in detail in section 5.2, there property reductions will be related to micro-structural changes.

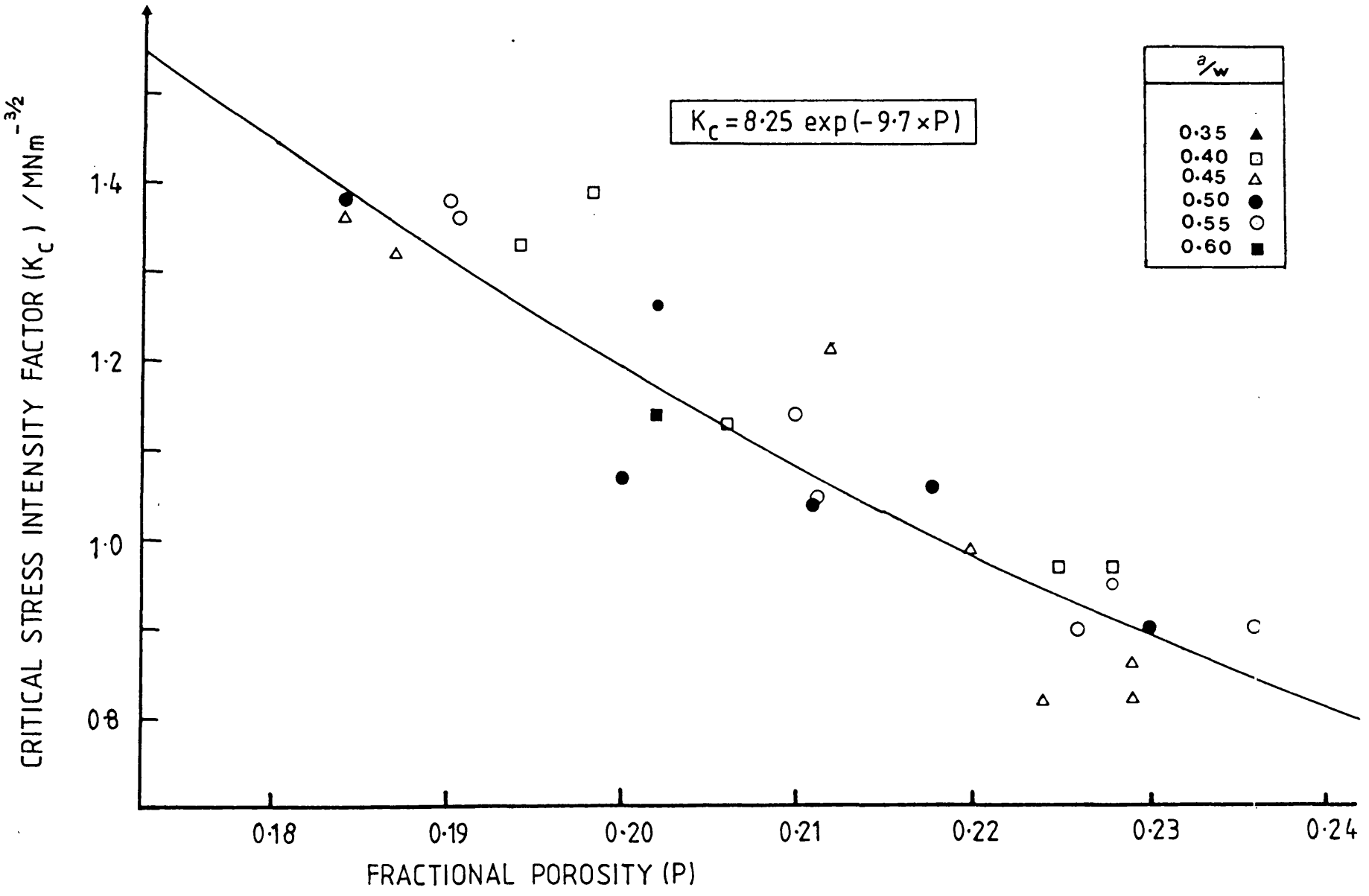

Fig. 4.10 Stress intensity factor (K_C) of IM1-24 as a function of pore volume fraction (P). The equation for the curve is shown in the inset.

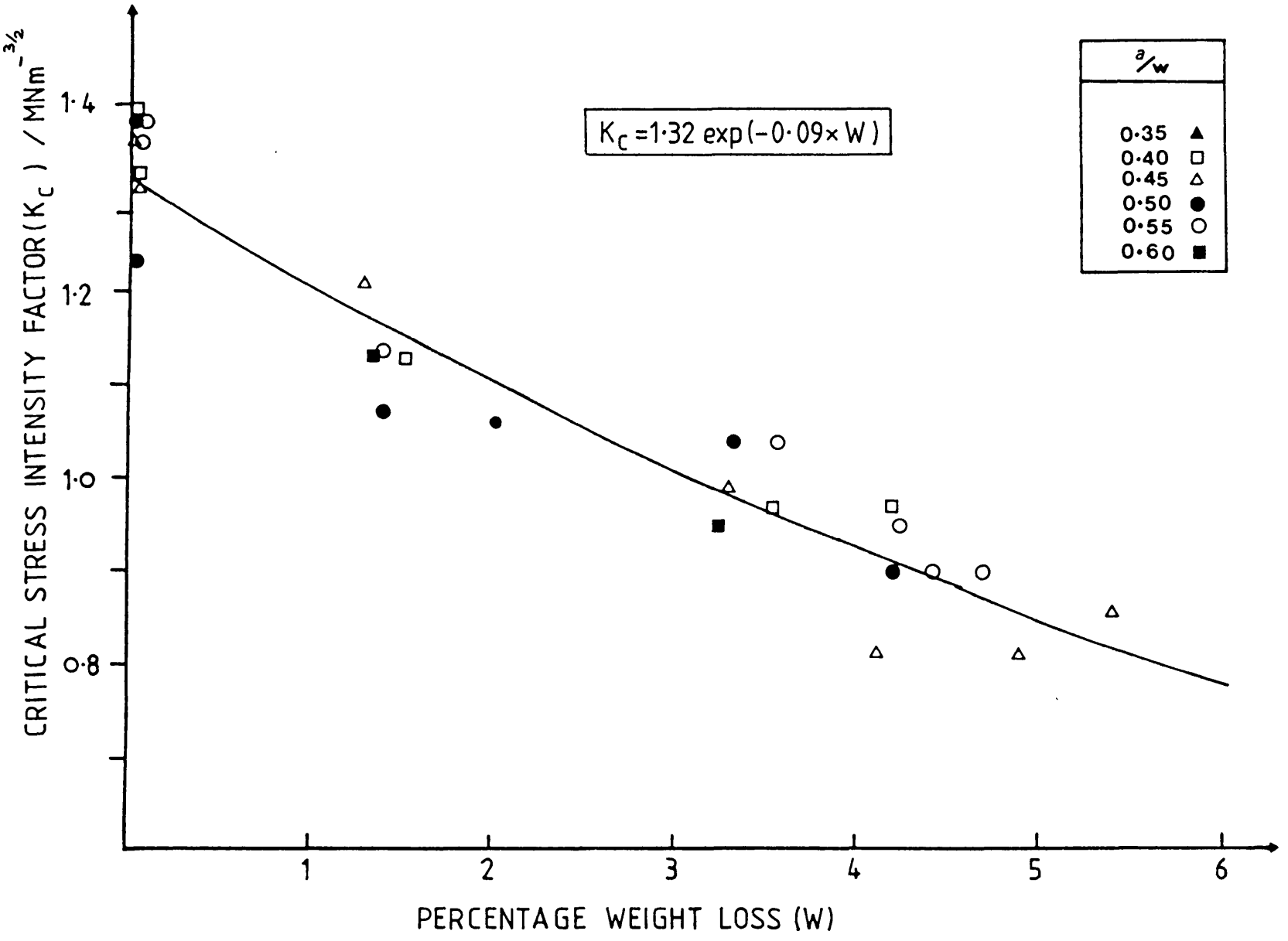

Fig. 4.11 Stress intensity factor (K_C) of IM1-24 as a function of weight loss (w). The equation for the curve is shown in the inset.

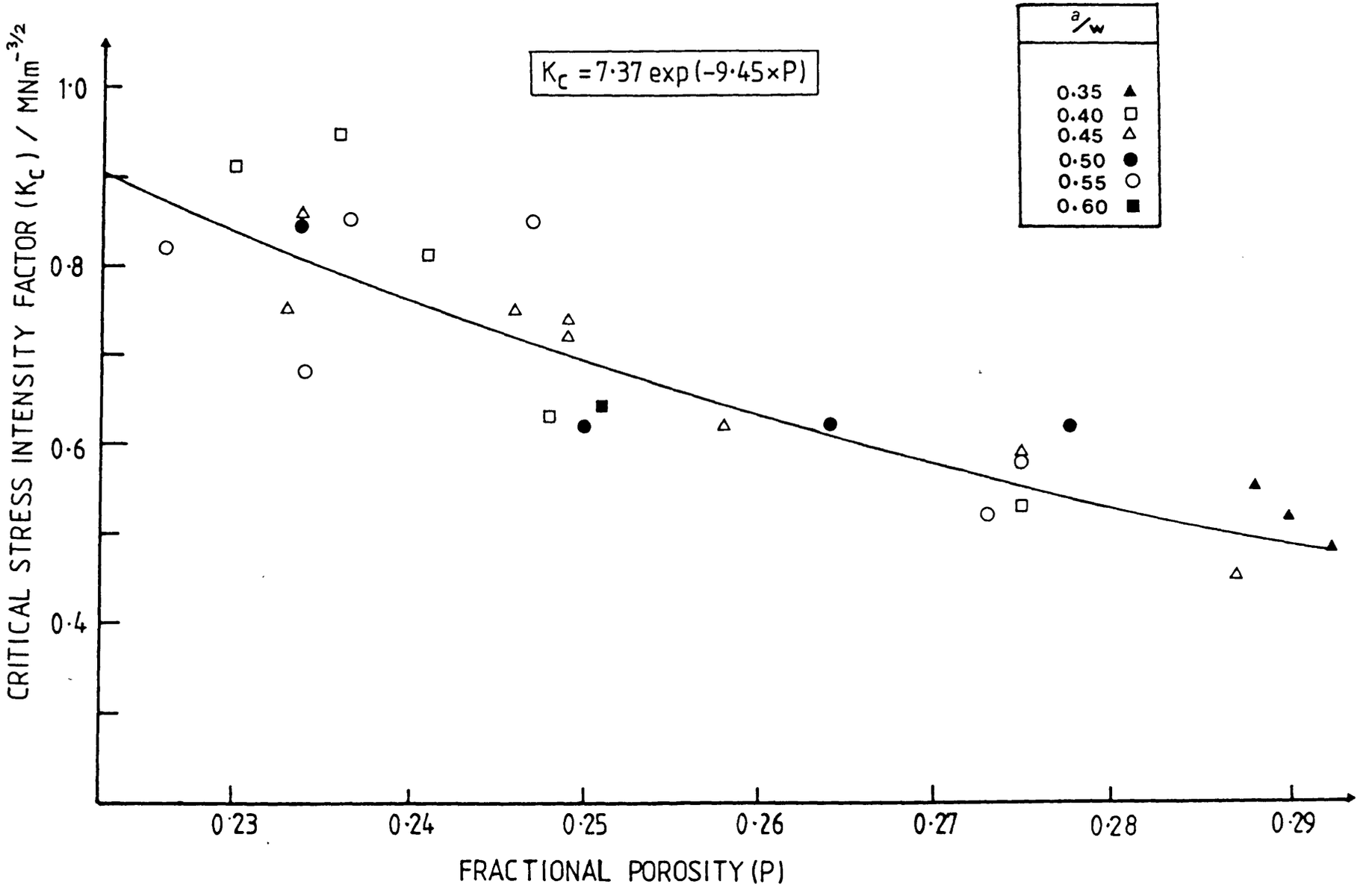

Fig. 4.12 Stress intensity factor (K_c) of PGA-AGL as a function of pore volume fraction (P). The equation for the curve is shown in the inset.

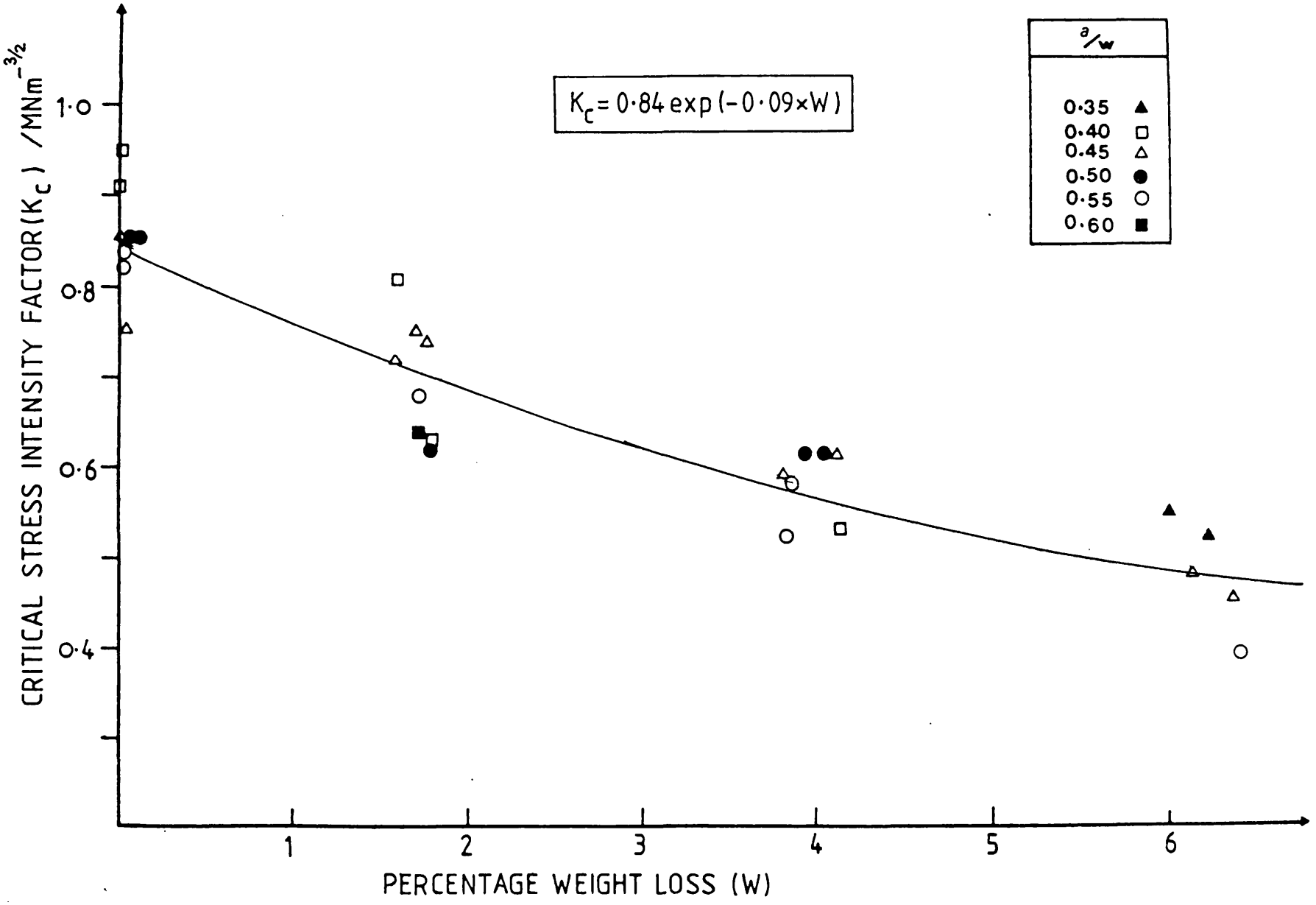

Fig. 4.13 Stress intensity factor (K_C) of PGA-AGL as a function of weight loss (w). The equation for the curve is shown in the inset.

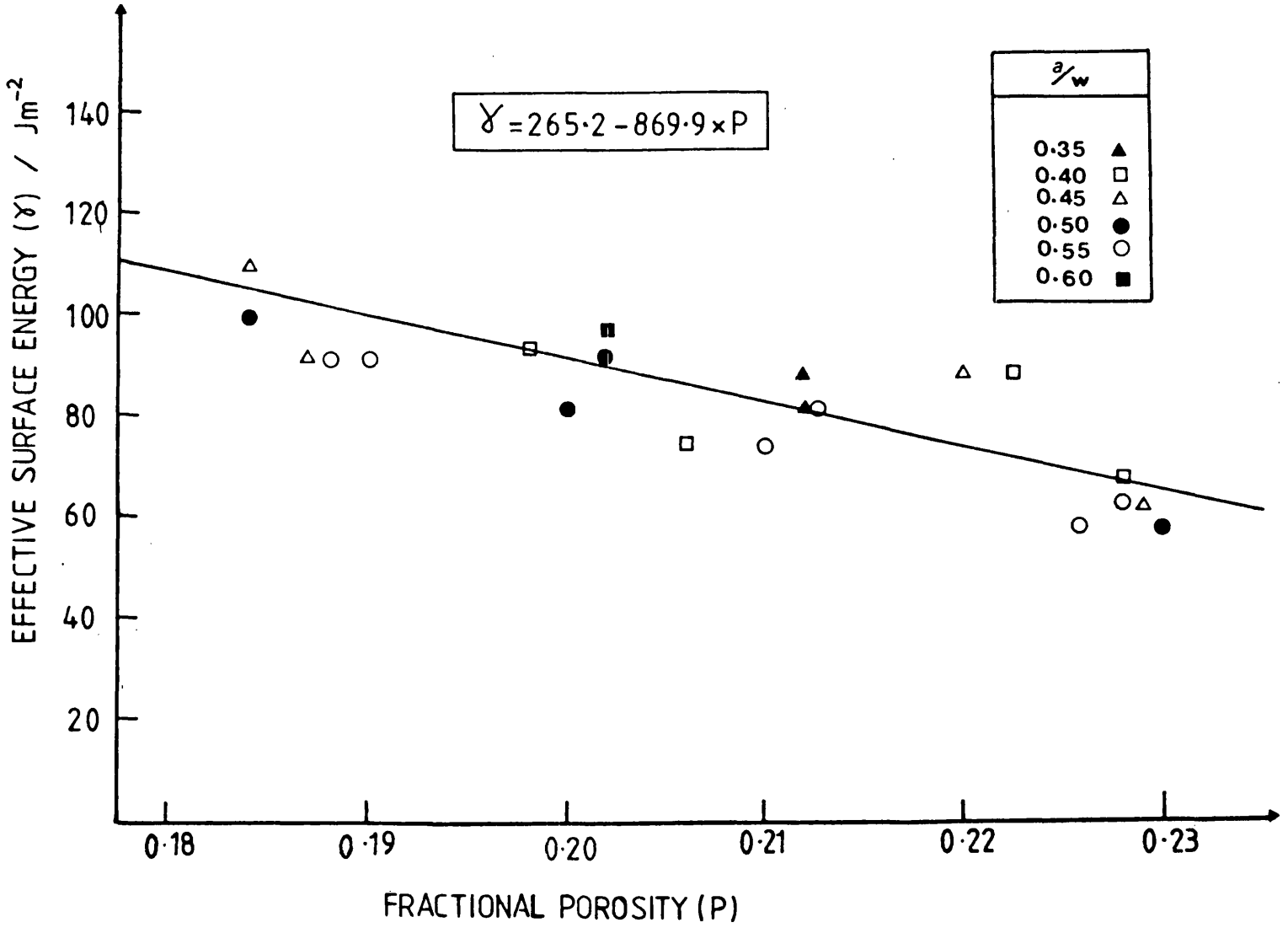

Fig. 4.14 Effective surface energy (γ) of IM1-24 as a function of pore volume fraction (P). The equation for the curve is shown in the inset.

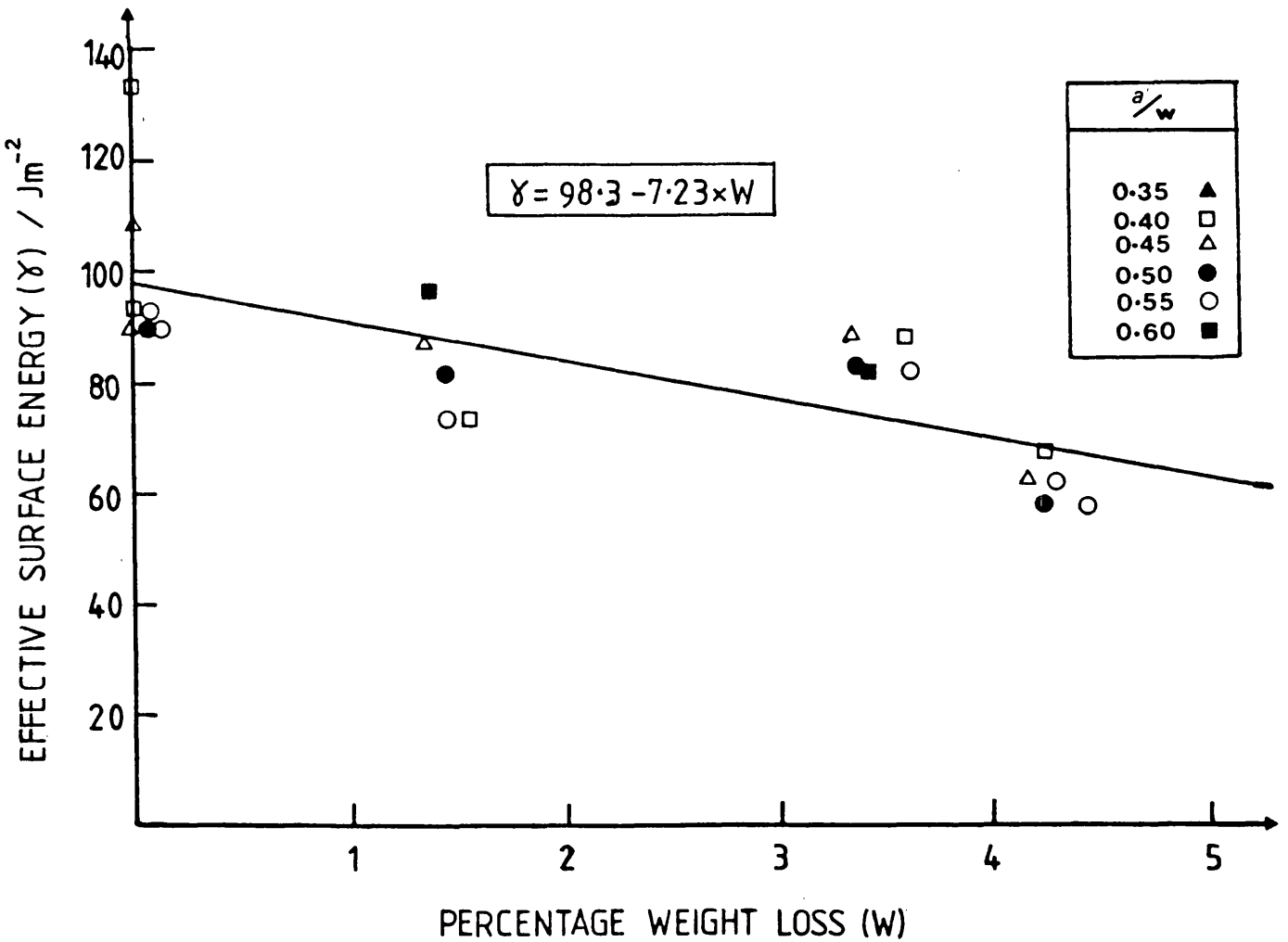

Fig. 4.15 Effective surface energy (γ) of IM1-24 as a function of weight loss (w). The equation for the curve is shown in the inset.

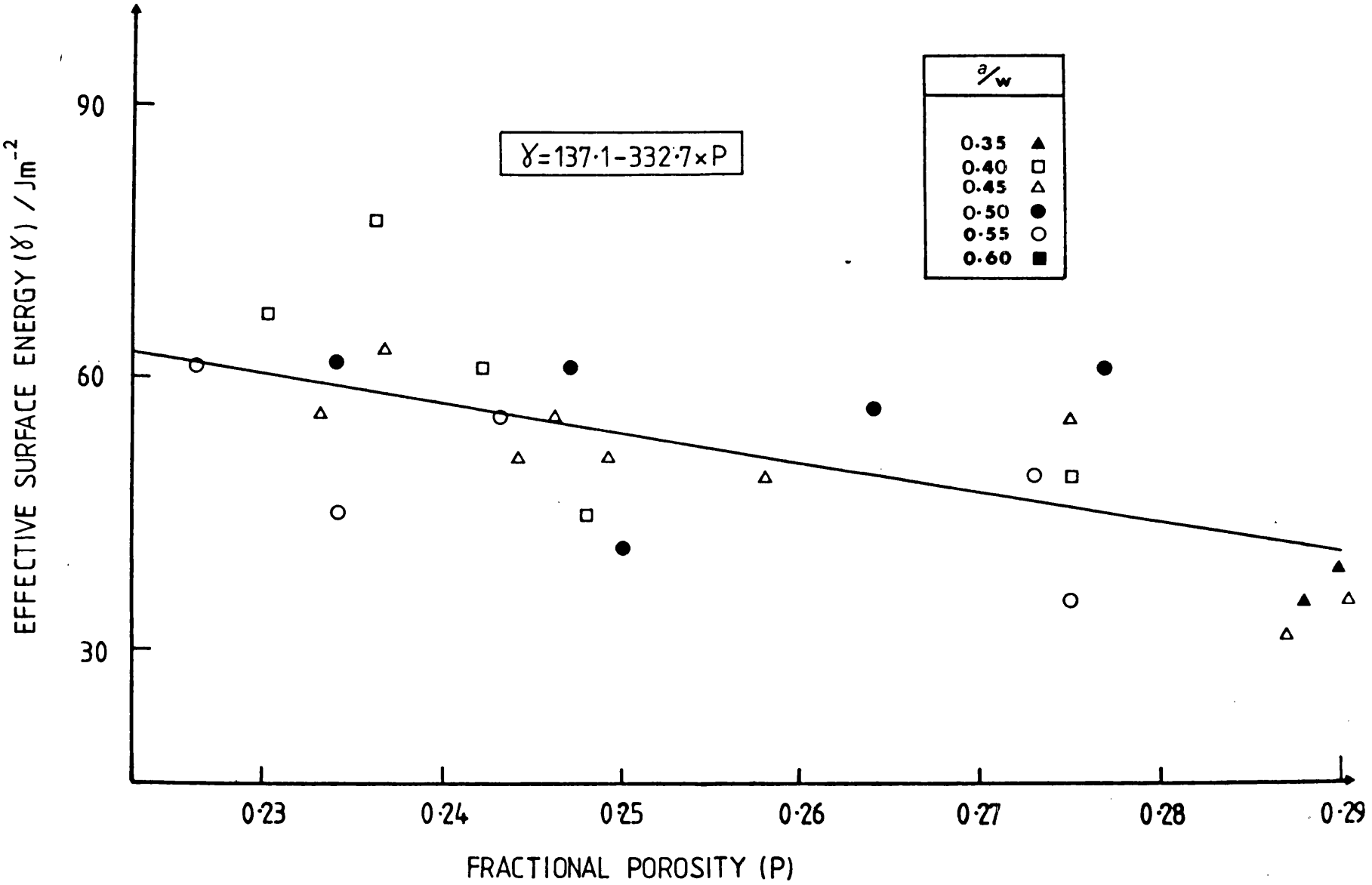

Fig. 4.16 Effective surface energy (γ) of PGA-AGL as a function of pore volume fraction (P). The equation for the curve is shown in the inset.

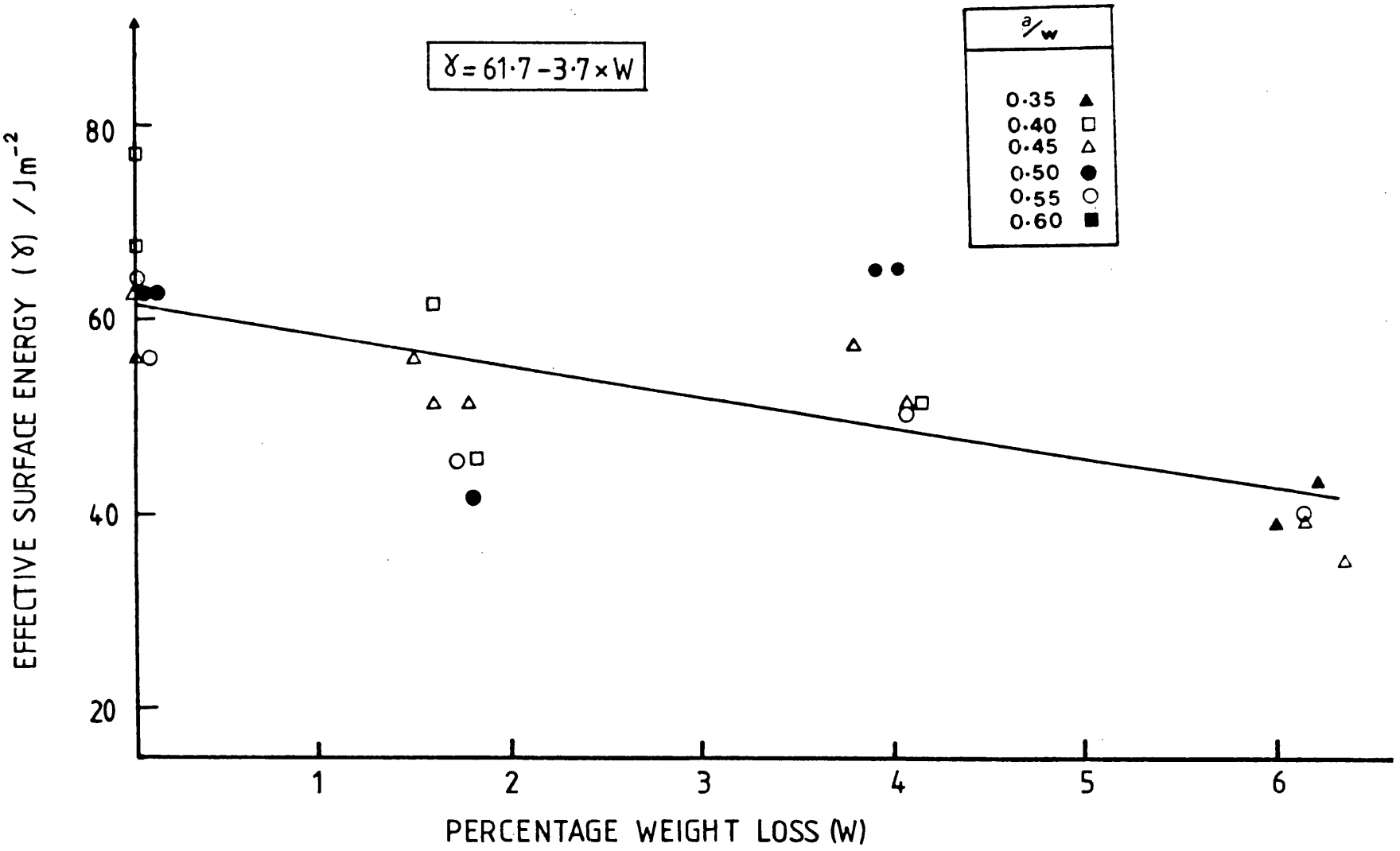

Fig. 4.17 Effective surface energy (γ) of PGA-AGL as a function of weight loss (w). The equation for the curve is shown in the inset.

TABLE 4.2 SUMMARY OF PROPERTY VALUES AT ZERO POROSITY OR ZERO WEIGHT LOSS, X_o, EXPONENTIAL FACTOR, b, AND CORRELATION COEFFICIENT, r, FOR σ_b, E, K_c, AND γ FROM THE BEST FIT CURVES (FIGS.4.2-4.17)

MATERIAL	$X = X_o e^{-b(P \text{ or } W)}$						$\gamma = \gamma_o - b^*(P \text{ or } W)$	
	σ_b/MNm^{-2}		E/GNm^{-2}		$K_c/MNm^{-3/2}$		γ /Jm^{-2}	
	P	W	P	W	P	W	P	W
IM1-24								
X_o	439	42.1	40.7	12.2	8.25	1.32	265	98.34
b	12.95	0.102	7.02	0.084	9.66	0.088	869.9	7.23
r	-0.94	-0.95	-0.86	-0.92	-0.93	-0.96	-0.75	-0.74
PGA-AGL								
X_o	353	21.9	65.93	12.1	7.37	0.84	137.1	61.74
b	11.67	0.098	7.49	0.069	9.45	0.093	332.7	3.67
r	-0.91	-0.89	-0.91	-0.92	-0.87	-0.93	-0.63	-0.74

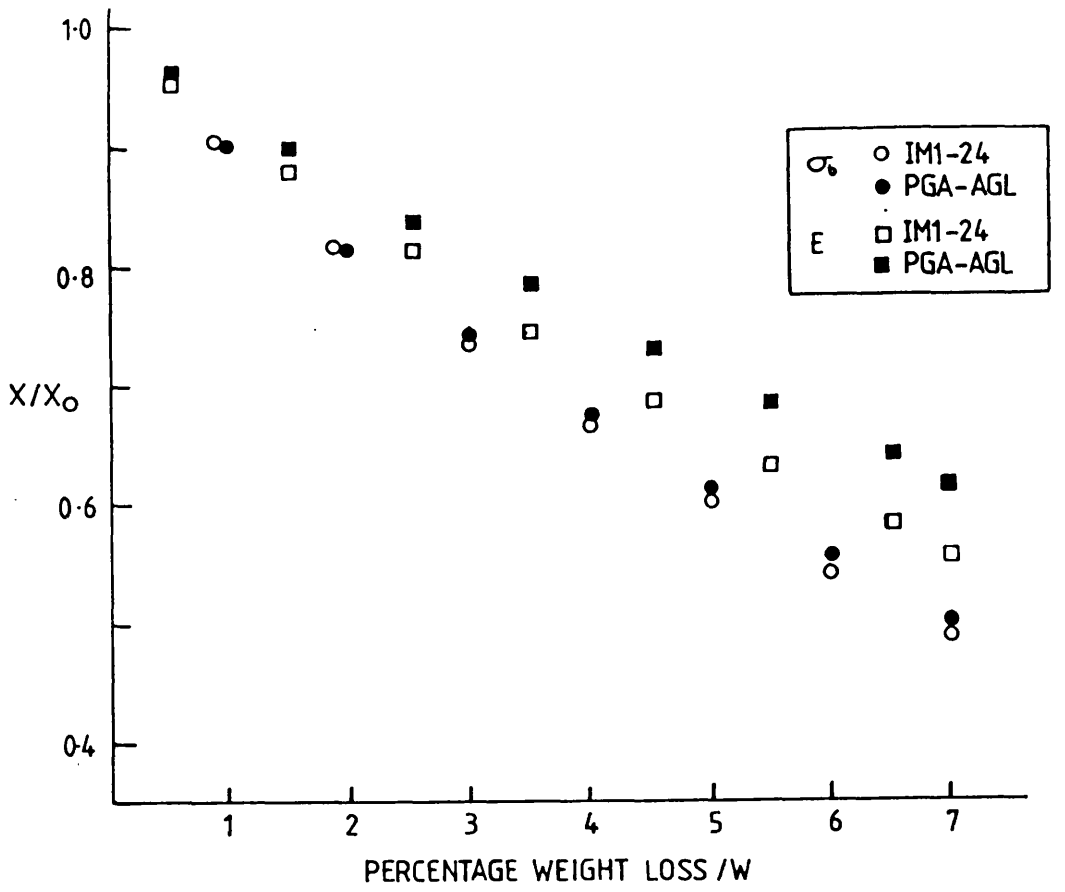

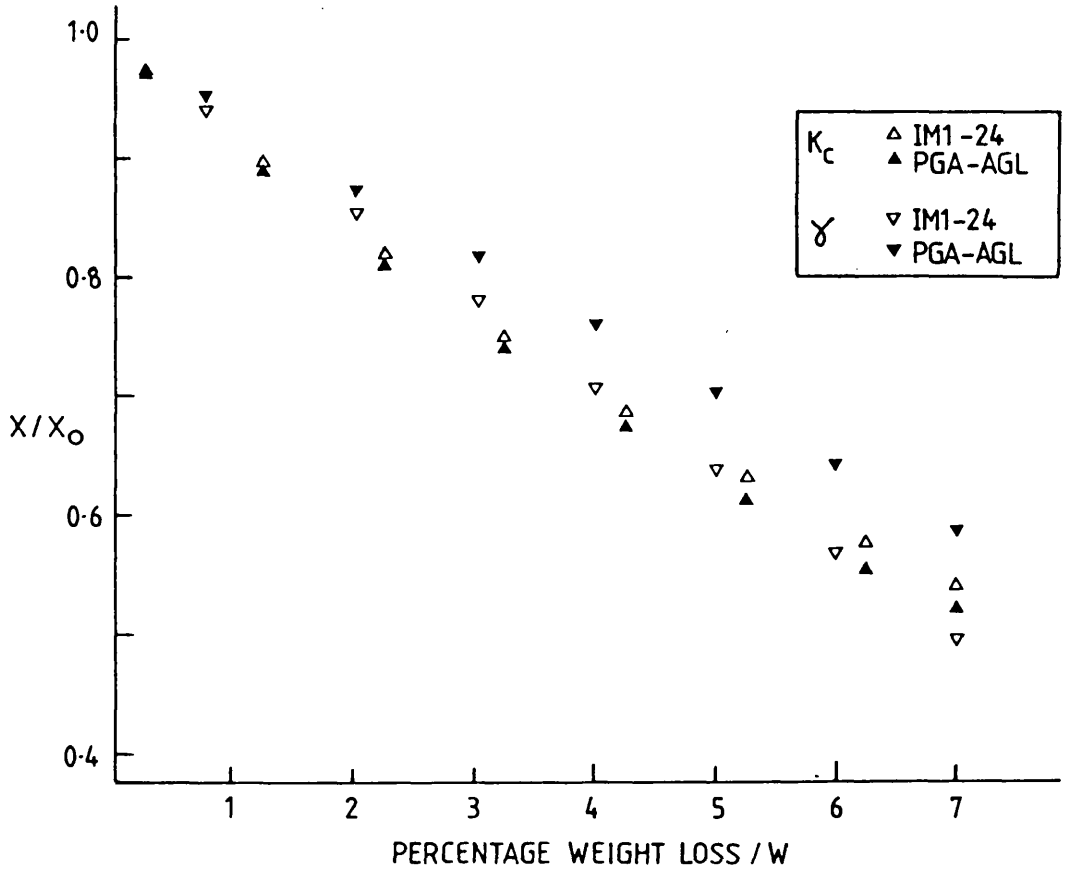

Fig. 4.18 The variation in normalised property, X/Xo, with weight loss; Xo is the value of property X at zero weight loss.

4.3 STRESS INDUCED ACOUSTIC EMISSION IN GRAPHITE

Stress induced acoustic emission was monitored during three point loading of the cylindrical specimens (see Fig. 3.10), using the apparatus described in section 3.4.1. Elastic stress waves due to micromechanical events occurring within the specimen are subject to extensive modification during their passage through the graphite and the transducer/specimen coupling and are therefore sensitive to experimental conditions. For this reason data from each of the graphites were taken under strictly comparable conditions, i.e. the transducer type, coupling agent and position on the specimen were always the same. The crosshead speed of the bend test machine was kept constant at 0.5 mm min^{-1}. Thus data comparison between tests in this work are self consistent, but it is important to realise that data may not be consistent with AE work undertaken using different systems.

Figure 4.19 is a plot of the cumulative acoustic emission, Σ(AE), (irrespective of amplitude) against the applied load for unoxidised, IM1-24, SM2-24 and PGA-AGL graphites. For each graphite type it can be seen that as the stress is increased there is a quiescent period before any emissions are detected. During this period there is an accumulation of strain energy and the possibility of

micromechanical events such as dislocation movement, however there are no events which release sufficiently energetic stress waves to be detected by the monitoring system. There is an onset stress, σ_o, at which AE is first recorded which is characteristic of each graphite.

IM1-24 and SM2-24 which have a finer microstructural texture than PGA-AGL have similar onset stresses (Table 4.3), circa 11 MNm^2 which are almost three times as great as PGA-AGL, ($\sigma_o \simeq 3.5$ MNm^2). The rate of accumulation of AE with load also varies with graphite type. The fastest rate of accumulation is from the coarest-textured graphite, PGA-AGL, whilst the slowest rate is from the finest- textured material, IM1-24.

For all the graphites, once emission starts it is continuous and the rate of accumulation with respect to load increases monotically until catastrophic failure. Table 4.3 gives the mean and range of Σ(AE) for each of the three unoxidised graphites. There is a large range in the total cumulative counts to failure for any given graphite. For example, the mean Σ(AE) at failure for IM1-24 is 179 for the unoxidised material with a standard deviation of 123.

Figure 4.20 shows the variation in Σ(AE) at fracture with increasing weight loss due to thermal

oxidation. For IM1-24 there is a progressive increase in Σ(AE) with increasing burn off, rising from a mean value of 180 for the unoxidised material to about 1000 for graphite oxidised to 5% weight loss. For PGA-AGL the relationship between Σ(AE) and burn-off is not as clear as with IM1-24. There is a large increase during the initial stages of weight loss, e.g. rising from a mean value of 1000 counts for the unoxidised material to 4500 at 2 percent burn-off. There appears to be a decrease in Σ(AE) at failure for burn-off levels of > 4.5%. Due to the variable nature of Σ(AE) data further measurements are required to confirm this trend.

In addition to presenting Σ(AE) data, the monitoring apparatus is also capable of presenting amplitude distributions at any stage during the loading cycle (see section 3.4.1). Figures 4.21, a and b show the development of amplitude distribution during loading up to and including fracture for IM1-24 and PGA-AGL, oxidised to 4%. As with the unoxidised graphite there is a quiescent period and an onset load at about 15 Kg for PGA and 30 Kg for IM1-24. The initial events are of low amplitude for both graphites. As load increases the events increase both numerically and in amplitude. It can be seen however that the proportion of high amplitude events for any given fraction of the failure load is greater for IM1-24 than PGA-AGL. For example, at ca.80% of the failure load, i.e. the last sub-critical plot in Figs.41 a and b, PGA-AGL has no events of amplitude

greater than 104 dB (channel 25), whereas IM1-24 at a similar percentage of the failure load has events of amplitude greater than 122 dB (channel 35). In Fig.4.21 b the amplitude distribution at failure for IM1-24 has been plotted on the same axes as the PGA-AGL distribution. It shows clearly that PGA-AGL not only has many AE events to failure but also that the proportion of low amplitude events is greater. A common way to quantify this variation is to use a power law

$$n(a) = (a/a_o)^{-b} \qquad 4.3$$

where n(a) is the fraction of AE events whose amplitude exceed a value a, a_o is the lowest detectable amplitude and b is a constant. The AETC 403 amplitude sorting apparatus was capable of displaying log Σ(AE) versus ampliutde on an oscilloscope. Photographs were taken at various stages during loading and also at fracture. Figure 4.22 is a plot of the log Σ(AE) versus amplitude channel taken directly from the photographs for unoxidised PGA-AGL, IM1-24 and SM2-24 at fracture. Each of the graphites produces a reasonable straight line relationship between log Σ(AE) and amplitude, a, and hence fits equation 4.3 quite well; the slope of the lines in Fig.4.22 are equivalent to -b. A high value of b denotes a high proportion of low amplitude events. From figure 4.22 it can be seen that there is a characteristic value of b for each

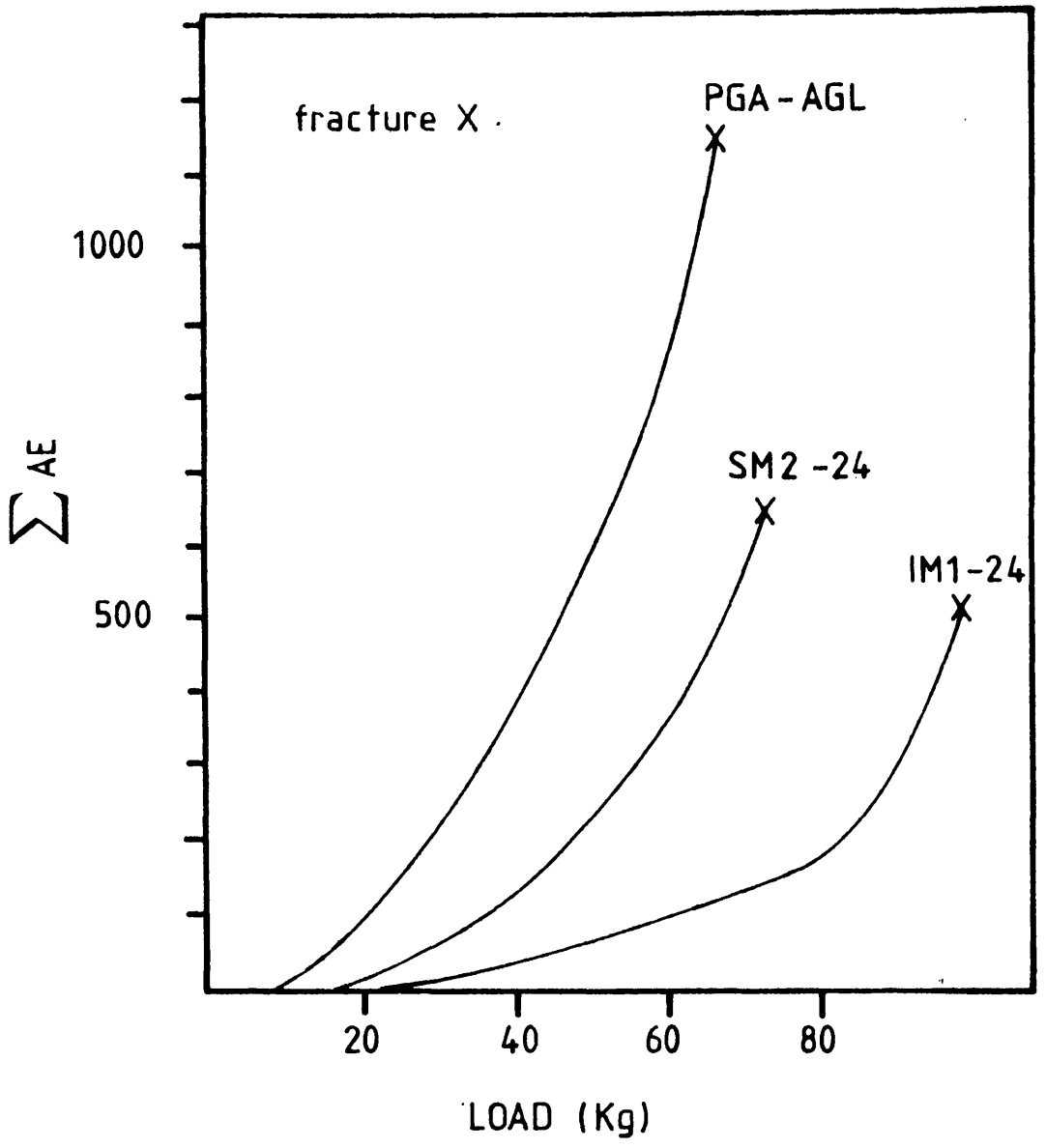

Fig.4.19 The accumulation of AE with increasing applied load

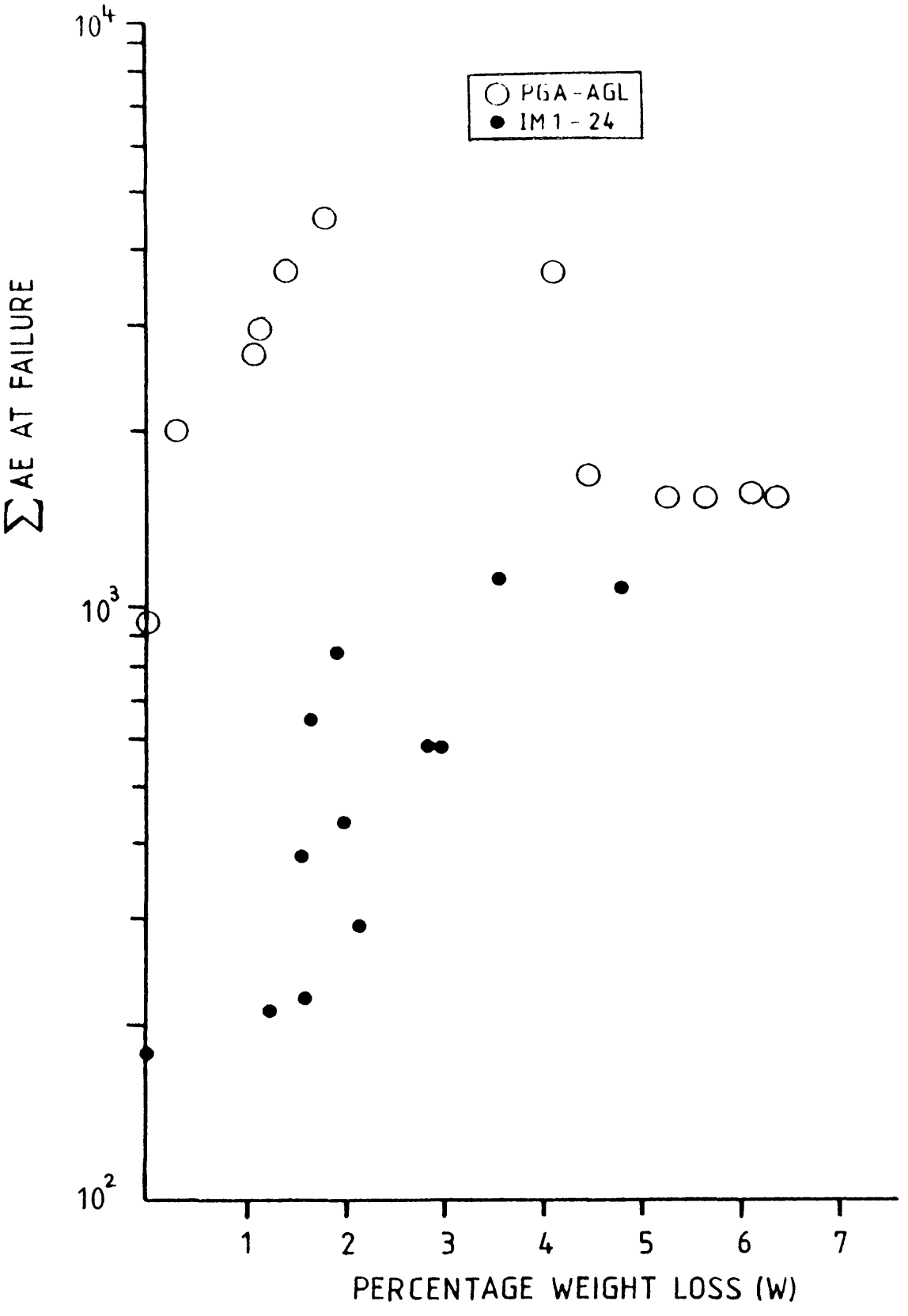

Fig.4.20 Variation of the total number of AE events at failure with weight loss.

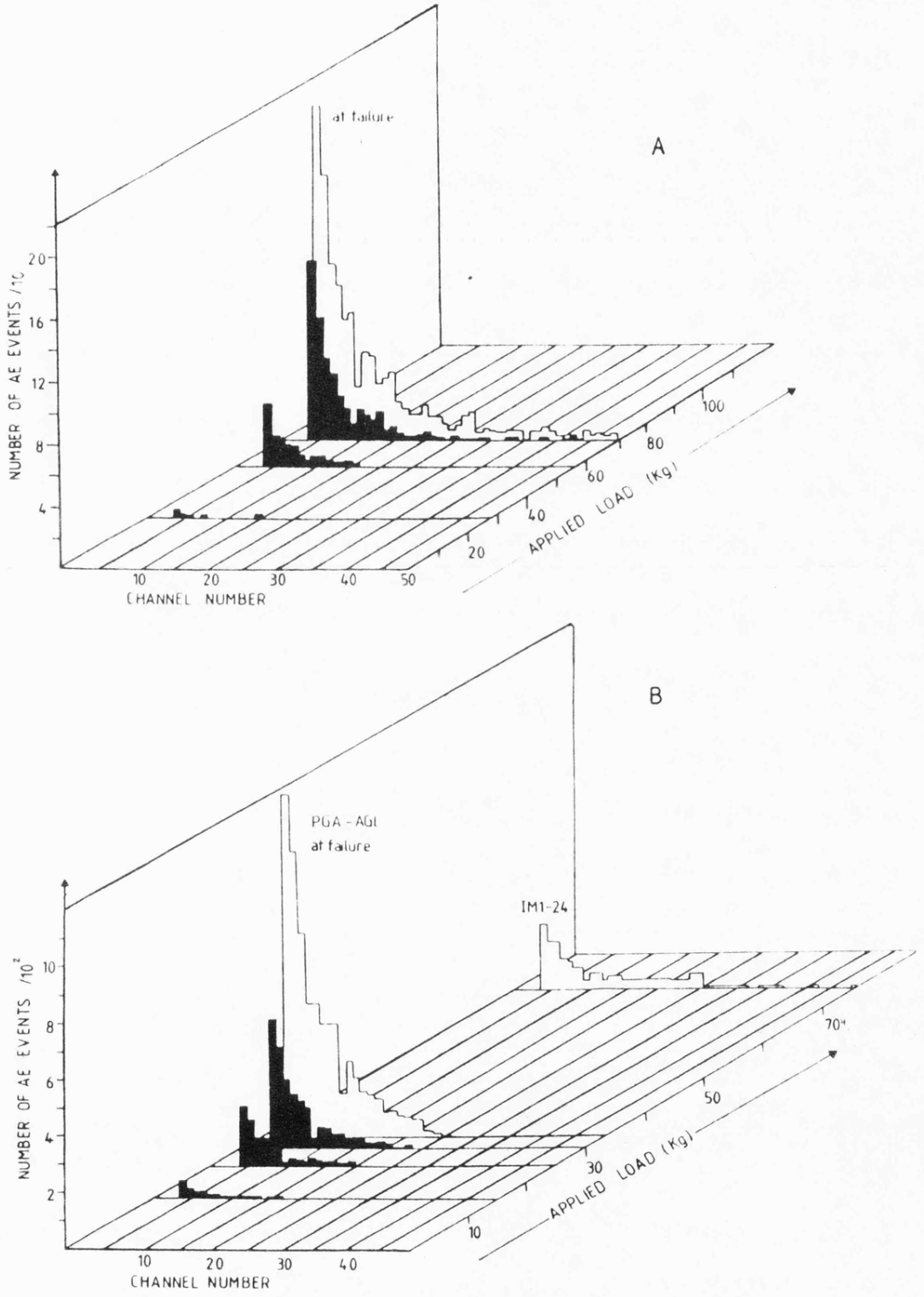

Fig.4.21 AE amplitude distributions at various sub-critical loads (black) and at failure (white). Data is presented for IM1-24(A) and PGA-AGL(B). In Fig.4.21B the AE distribution for IM1-24 at fracture is presented on the same axes as PGA-AGL for comparison.

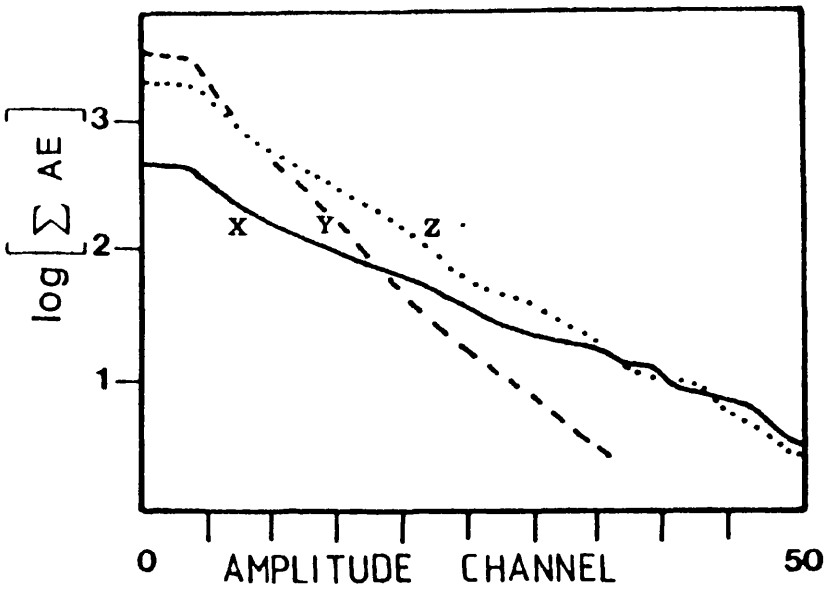

Fig.4.22 AE amplitude distributions at fracture for three graphites.
X:- IM1-24; Y:- PGA-AGL; Z:- SM2-24

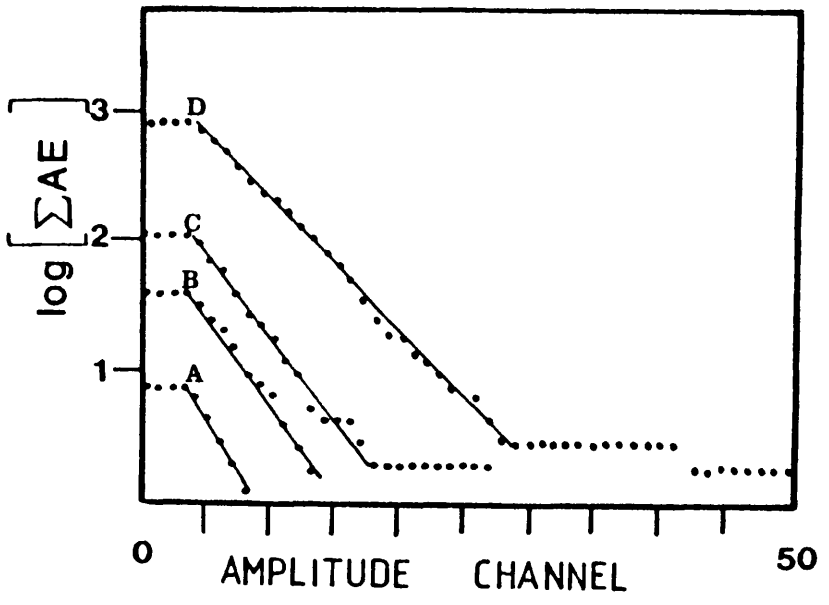

Fig.4.23 AE amplitude distributions for PGA-AGL graphite as as a function of load (kg) A:- load = 40, b = 1.46; B:- load = 50, b = 1.46; C:- load = 64, b = 1.46; D (at fracture): - load = 66, b = 1.39.

TABLE 4.3 ACOUSTIC EMISSION DATA FROM PGA-AGL, IM1-24 AND SM2-24.

MATERIAL	ΣAE UNOXIDISED *	b UNOXIDISED	b OXIDISED *	σ_o/Mnm^{-2}
IM1-24	179±123 50-500 range	0.68±0.11	0.67±0.12	11.9±3.8
SM2-24	410±224 140-780 range	0.93±0.09	-	10.8±3.9
PGA-AGL	945±427 280-1340 range	1.33±0.41	1.37±0.05	3.5±0.6

* AT FRACTURE

graphite type. A similar ranking order was found for b values as for Σ (AE) i.e. the coarsest material, PGA-AGL, had the highest value of b ≈ 1.33; the finest textured IM1-24 had the lowest, b ≈ 0.68 and SM2-24 has an intermediate structure and b value (b ≈ 0.92). The amplitude distribution and hence b value are affected by catastrophic failure. There is a slight decrease in b at failure due to the release of high amplitude stress waves at the moment of fracture. This tends to increment the higher amplitude channels by a few counts. Table 4.3 presents values of b for the three graphites. In Fig.4.23 the b slope is given for several sub-critical loads and also at failure for an oxidised PGA-AGL cylinder. The data were taken directly from photographs of the log Σ (AE) versus amplitude display on the oscilloscope. It shows that for sub-critical loads of 60,75 and 96 percent of the failure load the exponent b was similar at b = 1.46, however upon catastrophic failure the value reduced by about 6% to b = 1.37.

There is no systematic variation of the exponent b with oxidation, nor is there a large difference in b between oxidised or unoxidised material. This is demonstrated in Table 4.3 where the mean unoxidised value is compared with the mean oxidised value.

The acoustic emission data presented above will be

discussed in relationship to graphite microstructure and the micromechanisms of failure, in section 5.1.2.

4.4 Microscopical Examination

This description of microscopical examination is in three parts. The first part (4.4.1) is an evaluation of the general microstructure of unoxidised material where features are identified and related to the manufacturing process. Then on a more detailed scale, the sub-structure of mozaics and domains are characterised for each graphite and features related to this sub-structure are discussed. The second part (4.4.2) describes characteristic features in the fracture surface which gives an insight into fracture mechansims. The final part (4.4.3.) examines those features in the microstructure which have been affected by thermal oxidation.

4.4.1 (a) Microstructural Evaluation

PGA-AGL Graphite

This graphite is a large grained, extruded and hence anisotropic material. In Fig.4.24, a low magnification micrograph of PGA-AGL shows the general microstructure. Large elongated needle-coke grains have been identified by the letter A. The long axes of both the grains are approximately parallel to the extrusion directions, which is

also shown. The two grains sandwich an area of binder material, B. Throughout the microstructure there is a distribution of pores, the shape and nature of which varies greatly according to their position. It is possible to discern two distinctly different shapes of pores - large highly oriented pores within the grains; probably produced by cracking due to anisotropic contraction, during calcining or graphitisation, and smaller more spherical pores in the binder material. The latter type of pore is associated with gas entrappment and evolution during mixing and baking. When the binder is examined at higher magnification a third category of pore can be seen; these are indicated in Fig.4.25 by an arrow. They have a fine filamentary structure which has an angular appearance. The graphite specimen shown in Figs.4.24 and 4.25 have been impregnated with resin, as described in 3.5.1. Assuming 100% impregnation, it is possible to determine by different contrast levels which pores are interconnected open porosity, e.g. C in Fig.4.24 or closed porosity, e.g. D. In PGA-AGL each of the categories of pores has a proportion which are impregnated with resin. Some of the large oriented pores within the grains and the approximately spherical pores within the binder are closed, however the majority of these pores are open. The filamentary pores within the binder are invariably open.

IM1-24 Graphite

A low magnification micrograph of IM1-24, Fig.4.26, shows three gilsocarbon filler grains, A, surrounding an area of binder phase, B. The gilsocarbon grains are approximately spherical (see fig.3.5), however during manufacture grains may fracture producing irregular shaped features; such a grain is shown in the bottom left hand corner of Fig.4.26. The gilsocarbon grains are often referred to as having an onion skin texture, Fig.4.27. This is due to the lenticular shaped pores, C, which run parallel to the circumference of the grain. A second type of pore, D, due to entrapped gas can be seen in the binder phase in Fig. 4.26. These pores have a globular appearance and are usually about half the size of the grains. When the binder material is viewed at higher magnification Fig.4.28, a third type of porosity, E, can be identified. As in PGA-AGL this is a filamentary type, however their shape is irregular, in contrast with the angular pores in PGA-AGL. The filamentary pores in IM1-24 are often associated with the gas evolution pores in the binder. In IM1-24 the gas evolution porosity and the fine filamentary pores are impregnated with resin and are therefore of the open type. The lenticular pores within the gilsocarbon grains are nearly always unfilled and hence are of the closed type. This can be seen in Fig.4.27 where a gas evolution pore in the left of the micrograph is filled with grey resin and the pores within the grain on the right are unfilled and black.

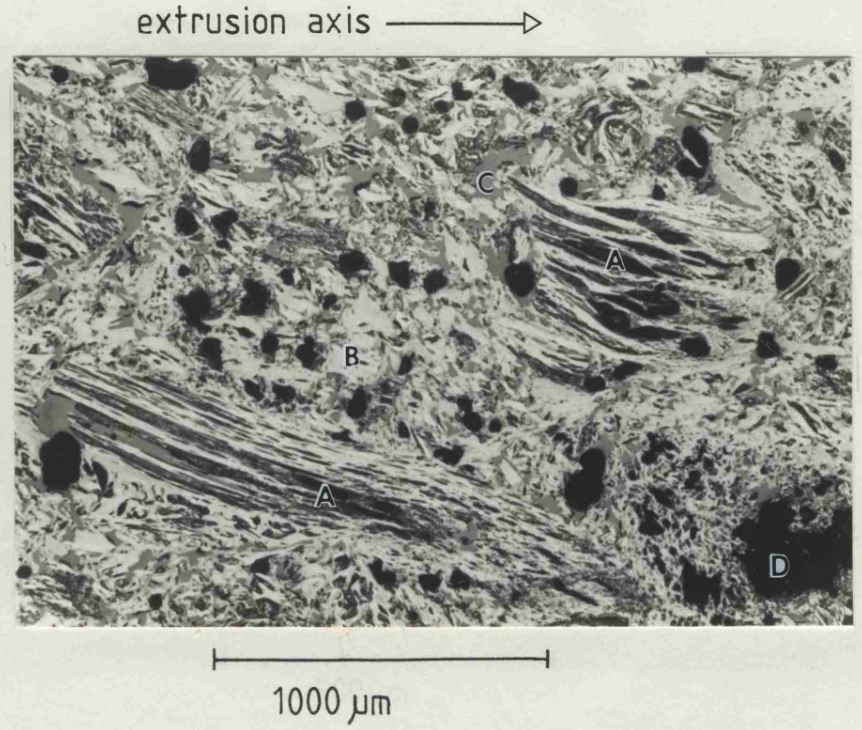

Fig. 4.24 General microstructure of PGA-AGL showing grains, A and binder, B. Open and closed pores have been identified by C and D respectively.

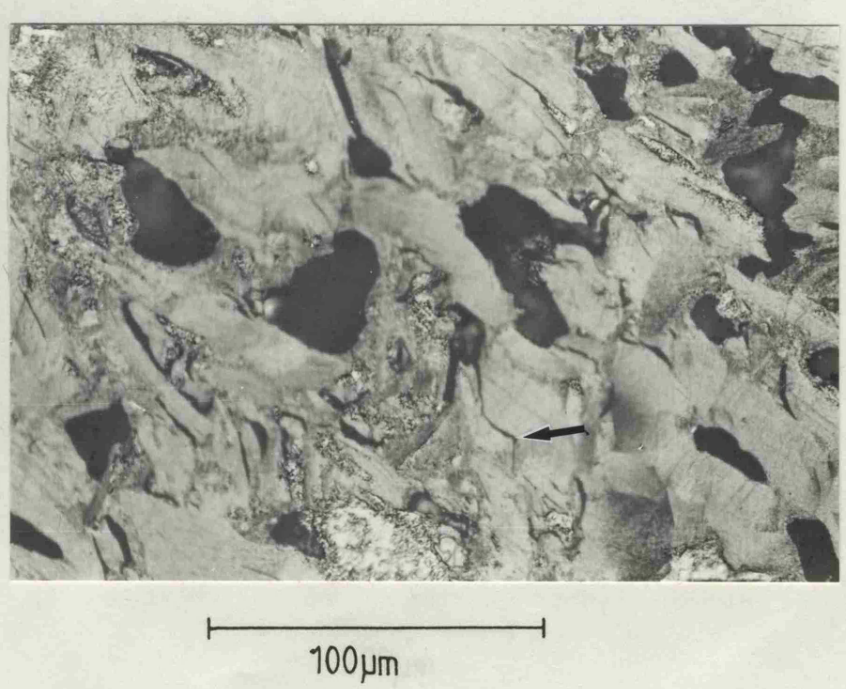

Fig. 4.25 Detail of the binder material, showing irregularly shaped gas entrappment pores and filamentary pores (arrowed).

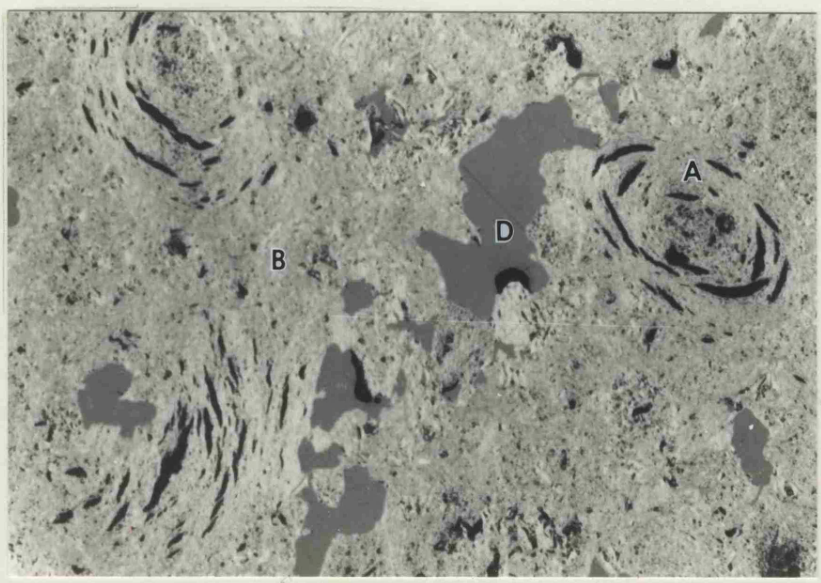

Fig. 4.26 General microstructure of IM1-24 showing filler grains, A and binder material, B. The binder material contains gas entrappment pores, D.

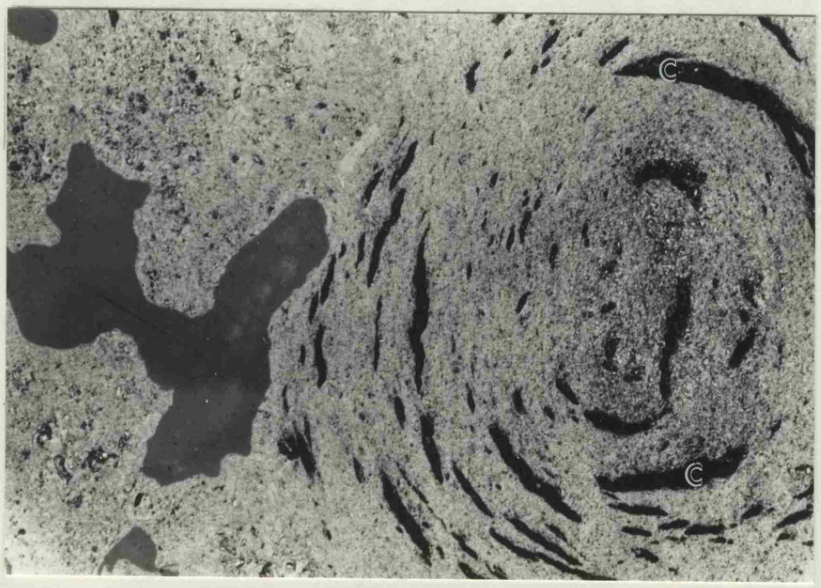

Fig. 4.27 Detail of a gilsocarbon filler grain containing lenticular porosity, C.

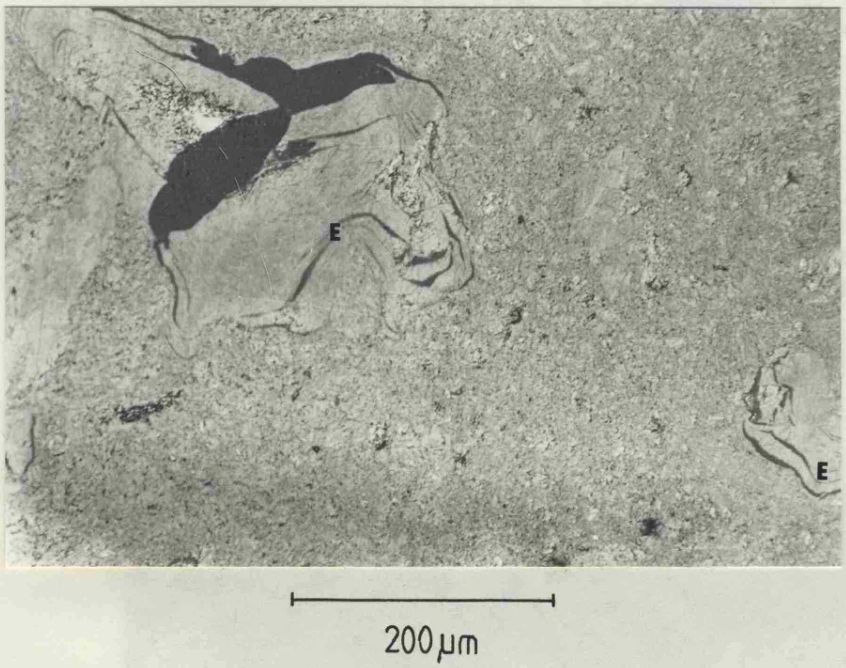

Fig.4.28 Filamentary pores in the binder of IM1-24.

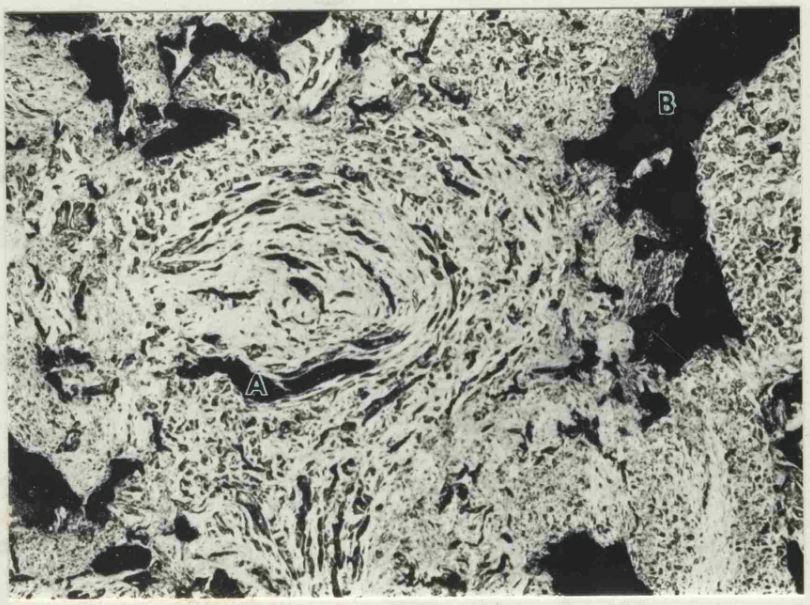

Fig.4.29 General microstructure of SM2-24 showing filler grains, A, surrounded by binder material. The binder material contains gas entrappment pores, B.

Fig.4.30 Filamentary pores in the binder of SM2-24,C.

SM2-24 Graphite

This graphite has large block shaped grains, one of which is identified by the letter A in fig.4.29. The grains are surrounded by binder material, which contains gas entrappment pores, B and filamentary porosity, C, fig.4.30.

(b) Characterisation of the sub-structure (optical texture)

Prior to discussing the comparative fine detailed structure of the three graphites, it is necessary to redefine the terms mozaic and domain as used in this thesis. A mozaic is an agglomeration of apparently randomly orientated isochromatic regions, where the maximum size of region is less than 10 μm. A domain is an isochromatic region greater than 10 μm.

Because of the contrast in optical texture of PGA-AGL, SM2-24 and IM1-24 it is possible to characterise the three graphites by estimation of the ratio of mozaic to domain structure and maximum domain size, Table 4.4. Figure 4.31 is a set of low magnification micrographs of the three graphites using a sensitive tint filter (3.5.1). For all three micrographs when prismatic edges of basal planes are aligned from top right to bottom left, they appear blue;

when rotated through 90° they appear orange, and at intermediate angles they appear purple. PGA-AGL has the coarsest optical texture, Fig.4.31a. In the microcgraph there is a needle-coke grain dominating the field with a small area of binder material on the right. Within the grain there is not one single domain but several large contiguous and commonly orientated domains, in contrast with the smaller and more randomly orientated domains in the binder. When areas of mozaic are viewed at low magnification, it is difficult to resolve the individual components and the resultant image is a dull purple region; this can be seen in large areas in SM2-24, Fig.4.31b, but it is notably absent in PGA-AGL. In the micrograph of SM2-24, there is a large grain, running diagonally across the field. This, like PGA-AGL has commonly orientated and contiguous domains running parallel with the axis of the grain. There is however a large difference in the size of the individual domains compared with PGA-AGL. The grain is surrounded by binder material, this has a mozaic structure, in contrast with the binder of PGA-AGL whose optical texture is coarser than the domains in the SM2-24 grain. The finest, overall optical texture of the three graphites is that of IM1-24, Fig.4.31c. The micrograph shows two gilsocarbon grains surrounded by binder material. Once again a common basal plane orientation can be seen in the grain on the top right of the field. However, in IM1-24 the size of the isochromatic areas of which this part of the field is constituted is so fine that individual areas cannot be resolved at this magnification. Even though some of the

Fig.4.31 Sensitive tint micrographs showing the general microstructure of PGA-AGL (A), SM2-24(B) AND IM1-24(c).

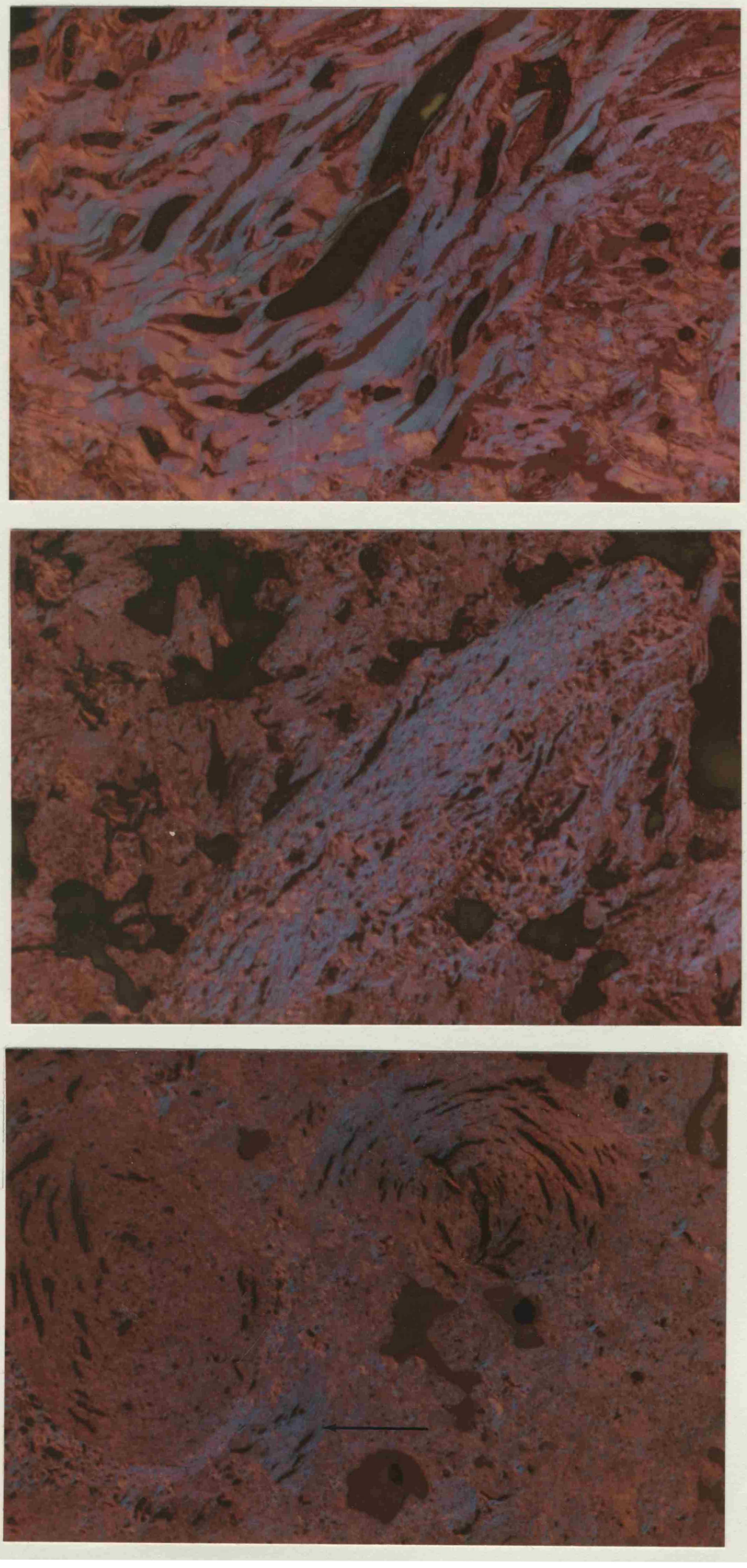
A
B
C
500µm

Fig.4.32 Sensitive tint micrographs of the detailed optical texture within binder of IM1-24.

A

B

20 µm

C

A

B

20µm

Fig. 4.33 Sensitive tint micrograph of filamentary pores in the binder of PGA-AGL, A and filamentary pores in grains, following the basal plane orientation, B.

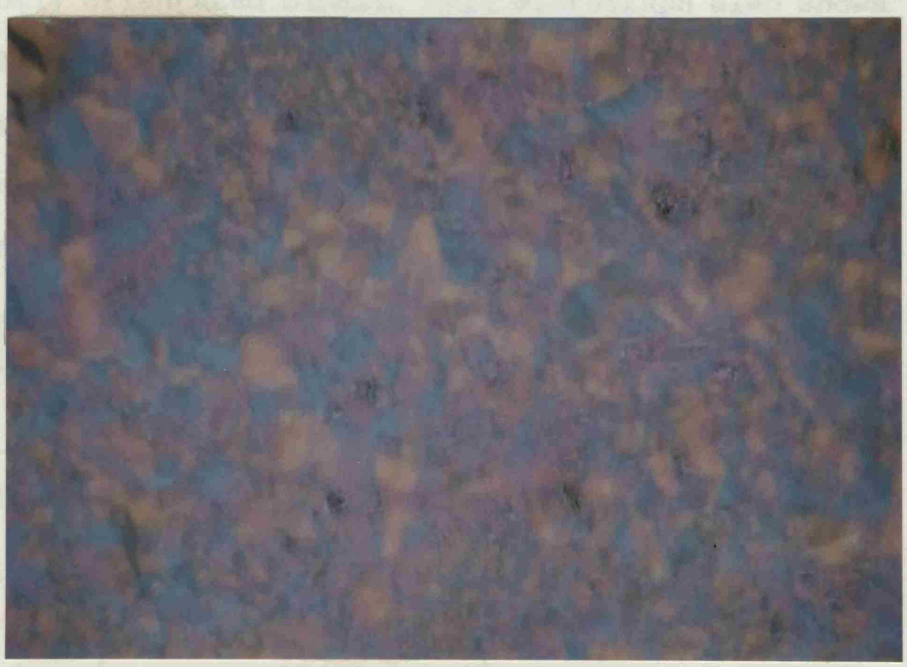

Fig. 4.34 Mozaic structure in the binder material of PGA-AGL.

small domains in the binder material can be resolved and are therefore obviously larger than the areas in the gilso particles, they do not produce areas of common basal plane orientation. This is clearly seen in the binder material below the grain on the left of the micrograph, where a fragment of gilso grain (arrowed) with strong basal plane orientation is surrounded by the more mottled and therefore more randomly orientated binder. This micrograph also shows the usefulness of the sensitive tint techniques for aiding distinction between grains and binder material. This is most clearly seen at the binder/grain interface of the lower left hand grain.

TABLE 4.4 ESTIMATION OF OPTICAL TEXTURE OF PGA-AGL, SM2-24 and IM1-24

GRAPHITE TYPE	MOZAIC/DOMAIN RATIO	MAX DOMAN SIZE/ μm
PGA-AGL	10/90	900
SM2-24	60/40	500
IM1-24	80/20	200

To resolve the microstructure of the mozaic regions, it is necessary to use much higher magnification. Figures 4.32, a, b and c are micrographs of the binder area of IM1-24 using a x 80 objective lens and the sensitive tint filter. They clearly reveal the mottled, mozaic structure of blue and yellow and purple. The mozaic structure, A, is contrasted with several areas of domains, B, in Figure 4.32a. The mozaic structure varies in its texture, becoming

coarser towards the right of the micrograph and eventually merging with the domain areas. The pores that are present are restricted to the domain structure. These pores are of the filamentary type that are shown in Figs.4.28. They tend to avoid mozaic areas and run parallel to the basal plane orientation of the domains, Fig.4.32.b. It was stated previously that filamentary pores are often associated with gas evolution porosity and their paths meandered through the binder material. The reason for this may be seen in Fig.4.32 c, where a filamentary pore runs from a gross, gas evolution pore at A and principally follows domain structure avoiding mozaic. Similar pores are seen in PGA-AGL, Fig.4.33.a, but they tend to be less tortuous than those in IM1-24 as they do not encounter the same amount of mozaic structure, but are only influenced by the orientation of the basal planes in the domain. Whilst they have been called pores, it may be more precise to call them cracks as they are the result of thermally induced stresses cleaving basal planes, similar to those discussed by Mrozowski (13). These thermally produced cracks are also present in the grains of PGA-AGL, but tend to be less numerous. Figure 4.33b shows a crack in a grain making a 90^{o} change in direction, following the basal plane orientation. PGA-AGL has a much smaller proportion of mozaic structure than either SM2-24 or IM1-24 and the mozaic that is present, is generally much coarser in optical texture cf. Figure 4.34 and 4.32.

Whilst there are obvious differences in scale and

distribution of microstructural features within the three graphites, there are some common and important features. For each of the graphites, the grains consist of contiguous areas of common basal plane orientation, thus providing sites for extensive cleavage. All three graphites contain a filamentary porous system which is interconnected and open to the atmosphere.

4.4.2 Fractography

It is difficult or even impossible to differentiate between sub-critical failure events and fast fracture events by examining the post-catastrophic fracture surfaces of graphites. However, fractography can identify characteristic features in the microstructure which influence the fracture path.

IM1-24

The overriding characteristic feature of the fracture surface of IM1-24 is the domed or spherically depressed appearance, Fig.4.35. This may be the result of either, the fracture path following the binder phase and therefore dipping and rising to avoid the grains, or the cleaving off of the outer layers of the gilsocarbon grains which then link with pores in the matrix. It is believed that the latter path description is the more accurate

representation, for the following reasons. In section 4.4.1 it was seen that the largest areas with good common basal plane orientation in IM1-24 were within the gilsocarbon grains. Thus a crack would require less energy to propagate through this area. It would therefore be a preferred site for sub-critical failure. A common feature in the fracture surface is shown in Fig.4.36; this is a micrograph of a section cut normally through a fracture face. It illustrates a gilsocarbon grain in which the graphite surrounding a lenticular pore has been fractured, leaving a flat fracture surface in a direction approximately parallel to the circumference of the grain. This is also parallel to the basal plane orientation. The large lenticular pore provides a good crack nucleation site and the basal plane orientation of the graphite parallel to the pore is good for easy propagation. Also in the same micrograph the fracture path can be seen to connect with adjacent gas evolution pores on either side of the grain. The scanning electron micrograph, Fig.4.37 shows the same type of fracture feature as that in 4.36, i.e. a gilsocarbon grain protruding from the surface. It appears that a large proportion of the outer surface has been cleaved off leaving a step in the lower region of the grain (arrowed). The surface of the grain has a generally stepped appearance; this is probably due to ligaments between lenticular pores failing, exposing the relatively flat pore surfaces.

PGA-AGL

This material has a very distinctive fracture appearance. The fracture path is strongly influenced by the large ansiotropic filler grains. When the grain is approximately normal to the tensile axis, cleavage of the grain is favoured, resulting in large flat features in the fracture surface. These bright features are shown in Fig.4.38, where two adjacent grains which are normal to the fracture surface have cleaved; they are surrounded by rougher textured binder material. The difference in energy expenditure between fracturing a highly orientated grain and the randomly orientated binder material may be realised by a comparison of the fracture surface texture of the two regions, Fig.4.39 a and b. A favourably orientated grain will be cleaved more easily than a region of binder material, however, if the grain is not favourably orientated, e.g. approximately parallel to the tensile axis, then the binder is a preferred fracture path. Thus a characteristic feature that is often seen in specimens whose tensile axis is parallel to the extrusion axis, is grains protruding from the fracture surface, Fig.4.40.

It is very difficult to quantitatively characterise the fracture surface of a graphite in terms of the proportion of grain to binder failure or the amount of crack path tortuosity. Therefore it is difficult to assess the effect of thermal oxidation upon the fracture path. However

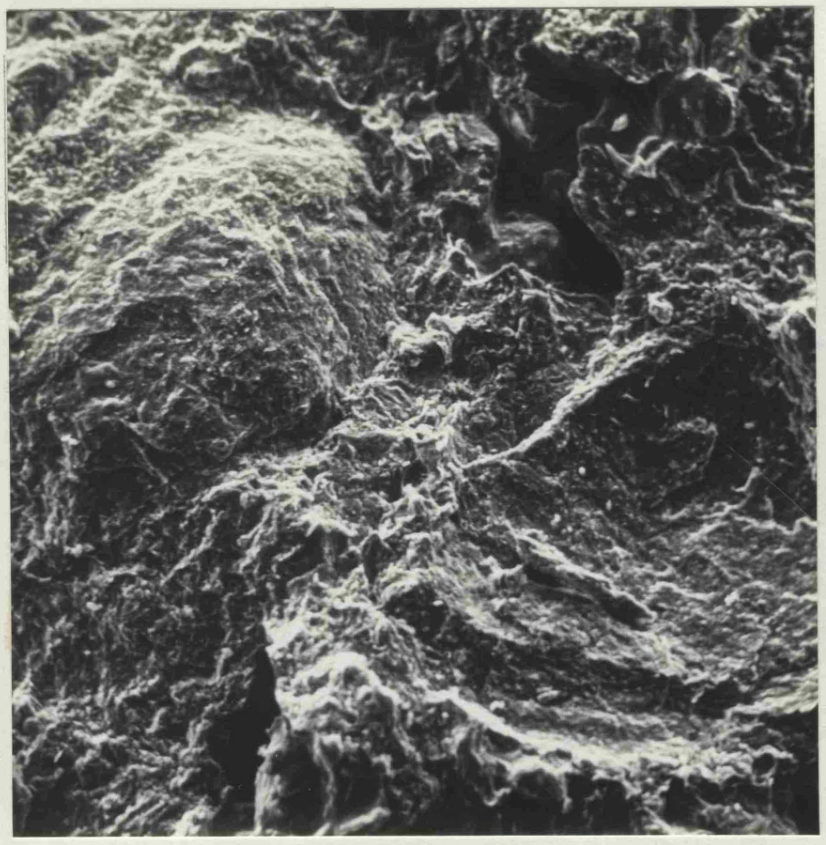

Fig. 4.35 SEM. of the domes and indentations which characterize the fracture appearance of IM1-24.

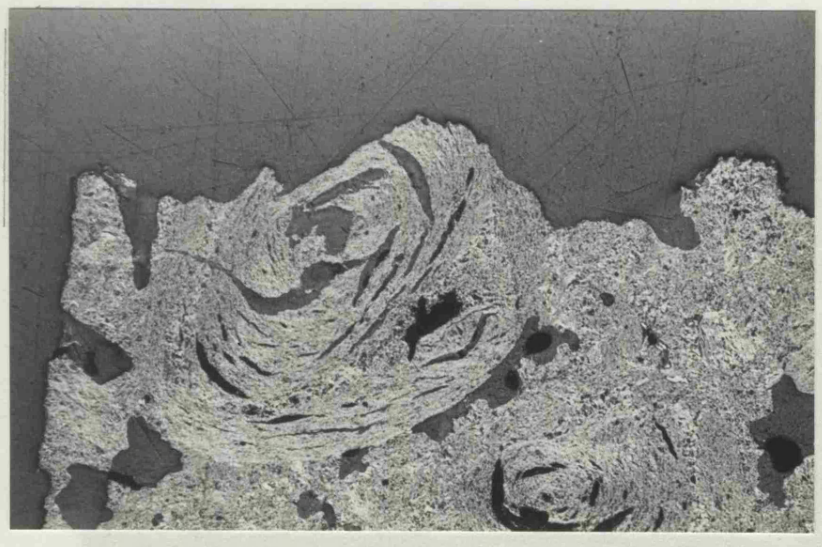

Fig. 4.36 A section through the fracture surface of IM1-24 showing a gilsocarbon grain which has failed.

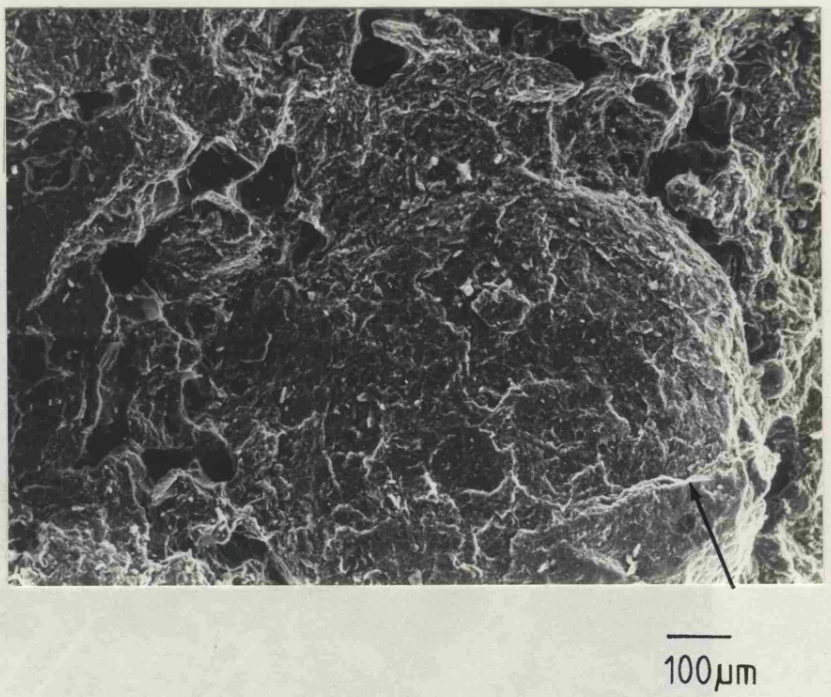

Fig. 4.37 SEM. of a gilsocarbon grain protruding from the fracture surface of IM1-24. The outer layer of the grain has been cleaved off, leaving a step (arrowed)

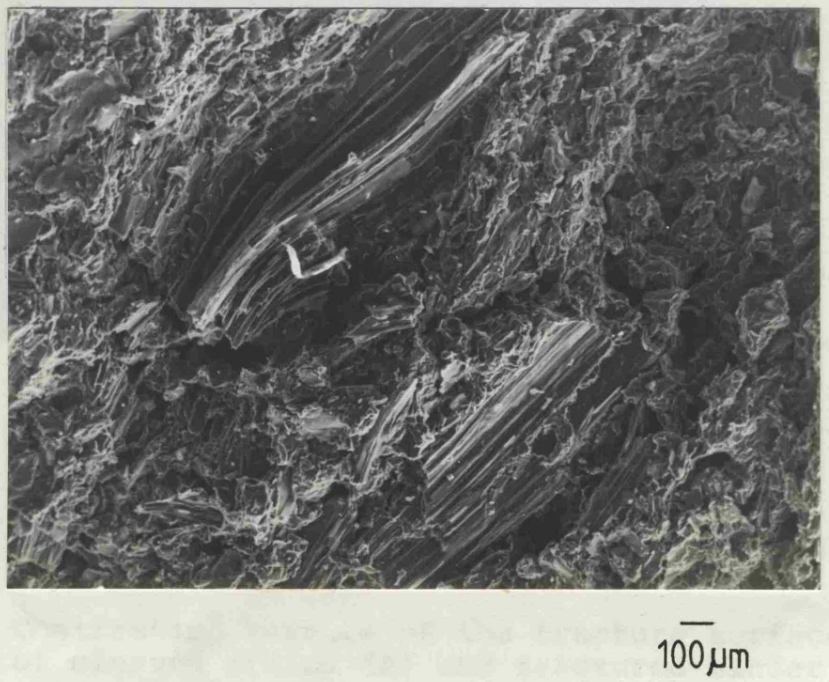

Fig. 4.38 SEM. of two adjacent cleaved grains on the fracture surface of PGA-AGL.

PGA-AGL

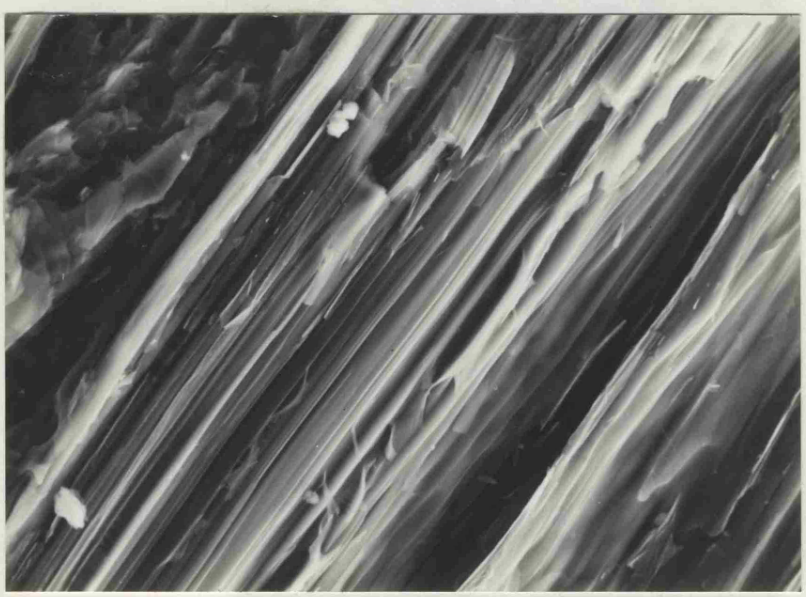

A

10µm

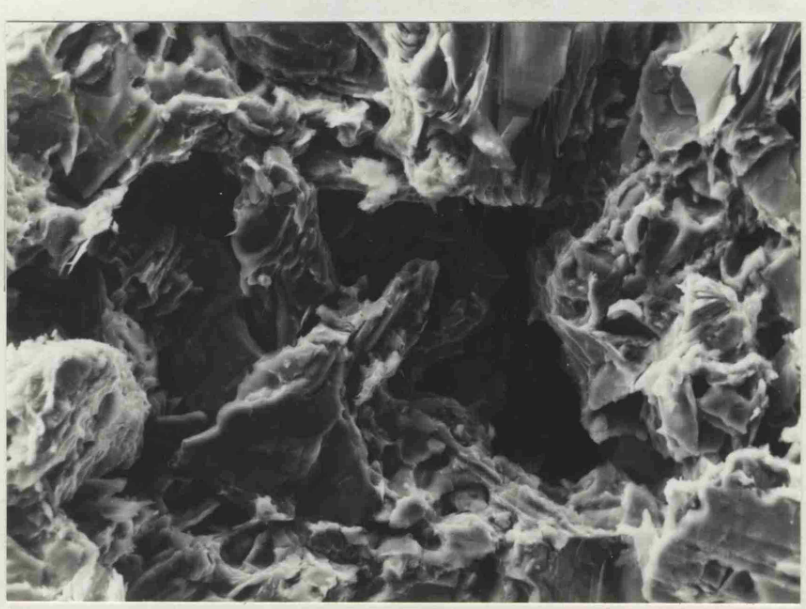

100µm

Fig. 4.39 Contrasting texture of the fracture surface of cleaved grains (A) and fractured binder material (B).

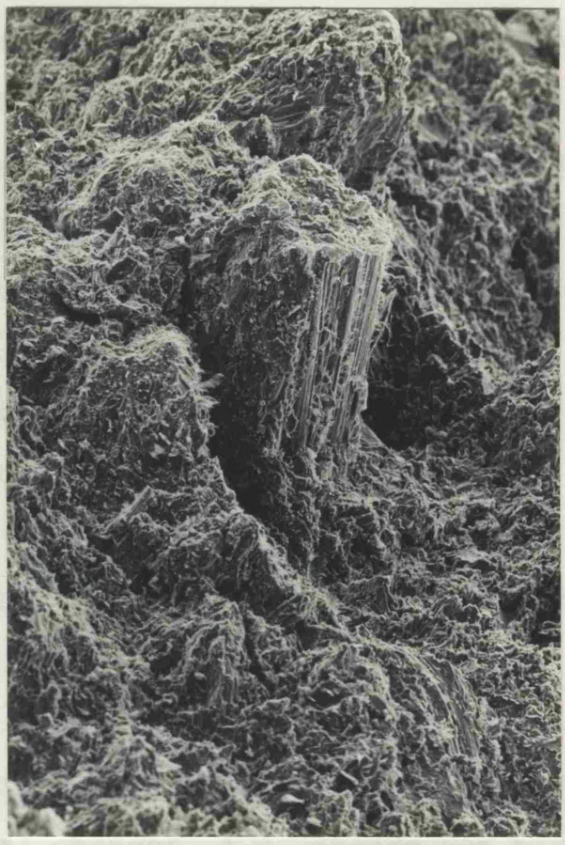

Fig. 4.40 SEM. of the fracture surface of PGA-AGL. It shows the characteristic feature of fracture specimens whose extrusion axis is parallel to the tensile axis, i.e. grains protruding from the fracture surface.

if there was a radical change in failure mechanism; for example, if the binder phase had become weakened to such an extent that the fracture path would preferentially pass through the binder, rather than a favourably orientated grain, then it would be reasonably easy to detect. However no such changes in failure mechanisms have been observed with weight loss due to oxidation. Thus on the basis of fractographic examination it is concluded that there are no radical changes in fracture mechanisms as a result of thermal oxidation up to 6% weight loss.

4.4.3. Microstructural changes as a result of thermal oxidation

Quite clearly, oxidation to 900^{o}C is not going to induce purely thermal changes, i.e. grains and binder will maintain their relative positions. Also the temperature involved in this oxidation programme is not sufficient either to cause further graphitisation or to change the optical texture. The only microstructural changes expected and found were those directly related to oxidation. The product of thermal oxidation of graphite with carbon dioxide is gaseous, therefore removal of material occurs. It was the purpose of this section of the investigation to determine which features in the microstructure were attacked preferentially. Graphite will only be removed from areas accessible to the reactant gas, for example, the outer surface and the interconnected open porosity. The weight loss from outer surface removal is small as there are no

detectable dimensional changes. Therefore the principal sites for graphite removal are those in the interior. A good way to evaluate changes is to impregnate the open porosity of oxidised and unoxidised material with fluorescent resin is described in section 3.5.1 and 3.5.3. In this way only the open pore system is illuminated which makes it easier to evaluate changes.

IM1-24

In section 4.4.1, three basic types of pore were identified: lenticular pores within the gilsocarbon grains; gross, gas evolution porosity in the binder and filamentary pores, which are also in the binder material. In the unoxidised condition only the latter two types are open pores. The first stage of this investigation was to determine any changes in the shape or size of the gas evolution porosity between the extremes of weight, i.e. 0 and 6%. Also to see if oxidation to this level made the lenticular porosity accessible to the reactant gas. Both these features are best examined at low magnification, therefore a x6 objective lens was used. In Figure 4.41, three micrographs of unoxidised graphite are presented alongside three micrographs of oxidised graphite (6.6% weight loss). The principal features in both sets of photographs are gas evolution pores. They appear white and have a strong contrast with the featureless black background. The pores are large and have an irregular,

globular appearance. There is no apparent difference in size or shape between the unoxidised and oxidised pores. It is however very difficult to detect small changes in size of pores by casual inspection of micrographs and therefore quantitative microsocpy has been employed; the results of this are discussed in the following section. The top micrograph in the unoxidised column in Fig.4.41 shows a number of gas evolution pores surrounding a gilsocarbon grain. None of the lenticular pores have been filled with resin. Similarly in the oxidised graphite micrographs, no lenticular pores are present. However, when examining a large number of fields of graphite which had been oxidised to around 6% weight loss or more, a few gilsocarbon grains are found which have been impregnated. This suggests that this extent of oxidation can open up the lenticular porosity, Fig.4.42.

There is a large effect of oxidation upon the third category of pores, i.e. the filamentary pores in the binder. Figure 4.43 is a collection of three micrographs of the binder material for unoxidised and oxidised IM1-24. These were taken at a higher magnification than those in Fig.4.41 using a X25 objective lens. There is an obvious increase in the quantity of the filamentary pores. The discontinuous pores in the unoxidised graphite, develop into a continuous network structure, linking gas evolution porosity by a greater number of routes. Also, there is a large increase in the number of sites of pores. Thus either new pores are

formed or more probably, previously unresolvable pores are developed into resolvable features.

PGA-AGL

The open pore system for unoxidised and oxidised (2.3% weight loss) PGA-AGL is iluustrated in Fig.4.44. This set of micrographs are of the same mangification as those in 4.43, i.e. using a x25 objective lens. Even at this moderate weight loss, there is an obvious difference between the pore structure of the oxidised and unoxidised material. There is no obvious difference in either the shape or size of the globular gas entrappment pores. However, as in IM1-24 the only microstructural changes which occur upon oxidation are confined to the filamentary pores, which exist principally in the binder phase, however unlike IM1-24, there are a small number of this type of pore within the grains Fig.4.33b. The effect of oxidation upon these pores is similar to that on the filamentary pores in IM1-24, i.e. a greater number of pores are present and their dimensions have increased, producing a network structure. The shape of the network of filamentary pores in PGA-AGL is more angular than the thread-like pores in IM1-24, this is associated with the optical texture of the matrix in which they are growing (4.4.1.).

The only microstructural change that has been

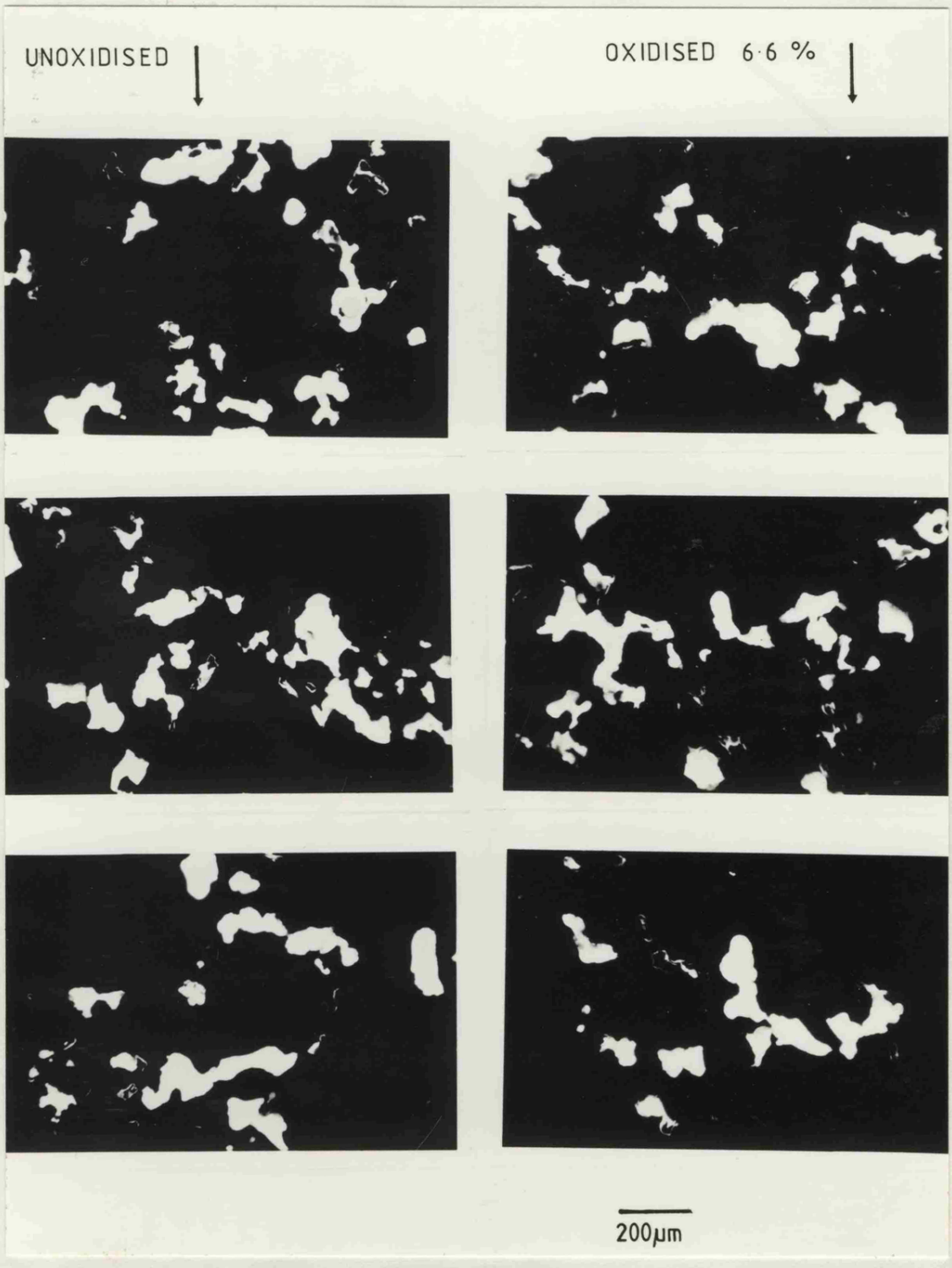

Fig. 4.41 Low magnification, fluorescence enhanced images of pores in unoxidised IM1-24 (left column) and oxidised IM1-24 (right column).

100μm

Fig.4.42 Fluorescence enhanced micrograph of lenticular porosity within a gilsocarbon particle which has been opened due to oxidation.

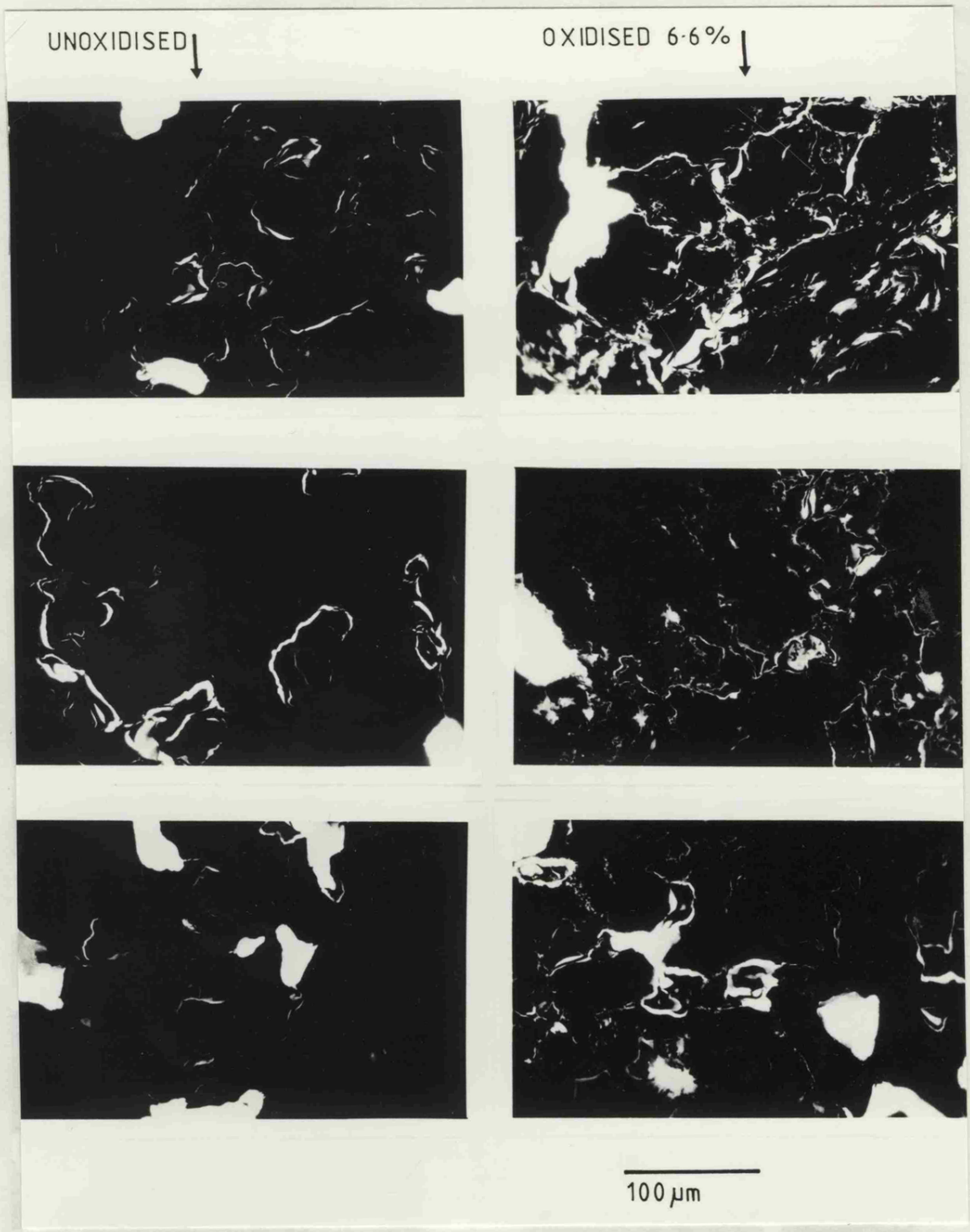

Fig. 4.43 High magnification, fluorescence enhanced images of pores in unoxidised IM1-24 (left column) and oxidised IM1-24 (right column).

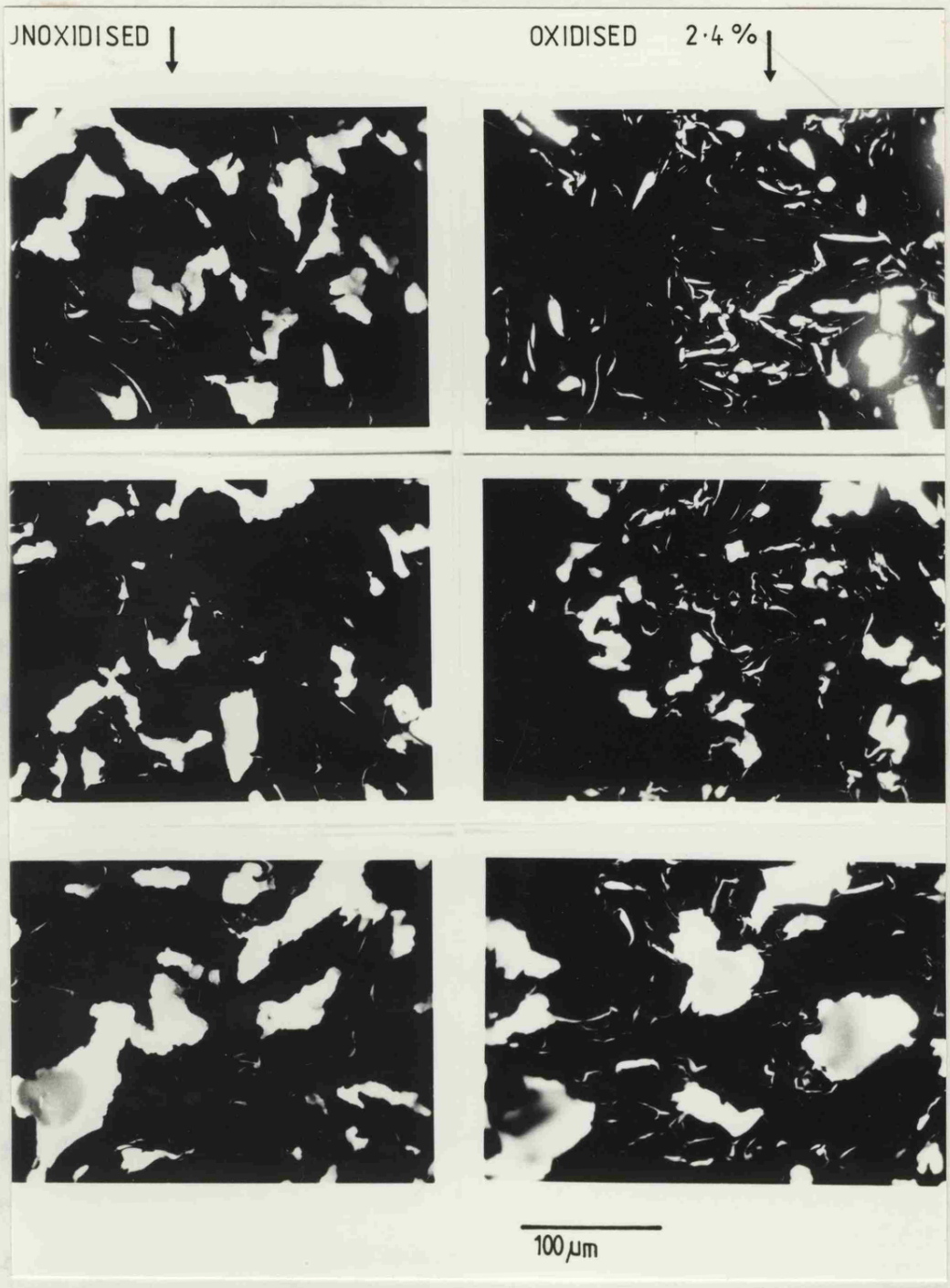

Fig. 4.44 High magnification, fluorescence enhanced images of pores in unoxidised PGA-AGL (left column) and oxidised PGA-AGL (right column).

observed when both PGA-AGL and IM1-24 have been thermally oxidised at weight losses up to 6%, is a selective attack of filamentary pores. This attack produces a network structure of pores within the binder phase. An attempt to quantify these changes is presented in the following section.

4.5 IMAGE ANALYSIS OF PORE DEVELOPMENT

In the previous section a qualitative description of the development of pores in IM1-24 and PGA-AGL was presented. For both graphites it appears that the principal development is in the fine porous network which is present as a result of anisotropic contraction. Image analysis has been employed to quantify the development of the open porosity. The techniques for specimen preparation and quantitiative image analysis have been discussed in section 3.5.3.

Data were taken for both graphites in the unoxidised condition and also at ca.6.5 percent weight loss. Sections were cut at random in IM1-24 and parallel to the extrusion axis for PGA-AGL. Thus a 2-dimensional comparison is possible for pore development before and after oxidation. The Simple Picture Evalaution Language programme was used in edge-tracking and feature counting mode to measure the areas of the pores. Pores with an area greater than 3000 μm^2 were measured using a x6 objective lens on

the microscope, giving a field of view of 832 x 832 μm. For pores less than 3000 μm^2 an objective lens of x63 was used (field of view 85.9 x 85.9 μm). A maximum of 2000 features can be counted using SPEL, which limited the number of fields that could be measured; up to 100 fields were examined. Histograms of pore area against number of pores were taken from the computer and have been replotted as the ratio of the number of pores in the oxidised specimen * for a specified pore area range; these are shown in Figs.4.45 and 4.46 for IM1-24 and PGA-AGL respectively. Thus if there is no change in the number of pores either due to oxidation or inherent pore size distribution, the ratio will be equal to 1. The limit of resoltuion of the I.A. system is determined by the relative area of one picture point to the field area. At the highest magnification used in this investigation, i.e. field area 85.9 x 85.9 μm^2, one picture point covered an area 0.2 μm^2, and therefore sub-micron area measurements were considered beyond the resolution of the system. From Fig.4.45, it can be seen that in IM1-24 for the area range, 1.5 μm^2 to 50 μm^2 there is a greater than threefold increase in the number of pores upon oxidation. The ratio drops sharply to 1 at ca. 200 μm^2 and for pore areas greater than 200 μm^2 up to the greatest measured pore area (≈ 50,000 μm^2), the ratio varies from a maximum of 1.6, for areas in the range 1000 to 2000 μm^2 to a minimum of 0.75 in the range 5,000 to 10,000 μm^2. Great care should be taken when interpreting these data as the ratio will not only vary due

INSERT * to the number of pores in the unoxidised specimen.

to the effects of oxidation, but also due to the large statistical variation in pore size spectra. For example the ratio of 0.75 in the 5,000 - 10,000 μm^2 range is obviously due to this statistical variation as oxidation will not cause a reduction in the number of pores in a particular area range without a corresponding increase in the number of larger pores. The extent of the effect of statistical variation upon the ratio is greatest where the number of pores in an area range is low. For example, in the 1,000 - 2,000 μm^2 range there are less than 20 pores, compared to ca.1000 pores in the 1.5 to 5 μm^2 and hence there can be less confidence in attributing the ratio of 1.6 in the large pore size range to the effects of oxidation than attributing the ratio of 3.3 to oxidation in the smaller pore size range. For this reason the number of pores counted in each area range, for the oxidised specimens has been included in Figs.4.45 and 4.46. From the data in Fig.4.45 it would appear that oxidation up to 6.5% weight loss in IM1-24, principally affects pores whose area is less than 200 μm^2. Similarly for PGA-AGL, Fig.4.46 indicates an increase in the number of pores with an area equal to or less than 100 μm^2. When the graphite is oxidised to ca. 6.5% weight loss. There is also apparently an increase in the number of pores with an area greater than 3000 μm^2. If this is due to oxidation, from the data in Fig.4.46 it would suggest enlargement of pores with an area less than 1000 μm^2, where there has been a slight reduction in the number of pores after oxidation. Assuming spherical

pores, this would require a diameter increase from 36 μm to at least 62 μm . Such large localised attack should be visible upon microscopic examination, however, no such development has been observed. It is therefore probable that the difference between the oxidised and unoxidised specimens for pore size greater than 3000 μm^2 is due to the statistical variation in the original samples rather than to the effects of oxidation. To indicate the contribution that a specified pore area range makes to the total open porosity area, the cumulative percentage area, ΣA, has been plotted against pore area, a. ΣA was determined using

$$\Sigma A = \sum_{i=0}^{i=n} \frac{X_i N_i}{A'} \qquad (4.4)$$

where X_i is the mid point of the area range, a_i, N_i is the frequency of pores in that range and A' is the total field area examined. Small class intervals were selected to minimise any skew within that interval. ΣA has been plotted against pore area in Fig.4.47 which shows the effect of ca.6.5% weight loss upon pore development in IM1-24. It shows that there is preferential development of pores with an area less than 150 μm^2 in the oxidised graphite. Pores with an area of less than or equal to 150 μm^2 constitute 8.3% of the total open pore area in the unoxidised material, whereas in the oxidised graphite they constitute 19.6%. Similarly in Fig.4.48 ΣA has been plotted gainst a, for oxidised and unoxidised PGA-AGL. This

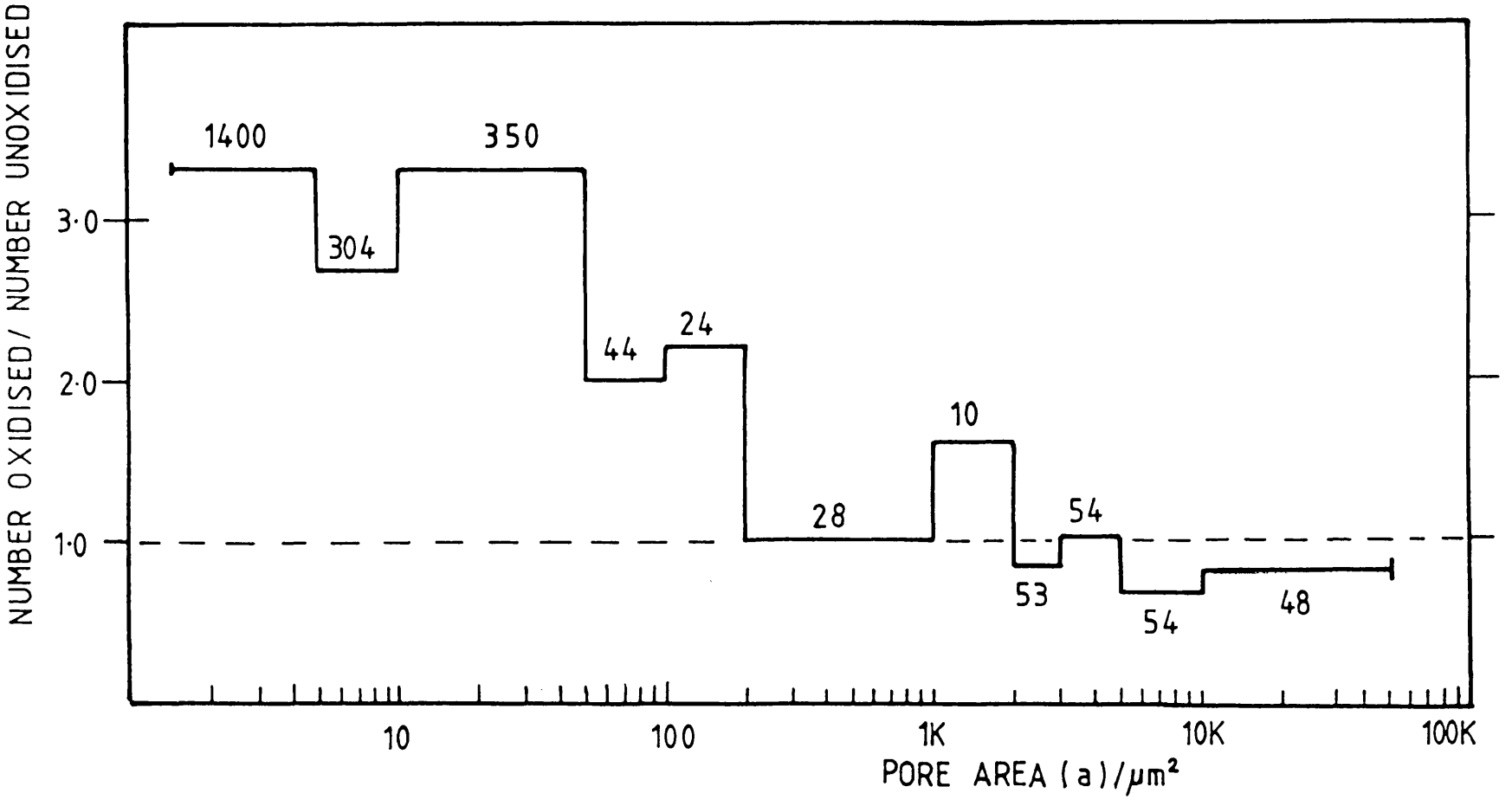

Fig. 4.45 Ratio of the number of pores in oxidised IM1-24 to the number observed in unoxidised material. The figures over each pore area range refer to the number of pores in the oxidised material.

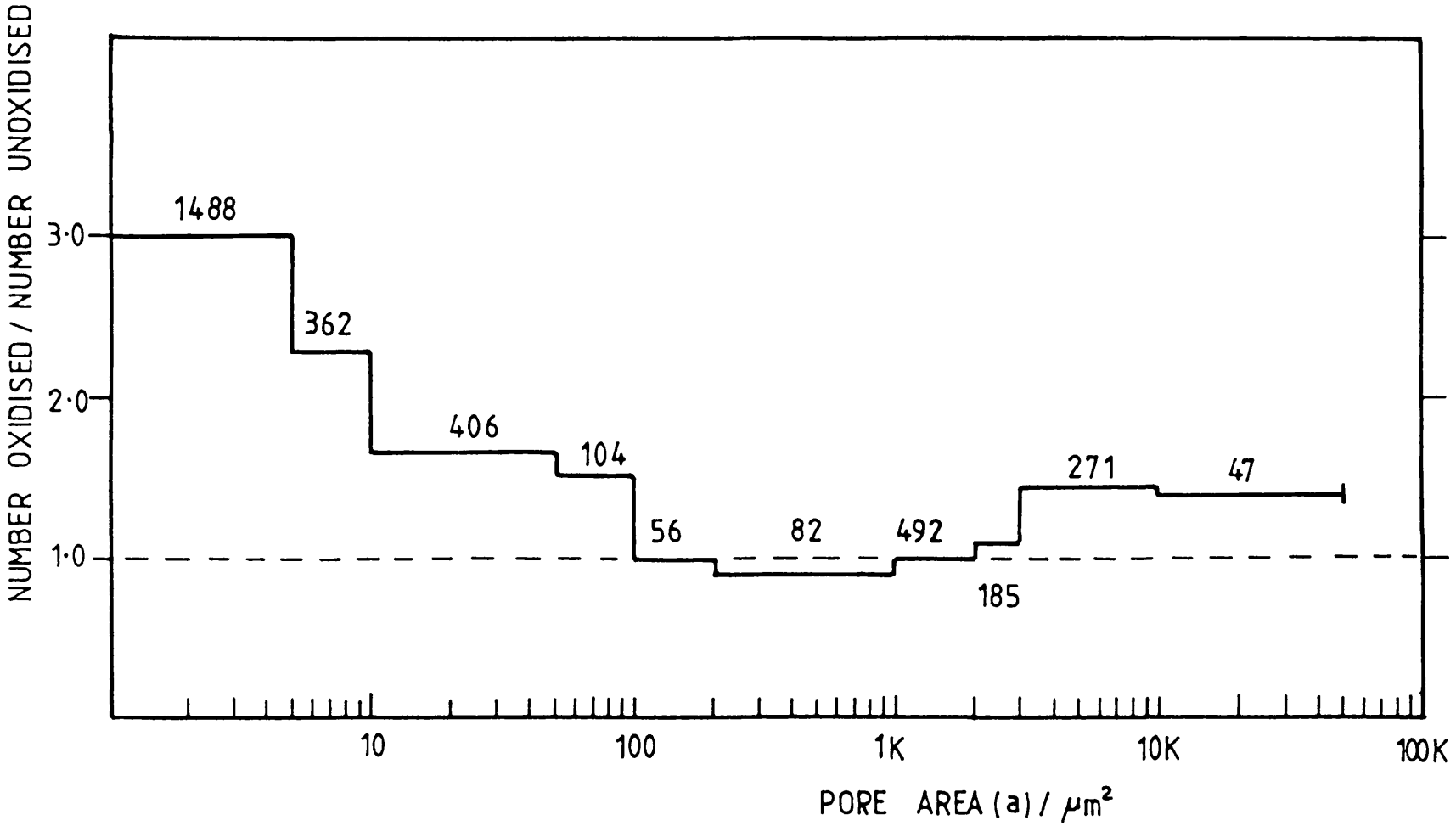

Fig. 4.46 Ratio of the number of pores in oxidised PGA-AGL to the number observed in unoxidised material. The figures over each pore area range refer to the number of pores in the oxidised material.

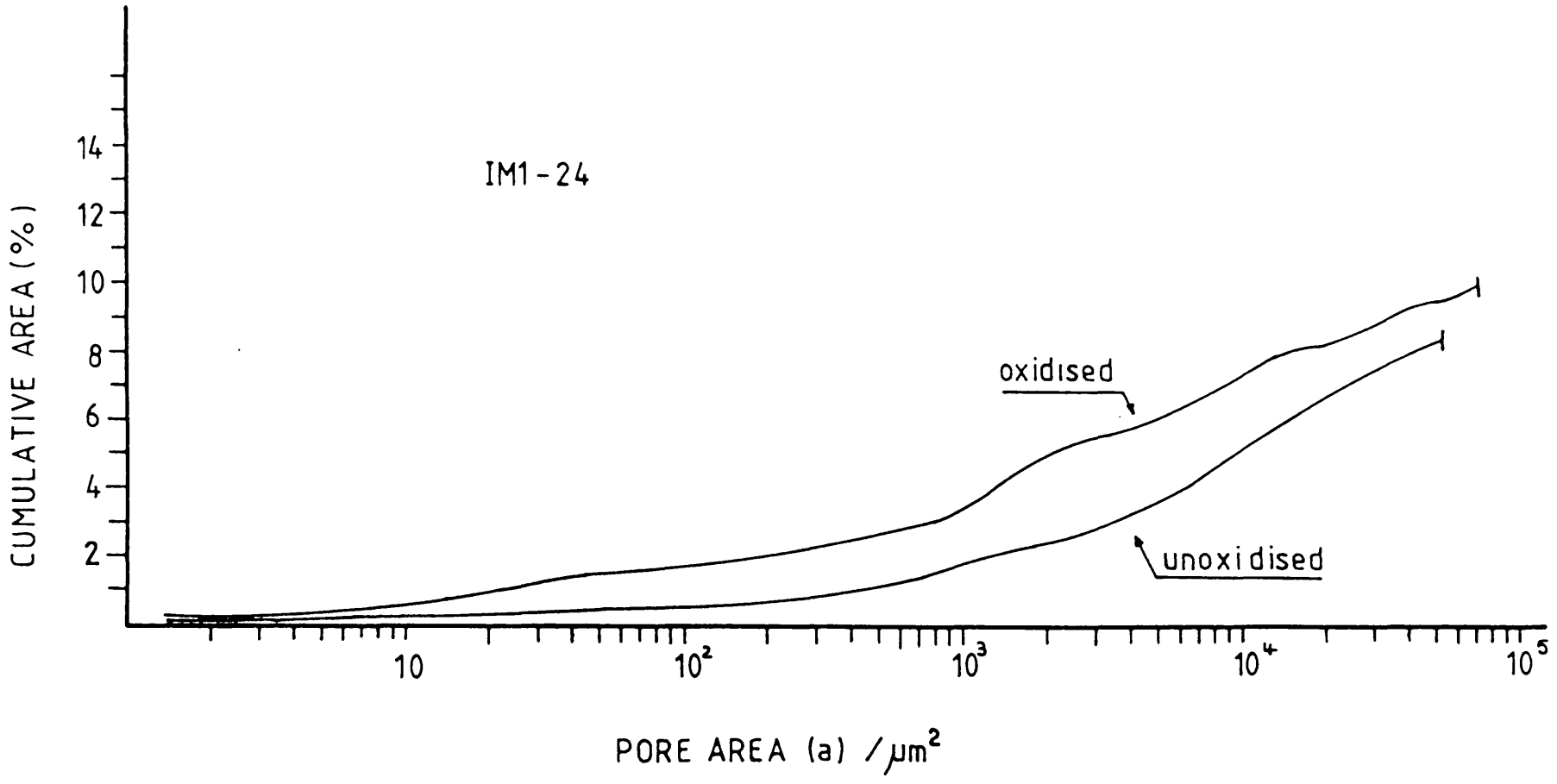

Fig. 4.47 Pore area distribution for unoxidised and oxidised (~6% weight loss) IM1-24 graphite.

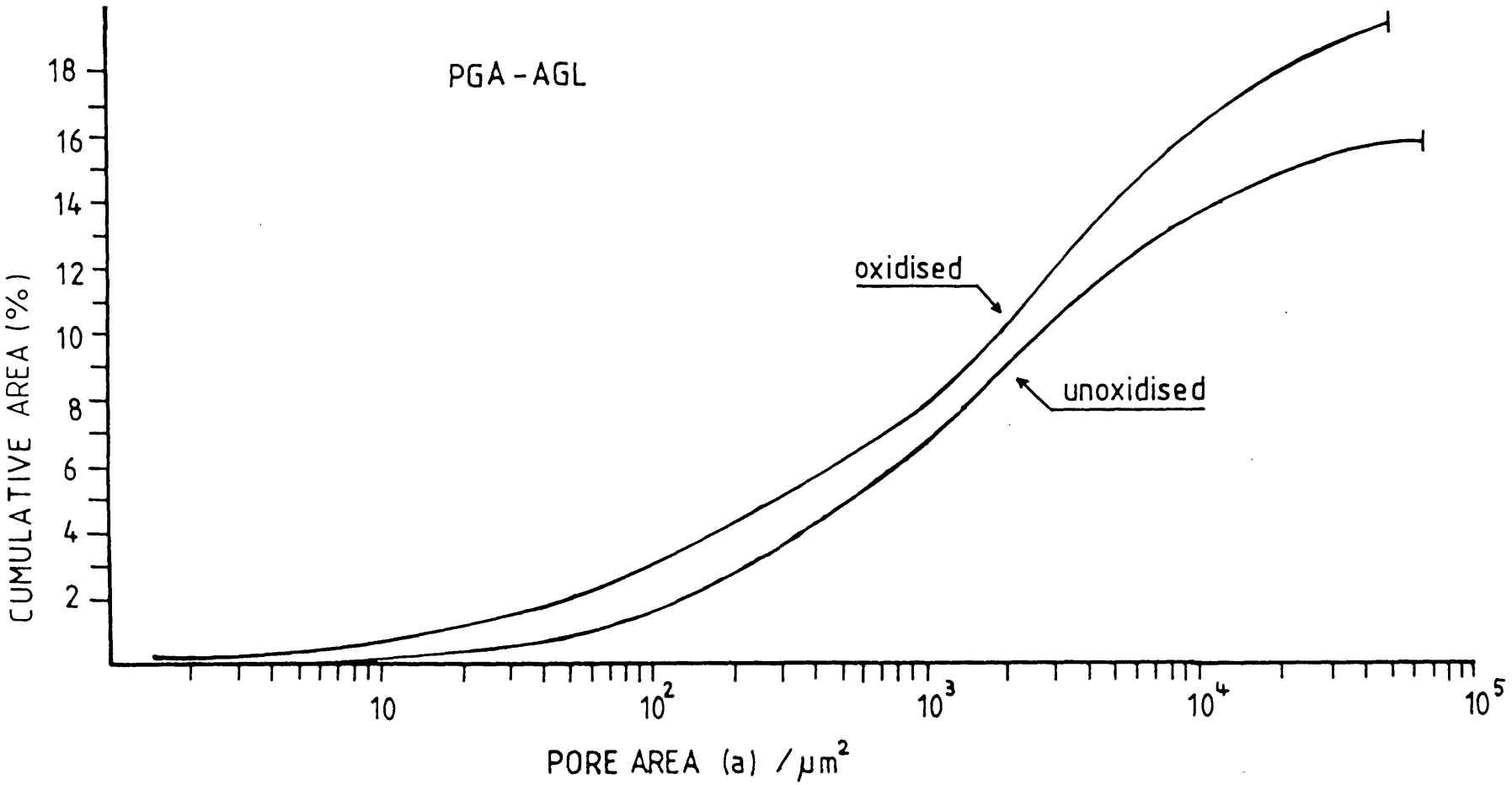

Fig. 4.48 Pore area distribution for unoxidised and oxidised (~ 6% weight loss) PGA-AGL graphite.

also shows preferential development of the smaller pores, i.e. those with an area less than 150 μm^2, which constitute 14.5% of the total open pore area in the unoxidised graphite and 20.5% in the oxidised material.

Image analysis provides 2-dimensional data which must be used with caution in relation to changes in 3-dimensional pore structure. However, it is interesting to note that the total open pore area calculated using equation 4.4 for unoxidised IM1-24 and PGA-AGL, (8.5% and 15.7 respectively) is roughly comparable with the open pore volume percent determined by pyknometry (ca. 8.8% and 18 2% for IM1-24 and PGA-AGL respectively, see Table 3.1).

The pore area development is principally in pores with an area less than 150-200 μm^2. Therefore if cumulative pore area is equivalent to cumulative pore volume and the IA system is adequately measuring open pore area, then the majority of the weight difference should be accounted for by the difference in $\Sigma A\%$ between the unoxidised and oxidised graphite for pore areas less than 200 μm^2. A 6.6% weight loss will be produced by a change in pore volume fraction of 5%, however the difference in $\Sigma A\%$ at a = 200 μm^2 is approximately 1.3 and 1.6 for IM1-24 and PGA-AGL respectively. The discrepancy may be due in part to the differences in the inherent proportion of open to closed

porosity between the unoxidised specimen and the oxidised specimen, prior to oxidation. It is also likely that with the range of pore shapes that exist in both graphites, that some 2-dimensional shapes will better represent a 3-dimensional image than others. It is felt that image analysis of the complex porous system that exists in PGA-AGL and IM1-24 is useful as a comparative technique but great care should be taken when relating ΣA% to absolute values of pore volume percentage.

CHAPTER 5

DISCUSSION

5.1 Failure Mechanisms

5.1.1 The analytical fracture model

In chapter two, observations of fracture mechanisms for a variety of graphites have been reported. The importance of basal planes which control the crack path has been highlighted as well as porosity which tends to link failed grains. The observations of previous workers have been verified in this present work. For example the role of regions of contiguous areas of common basal plane orientation like those observed in the graphite grains of PGA-AGL, SM2-24 and IM1-24, is quite apparent; where these regions are aligned normally to the tensile axis they tend to cleave, however if they are not favourably aligned they deflect or arrest the crack. Where basal planes extend the full length of the filler grain (as is the case in PGA-AGL) it is quite common that the entire grain may fail due to cleavage, leaving a planar fracture surface (Fig.4.38). IM1-24 does not have these large areas of contiguous basal planes, yet the outer surfaces of the gilso carbon filler grain appear to be cleaved; the fracture path following the macroscopic orientation of basal planes which run

circumferentially around the filler grain , Fig.4.31C.

Studies of sequential separation of fracture surfaces and fractography provide useful information on the microstructural features which control fracture mechanisms. However as an aid to understanding the relative importance of the contribution of individual microstructural features, it is helpful to model the sub-critical failure mechanisms. Buch (53) produced an analytical fracture model for fine grained aerospace graphites of the type used for nose tips in re-entry missile systems. The model is based upon a fracture mechanics failure criterion where the development of sub-critical micro-fracture with increasing stress is modelled, and hence the stress at which a critically sized flaw is attained, may be predicted. The principal input parameters to the model are microstructural.

The model makes several assumptions:-

a) the microstructure consists of a simple block of grains and pores, Fig.5.1;
b) the grains have a plane of weakness which is associated with basal planes;
c) when the grains are stressed in tension they fail due to cleavage;
d) the stress distribution within the material is homogeneous.

If the angle between the normal to the plane of weakness (basal plane) and the direction of the applied tensile stress is Φ, there is a tensile component of stress perpendicular to the plane, σ_n, (i.e. in a direction which favours cleavage).

$$\sigma_n = \sigma_a \cos^2\Phi \qquad (5.1)$$

σ_a is the applied stress. The plane is assumed to have a characteristic strength, σ_c, therefore when σ_n exceeds σ_c, then the plane will cleave.
That is if

$$\sigma_c < \sigma_a \cos^2\Phi \qquad (5.2)$$

Therefore the probability that a random grain will be fractured at an applied stress, σ_a, is determined by

$$\Phi < \cos^{-1} [\sigma_c / \sigma_a]^{0.5} \qquad (5.3)$$

It can be shown that for randomly orientated grains the probability of cleavage, P_c, will be given by

$$P_c = 1-(\sigma_c/\sigma_a)^{0.5} \text{ when } \sigma_a > \sigma_c \qquad (5.4)$$

If the graphite is anisotropic, i.e. the number of basal planes varies according to the angular position within the graphite, as is the case in PGA-AGL, then the probability of individual grain cleavage is

$$P_c \text{ (anisotropic)} = \frac{\int_o^{\phi} \Omega(\phi)\sin\phi \, d\phi}{\int_o^{\pi} \Omega(\phi)\sin\phi \, d\phi} \qquad (5.5)$$

$\Omega(\Phi)$ is the crystallite orientation distribution which was determined by x-ray diffraction, (section 3.3.3). For PGA-AGL $\Omega(\Phi) \approx \sin^{3.5}\Phi$

A pore is modelled as an already-cleaved grain and therefore the probability that any site within the bulk of the idealised structure will behave in a crack-like manner will be equal to the probability, P_i, that a site is either a pore or if not, then a failed grain, i.e.

$$P_i = P + (1 - P)(P_c) \qquad (5.6)$$

where P is the pore volume fraction.

If in an array of n grains, there are N contiguous, cracked grains or pores, the probability that a random grain

and N-1 of its planar neighbours will be cleaved is given by P_i^N. Therefore the probability, P^* , of a given site being the centre of N cracked grains is given by

$$P^* = P_i^N/N \qquad (5.7)$$

In a collection of n grains, the probability of P_n, of an alignment of an array of N continguous cracked grain is

$$P_n = 1 - [1 - P_i^N/N]^n \qquad (5.8)$$

Fig.5.1 represents the idealised, model structure and indicates failed basal planes within grains and also pores. It can be seen that many grains have failed and at various angles to the applied stress, however there is a contiguous crack array extending over four grain sites, this is known as a microcrack array. The probability of attaining this is given by equation 5.8 where N = 4.

The process of sub-critical crack development by the formation of contiguous arrays may continue until an array reaches a size that will propagate catastrophically. If a uniform grain size, g, is assumed and a planar penny shaped crack, the number of grains, N_c, required to create a critical crack for a given applied stress may be calculated using a fracture mechanics approach.

$$N_c = \pi^3/g^2[K_{Ic}/2\sigma_a]^4 \qquad (5.9)$$

Therefore, for any value of applied stress the probability of attaining a critically sized, contiguous crack array may be calculated by substituting the value of N_c into equation 5.8. A computer programme (appendix 1) has been written based upon the model which calculates the probability of failure for incremental applied stress values.

The input parameters to the analytical model and the method of determination are as follows:-

i) stress intensity factor, K_{IC}, using the technique described in section 3.4.3;

ii) total fractional, porosity, from apparent density measurements, section 3.3.2;

iii) grain size; it is difficult to determine a unique grain size for a specific graphite for the reasons discussed in section 3.3.1. However for the purpose of the model, the grains size was taken arbitrarily (from Fig.3.4) as the size corresponding to a cumulative fraction of grains equal to 0.7. The relevant grain sizes are 0.5 mm and 0.95 mm for

IM1-24 and PGA-AGL respectively;

iv) number of grains in the stressed volume. The model was originally proposed for uniaxial tension, where all of the grains in the bulk of the graphite are subjected to the nominal tensile stress. However in this study the model has been used to predict the failure probability of a graphite body subjected to non-uniform stress, i.e. 3-point bending. In this situation the stressed volume is vastly reduced, and for the purpose of the model is arbitrarily considered to be equal to a segment of 45^{o} from the neutral axis to the exterior surface of cylinders of 15 mm diameter along the line of maximum deflection and extending along the neutral axis to a distance of ±1 grain, Fig.5.2.

The extent of the stressed volume along the neutral axis is arrived at by observation of fracture surfaces. From this volume, which is assumed to be under uniform tensile stress and the grain size, the number of grains under tension can be estimated; these are 350 and 50 for IM1-24 and PGA-AGL respectively. It will be shown later in this section that errors in estimating the number of grains due to the simplified model of stress distribution, are small as the failure model is relatively insensitive to the number of grains;

v) grain cleavage strength, σ_o. The stress at the onset of acoustic emission during three point loading was

taken to be the grain cleavage strength, i.e. where the stress on the most favourably aligned grains exceeds a critical resolved cleavage stress. Values of σ_o determined this way are comparable with those found by Meyer and Zimmer (26) by direct observation of graphite specimens stressed in an electron microscope. The AE method has the advantage of monitoring the internal and external material, whereas the direct observation technique is limited to the visible surface. Acoustic emission is discussed in more detail in section 5.2;

vi) anisotropy factor was determined using the technique described in section 3.3.3.

The cumulative failure probability data from the three-point bend tests of IM1-24 and PGA-AGL are presented together with the theoretical cumulative failure probability from the analytical model in Fig.5.3. In order to illustrate the effects of inevitable variations in materials' properties, the dashed lines in Fig.5.3 show the range of failure probabilities, calculated by varying the input parameters by up to two standard deviation about the mean and with the parameters randomly combined using the computer programme. The same number of curves were generated as the number of data points, the dashed lines represents the extremes of the predictions. There is generally a reasonable agreement between the data and the model. The agreement is better for the isotropic IM1-24 than the coarser PGA-AGL. At failure probabilities less than 0.2, the experimental

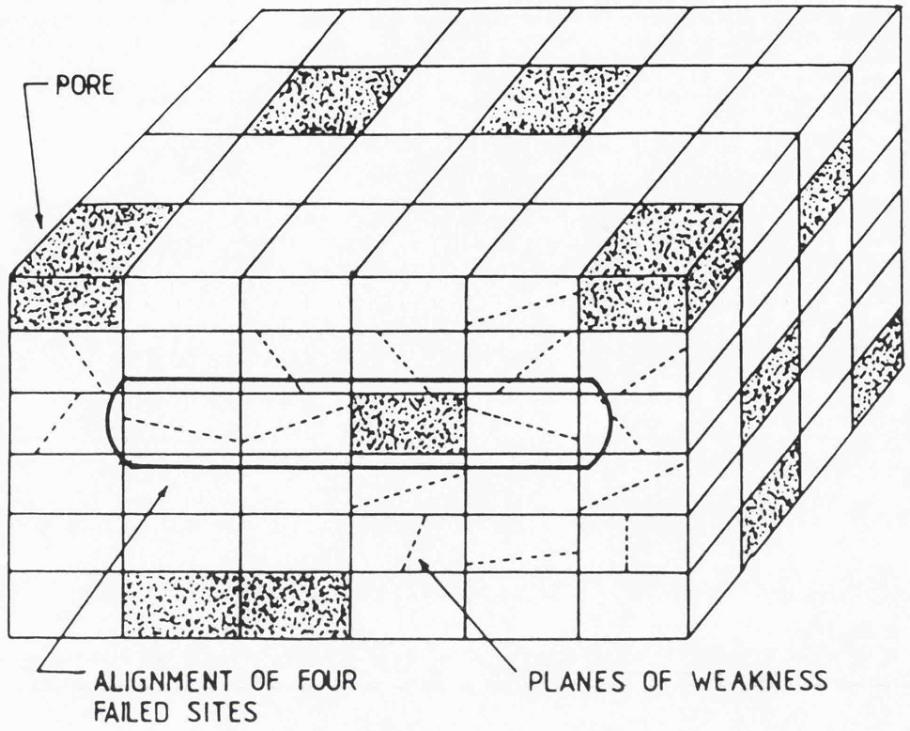

Fig.5.1 The idealised graphite microstructure from the fracture model.

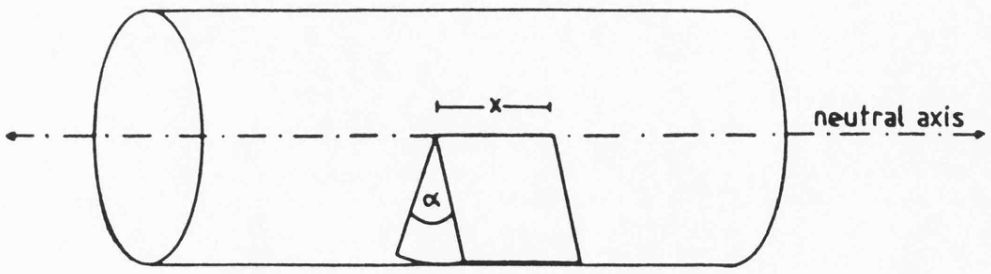

Fig.5.2 The arbitrary stressed volume used in the analytical model. X is twice the grain size and $\alpha = 45^{\circ}$.

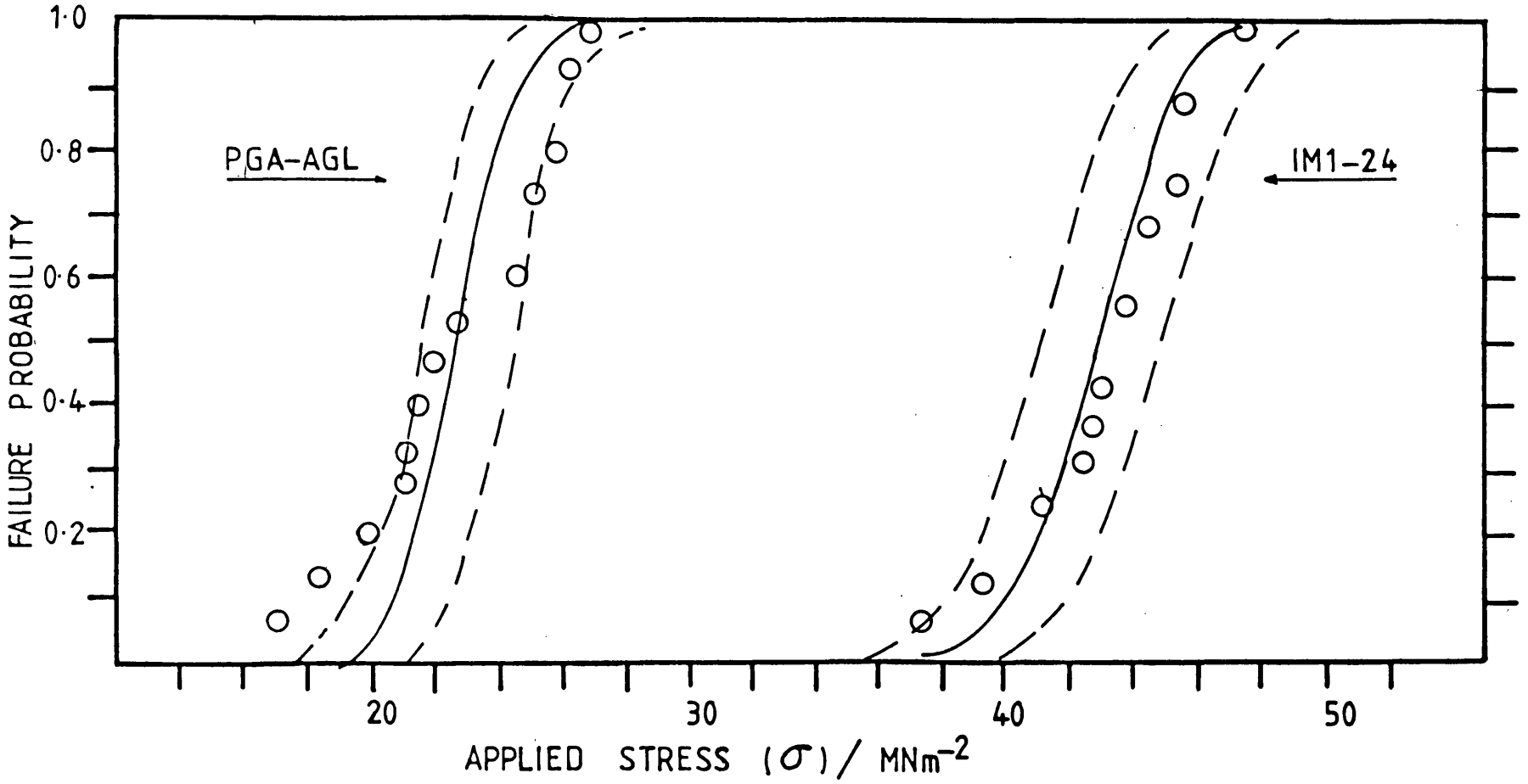

Fig. 5.3 Failure probability versus applied load for unoxidised IM1-24 and PGA-AGL; solid lines are calculated from the model; dashed lines, effect of variation of ± 2 standard deviations about the mean to the input parameters; circles, experimental data.

failure probabilities are higher than predicted by the model. This underestimation is probably due to macroscopic features in the fracture surface which are not accounted for in the model, e.g. an inhomogeneous distribution of pores, as is shown in Fig.5.4. The model has been used in this investigation to indicate the relative effects of the independent parameters which combine to control the strength of graphite and hence indicate which parametes will dominate the srength changes upon oxidation. To do this, the 50% failure probability stress, P_f (0.5) of PGA-AGL has been selected as a datum point and the effect of independent parameter variation upon this stress have been plotted, Fig.5.5. It can be seen from Fig.5.5 that variation of each of the six input parameters has different effects upon $P_f(0.5)$.

Stress intensity factor has the most marked effect, followed by grain size, pore volume fraction and grain cleavage strength. Variation of anisotropy factor and the number of grains in the stressed volume have the least effect upon $P_f(0.5)$. Of the six input parameters only three are likely to vary as a result of the thermal oxidation: stress intensity factor, pore volume fraction and grain cleavage stress. It has been shown in section 4.3 that the onset stress does not vary significantly due to oxidation, thus only K_c and P vary. For a 7% weight loss P varies by ca. 30% which will have a very small effect on the $P_f(0.5)$ according to the analytical model. However

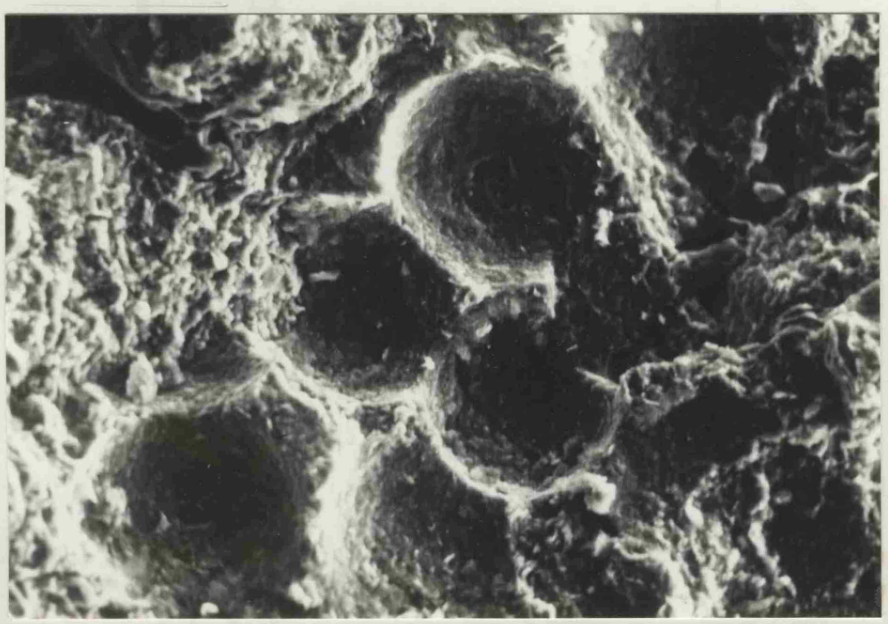

Fig. 5.4 A cluster of gas bubbles in the fracture surface of IM1-24

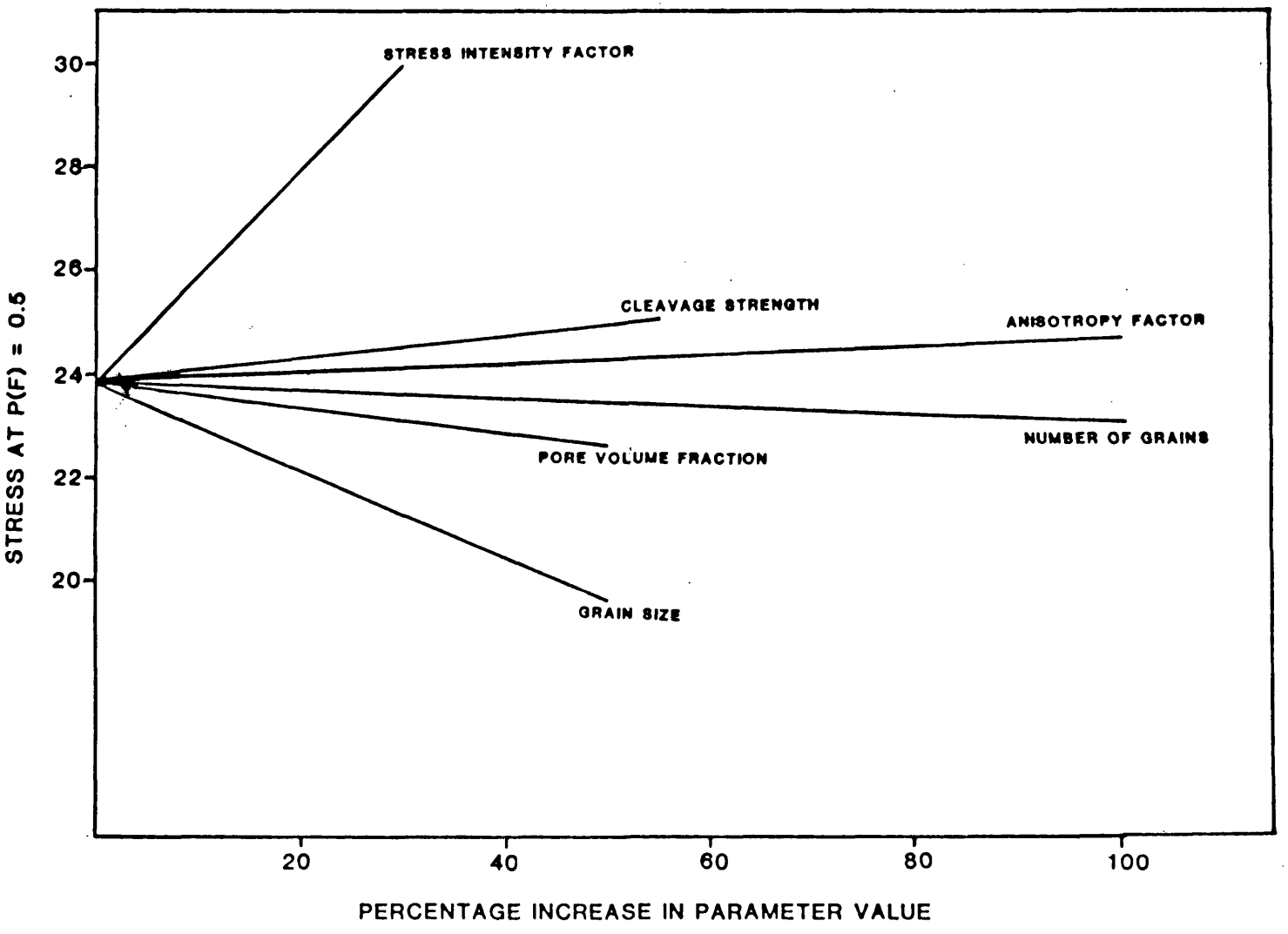

Fig. 5.5 The effect of independent parameter variation to the fracture model upon the 50% failure probability.

for a similar weight loss, K_c changes by ca 50%, which, if varied independently, would change $P_f(0.5)$ by ca 40%. Hence the model indicates the dominance of K_c in controlling the strength changes which occur as a result of oxidation.

The effect of inaccurately estimating the number of grains in the stressed volume is not particularly serious as a 100% variation in the number may affect $P_f(0.5)$ by as little as 4%. The model is sensitive to grain size and this is probably one of the greatest sources of inaccuracy because most graphites do not have a unique grainsize.

The model indicates the dominance of K_c in controlling the strength changes which occur during thermal oxidation and, since K_c varies as a function of E and γ, it also highlights the importance of these two properties. These considerations are developed in section 5.2.2.

5.1.2 The influence of microstructure upon acoustic emission

5.1.2(a) The onset of acoustic emission

In section 4.3 the onset stress, σ_o, at which

AE was first detected, was correlated with the microscopic texture of the graphites and it was proposed that σ_o is a chracteristic property. It was found that the onset stress bears an inverse relationship to the isochromatic domain sizes; with PGA-AGL, which may have domains greater than 1.5 mm, having the lowest σ_o at ca 3.5 MNm^{-2}, whereas IM1-24 with domains of not more than 200 µm has the highest σ_o at ca 11.MNm^{-2}.

At least three factors may be proposed to explain the inverse correlation between σ_o and grain size:-

i) A grain, or rather domain will fail when a combination of applied stress and residual stress exceeds its failure stress. Larger grains are subject to greater residual strain energy, for example as a result of anistropic thermal contraction on cooling from graphitisation temperatures. There is some relief of residual stresses by formation of Mrozowski cracks (13) but there will always be some residual stress which may be any value up to the inherent grain strength. Thus if two graphites with different grain sizes have the same inherent cleavage strength, the larger grain material would require less applied stress to failure, giving an apparently lower cleavage strength. This may be the case when comparing σ_o values for PGA-AGL and IM1-24.

ii) Graphites formed from different parent carbons or pitches may have distinctly different microstructures (section 2.1.2) and also the degree of graphtisation may vary considerably. A highly graphitised carbon with well formed planar arrays will have a lower interlamellar shear strength than a less well graphitised material. PGA-AGL forms more extensive domains of common basal plane orientation than either IM1-24 or SM2-24. It is possible that these large domains are more highly graphitised and consequently have a lower cleavage strength (83).

iii) Grains which have been ground more severely to produce a smaller grain size will have cleaved on weaker planes during grinding resulting in an increased average cleavage strength.

It is difficult to isolate any of the above factors and attribute the relationship between σ_o and grain size to it alone. It is more probable that all the factors contribute to some degree and there may be others which have not been proposed.

5.1.2(b) Acoustic event counts, Σ(AE)

It was shown in Fig.4.19 that the rate of accumulation of AE events and the total number at fracture are highest

for the coarse textured PGA-AGL and lowest for the fine textured IM1-24.

The large isochromatic domains in PGA-AGL contain sizeable linear cracks which may extend for hundreds of microns Fig.4.33b. Under applied load these will act as sites for stress concentration which initiate microcracking and hence AE at low applied loads. In contrast, cracks in domains of IM1-24 are smaller and more tortuous than those found in PGA-AGL, and consequently require a higher applied load to initiate cracking. Therefore for a given applied load there will be more microcracking and AE in PGA-AGL than in IM1-24. Furthermore the volume fraction of domain structure in PGA-AGL (≈ 90%) is much larger than that in IM1-24 (≈ 20%) and consequently the number of stress concentration sites in the former is larger. SM2-24 has an intermediate volume fraction of domain structure and also an intermediate rate of accumulation of AE and counts to failure. A similar correlation between AE and microscopic texture of ceramics has been noted (84).

The total cumulative AE at failure increases with oxidation, Fig.4.20, in both PGA-AGL and IM1-24. It has been shown in section 4.4.3 that oxidation develops filamentary pores in the binder of the graphites into a more elongated structure. The effect of increasing the length of a flaw in a stressed body

is to intensify the localised stress to a greater extent. Therefore pores which are subjected to a given stress prior to oxidation may not locally intensify the stress sufficiently to fracture the surrounding graphite. However, when oxidised and subjected to the same stress the pores may have grown to a sufficient size to cause local failure and hence increment ΣAE. There will also be an effect upon the adjacent grains; as the modulus of the binder is reduced due to oxidation, there will be an intensification of stress in adjacent grains. (This is discussed more thoroughly in sections 5.2.3 and 5.3). Also as the average modulus of the specimen is reduced due to oxidation, there will be an increased volume of material subjected to stresses which can induce AE. In Fig.4.20 ΣAE at failure for PGA-AGL reaches a maximum at ~3% weight loss and then decreases on further oxidation. To explain this phenomenon, the following mechanism is postulated. As oxidation increases, the probability of failure in less favourable orientated basal planes also increases for the reason outlined above. However, as oxidation proceeds further, the failure strength is reduced to a level where a critical flaw size is produced before the cleavage strength is attained on the less favourably orientated grains, causing a reduction in AE. There is no maximum in the ΣAE versus weight loss curve for IM1-24. It is possible that a maximum in ΣAE may be observed for IM1-24 at greater degrees of oxidation than were used in this work. These proposals are tentative and further work is required to elucidate the effect of oxidation on ΣAE of different graphite types.

5.1.2(c) Acoustic emission amplitude distribution

Sub-critical cracking within the aggregate structure is characterisied by basal plane cleavage, both in well-orientated needle coke particles and in the more complex structures found in binder phases and in filler particles such as gilsocarbon. At any stress above σ_o there will be a pattern of microcracks generated which is characteristic of the graphite structure. At low stresses the volume elements of the structure containing the cracks will be those with basal planes orientated favourably to the tensile axis, i.e. ~ 90^o. The energy dissipated by cracking and the amplitude of the associated AE will be small, although their distribution, (i.e. b value) will be characteristic of the microstructure Fig.4.22. That is, a variety of different features will have failed in the microstructure, each giving rise to its individual amplitude associated with fracture. At higher stresses further cracks will form in volume elements of the microstructure containing basal planes less-favourably orientated to the applied stress. The energy dissipated and amplitudes of the associated AE will be higher, but, because it is the same range of features that are failing, the amplitude distributions, denoted by b, remain characteristic of the microstructure. Oxidation of the graphites does not significantly alter the b value, (Table 4.3) suggesting that failure mechanisms remain unchanged as a result of oxidation.

5.2 The effect of oxidation upon mechanical properties

5.2.1 The relationship between strength and weight loss

It has been demonstrated in section 4 that a severe strength loss in graphite results from small amounts of weight loss, due to thermal oxidation. It was the objective of this work, not only to quantify these reductions, but also to identify the physical features in the microstructure which control the strength and to observe how those features are affected by thermal oxidation. The analytical fracture model has been used with a fair degree of success to predict the unoxidised graphite strength from a microstructural and fracture mechanics approach (section 5.1.1). It has also been used to predict the variation of bend strength with weight loss, Fig.5.6. Of the six input parameters to the model, only two are likely to vary as a result of oxidation; these are, pore volume fraction and stress intensity factor. Using appropriate values of the above parameters, for a specific weight loss, determined from the functions produced by regression analysis (Table 4.2), the 50% probability failure stress has been calculated and shown to vary as a function of weight loss. In Figure 5.6, the 50% failure probability stress, computed in this way, has been plotted over the experimental data of bend strength versus weight loss for PGA-AGL and IM1-24. The theoretical line reasonably represents the data. However, for both graphites, the

predicted line from the analytical model and the regression analysis line diverge as weight loss increases. For each graphite the divergence takes the same form, with the prediction overestimating the strength for a given weight loss. However, even at 6% weight loss, the regression line does not fall outside the failure probability range, (indicated by the bar on each line). The probability range is calculated by varying the input parameters to the model by ± two standard deviations about the mean. Only K and P were varied in the model, and the effect of variation of K upon failure probability is far greater than variation of P. Therefore the reasonable fit of the model supports the proposition that strength reduction in graphite is dominated by the reduction of K_c, at least for small levels of weight loss. Whilst the fit of the model is reasonable for both graphites, even though they have distinctly different microstructures, there is a systematic deviation of the theoretical line from the best fit to the data. Possible reason for this are as follows .

a) The modelled microstructure of an homogeneous distribution of grains and pores is not matched by the real microstructure, which contains a non-uniform distribution of grains and pores and may also contain other extraneous features which are not accounted for in the model.

b) The model assumes that the only sub-critical failure

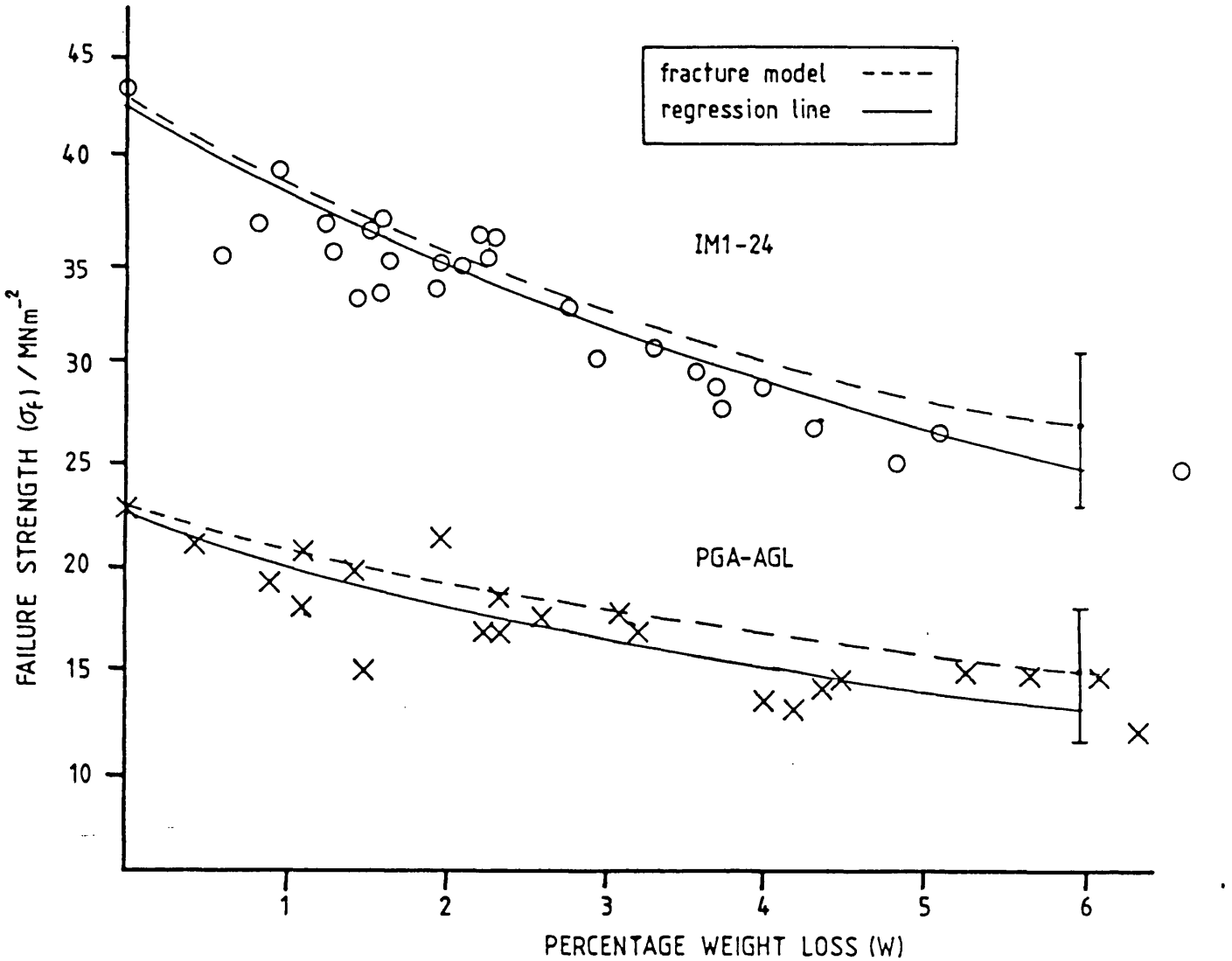

Fig. 5.6 A comparison of the experimental failure strength variation with weight loss and the theoretical variation predicted by Buch's Model. The bars on the theoretical curves represent a range of ± 2 standard deviations to the input parameters.

event is grain cleavage, which links with pores to produce the critical flaw. This obviously is not true, as binder material will inevitably fracture in linking failed grains. It is possible the amount of binder failure increases with increasing weight loss and this may produce a deviation from the strength predicted by the model. Board and Squires (60) reported an increasing proportion of binder failure during strength testing, in PGA for weight loss greater than 5%. In this work, fractography before and after thermal oxidation of weight losses up to 6%, has not revealed a variation in the proportion of binder failure. It is difficult to quantify the proportion of binder failure, (except where there has been a radical change in failure mechanism) and impossible to distinguish sub-critical and fast fracture failure features in the fractographic surface. It is therefore impossible to say that there is not a slight change in fracture mechanism during the first few percent weight loss due to thermal oxidation.

5.2.1 The critical defect size

It is possible to calculate the size of defect which will cause catastrophic failure, using fracture mechanics. This has been done for PGA-AGL and IM1-24 using the unnotched bend strength data and stress intensity data (Section 3.4.1 and 3.4.3) and substituting them into equation 2.16, i.e.

$$a' = \frac{1}{\pi}(K_{Ic}/\sigma_f)^2 \qquad (2.16)$$

The values of critical flaw size for both graphites in the unoxidised condition and also various weight loss values (upto 6%) are presented in Table 5.1. Appropriate values of σ_f and K_c at the various weight losses were taken from the regression analysis line fit to the data (Table 4.2). In the unoxidised condition PGA-AGL and IM1-24 have a critical defect size, a' , of 0.44 mm and 0.30 mm respectively. It is notable that the coarser textured PGA-AG1 has a value of a' which is ca. 50% greater than IM1-24.

The critical defect parameters, a', is sometimes referred to as the inherent flaw size, the implication being that it is an intrinsic feature of the microstructure which is present in the unoxidised material. Previous workers have correlated a' with the linear dimension of inhomogeneities within the microstructure, e.g. a pore (66), grain (24) or the sum of the maximum pore and grain size (67). It may be a misleading concept to make a comparison of the one-dimensional critical defect parameter, a', with the microstructure for the following reasons. Fracture mechanics relates K_c, σ_f and a', however, the relationship used to calculate a', i.e. equation 2.16 takes no account of the shape of the flaw. K_c is not only a function of flaw size, but also of the shape, and thus equation 2.16 is modified to

TABLE 5.1 σ_f, K_c AND a' VARIATION WITH WEIGHT LOSS

PERCENTAGE WEIGHT LOSS		0	1	2	3	4	5	6
IM1-24	σ_f/MNm^{-2}	43.56	38.01	34.33	31.00	27.99	25.88	22.83
	K_c/MNm$^{-3/2}$	1.34	1.21	1.11	1.01	0.93	0.85	0.78
	a'/mm	0.30	0.32	0.33	0.34	0.35	0.36	0.37
PGA-AGL	σ_f/MNm^{-2}	22.79	19.85	18.00	16.32	14.79	13.42	12.16
	K_c/MNm$^{-3/2}$	0.85	0.76	0.69	0.64	0.58	0.53	0.48
	a'/mm	0.44	0.47	0.47	0.49	0.49	0.50	0.50

$$(a/Q) = K_{Ic}^2/1.21\sigma_f^2\pi \quad \text{(surface flaws)},$$
$$(a/Q) = K_{Ic}^2/\sigma_f^2\pi \quad \text{(internal flaw)} \qquad (5.10)$$

where Q is a flaw shape parameter which was derived by Irwin (69, 70) and is given by the following expression

$$Q = [\Phi^2 - 0.212\ (\sigma/\sigma_{ys})^2] \qquad (5.11)$$

where Φ is a complete elliptical integral of the second kind and σ_{ys} is the 0.2% proof stress. The relationship between Q and the aspect ratio of the flaw is shown in Fig.5.7.

In any flaw size analysis it is necessary to know two of the following three quantities :

1) K_c

2) σ_f

3) Flaw shape and size.

Flaw shape and size are the unknown quantities in this case, so it is necessary to assume a likely aspect ratio and therefore at least a 2-dimensional comparison between critical flaw and microstructure is required.

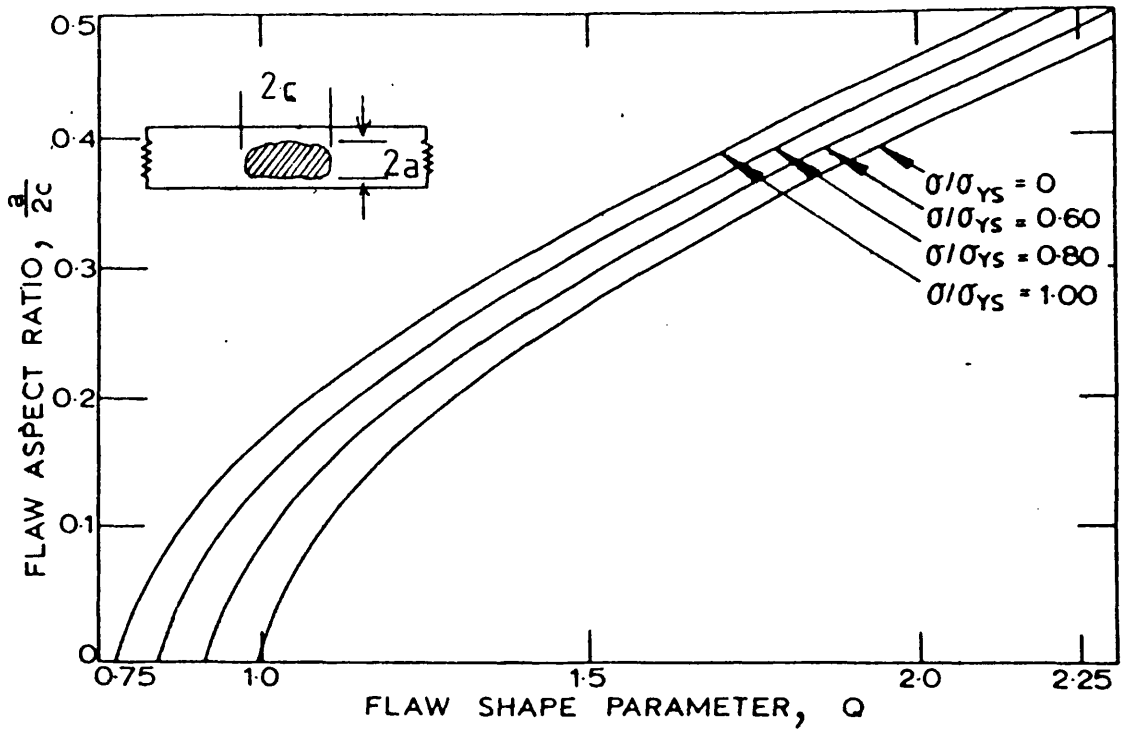

Fig. 5.7 The relationship between flaw shape parameter, Q, and flaw aspect ratio, $^{a}/2c$ (from ref. 34).

The critical flaw area has been compared with the microstructure of IM1-24 (Fig.5.8) and PGA-AGL (Fig.5.9). The critical flaw area has been calculated for two flaw shapes. Firstly, when Q = 1 and therefore a' = a. This corresponds to the situation when the shape factor is neglected, but as can be seen from Fig.5.7 at σ/σ_{ys} = 1 the aspect ratio, for an internal flaw, of a/2c = 0.19. Using the calculated value of a' and the aspect ratio of the pore, a 2-dimension scale representation of the critical flaw area has been drawn alongside the micrograph. A second flaw considered is a penny shaped crack where a/2c = 0.5 and Q = 2.0.

In Figs 5.8 and 5.9 it can be seen that the critical flaw area for either aspect ratio is considerably larger than the largest individual microstructural feature. This means that for catastrophic failure to occur there needs to be an accumulation of sub-critical failure events which link to form a contiguous crack array of sufficient size to be critical. Also in Figs. 5.8 and 5.9 the linear dimension of 2a' is included; this is the dimension which is often compared to the microstructure to identify an "inherent" critical flaw. It is apparent for both types of graphite that if the flaw shape, and hence flaw area is not considered, the linear dimension, 2a', is comparable with the maximum dimension of a grain or a grain and a pore

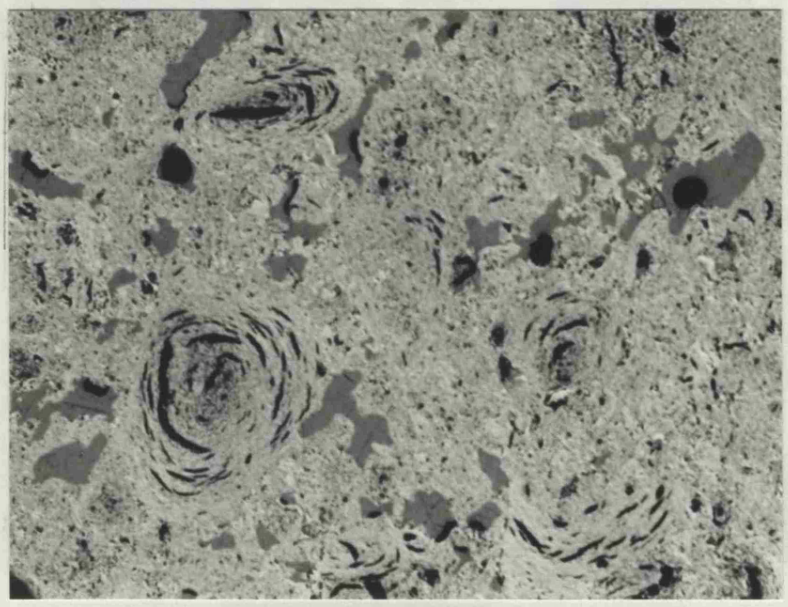

500 μm

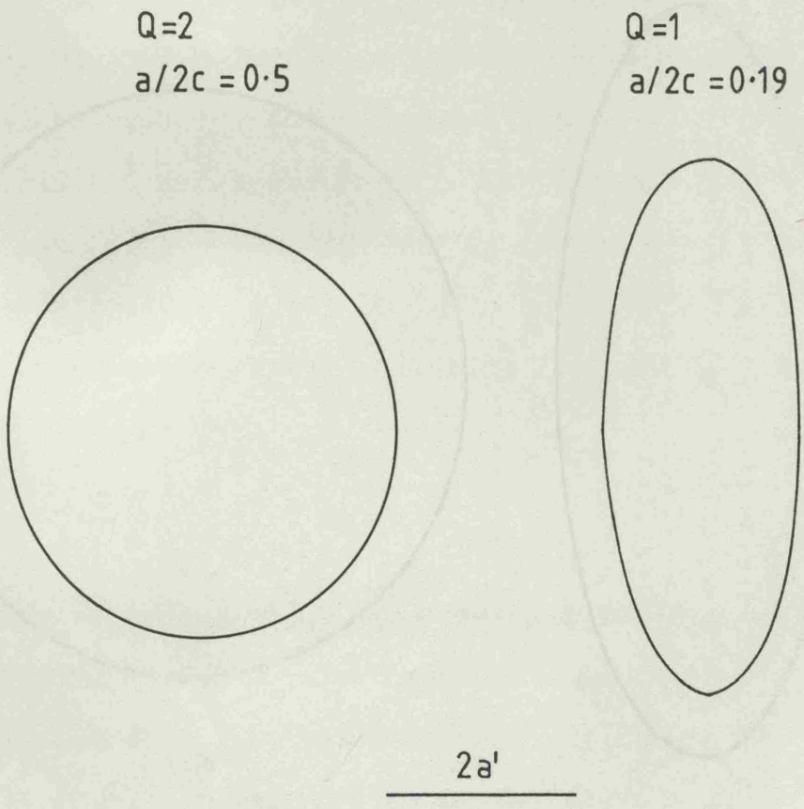

Fig. 5.8 The microstructure and scale representation of the critical flaw area for unoxidised IM1-24.

500μm

Q =2
a/2c = 0·5

Q=1
a/2c = 0·19

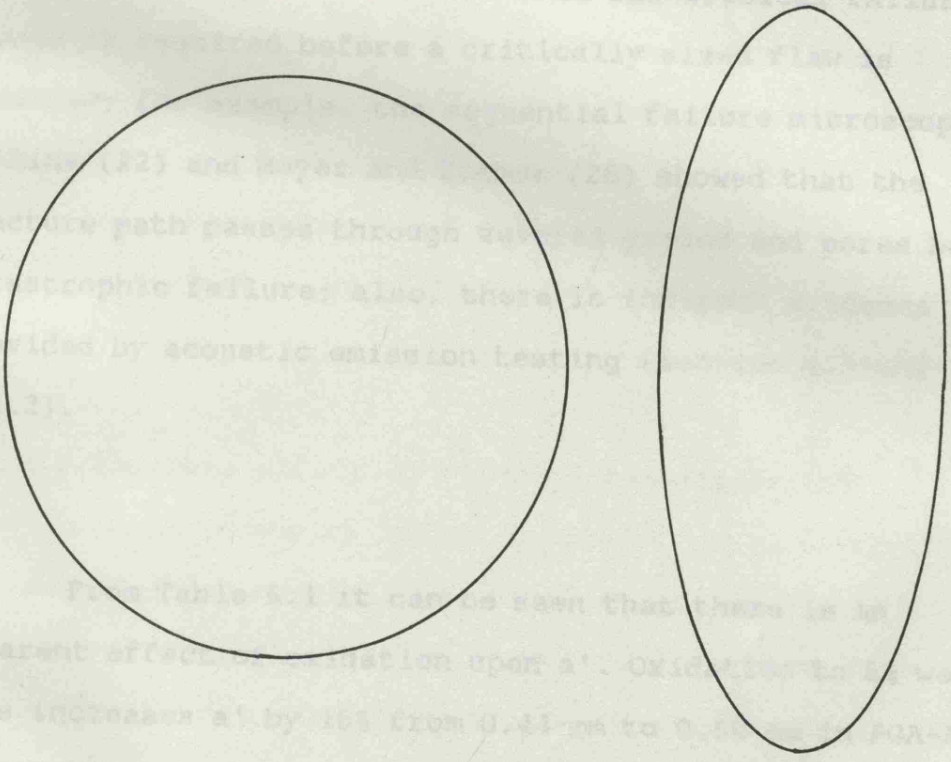

2a'

Fig. 5.9 The microstructure and scale representation of the critical flaw area for unoxidised PGA-AGL.

Darby (41) points out that critical flaw sizes calculated from strength and stress intensity factor data vary according to the severity of the stress gradient in the strength test specimens; increasing stress gradient reduces the calculated critical flaw area. Experimental work by Brocklehurst (21) showed that critical flaw size calculated from bend tests may be a factor of 2 lower than data from tension tests. Thus, flaw areas in Figs.5.8 and 5.9, calculated from three point bend test data will produce minimum estimates of flaw area.

There is a good deal of evidence to support the proposition that an accumulation of sub-critical failure events is required before a critically sized flaw is attained; for example, the sequential failure microscopy of Jenkins (22) and Meyer and Zimmer (26) showed that the fracture path passes through several grains and pores before catastrophic failure; also, there is indirect evidence provided by acoustic emission testing (section 4.3 and 5.1.2).

From Table 5.1 it can be seen that there is an apparent effect of oxidation upon a'. Oxidation to 6% weight loss increases a' by 16% from 0.44 mm to 0.50 mm in PGA-AGL and by 23% from 0.30 mm to 0.37 mm in IM2-24. However, when

Pagination error; the text on p.191 follows on from p.187.

the experimental uncertainty of Kc and σ_f determination is taken into account the value of a', for both graphites at 6% weight loss is within a single standard deviation of the mean unoxidised value. A t-distribution analysis (72) shows that for there to be a significant difference at the 5% level. The value of a' for IM1-24 needs to be equal to or greater than 0.37 mm (cf. 0.37 mm at 6% weight loss), and for PGA-AGL needs to be equal to or greater than 0.62 mm (cf. 0.50 mm at 6% weight loss). Thus it appears that for IM1-24, the apparent increase in a' as a result of 6% weight loss is bordering on being significantly greater than the unoxidised value. However, before drawing conclusions, it should be borne in mind that whilst the 5% significance level is often used as a criterion for accepting or rejecting a hypothesis that two mean values are significantly different, it is still rather inconclusive, usually the 1% significance level is preferred. The increase of a' in PGA-AGL as a result of oxidation is well within the experimental uncertainty of the unoxidised value and may not be significant.

5.2.2 Parameters affecting stress intensity factor

Stress intensity factor is one of the principal parameters which control the strength and changes in strength of graphites. It is therefore important to examine independently the parameters which control stress intensity factor, i.e. elastic modulus and the effective surface energy. Values of both these parameters have been determined

Pagination error; the text on p.191 follows on from p.187.

for PGA-AGL and IM1-24 for oxidised and unoxidised material (section 4.2.2. and 4.2.4).

By combining equations 2.10 and 2.14, Kc is related to E and γ by

$$K_c = (E^*2\gamma)^{0.5} \qquad 5.12$$

where E^* is E for plane stress and $E/(1-\nu^2)$ for plane strain. When modulus and surface energy data from the unoxidised graphites are substituted into the equation, the resultant calculated K_c is appreciably greater than the experimentally determined stress intensity factor. For IM1-24, K_c (calculated = 1.57 $MNm^{-3/2}$ compared with the experimental value of 1.34 $MNm^{-3/2}$, which represents a 17% overestimate. The situation is worse for PGA-AGL where the calculated value is ~ 46% greater than the experimentally determined value, i.e. 1.24 $MNm^{-3/2}$ (calculated) compared with the experimental value of 0.85 $MNm^{-3/2}$. Experimental and calculated values of K_c have been plotted against weight loss for IM1-24 and PGA-AGL in Figures 5.10a and b respectively. The independently determined E and γ data which were used to calculate K_c are presented in Table 5.2.

The relationship between K_c (calc.) and weight loss closely resembles that of K_c(exp) although the

TABLE 5.2 A COMPARISON OF K_c (CALCULATED) WITH K_c (EXPERIMENTAL) AT VARIOUS WEIGHT LOSS VALUES, USING E AND γ DATA FROM REGRESSION ANALYSIS (TABLE 4.2).

	PERCENTAGE WEIGHT LOSS	0	1	2	3	4	5	6
IM1-24	E/GNm^{-2}	12.4	11.21	10.31	9.48	8.72	8.02	7.37
	γ/Jm^{-2}	99.47	91.17	83.88	76.65	69.42	62.19	54.96
	K calc/$MNm^{-3/2}$	1.57	1.41	1.31	1.21	1.10	0.99	0.90
	K exp/$MNm^{-3/2}$	1.34	1.21	1.11	1.01	0.93	0.85	0.78
PGA-AGL	E/GNm^{-2}	12.1	11.29	10.54	9.84	9.18	8.57	7.99
	γ/Jm^{-2}	63.46	58.07	54.40	50.73	47.06	43.39	39.72
	K calc/$MNm^{-3/2}$	1.24	1.18	1.07	0.99	0.93	0.87	0.79
	K exp/$MNm^{-3/2}$	0.84	0.76	0.69	0.64	0.58	0.53	0.48

curve is displaced upwards. Thus whilst the relationship $K_c \propto Y \sqrt{EG}$ appears to be true the value of the proportionalty constants differ from 2, i.e. the value given in equation 5.12. By calculating the value of Y required to equalise K_c (calc.) and K_c (exp) for the unoxidised graphites and using this value to calculate K_c(calc) at various levels of oxidation, it is possible to see just how closely the relationship between K_c(calc) with weight loss follows K_c(exp), Fig.5.10a and b. For IM1-24 using Y = 1.20 the experimental and calculated curves lay on the same line, suggesting that K_c reduction, as a result of weight loss, is entirely accounted for by the reduction in E and γ. Using the same procedure for PGA-AGL with Y = 0.97, there is also a close relationship between the experimental and calculated curves. Whilst not as close as the relationship for IM1-24 there is not a significant difference when the experimental uncertainty is considered. It is notable that the proportionality constants for the two graphites are different. This poses the following questions; why does the proportionality constant not equal 2 and why does it vary with microstructure? Firstly, the possibility that there is a fixed error in the measurement of either γ or E has been considered. If the difference between the experimental and calculated proportionality constant for the unoxidised material was due to modulus, it would require a 27% error in estimation of IM1-24 modulus and 53% error in PGA-AGL. The most sensitive factor in modulus determination is the fundamental frequency measurement, since $E=A_c m f^2/d$.

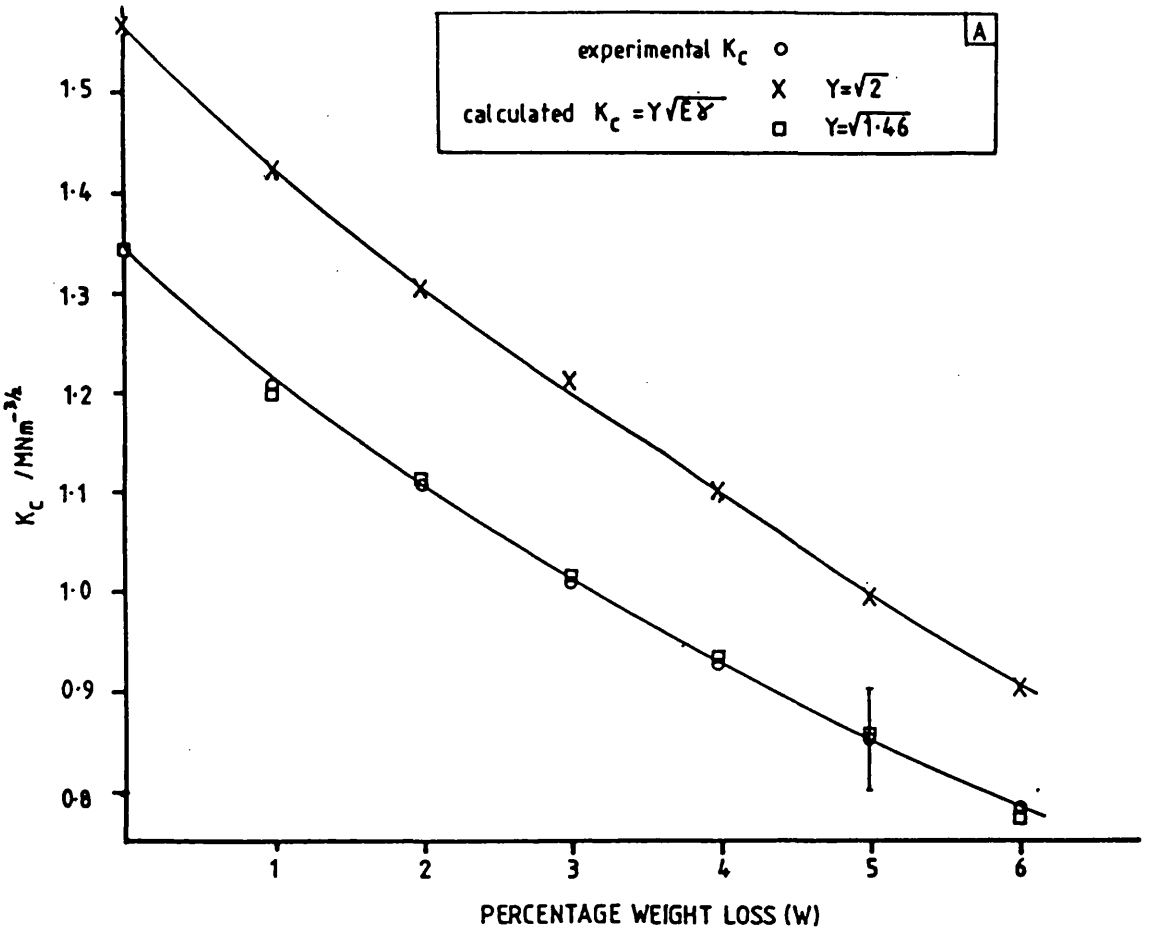

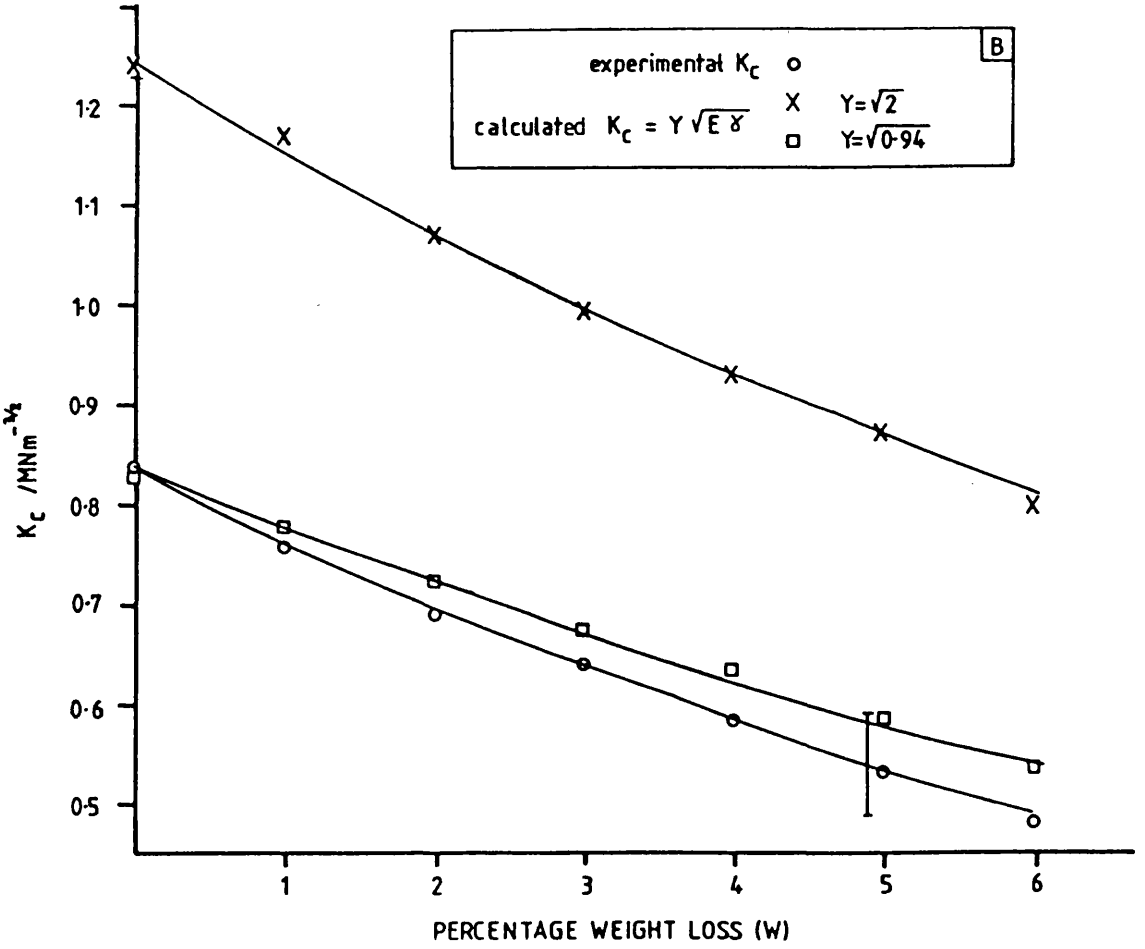

Fig. 5.10 Stress intensity factor variation (calculated and experimental) with weight loss. The bars on the experimental curve represent a variation of one standard deviation about the mean.

This would require a 14% and 31% overestimation of fundamental frequency for IM1-24 and PGA-AGL respectively. This is not consistent with there being a fixed error in the method of determination. This overestimation is also unlikely, as the fundamental frequency can be reproduceably found to be within a range of less than 5 Hz which is much less than 100 or 200 Hz required to account for the difference. γ is determined using $\gamma = \delta_f^2 \frac{\partial K}{\partial A} /2$, and therefore the greatest errors in determining γ are associated with errors in measurement of deflection at failure, δ_f. To account for the difference between K_c(calc.) and K_c(exp.) it would require a 16% and 30% overestimation of δ_f for IM1-24 and PGA-AGL respectively. Again the difference in required error of γ_f, between the two types of graphite, suggests that the variation in proportionality constant is not due to a fixed error in determination of γ. The difficulty in accurately determining δ_f is a likely source of error and almost certainly responsible for the large values of standard deviation that are observed in γ determination for both graphites. The most probable reason for the discrepancy between the theoretical and experimental proportionalty constant is associated with energy consuming sub- critical fracture events which occur in the process zone. The theoretical proportionality of constant of $\sqrt{2}$ arises from the way in which γ and G are defined. G is the rate of strain energy release per unit ligament area fractured whereas, γ is the strain energy released per unit surface area. Thus for elastic solids

where there is a very small process zone and almost all the elastic strain energy released is expended creating the two new surfaces, the proportionality constant might be approximately equal to $\sqrt{2}$. However when examining materials with a significantly sized process zone, as is the case in this study, then an amount of energy expenditure associated with failure events in the process zone is incorrectly attributed to creating the new surfaces, when using the relationship $G = 2\gamma$. Turner(88) has shown, by integrating well known and accepted functions for stress intensity factor such as those of Brown and Srawley (89), that the proportionality constant will also be affected by specimen goemetry. However, if specimens geometry influences the value of the proportionality constant, Y, it will make an equal contribution to both graphite types.

The difference in microstructure between IM1-24 and PGA-AGL will cause a variation in the size of the process zone that exists around the stressed crack tip. It is therefore not surprising that there is a difference in proportionality constant when the equalisation of K_c(exp.) and K_c(calc.) is performed. PGA-AGL with its coarser microstructure will most likely have the larger process zone of the two materials and therefore more strain energy 'sinks' compared with IM1-24. Consequently, PGA-AGL requires a greater reduction in the proportionality constant to allow for this extra energy expenditure.

The most significant apsect of comparing the

variation with weight loss of experimentally determined K_c and of calculated K_c (from indendentally determined E and γ), is that for both graphites the reduction of E and γ with weight loss accounts for the observed reduction in K_c. The following section considers the effect of the observed microstructural changes upon E and γ.

5.2.3 The effect of porosity development upon E and γ.

Elastic modulus and specific surface energy by their effect upon K_c are the dominant parameters controlling strength reductions which result from thermal oxidation. The only observed microstructural changes upon oxidation are those which occur in the open pore system in both IM1-24 and PGA-AGL (sections 4.4.3 and 4.5). It is therefore useful to examine the extent to which development of pores of a particular shape influences the reduction of either E and γ.

Elastic Modulus

The reduction of modulus in both graphites due to oxidation can be described reasonably by the exponential relationship : $E = E_o e^{-bP}$ 2.1 (section 4.2.2), where the exponential constant, b, was 7.49 and 7.02 for PGA-AGL and IM1-24 respectively. This empirical constant was assumed to be indicative of the type of porosity present (31, 32).

A theoretical derivation of equation 2.1 has been made by Buch (80, 81) which takes into account the effect of pore shape. He considers the effect of a pore or crack upon the stress and displacement perturbation of an isotropic medium under applied stress. Pores will cause both near and far field displacements. Buch examines the effect on far field displacement which is dominated by the projected area of the pores. By considering the effect of a single type of pore upon the axial strain ϵ_z, he derives the following expression for modulus decrement, ΔE,

$$\Delta E = -E_o \left(\frac{\lambda}{\eta} + 1\right) \Delta P$$

Where $\eta = \frac{\Delta P}{xy^2}$; ΔP is the change in porosity.

due to a single elliptical pore whose major and minor diameters are X and Y respectively and $\lambda = \Delta\epsilon_z E_o xy^2 \sigma$

As $\Delta P \rightarrow dP$ and $\Delta E \rightarrow dE$ then

$$\frac{dE}{E} = -\left(\frac{\lambda}{\eta} + 1\right) dP$$

and by integration

$$E = E_o \exp - \left[\left(\frac{\lambda}{\eta} + 1\right)P\right] \qquad 5.13$$

Equation 5.13 is of the same form as the empirical exponential relationship between E and P, where $b = \left(\frac{\lambda}{\eta} + 1\right)$

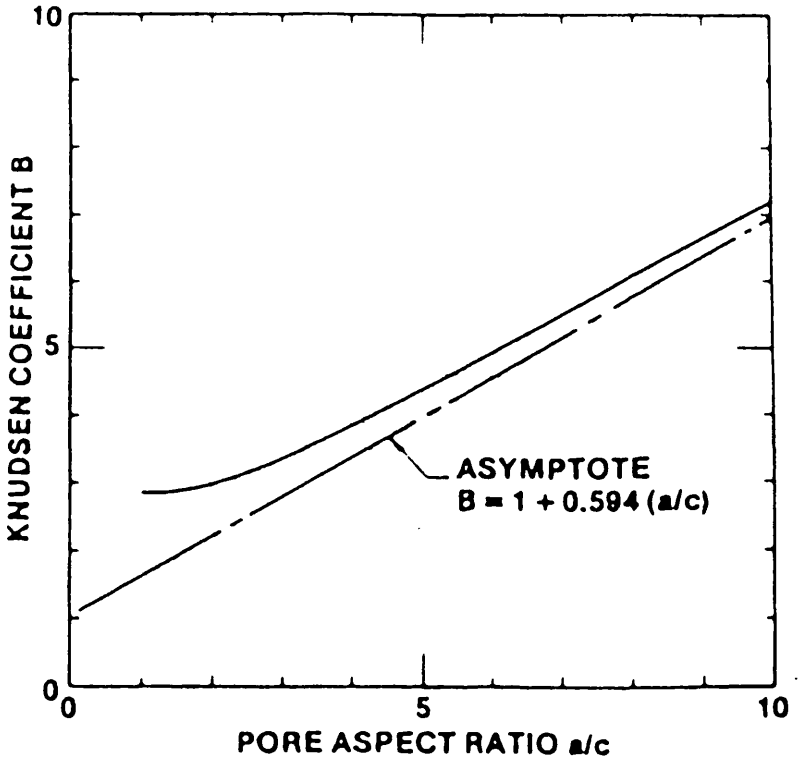

Fig. 5.11 The relationship between the Knudsen coefficent, b, and pore aspect ratio (from ref. 80)

1). Since both λ and ν are functions of the pore shape parameter X and Y, the exponent b will vary with pore shape. For example, for cylindrical pores

$$b = \frac{16}{3\pi^2} \{(2-\nu)\ (1+\nu)(a/c)\ +1\}$$

where a is the length and c is the diameter. Thus b will increaseas pore aspect ratio increases, Fig.5.11. Using the relationship shown in Fig.5.11, the experimental values of b found in the present work correspond to average pore aspect ratios of 10.1 and 10.9 for IM1-24 and PGA-AGL respectively. From this analysis it can be seen that the pores which mainly determine the modulus are slit-shaped; this is in qualitative agreement with the microscopical evidence (section 4.4).

Of course this is a simplistic model since it only considers one type of pore and is therefore far removed from the actual pore morphology observed and described in Chapter 4. However, it is useful in that it shows that the severity of modulus decrement increases with the ratio of the pore projected area to pore volume. The significance of this may be seen by comparing the projected area/volume ratio for two classes of pores for a given pore volume, e.g. 8 mm^3.
The open pore structure of IM1-24 may be simplified into two kinds: -

i) the gas entrappment porosity, having an approximately

cubic shape, of side length, l, with an orientation which presents the largest projected area, PA, to a plane normal to the applied stress and ii) the filamentary pores, having a cylindrical geometry with an aspect ratio, l/d of 20:1, which also presents the largest projected area. The values of the pore shape parameters for the two pore types are shown in Table 5.3.

Thus, if oxidation preferentially developed filamentary pores there would be a greater modulus decrement than if gas entrappment pores had been preferentially developed since filamentary poreshave a PA/V ratio nearly double that of gas entrappment pores.

Different shaped pores have different b values, therefore when an experimentally determined exponential relationship between E and P produces a value of b it is a composite value, with each category of pore contributing to a greater or lesser extent, depending upon the shape and volume fraction. Thus b might better be expressed by

$$b = f(b_i, P_i, P) \qquad 5.14$$

where b_i is the coefficient associated with the ith type of pore, P_i is the fractional porosity of the ith type of pore and P is the total porosity. This expression is

TABLE 5.3 PROJECTED AREA/VOLUME RATIO FOR CUBIC CYLINDRICAL PORES

PORE TYPE	SHAPE	PA	V	PA/V
Gas Entrappment	Cubic	$\ell^2\sqrt{3}$	ℓ^3	$\sqrt{3}/\ell = 0.87$
Filamentary	Cylindrical	ℓd	$\frac{\pi d^2 \ell}{4}$	$\frac{4}{\pi d} = 1.60$

similar to that proposed by Brown et al (66) who attributed strength reduction to the reduction of area of solid material in a plane normal to the tensile axis, i.e.

$$b = \sum_i \alpha \frac{P_i}{P}$$

where $\alpha = \frac{x_i a_i}{V_i}$; x_i is the characteristic length of the ith type of pore required to describe pore size, a_i is the projected area and v_i the volume associated with a single pore.

The coeffiicient b is a function of pore shape; thus, if upon oxidation there is preferential development of a certain category of pore, then not only will modulus vary with P, but also b will vary with P. For both IM1-24 and PGA-AGL there has been a very clear preferential development of pores of high aspect ratio. Thus modulus has decreased not only as a consequence of increased porosity but also because the proportion of pores with high aspect ratio has increased. It follows therefore that the value of b increases with increase of porosity. This would have the effect of staightening out the simple exponential curve, Fig.5.12. This is possibly a further explanation (apart from the small range of fractional porosity values) why the modulus, strength and stress intensity reductions were nearly as well-represented by a straight line as by an exponential relationship (section 4.2).

The modulus will not only vary with b and P but also with changes in spatial distribution of pores. This was examined by Rice (82) in response to the large variability of elastic modulus in various ceramics. He quantitatively estimated the effects of spatial pore distribution upon modulus by considering three commonly-used functional porosity relationships:

$$f_1(P) = (1 - bP)$$

$$f_2(P) = e^{-bP}$$

$$f_3(P) = 1 - \frac{bP}{1 + (b-1)P}$$

Rice estimated the modulus in two ways: i) by substituting one of the above relationships into, $E_1 = E_o f_i(\bar{P})$ where $\bar{P}$ is the average porosity and ii) by considering the body of material to be a collection of n slabs, each slab having homogeneous porosity, but the collection having a simple symmetrical distribution of fractional porosity with an average porosity, $\bar{P}$. In the latter case, the average strain, $\bar{e}$, can be calculated from the zero-porosity modulus, E_o, and stress in each slab; the average modulus can be calculated from

$$E_2 = \frac{\sigma}{\bar{e}} = \frac{\sigma}{n\sigma / E_o \Sigma_j^n f(P_j)} = \frac{E_o \Sigma_j^n f(P_j)}{n} \qquad 5.15$$

Where P_j is the fractional porosity of the jth slab.

Rice found that when the linear functional relationship was used, $E_2 = E_1$. However, when the non-linear functions were used $E_2 > E_1$. Furthermore, in the second case, if an assembly of slabs was considered, with an asymmetrical porosity distribution, biased towards high porosity, then the value of E_2 was reduced. This work shows that the modulus decrement due to pore development is influenced by the spatial distribution of pores and that localised development of pores enhances the modulus decrement. In both the graphites examined in this study the principal pore development upon oxidation has been in the binder. It is likely that this pattern of pore development is more detrimental to modulus than a pore development which was distributed uniformly across the graphite microstructure.

The exponential relationship $E = E_o e^{-bP}$ is a simplistic expression for describing the reduction in modulus in materials with a complex spatial distribution of pores of different shapes. From the discussion presented above the data required to describe the relationship between E and P more accurately are as follows:-

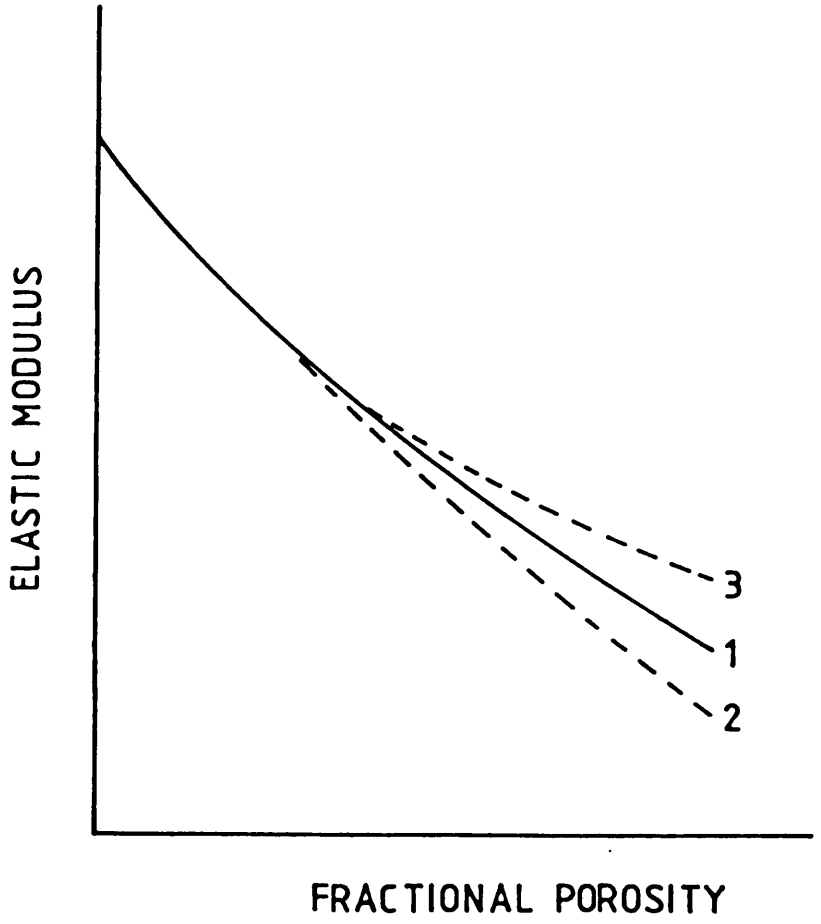

Fig.5.12 Schematic representation of the exponential relationship between E and P, i.e. $E = E_o \exp(-bP)$. The three curves represent the following situations: (1) when all categories of pores develop equally and b remains constant; (2) when there is preferential development of high aspect ratio pores and b increases with P; (3) when low aspect ratio pores develop preferentially and b decreases with P.

i) both open and closed pores classified into various pore shapes;

ii) the fractional porosity of each shape class;

iii) preferential orientation of any class of pore, as this will influence the projected area to volume ratio;

iv) any inhomogeneity of spatial distribution of pores.

At present there is no expression for modulus variation which fully integrates the considerations presented above. A combination of equations 5.14 and 5.15 might produce a better expression, e.g.

$$E = \frac{E_o \Sigma_j^n e^{-b_j P_j}}{n}$$

where b_j is the composite b value for the jth slab and $b_j = f(b_i P_i P_j)$. However, the functional relationship for b_j has not been determined.

In section 2.2.6 it was shown that for a given weight loss, radiolytic corrosion is less detrimental to the strength and modulus than thermal corrosion. This may in part be due to the radiation hardening increasing modulus (85) and thus mitigating some of the mechanical property reduction which results from weight loss. However, some of the differences in strength reduction due to thermal and radiolytic oxidation can be accounted for by a con-

sideration of the differences in pore development and the arguments presented above. Fig.5.13 a and b shows the pores in the binder material of IM1-24 radiolytically oxidation in an atmosphere of 98CO_2, 2%CO .*

The graphite in Figs.5.31a and b has been oxidised to 4.95% and 13% weight loss respectively. Pores in these two micrographs appear dark as they have been illuminated using visible light, whereas pores in Figs.5.13c and d are filled with fluorescent resin and illuminated with u.v. and consequently appear white. The principal features in the radiolytically oxidised graphite, Fig.5.13a, are a large gas entrappment pore onthe left of the micrograph and a smaller pore in the upper right hand region of the micrograph, from which several filamentary pores emanate. The sharp, discontinuous nature of these pores better resembles the filamentary pores of the unoxidised material, Fig.5.13c, than those which have been thermally oxidised to a similar weight loss $\sim$ 6%, Fig.5.13d. At much higher levels of weight loss, i.e. 13%, the radiolytically oxidised

---

*The radiolytic corrosion was undertaken at Berkeley Nuclear Laboratories by J V Best (86) and W J Stephen, as part of a project unrelated to this work. The author is grateful to Mr Stephen for providing micrographs, Fig.5.13a and b.

graphite, Fig.5.13b shows clearly that there has been enlargement of the gas entrappment porosity. However, the spurs on the smaller radius corners of this type of pore (arrowed), which generally develop lengthways into the network of filamentary pores upon thermal oxidation appear to have dilated with little or no length extension. The difference in pore development between thermally and radiolytically oxidised graphite can be explained by a consideration of the nature of the different pore surfaces, their reactivities and the reactivity of the oxidising environment. The open porosity in IM1-24 consists of gas entrappment and filamentary pores. Gas entrappment normally occurs when gas bubbles percolate through well developed mesophase, bending the mesophase so that the bubble becomes enveloped. This results in basal planes being oriented parallel to the surface of the pore section(2.1.2). Where the mesophase has been most severely bent and twisted, disclinations are formed, i.e. at the sharpest radius and these may nucleate microcracks which form the spurs seen in Fig.5.13b. In section 4.4.2, it is shown that filamentary pores follow a direction parallel to basal planes and therefore the sides of filamentary pores are orientated parallel to basal planes. Since basal planes are 2 to 3 orders of magnitude less reactive than prismatic edges (90), a mildly oxidising environment, such as that experienced in thermal corrosion, will be selective in its attack. This results in the gas entrappment pores remaining virtually unaffected, whereas the filamentary pores resist dilation and preferentially elongate. The discontinuous nature of the

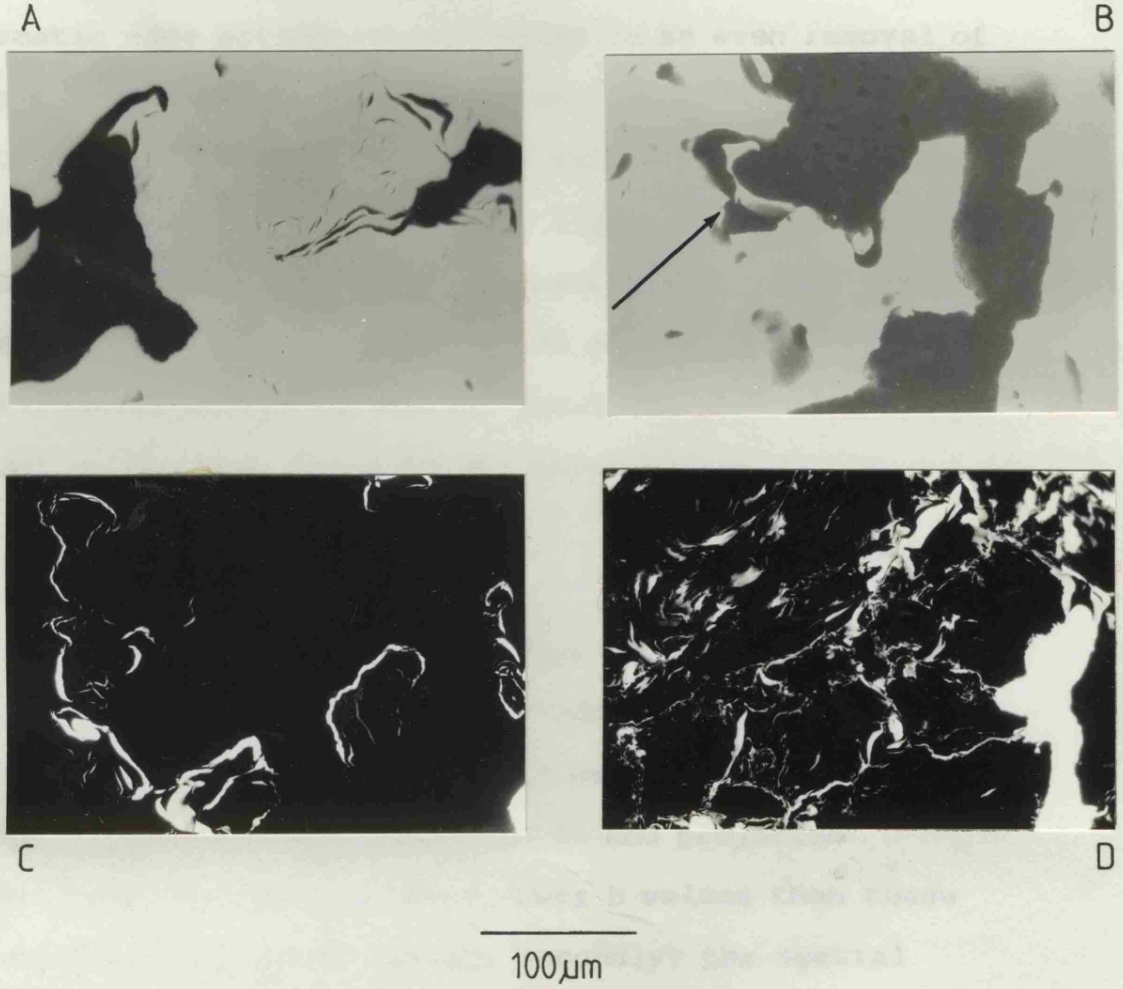

Fig. 5.13 Pores in radiolytically oxidised IM1-24 to 4.95% weight loss (a) and 13% weight loss (b). Figures c and d are of pores in unoxidised and thermally oxidised IM1-24 (6% weight loss) respectively.

filamentary pores is most likely due to the thermally-induced cracks encountering non-favourably orientated primastic edges which prevent further propagation. Thus the extremities of the unoxidised filamentary pores are more reactive than the walls and will be attacked preferentially causing the observed elongation. However when the oxidising environment is much more severe, as is the case in the radiolytically active, oxidising species, the rate of basal plane attack is not significantly different to the rate of prismatic edge attack. This results in an even removal of graphite from all classes of pores. This has been observed by Best (86) when radiolytically oxidising IM1-24 in CO_2 with small amounts of inhibitor, i.e. 1000 vpm CO. At levels of CO comparable with the atmosphere that was used to oxidise the graphties in Figs.5.13 a and b there is some preferential attack of smaller pores, but not to the same extent as has been found in the present work.

The result of the difference in selectivity of pore development between thermal and radiolytic oxidation is twofold:- firstly, the pores that develop upon radiolytic oxidation are of lower aspect ratio and projected area/volume and hence produce lower b values than those involved in thermal oxidation; secondly, the spatial distribution of pore development in radiolytic corrosion is more uniform than in thermal oxidation and therefore less detrimental to mechanical properties such as modulus. Thus for a given weight loss the difference in mechanical

properties of radiolytically and thermally oxidised graphites can be qualitatively accounted for by differences in pore development.

EFFECTIVE SURFACE ENERGY

The cause of effective surface energy reduction with pore development is very similar to that of modulus reduction. This is not surprising as it can be seen from the method of determination of γ that E and γ are very closely related. γ is determined using equation, 3.7, i.e.

$$\gamma = \delta_f \left(\frac{\partial k}{\partial A}\right)/2$$

As a result of oxidation, the stiffness is reduced for a given crack area; therefore $\partial k/\partial A$ is reduced and so is γ. This change in stiffness results from the associated reduction in modulus and therefore the arguments presented earlier in this section for E decrement with specific types of pore development hold true for γ. It is possible that filamentary pore development may increase the amount of sub-critical crack branching; thus increasing the amount of sub-critical AE (section 5.1.2). This would have the effect of increasing the apparent strain energy reduction for a given crack extension area.

Thus, whilst there is a net reduction in γ due

to oxidation there are two opposing trends:

i) pore development decreasing modulus and hence γ and

ii) increasing sub-critical crack branching which increases γ. This latter effect is probably a further reason for the poor fit to the exponential relationship between γ and P or w, apart from the inherent difficulties in measuring δ_f and the limitations of the simple exponential relationship.

5.3 Summary of the Effects of oxidation upon the Strength of Nuclear Graphites

Extended areas of contiguous and commonly orientated basal planes are found in the grains of all three graphites examined in this study. Where these areas are favourably orientated to the tensile axis they cleave in preference to the less well ordered binder material. The optical texture of the areas which contain these planes of weakness varies from graphite to graphite and confers a characteristic strength upon the planes. This grain cleavage strength, σ_c, is apparently unaffected by oxidiation to weight loss levels of ~ 6%. The general microstructure will determine the macroscopic stress distribution and the tolerance of the graphite to flaws. For any applied stress greater than the individual grain cleavage strength there is

a probability of planes of weakness failing and linking together. A fracture model has been used to predict the probability of attaining critically sized flaws as determined by fracture mechanics. Some limitations of the model have been discussed (section 5.1.1) and further limitations, in light of the latter part of the discussion will be discussed in this section.

Oxidation principally develops filamentary shaped pores (section 5.2.3) in the binder of the graphites, which reduces the elastic modulus and effective surface energy. The reduction E and γ accounts for the observed reduction in stress intensity factor (section 5.2.2). This results in a reduction of the maximum size of flaw that is tolerable for a given applied stress. The failure strength may be expressed by the 50% probability of specimens attaining a flaw size that is critical. Since the probability of attaining a specific flaw size increases with increasing applied stress, it follows that as the critical flaw size is reduced, the failure strength also reduces. This is the underlying principle of Buch's model. However, the model assumes an homogeneous stress distribution, which is an unlikely situation in such a heterogeneous microstructure as graphite. For a specific strain, the nominal stress will be determined by the average modulus of the material. However, regions of higher modulus will have localised stresses which are greater than the nominal stress. Thus as weight loss (principally from the binder) increases, the inhomogeneity of stress distribution

increases, raising the localised stress in the grains. This effect is not allowed for in the Buch analytical model. Despite this the model represents the strength reduction with weight loss quite well, Fig.5.6. However, the theoretical prediction slightly underestimates experimental reduction in strength and the discrepancy systematically increases with increasing weight loss.

One of the reasons for this discrepancy may be associated with the variation of stress distribution with weight loss. The variation of critical flaw size, a'_c with applied stress, σ_{app}, has been plotted for three K_c values appropriate to 0%, 3% and 6% weight loss for IM1-24, Fig.5.12, using $a'_c = \frac{1}{\pi}\left(\frac{K_c}{\sigma_{app}}\right)^2$

Also shown on the curves are : -

(i) the values of the experimental failure strengths (these are linked by line A);

(ii) the value of failure strength calculated from the analytical model (linked by line B). At 0% weight loss the experimental and calculated failure strengths are close and therefore so are the critical defect sizes obtained from lines A and B. As oxidation increases the differences between the theoretical and experimental failure strength and associated critical flaw size increases. This discrepency may possibly be explained by the increasing difference between the nominal applied stress on the

specimen and the localised stress on the grain as oxidation proceeds. At 6% weight loss the experimental failure strength is lower than that from the model (line B). However the experimental failure strength indicated is the nominal strength; it is likely that the grains are experiencing a higher local stress and would therefore require a lower critical flaw size than is indicated in line A. There are two implications : -

i) the value of critical flaw size calculated from experimental K_c and σ_f values is subject to a degree of uncertainty according to the severity of macroscopic stress intensification on the features in the microstructure which form the critical flaw;

ii) the analytical model does not allow for localised stress intensification and therefore may be inappropriate for graphites in which this is significant, e.g. where there has been severe preferential oxidation of the binder phase.

The severity of the strength loss for a specific weight loss is ultimately determined by the nature of the pore development. Development of pores with a high projected area to volume ratio and inhomogeneous spatial distribution will produce a more severe reduction in E and γ (section 5.2.3) and consequently K_c and σ_f. This is probably one of the reasons why highly selective thermal oxidation produces a greater reduction in strength and

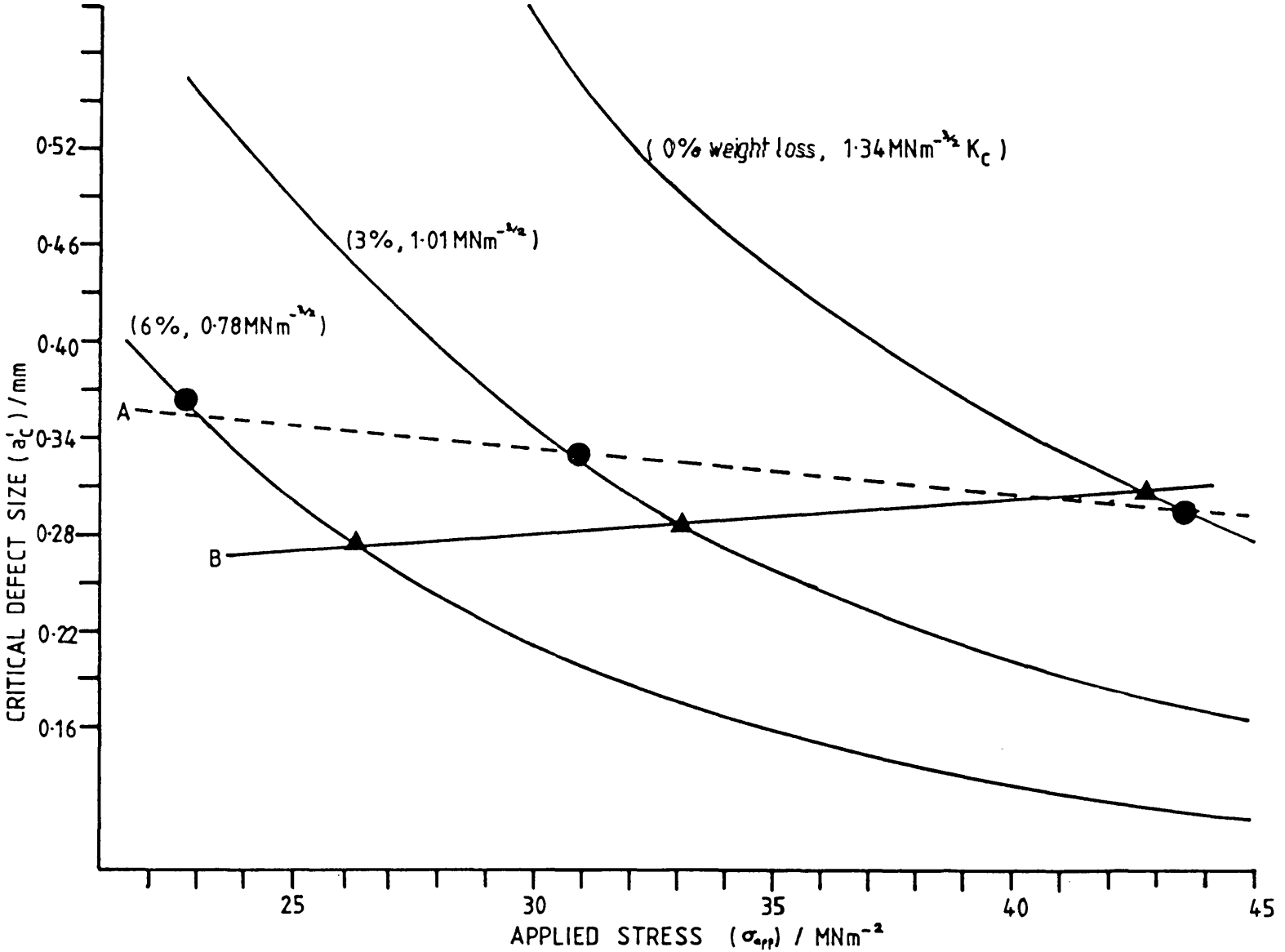

Fig. 5.14 The critical defect size of IM1-24 as a function of applied stress for three values of K_c appropriate to 0%, 3% and 6% weight loss. Lines A and B represent the variation in a'_c with oxidation from experiment and the Buch Model respectively.

modulus than the same extent of weight loss due to radiolytic oxidation, which produces a more even development of pores.

CHAPTER 6

CONCLUSIONS AND SUGGESTIONS FOR FURTHER WORK

The significant conclusions drawn from this study are listed below.

1) When nuclear grade graphites are thermally oxidised in an atmosphere of 5% CO/CO_2 at 900°C, oxidation is in the chemical control regime and produces apparently homogeneous internal weight loss. This type of weight loss caused similar and severe reductions in the mechanical properties of two microstructurally dissimilar graphites, IM1-24 and PGA-AGL. The relationship of four mechanical properties, failure strength, σ_f, critical stress intensity factor, K_c, elastic modulus, E and effective surface energy, γ, to weight loss were examined. A reduction in mechanical property values of between 40 and 50% has been produced by 7% weight loss due to thermal oxidation.

2) The critical defect size in both graphites is greater than any single microstructural feature. This implies the development of a critical flaw by the linking together of smaller flaws, i.e. those produced by sub-critical fracture and inherent microstructural flaws. Preferred sites for sub-critical failure are areas of contiguous and commonly-orientated basal planes, which are found in the grains of the graphites rather than in the binder material. Oxidation

does not appreciably affect the critical defect size, nor does it noticeably affect the fracture path. Thus the principal reason for a reduction in failure strength is a corresponding reduction in the tolerance of flaws to applied stress, i.e. a reduction in the critical stress intensity factor.

3) The observed reduction in critical stress intensity factor is accounted for by the observed reduction in elastic modulus and effective surface energy, K_c is related to E and γ by $K_c = Y\sqrt{E\gamma}$, where Y = 1.20 and 0.97 for IM1-24 and PGA-AGL respectively. The value of the constant Y is believed to be related to the size of the process zone of the graphite and hence the number of elastic strain energy sinks.

4) The large reduction in elastic modulus and effective surface energy results from the preferential development of a network of filamentary pores in areas of domain structure within the binder. These pores have a high ratio of projected area to volume and have a heterogeneous spatial distribution; this produces a more severe reduction in modulus and effective surface energy than would be expected from a more general development of pores.

5) The filamentary pores which are preferentially attacked are nucleated as a result of anisotropic thermal contraction which cleaves open basal planes, thus the pore walls are principally basal planes. The extremities of this

class of pore many terminate at non-favourably orientated basal planes or prismatic edges. In thermal oxidation basal planes are much less reactive than prismatic edges, consequently the extremeties are preferentially attacked. This results in elongation of the pore and an increase in the ratio of projected area to volume. Because the reactivity of basal planes and prismatic edges is not significantly different in the much more aggressive oxidising atmosphere generated in radiolytic oxidation, pore development is less selective than thermal oxidation. This general development is less detrimental to modulus and effective surface energy than the selective attack due to thermal oxidation and consequently less deterimental to stress intensity factor. It follows that thermal oxidation will reduce the strength of a graphite to a greater extent than radiolytic oxidation to the same weight loss.

6) Stress induced acoustic emission is characteristic of the graphite microstructure, particularly the fine scale optical texture. The number of events to failure and the slope of the amplitude distribution, i.e. the b value, increases as the coarseness of the optical texture increases.

There is threshold stress below which AE does not occur, this is also a characteristic of the optical texture and is believed to be indicative of the cleavage strength of the areas of contiguous basal plane orientation which exists primarily in the grains.

SUGGESTIONS FOR FURTHER WORK

1) In view of the importance of the nature of pore development upon the strength of graphite, it would be useful if an Image analysis programme were developed to analyse and compare pore structure and development of thermally and radiolytically oxidised material in the following manner:-

i) pores categorised into a number of classes according to their shape;

ii) the contribution of each class of pore to the total porosity determined;

iii) quantitative measurements of the spatial distribution and preferred orientation of each class of pore.

Using these data it may be possible to predict the effect of pore development on the elastic modulus, using the type of analysis discussed in section 5.2.3.

2) Further studies are required to determine the relationship between the optical texture of graphite and stress induced acoustic emission. This would require a detailed characterisation of the optical texture, along the lines adopted by Ragan and Marsh (87) of a wide range of microstructures, e.g. from coarse electrograde graphites,

with grains which are several millimetres in length to high density nuclear graphites which have grain sizes of the order of a few microns. Using AE equipment with amplitude analysis and computerised data acquisition (76) it would be useful to correlate microstructural features with the characteristic b values and ΣAE.

3) Techniques used in this work and those suggested above may be adopted to examine a wider range of porous carbons, e.g. glassy carbons, metallurgical cokes, C-C composites. It will also be interesting to examine the effects of varying the oxidising conditions, for example by oxidising in diffusion control, which produces a less homogeneous weight loss, or in different atmospheres.

7. REFERENCES

1. Girifalco, L.A., Lad, R.A. (1956), J.Chem.Phys., 25, pp.693-697.
2. Boehm, H.P., Coughlin, R.W. (1964), Carbon, 2, pp.1-6.
3. Darney, A. (1958), Proc. 1st Conference on Industrial Carbon and Graphite, Soc. Chem. Ind., London pp.152-161.
4. Ragan, S. (1982), Properties of Cokes, PhD Th esis, University of Newcastle upon Tyne, pp.1-31.
5. Marsh, H. (1974), Proc. 4th conference on Industrial Carbon and Graphite, Soc. Chem. Ind., London, pp.2-38.
6. Brooks, J.D., Taylor, G.H. (1968), Chemistry and Physics of Carbon, 4, pp.243-285.
7. Friedel, G. (1928), An Physique, 18, p.273.
8. Evans, M., (1978), Porosity in Graphite, PhD Thesis, University of Newcastle upon Tyne.
9. Chard, W., Conaway, M., Neisz, D. (1976), Petroleum Derived Carbons, American Chemical Society, Deviney and O'Grady eds., Symposium Series 21.
10. Reynolds, W.N. (1968), Physical Properties of Graphite, London, Elsevier.
11. White, J.L., Zimmer, J.E., (1976), Surface and Defect Properties of Solids, The Chemical Society, 5, pp.16-35.
12. I.U.P.A.C. (1974), Appendices on Provisional Nomenclature, Symbols units and Standards, 39, Definition Terminology and Symbols in Colloids and Surface Chemistry, Heterogeneous Catalysis, 11.
13. Mrozowski, S. (1953/54), Proc. 1st and 2nd Conferences on Carbon, Waverley Press, U.S.A., p.31.

14. Fujita, F.E., Izui, K.J. (1961), Phys. Soc. Japan, 16, p.1032.

15. Jenkins, G.M., (1973), Chemistry and Physics of Carbon, 11, pp.189-242.

16. Arragon, P., Berthier, R. (1958), Proc. 1st Conference on Industrial Carbon and Graphite, Soc. Chem. Ind., London, p.565.

17. Souele, D.E., Nezbeda, C.W., (1968), J. Appl. Phys., 39, p.5122.

18. Hall, E., (1965), J. Nucl. Mater., 15, p.137.

19. Groves, G.W., Kelly, A. (1963), Phil. Mag., 8, p.877.

20. Griffith, A.A. (1920), Phil. Trans. Roy. Soc., 221, p.163.

21. Brocklehurst, J.E. (1977), Chemistry and Physics of Carbon, 13, p.164.

22. Jenkins, G.M. (1962). J. Nucl. Mater., 24, p.174.

23. Slagle, O.D., (1967), J. Amer. Ceram. Soc., 50(19), p.495.

24. Knibbs, R.H. (1967), J. Nucl. Mater., 24, p.174.

25. Meyer, R.A., Buch, J.D., (1973), 11th Carbon Conference, CONF.-73061, p.229.

26. Meyer, R.A., Zimmer, J.E., Almon, M.C. (1974), U.S. Aerospace Report, ATR-74(7408)-2.

27. Knudsen, F.P. (1959), J. Amer. Ceram. Soc., 42(8), pp.376-387.

28. Duckworth, W. (1953), J. Amer. Ceram. Soc., 36(2), p.65.

29. Barrachin, A.M., Joquet, G., Micaud, G., Patton, F. (1966), J. Nucl. Mater., 20, p.294.

30. Nazare, S., Ondracek, G.,(1974), Microscope, 22, p.39.

31. Stacey, A.E. (1980), The Mechanical Properties and Structure of Metallurgical Cokes, PhD Thesis, University of Leeds.

32. Rossi, R.C. (1968), J. Amer. Ceram. Soc., 51(8), p.433.

33. Hasselman, D.P. (1964), J. Amer. Ceram.Soc 47(1), p.52.

34. May, M.J. (1968), Application of fracture mechanics. In : Fracture Toughness, ISI Publication 121, p.89.

35. Pampuch, R., Konsztowicz, (1974), Prace Komisji Ceramicznei, 21, p.355.

36. Knott, J.F. (1973), Fundamentals of Fracture Mechanics, Butterworths, London.

37. Orowan, E. (1950), Fatigue and Fracture of Metals, Symposium at Massachusetts Institute of Technology: John Wiley and Sons Inc., N.Y.

38. Irwin, G.R., Kies, J.A., Smith, H.L. (1958), ASTM Proc., 58, pp.640-660.

39. Westergaard, H.M. (1939), J. Appl. Mech., A49.

40. Davidge, R.W., Tappin, G. (1968), J. Mat. Sci., 3, pp.165-173.

41. Darby, M.I. (1976), Journal of Fracture, 5, pp.745-757.

42. Yahr, G.J., Valachovic, R.S. (1972) Proc. Conference on Continuum Aspects of Graphite Design, USAEC CONF-701105, p.533.

43. Yahr, G.J. Valachovic, R.S., Greenstreet, W.L. (1972), Conference in Graphite Structures for Nuclear Reactors, Organised by the Nuclear Energy Group of the Institute of Mechanical Engineers.

44. Buresch, F.F. (1981) Advances in Fracture Research, 5, pp.2293-2301.

45. Sato, S., Awaji, H., Akuzama, H. (1978), Carbon, 16, pp.95-102.

46. Szendi-Horvath, G., (1980), Engineering Fracture Mechanics, 13, pp.955-961.
47. Weibull, W. (1951), J. Appl. Mech., 18, pp.293-297.
48. Brocklehurst, J.E., Darby, M.I. (1974), Mater. Sci. Engr., 16, p.91.
49. Marshall, P., Priddle, E.K. (1973), Carbon, 11, pp.627-631.
50. Mason, I.B. (1961), Proc. 5th Carbon Conference, 2, Pergammon Press, p.597.
51. Ho, F. (1979) Proc. 14th Biennial Carbon Conference, American Carbon Society, p.338.
52. Buch, J.D., (1982), US Aerospace Report, ATR-81 (7750)-1 Aerospace Corporation, El Segundo, California 9024.
53. Buch, J.D. (1976), ASTM STP 605, pp.124-144.
54. Rose, A.P.G., Tucker, M.O., Cooke, R.G. (1982), Proc. British Ceramic Society, 32, 181-190.
55. Gilchirst, K.E., Wells, D. (1969), Carbon 7, p.627.
56. Kraus, G., Semmler, J. (1978), Carbon, 16, pp.185-190.
57. Kaiser, J., (1950), Thesis, Munich Technical College.
58. Dalgleish, B.J., Pratt, P.L., Rawlings, R.D., Fakhr, A. (1980), Mat. Sci. Eng., 45(2), pp.9-20.
59. Hawkins, N. (1966), Proc. 2nd Conference on Industrial Carbon and Graphite, Soc. Chem. Ind., London, p.355.
60. Board, J.A., Squires, R.L. (1966), Ibid, p.289.

61. Rounthwaite, C., Lyons, G.A., Snowdon, R.A., Ibid., p.299.

62. Brocklehurst, J.E., Brown, R.G., Gilchrist, K.E., Labaton, V. (1970), J. Nucl. Mater., 35, p.183.

63. Knibbs, R.H., Morris, J.B. (1971), Proc. 3rd Conference on Industrial Carbon and Graphite, Soc. Chem. Ind., London, p.297.

64. Wood, J.L., Bradt, R.C., Walker, P.L. (1980), Carbon, 18, pp.179-189.

65. Thrower, P.L., Bognet, J.C. (1977), 13th Biennial American Carbon Conference, Amer. Carbon Soc., p.265.

66. Brown, S.D., Biddulph, R.B., Wilcox, P.D., (1964), J. Amer. Cer. Soc., 47(7), p.320.

67. Taylor, R., Brown, R.G., Gilchirst, K., Hall, E., Hodds, A.T., Kelly, B.T., Morris,F., (1967., Carbon, 5, p.519.

68. Stephen, W.J. (1979), CEGB, BNL, Report, RD/B/N4446.

69. ASTM Special Committee on Fracture Testing of High Strength Materials, Mat. Res. Stand., (1964), 4, No.3, March, 107.

70. Irwin, G.R., (1962), J. Appl. Mech., 84E, Dec., pp.651-654.

71. Bacon, G.E., (1956), J. Appl. Chem., 6, pp.477-481.

72. Chatfield, C. (1978), Statistics for Technology, 2nd ed. Chapman and Hall, London, p.133-148.

73. Bulk Densities of Graphite from Water Displacement, DIN 51056.

74. Stephen, W.J. (1980), CEGB BNL, Report RD B N4793.

75. Androutsopoulos, G.P., Mann, R. (1979). Chem. Eng. Sci., 34, p.1203.

76. Guild, F.J., Ackerman, F.J., Phillips, M.G., Harris, B. (1983), First International Symposium on Acoustic Emission from Reinforced Composites, The Society of the Plastics Industry, p.1-8.

77. Moduli of Elasticity and Fundamental Frequencies of Carbon and Graphite Materials by Sonic Resonance (1974), ASTM Standard ANS1/ASTM C747-74

78. Wicke, E. (1955), Fifth Symposium on Combustion, Reinhold, New York, p.245.

79. Thiele, E.W., (1939), Ind. Eng. Chem., 31, p.916.

80. Buch, J.D., (1983), Proc. 16th Biennal Carbon Conference, American Carbon Society, p.400

81. Buch, J.D., (1980), U.S. Aerospace Technical Report, ATR-80(7750) - 1 Nov.

82. Rice, R.W. (1975), J. Amer. Ceram. Soc., 58, p.458.

83. Nightingale, R.E. (1962), Nuclear Graphite, Academic Press, London, p.111.

84. Cooke, R.G., (1981), Advances in Fracture Research (ICF 5), Francois, D., ed., Pergamon, 2, p.1083.

85. Kelly, B.T. (1982), Physics of Graphite, Applied Science Publishers, London, pp.440-445.

86. Best, J.V. (1982), Proc. 6th London International Carbon and Graphite Conference, Soc. Chem. Ind., p.341.

87. Ragan, S., Marsh, H. (1983), Carbon, 21, pp.157-165.

88. Turner, C.E., (1973), Materials Science and Engineering, 11, pp.275-282.

89. Brown, W.F., Srawley, J.E. (1966), ASTM.STP.410.

90. Lewis, J.B. (1970), Thermal Gas Reactions of Graphite. In: Modern Aspects of Graphite Technology, Blackman L.C.F. ed., Academic Press, London, p.150.

ACKNOWLEDGEMENTS

The author would like to thank the following people who have helped in this research programme. Dr B McEnaney and Dr R G Cooke for their advice and encouragement throughout the period of research.

Mr W Stephen and Dr T Swan at Berkeley Nuclear Laboratories (BNL) for advice on oxidation kinetics and image analysis and general liaison between the author and BNL.

Mr P Taylor, Mr P Wakeford and Mr S Bowman of the University of Bath for technical support, particularly mechanical and electrical engineering.

The Science and Engineering Research Council and the cooperating body, Berkeley Nuclear Laboratories for financial support.

APPENDIX 1

PROGRAMME FOR THE ANALYTICAL FRACTURE MODEL (CBM BASIC)

```
1 OPEN1,4
5 DIMA(3)
10 DIMC(10)
15 DEFFND(X)=-ATN(X/SQR(-X*X+1))+π/2
20 INPUT"NO.OF GRAINS";C(1)
25 INPUT"GRAIN SIZE/M";C(2)
30 INPUT"K1C,   MN/M↑2";C(3)
35 INPUT"PORE VOL. FRACT.";C(4)
40 INPUT"CLEAVAGE STRENGTH,MN/M↑2";C(5)
43 INPUT"IS MATERIAL ISOTROPIC";B$
44 IFB$="YES"THEN49
45 INPUT"IS TENSILE AXIS WITH OR AGAINST THE GRAIN";A$
46 INPUT"ANISOTROPY FACTOR";C(6)
47 IFA$="AGAINST"THEN49
48 C(6)=C(6)+1
49 INPUT"RANDOM PARAMETER VARIATION? YES/NO";D$
50 IFD$="NO"THEN55
51 GOSUB499
53 GOSUB620
55 INPUT"STRESS APPL. LOWER LIM.";C(7)
60 INPUT"STRESS APPL. UPPER LIM.";C(8)
65 INPUT"STRESS INTERVAL";C(9)
66 INPUT"DO YOU WANT A PRINTOUT?";Q$
67 IFQ$="NO"THEN70
68 GOSUB405
70 PRINT"APPLIED STRESS","PROB.FAIL"
75 FORE=C(7)TOC(8)STEPC(9)
80 Y=(C(5)/E)↑.5
85 B=FND(Y)
90 A=0
100 IF B$="NO"THEN135
110 V=1-(C(5)/E)↑.5
120 GOTO360
135 N=0
140 H=(B-A)/32
150 S=0
160 FORP=A+HTOB-HSTEP2*H
165 IFA$="WITH"THEN180
170 K=(COS(P)↑C(6))*SIN(P)
175 GOTO185
180 K=SIN(P)↑C(6)
185 S=S+K
190 NEXTP
200 R=0
210 FORT=A+2*HTOB-2*HSTEP2*H
220 IFA$="WITH"THEN235
225 Y=(COS(T)↑C(6))*SIN(T)
230 GOTO240
235 Y=SIN(T)↑C(6)
240 R=R+Y
250 NEXTT
```

arcsin

input parameters

applied stress range

ø crit.

eqn. 5.4

numerical integration of eqn. 5.5

continued

```
260 IFA$="WITH"THEN290
270 I=(1/3)*H*((COS(A)↑C(6))*SIN(A)+(COS(B)↑C(6))*SIN(B)+4*S+2*R)
280 GOTO300
290 I=(1/3)*H*(SIN(A)↑C(6)+SIN(B)↑C(6)+4*S+2*R)
300 N=N+1
310 A(N)=I
320 IFB=1.57079THEN350
330 B=1.57079
340 GOTO140
350 V=A(1)/A(2)
360 M=C(4)+(1-C(4))*V
370 Z=(π↑3/C(2)↑2)*((C(3)/(2*E))↑4)
380 L=1-(1-M↑Z/Z)↑C(1)
390 PRINTE,L
391 IFQ$="NO"THEN399
395 PRINT#1,E,L
399 NEXTE
400 IFQ$="NO"THEN403
404 STOP
405 PRINT#1,"INPUT PARAMETERS"
406 PRINT#1,"————————————"
410 PRINT#1,"NO. OF GRAINS",C(1)
420 PRINT#1,"GRAIN SIZE/M",C(2)
430 PRINT#1,"K1C/MNM↑-3/2",C(3)
440 PRINT#1,"PORE VOLUME FRACTION",C(4)
450 IFB$="YES"THEN460
451 IFA$="AGAINST"THEN459
452 PRINT#1,"ANISOTROPY FACTOR",C(6)-1
453 GOTO460
459 PRINT#1,"ANISOTRPY FACTOR",C(6)
460 PRINT#1,"GRAIN CLEAVAGE STRENGTH",C(5)
465 IFB$="YES"THEN467
466 PRINT#1,"TENSILE AXIS"; A$ "GRAIN"
467 PRINT#1,
468 PRINT#1,"APPL.STRESS      P(FAIL)
469 PRINT#1,
470 RETURN
499 DIMF(15)
500 INPUT"GRAIN-LOWER LIM.";F(1)
530 INPUT"GRAIN-UPPER LIM.";F(2)
540 INPUT"K1C-LOWER LIM.";F(3)
550 INPUT"K1C-UPPER LIM.";F(4)
560 INPUT"PORE-LOWER LIM.";F(5)
570 INPUT"PORE-UPPER LIM.";F(6)
580 INPUT"CLEAVAGE-LOWER LIM.";F(7)
590 INPUT"CLEAVAGE-UPPER LIM.";F(8)
600 RETURN
620 A=1
630 B=RND(A)
640 C(2)=(F(2)-F(1))*B+F(1)
650 B=RND(A)
660 C(3)=(F(4)-F(3))*B+F(3)
670 B=RND(A)
680 C(4)=(F(6)-F(5))*B+F(5)
690 B=RND(A)
700 C(5)=(F(8)-F(7))*B+F(7)
710 RETURN
```

eqns. 5.6, 5.9, 5.8

print commands

upper & lower limits of experimental uncertainty

random selection of parameter between upper and lower limits